MAGNETIC TRANSITIONS IN $BiFeO_3$ AND $Ca(Fe_{1/2}Nb_{1/2})O_3$ WITH AND WITHOUT SUBSTITUTIONAL DISORDER

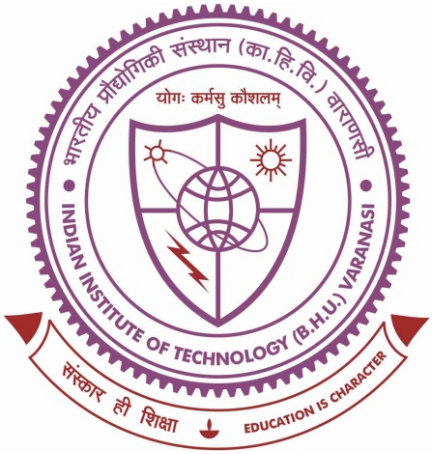

Thesis submitted in partial fulfillment for the Award of Degree

Doctor of Philosophy

By

Arun Kumar

SCHOOL OF MATERIALS SCIENCE & TECHNOLOGY
INDIAN INSTITUTE OF TECHNOLOGY
(BANARAS HINDU UNIVERSITY)
VARANASI - 221005
INDIA

Roll No. 13111002

2019

Dedicated to

Prof. Dhananjai Pandey

&

My Beloved Family

CERTIFICATE

It is certified that the work contained in the thesis titled *" MAGNETIC TRANSITIONS IN $BiFeO_3$ AND $Ca(Fe_{1/2}Nb_{1/2})O_3$ WITH AND WITHOUT SUBSTITUTIONAL DISORDER "* by *"ARUN KUMAR"* has been carried out under my supervision and that this work has not been submitted elsewhere for a degree.

It is further certified that the student has fulfilled all the requirements of Comprehensive, Candidacy and SOTA for the award of Ph.D. degree.

Date: 31.7.2019

Place: Varanasi

D Pandey

Prof. Dhananjai Pandey
(Supervisor)
School of Materials Science & Technology
Indian Institute of Technology
(Banaras Hindu University)
Varanasi

Institute Professional/संस्थान आचार्य
School of Materials Science & Technology/पदार्थ विज्ञान एवं प्रौद्योगिकी स्कूल
Indian Institute of Technology/भारतीय प्रौद्योगिकी संस्थान
(Banaras Hindu University) वाराणसी

DECLARATION BY THE CANDIDATE

I, ***ARUN KUMAR***, certify that the work embodied in this Ph.D. thesis is my own bonafide work carried out by me under the supervision of **PROF. DHANANJAI PANDEY** for a period from **JULY 2013** to **JULY 2019** at the **SCHOOL OF MATERIALS SCIENCE AND TECHNOLOGY**, Indian Institute of Technology (BHU), Varanasi. The matter embodied in this Ph.D. thesis has not been submitted for the award of any other degree/diploma. I declare that I have faithfully acknowledged and given credits to the research workers wherever their works have been cited in my work in this thesis. I further declare that I have not willfully copied any other's work, paragraphs, text, data, results, *etc*., reported in journals, books, magazines, reports dissertations, thesis, *etc*., or available at websites and have not included them in this thesis and have not cited as my own work.

Date. 31.07.2019

Place: Varanasi

Arun Kumar

(Arun Kumar)

CERTIFICATE BY THE SUPERVISOR

This is to certify that the above statement made by the candidate is correct to the best of my knowledge.

Prof. Dhananjai Pandey
(Supervisor)
School of Materials Science & Technology
Indian Institute of Technology
(Banaras Hindu University)
Varanasi

Institute Professor/संस्थान आचार्य
School of Materials Science & Technology/पदार्थ विज्ञान एवं प्रौद्योगिकी स्कूल
Indian Institute of Technology/भारतीय प्रौद्योगिकी संस्थान
(Banaras Hindu University), Varanasi/काशी हिन्दू विश्वविद्यालय

Dr. A. K. Singh
(Coordinator)
School of Materials Science & Technology
Indian Institute of Technology
(Banaras Hindu University)
Varanasi

Coordinator/समन्वयक
School of Materials Science & Technology/पदार्थ विज्ञान एवं प्रौद्योगिकी स्कूल
Indian Institute of Technology/भारतीय प्रौद्योगिकी संस्थान
(Banaras Hindu University), Varanasi/काशी हिन्दू विश्वविद्यालय, वाराणसी

COPYRIGHT TRANSFER CERTIFICATE

Title of the Thesis: "***Magnetic Transitions in $BiFeO_3$ and $Ca(Fe_{1/2}Nb_{1/2})O_3$ With and Without Substitutional Disorder***"

Candidate's Name: Mr Arun Kumar

Copyright Transfer

The undersigned hereby assigns to the Indian Institute of Technology (Banaras Hindu University), Varanasi all rights under copyright that may exist in and for the above thesis submitted for the award of the *Doctor of Philosophy*.

Date. 31.07.2019

Place: Varanasi

Arun Kumar

(Arun Kumar)

Note: However, the author may reproduce or authorize others to reproduce materials extracted verbatim from the thesis or derivative of the thesis for author's personal use provided that the source and the Institute's copyright notice are indicated.

Acknowledgements

First and Foremost, I wish to express my sincere gratitude to my esteemed supervisor, Prof. Dhananjai Pandey, for his guidance, support and valuable suggestions throughout my Ph.D. work. His constant monitoring and interest in my work over the last six years will always remain as a happy memory. His patient and enthusiastic approach for my training in the field of crystallography, multiferroics and structural phase transitions cannot be expressed in words and I will always remain thankful to him.

I would also like to express my gratitude towards the faculty members of the School of materials Science and Technology, Prof. R. Prakash, Prof. P. Maiti, Dr. (Mrs) C. Rath, Dr. A. K. Singh (Coordinator), Dr. C. Upadhyay, Dr. A. K. Mishra (DPGC convener), Dr. S. K. Mishra, and Dr. S. Singh, Dr. S. R. Singh, Prof. J. Kumar, Dr. Ashish Singh for providing constant encouragement and invaluable suggestions during my PhD work which greatly helped me to complete my work with confidence.

I am very grateful to Dr. S. D. Kaushik, Dr. V. Siruguri, BARC, Mumbai, and Dr. A. Senyshyn, FRM II, Germany, for providing powder neutron diffraction data,

I am also very thankful to my external RPEC member Dr. Preetam Singh (Ceramic Engg., IIT BHU), for their valuable suggestions and help during my PhD work.

I would like to express my extreme gratefulness towards my seniors; Dr. A. Singh, Dr. S. Bhattacharjee, Late Dr. R. S. Solanki, Dr. S. Tripathi, Dr. J. P. Patel, Mr. Pappu Kumar, Dr. V. Tiwari, Dr. D. K. Patel, Dr. A. Upadhyay, Dr. A. Mahanta, Dr. Madhu, Mr. S. Pandey, Mr. S. Kumar, for helping me during whole period of my PhD work, whenever I needed.

Words fail to express my earnest thanks to all my friends: Shivam, Girish, Nirmal, Vinay, Vaibhav, Sanjeev, Vivek, Himansu, Pramod, Narendra, Arpan, Preeti, Pinki, Dinesh, Chandrabhal, Rajesh, Kamini, Sachchidanand, Khusbu, Amodini, Farheen for giving me moral support, pleasant company and confidence to complete my work with a 'smile'.

I am also thankful to all my juniors: Keshav, Aravintha, Satyaveer, Anand, Sandeep, Priyanka, Anupama, Aparna, Bharti, Richa, Pragya, Dipti, Majari, Monika, Nitesh, Anupam, Amit, Deepti, Pragyanand, Bisnu, Shyam Babu, Gaurav Chandra, Manish, Krishna Kant, Raman, Nisha, Gaurav, Ishita, Aditya, Vikas, Payal, for providing pleasant, encouraging and friendly environment.

I am also very thankful to technical and non-technical staff of my school: Mr. Amarnath, Ambresh Rai, Kallu Ram, Ashwani, Sitaram Tiwari, Samir Dubey, Mahendra, Dharmendra, Waris, Awanish, Ankit, Sudhakar, Dinesh, Sajan and Jaislaal for the cooperation and help. Special thanks to Mr. Amod Kumar Pandey and Kumar bhaiyya for the help throughout my PhD work.

I would like to express my heart-felt gratitude towards my parents Sri Balbeer Prasad and Smt. Dev Mani for their constant encouragements, moral support and blessing at every step of my life cannot be expressed in words. I am greatly thankful to my elder sister Mrs. Saroj Kumari for their continuous support and encouragement throughout my life. My special thanks are due to my younger sister Ms. Annapurna and brothers Mr. Ankit Kumar and Mr. Anuj Kumar for his love and affection. My love and wishes are always with them. I would also like to express my love and wishes to my niece Arushi and Palak.

*Finally, I thank **GOD** for giving me strength to complete my thesis successfully.*

Date. 31.07.2019

Place: Varanasi

Arun Kumar

(Arun Kumar)

Table of Contents

List of Figures

List of Tables

Abbreviations

AFM	Antiferromagnetic
CFMS	Cryogen Free Measurement System
CSG	Cluster Spin-Glass
CCR	Close Cycle Refrigerator
C-W	Curie-Weiss
A-T	de Almeida-Thouless
DSC	Differential Scanning Calorimetry
DTA	Differential Thermal Analysis
DFT	Density Functional Theory
D-M	Dzyaloshinskii-Moriya
EDX	Energy Dispersive X-ray Spectroscopy
EPMA	Electron Probe Micro Analyzer
FM	Ferromagnetic
FIM	Ferrimagnetic
Irrep	Irreducible Representation
G-T	Gabay-Toulouse
PM	Paramagnetic
eeo	Even-Even-Odd
ooo	Odd-Odd-Odd
ooe	Odd-Odd-Even
FC	Field Cooled
LST	Lyddane-Sachs-Teller
LO	Longitudinal Optical
LRO	Long-Range Ordered
ME	Magnetoelectric

NPD	Neutron Powder Diffraction
pc	Pseudo cubic
T_{max}	Peak Temperature
PPMS	Physical Properties Measurement System
PDF	Pair Distribution Function
RKKY	Ruderman-Kittel-Kasuya-Yosida
RFE	Relaxor Ferroelectric
SPM	Superparamagnetic
SEM	Scanning Electron Microscope
SXRD	Synchrotron X-ray Powder Diffraction
SRO	Short Range Ordered
TO	Transverse Optical
RC	Time Constant
TRM	Thermoremanent Magnetization
VTI	Variable Temperature Insert
V-F	Vogel–Fulcher
VSM	Vibrating Sample Magnetometer
XRD	X-ray Powder Diffraction
XPS	X-ray Photoelectron Spectroscopy
ZFC	Zero Field Cooled

Symbols

T_c	Curie Temperature
C	Curie constant
H_C	Coercivity at M=0
ΔP_s	Change in Spontaneous Polarization
θ_{CW}	Curie-Weiss Temperature
ξ	Correlation Length
χ_{DC}	DC Magnetic Susceptibility
Θ_D	Debye Temperature
E	Electric Field
μ_{eff}	Effective Magnetic Moment
ω	Frequency
E	External Electric Field
H	Magnetic Field
P_s	Spontaneous Polarisation
M_s	Spontaneous Magnetization
β	FWHM
ε	Dielectric Constant
$\varepsilon'(\infty)$	High Frequency Dielectric Constant
$\varepsilon'(0)$	Static Dielectric Constant
$1/\chi$	Inverse of Susceptibility
T_{irr}	Irreversibility Temperature
$\tan\delta$	Loss Tangent
C_p	Specific Heat
C_m	Magnetic Specific Heat
C_l	Lattice Specific Heat
T_N	Néel Temperature

χ_3	Nonlinear Susceptibility (Third Hormonic)
c_p	Percolation Threshold Concentration
τ	Relaxation Time
T_f	Spin-Glass Freezing Temperature
T_{SG}	Spin-Glass Transition
SG	Spin Glass
$\chi(\omega, T)$	AC Susceptibility
D	Single Ion Anisotropy
T	Temperature
T_w	Waiting Temperature
t_w	Waiting temperature
γ	Anti-Phase Tilt Angles
φ	In-Phase Tilt Angles

Preface

Study of spin glass (SG) transition in dilute and concentrated disordered magnetic systems has been a time-honoured problem in the field of solid state and materials sciences. In concentrated systems with disorder content close to the percolation threshold, the long-range ordered (LRO) percolative phase, for both the Ising and Heisenberg systems, has been reported to undergo another transition to the SG state. There are several controversial issues that continue to remain unresolved for such systems: (1) What is the true ground state? (2) Does the LRO phase coexists with the SG phase in the ground state? (3) If both the phases do coexist, what is the proof that the SG phase has resulted from the same magnetic sublattice that led to the LRO phase? (4) Is the coexistence of SG phase with the LRO phase due to coexistence of isolated short range ordered (SRO) superparamagnetic (SPM) clusters with LRO clusters on two different magnetic sublattices as a result of segregation and clustering? The theoretical treatments for such concentrated Ising as well as Heisenberg systems predict that the SG state can result from freezing of either the longitudinal or transverse components of the spin in the LRO phase and that it can coexist with the LRO phase on the same magnetic sublattice. These theoretical predictions cannot be verified using macroscopic measurements (DC and AC susceptibilities) alone and require microscopic tools (e.g. neutron scattering, Mössbauer spectroscopy etc.) which have been used for a few systems in support of the longitudinal/transverse freezing model in both the Ising and Heisenberg systems. More interestingly, yet another interesting situation has been predicted theoretically for concentrated Heisenberg systems with small single ion anisotropy (D) as compared to the magnetic exchange interaction (J), where both the longitudinal and transverse components can freeze successively leading to two SG transitions below the so-called Almeida-Thouless (A-T) and Gabay-Toulouse (G-T) lines, respectively. While evidence

for two SG transitions has been obtained in several systems using macroscopic measurements, the results are rather controversial as it is not clear if the LRO and the SG phases are formed on the same or separate magnetic sublattices. Unambiguous evidence confirming the occurrence of two SG transitions and coexistence of the two SG phases (SG1 and SG2) with the LRO phase on the same magnetic lattice using microscopic tools are rather sparse in such systems.

SG phase has been reported in several multiferroic systems also. Unlike the conventional SG systems, the multiferroic SG systems offer the possibility of verifying the theoretical predictions for concentrated systems through a study of the change in ferroelectric polarization and strain as a result of magnetoelectric and magnetoelastic couplings across the SG transition using diffraction techniques. In this context, it is interesting to note that the single ion anisotropy (D) of Fe^{3+} in the well-known multiferroic compound $BiFeO_3$, a canonical Heisenberg system, is rather small as compared to exchange interaction (J) D/J ~0.001 which falls within the range where two SG phases have been reported in non-multiferroic disordered systems like MgMn. Further, $BiFeO_3$ has been reported to undergo a SG transition around 25K on the basis of magnetic AC susceptibility studies as a function of temperature and frequency ($\chi(\omega, T)$) but there are several controversies associated with it including lack of understanding of the origin of the SG transition in ordered compound without any apparent disorder or geometrical frustration. In addition to the low temperature SG transition, another transition around 250K has been reported to have SG character based on the study of history dependent effects in DC magnetization measurements.

One of the major achievements of the present thesis is in providing the first experimental evidence in support of theoretical predictions for two SG phases below the A-T and G-T lines in coexistence with the LRO phase on the same magnetic sublattice in

the multiferroic solid solution $(Bi_{1-x}Ba_x)(Fe_{1-x}Ti_x)O_3$ (BF-xBT) system using a combination of macroscopic (DC magnetization M(H, T), relaxation of thermoremanent magnetization M(t), AC susceptibility ($\chi(\omega, T)$) and specific heat (C_p)) and microscopic (x-ray and neutron scattering) measurements. $BaTiO_3$ based solid solution of $BiFeO_3$ was selected for this study as this solid solution system has received considerable attention in recent years due to its large ferroelectric polarization, highest depolarization temperature for piezoelectric applications and destruction of spin cycloid leading to large remnant magnetization as well linear magnetoelectric coupling. From the analysis of neutron and x-ray diffraction data on this system, we have presented evidence for a succession of two SG transition below the Néel transition with two distinguishing features: (1) very strong and moderate magnetoelastic couplings associated with the SG1 and SG2 transitions, respectively, as revealed by the change in the unit cell volume (ΔV) with respect to the theoretically predicted values based on Debye-Grüneisen model, that scales quadratically with the spontaneous magnetization (M_s^2) and (2) strong magnetoelectric coupling at both the SG transitions as revealed by the large change in spontaneous polarization (ΔP_s), calculated from the atomic coordinates obtained by Rietveld refinements of the nuclear structure and the Born effective charges (BEC), across the two SG transitions. We have also constructed a phase diagram showing all the magnetic transitions occurring below room temperature. In this context, we have also revisited the SG and other low temperature transitions in $BiFeO_3$ which have been quite controversial. Finally, we have also carried out a careful study of the low temperature specific heat of $BiFeO_3$ and its solid solutions to present evidence for coexistence of SG and LRO antiferromagnetic (AFM) phases, in the ground state. To the best of our knowledge, this is the first evidence for the coexistence of the two phases using specific heat measurements.

The second major contribution of this thesis is about the origin of SG phase in complex perovskites with a general formula of $A(Fe_{1/2}B'_{1/2})O_3$, where A = Pb, Ba, Sr, Ca and B' = Nb, Ta, Sb and W. These compounds were synthesized by Russian Scientists nearly six decades back to achieve multiferroicity, where the magnetic Fe^{3+} would provide magnetic ordering and B' ion with $4d^0$ and $5d^0$ configuration would lead to ferroelectric ordering. Among such complex perovskites with B-site disorder, $Pb(Fe_{1/2}Nb_{1/2})O_3$ (PFN) has emerged as a model type-I multiferroic niobate system like $BiFeO_3$. It undergoes a paraelectric (space group Pm-3m) to ferroelectric (space group Cm) transition at T_c ~385K, G-type LRO AFM phase below T_N ~150 K and a SG freezing at T_f ~10 K. The LRO AFM is of percolative type in which all the six nearest neighbour superexchange Fe^{3+}-O^{2-}-Fe^{3+} bonds are not necessarily satisfied everywhere (unless there is clustering and segregation of Fe). Interestingly, this LRO AFM phase is found to coexist with the SG phase below T_f ~10K but there is a controversy about the exact origin of the coexistence of the two phases. According to one of these models based on macroscopic measurements, the LRO AFM phase of PFN results from the infinite percolative clusters of Fe^{3+} spins while the glassy phase is a consequence of the freezing of the finite size isolated clusters with uncompensated Fe^{3+} spin. This model implies that the SG and LRO AFM phases occur on two separate sublattices. However, no direct evidence for the presence of such nanoscale heterogeneities has been presented in the literature as it requires microscopic probes like neutron scattering and Mössbauer studies. In the second model, which is supported by microscopic measurements (e.g., neutron and Mössbauer techniques), on the other hand, the SG phase is argued to result from the LRO AFM sub-lattice system itself due to freezing of the transverse component of the spin in a glassy manner. Unlike PFN, the Pb-free site- and charge-disordered $A(Fe_{1/2}B'_{1/2})O_3$ type compounds with A = Ba, Sr, Ca and B' = Nb and Ta do not display LRO ferroelectric and

AFM phases, despite Nb^{5+} being a ferroactive ion of $4d^0$ type and the concentration of $3dFe^{3+}$moments at the B-site being higher than the critical percolation threshold value, respectively. However, the Pb-free complex perovskite niobates and tantalates are also reported to exhibit SG freezing at low temperatures like PFN, though with a higher T_f ~25K. Since the controversy about the origin of the SG phase in PFN is essentially due to the coexistence of the LRO and the SG phases, the Pb-free complex perovskite niobates and tantalates with no such coexistence offer an excellent platform to verify the origin of SG phase in such complex perovskites. With this objective in mind, we have presented the results of a comprehensive study on $Ca(Fe_{1/2}Nb_{1/2})O_3$ (CFN) using both macroscopic and microscopic measurements. The previous reports of SG state in Pb-free complex perovskite niobates and tantalates, including CFN, were restricted to the observation of the history dependent irreversibility of zero field cooled (ZFC) and field cooled (FC) dc magnetization M(T) plots only which is not conclusive since such an irreversibility can also occur due to superparamagnetic (SPM) blocking. Further, unlike PFN, there is no neutron scattering study which could have provided direct evidence for the presence of short-range ordered (SRO) AFM spin clusters in such compounds. We have used multiple criteria based on dc magnetization (M(T, H), M(t)) and AC susceptibility ($\chi(\omega, T)$) measurements for confirming the existence of the SG phase in CFN. In addition, we use neutron scattering measurements to confirm the presence of SRO AFM spin clusters in CFN which take part in the SG freezing with T_f ~25K.

The third major achievement of this thesis is about the absence of LRO magnetic phases in Pb-free complex perovskites of $A(Fe_{1/2}B_{1/2})O_3$ where A = Ca, Sr, Ba and B =Nb, Ta, Sb, W etc whereas their Pb-based counterparts like $Pb(Fe_{1/2}Nb_{1/2})O_3$ do exhibit LRO AFM transition. This has been an intriguing issue since the Fe^{3+} content at the B-site of such Pb-free compounds is within the percolation threshold range required for

developing LRO AFM phase. Using neutron diffuse scattering studies in conjunction with the change in the structural parameters, we have presented first evidence that $Ca(Fe_{1/2}Nb_{1/2})O_3$ (CFN) is an incipient AFM with T_N close to 175K at the verge of acquiring LRO AFM state. We also demonstrate that the LRO AFM phase can be stabilized in CFN through a substituting of 10% $BiFeO_3$ or $LaFeO_3$, which, we believe, enables CFN to reach the critical percolation threshold concentration of Fe^{3+} ions in the magnetic sublattice. This study involves not only magnetization studies but also detailed neutron scattering studies.

The thesis is organized into seven chapters,

Chapter I gives a brief introduction to various types of transitions in perovskites along with an overview of the current literature on the systems of study.

Chapter II presents detailed study of the magnetic transitions in $BiFeO_3$. Based on the results of dc magnetization, ac susceptibility, dielectric permittivity and XRD studies, we conclude that the low temperature transitions of $BiFeO_3$ occurring around 25 K, 150 K and 260 K are intrinsic to $BiFeO_3$. We have also resolved the issue of physically unrealistic situation of $T_{SG} > T_f$ where T_f is the field (H) and frequency (ω) dependent SG freezing temperature (i.e., $T_f(\omega, H)$) whereas T_{SG} is the SG transition temperature in the limit of H and ω tending towards zero reported by previous workers and discovered magnetoelastic coupling at the SG freezing temperature T_f ~25K which confirms the intrinsic nature of the SG transition in this system.

Chapter III presents results of spin-glass transitions in solid solutions of $BiFeO_3$ with $BaTiO_3$. It is shown that the anomalous frequency dependence of ac susceptibility in the SG phase of $BiFeO_3$ is not linked with the spin cycloid as it is present even after its

destruction as a result of the solid solution formation. Using a series of macroscopic and microscopic techniques, we have presented evidence for two SG transitions in the BF-0.20BT system and verified for the first time the theoretical predictions of SG transition in Heisenberg systems about the successive freezing of the longitudinal and transverse components of the spins leading to two spin glass phases which coexist with the LRO AFM phase. We have also presented evidence for magnetoelastic and magnetoelectric couplings at the two spin glass transitions.

Chapter IV presents results of specific heat studies on (1-x)$BiFeO_3$-x$BaTiO_3$ solid solutions with x = 0, 0.10, 0.20, 0.40, and 0.60. Careful analysis of the magnetic contribution to the total specific heat, obtained after subtracting the phonon contributions, confirms that the ground state consists of coexisting LRO AFM and SG phases, as shown by other techniques in the preceding chapter.

Chapter V presents the results of a detailed study on SG transition in $Ca(Fe_{1/2}Nb_{1/2})O_3$ (CFN) with a view to address the existing controversies about the origin of SG phase in such complex perovskites. We have presented evidence for the existence of short range ordered AFM clusters in CFN which freeze below T_f ~25K into a cluster spin glass state.

Chapter VI addresses one of the biggest puzzle in the Pb-free site- and charge-disordered $A(Fe_{1/2}B'_{1/2})O_3$ type compounds with A = Ba, Sr, Ca and B' = Nb and Ta which do not display LRO ferroelectric and AFM phases, despite Nb^{5+}/Ta^{5+} being ferroactive ions of $4d^0$ type and the concentration of 3dFe^{3+}moments at the B-site being higher than the typical percolation threshold value, respectively. Taking $Ca(Fe_{1/2}Nb_{1/2})O_3$ as an example, we explain why such compounds do not exhibit LRO AFM transition using DC magnetization, dielectric, XRD and neutron diffraction techniques. We use percolation concept to stabilize the LRO AFM state of $Ca(Fe_{1/2}Nb_{1/2})O_3$ by substituting 10% $BiFeO_3$

or $LaFeO_3$. We confirm the appearance of LRO AFM state in these solid solutions by magnetization and neutron scattering studies.

Chapter VII gives a brief summary of the main findings of the present work and suggestions for future investigations.

Chapter 1 Introduction and Literature Review

1.1. Introduction

In this chapter, we present a brief introduction to the various phenomena relevant to the subject of study and a brief review on the multiferroic $BiFeO_3$ and its solid solutions with perovskites as well as magnetic transition in complex perovskites of the type $A(B'_{1/2}B''_{1/2})O_3$.

1.2. Perovskites:

The oxide materials with chemical formula ABO_3, where 'A' and 'B' are two cations and 'O' is an anion are classified as perovskites, e.g. $SrTiO_3$, $BaTiO_3$, $CaTiO_3$ etc. The geometrical requirement for the formation of the perovskite structure is given by the so-called Goldschmidt criterion [1] in terms of the ionic radii R_A, R_B and R_O of A, B and the O ions, respectively:

$$t = \frac{R_A + R_O}{\sqrt{2}(R_B + R_O)} \qquad \ldots\ldots \quad (1.1)$$

where t is known as the tolerance factor. It measures the degree of distortion in the perovskite structure. The perovskite structure is stable if t lies in the range $0.80 < t < 1.1$. For $t = 1$, the structure is expected to adopt ideal cubic perovskite structure (e.g. $SrTiO_3$). For $t > 1$, the compounds are known to show ferroelectricity (e.g. $BaTiO_3$). The compounds with $0.8 < t < 0.95$ show distorted perovskite structure (e.g. $CaTiO_3$, $SrZrO_3$).

The ideal cubic perovskite structure belongs to the $Pm\bar{3}m$ space group symmetry and the unit cell consists of one formula unit of ABO_3 in which all the ions occupy the special Wyckoff positions given below,

A cation at 1(a) Wyckoff site with position (0, 0, 0)

B cation at 1(b) Wyckoff site with (1/2, 1/2, 1/2) positions

O anion at 3(c) Wyckoff site with (1/2, 1/2, 0) positions.

A schematic representation of the cubic perovskite structure is given in Fig. 1.1. In this perovskite structure, the B-site cations occupy the center of the unit cell and form BO_6 octahedra while the A-site cations occupy the eight corners in the unit cell and are coordinated with twelve oxygen anions.

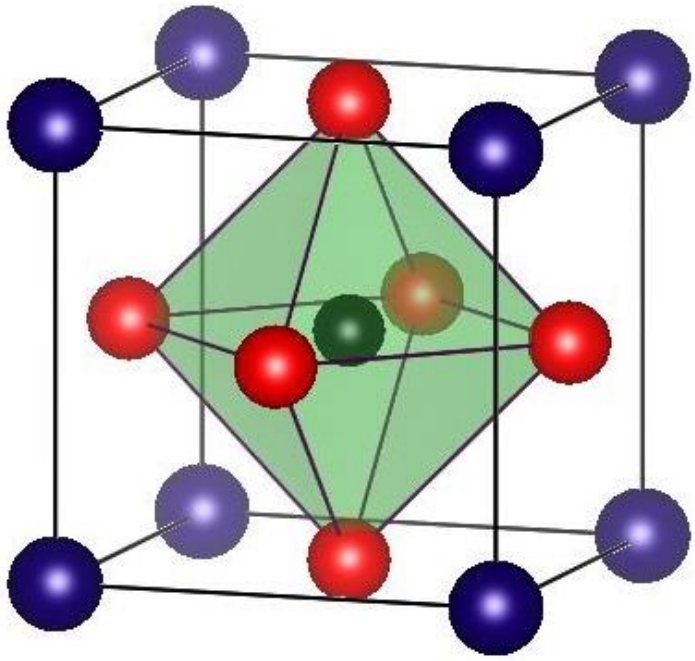

Figure 1.1: Schematic view of the ideal cubic perovskite structure: A cation occupy on the cubic corner position (0, 0, 0) (shown by blue sphere), B cation sits on the (1/2, 1/2, 1/2) position (shown by dark green sphere) and O anion sits on the face diagonal (1/2, 1/2, 0) positions (shown by red sphere).

1.3. Ferroelectricity:

The ferroelectric materials possess spontaneous electric polarization (P), even in the absence of an external electric field (E), whose direction can be switched by applying an electric field. This phenomenon is known as ferroelectricity and is usually observed in the polar class of non-centrosymetric crystals. The typical P-E hysteresis loop for ferroelectric materials is shown in Fig. 1.2. The development of the polar axis in ferroelectrics is usually attributed to a structural phase transition between high

temperature paraelectric phase to low temperature ferroelectric phase at a characteristic temperature called Curie temperature. The transition from the paraelectric to ferroelectric phase is accompanied by pronounced anomaly in the dielectric permittivity. The temperature dependence of dielectric permittivity above the transition temperature obeys Curie-Weiss law,

$$\varepsilon' \approx \frac{C}{T-T_c} \quad , T>T_C \qquad \ldots\ldots(1.2)$$

where ε' is dielectric permittivity or dielectric constant, C is the Curie constant and T_C is the Curie-Weiss temperature. The Curie-Weiss temperature for ferroelectric materials is generally positive. The examples of ferroelectric materials are $BaTiO_3$, $PbTiO_3$ and $KNbO_3$ [2].

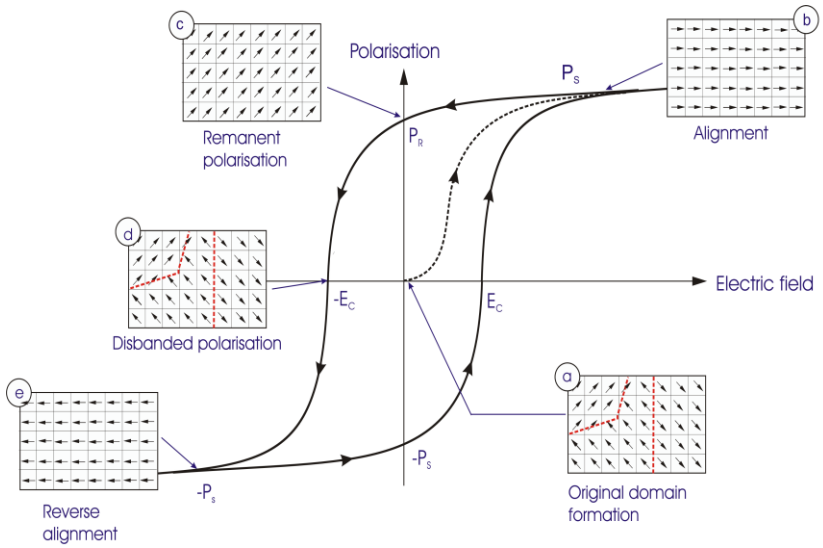

Figure 1.2: Typical P-E hysteresis loop for ferroelectric materials. P_S = Saturation polarization, P_R = Remnant polarization, E_C = Coercive field [3].

1.4. Antiferroelectricity:

Antiferroelectric materials possess antiparallel displacement of ions with respect to their ideal cubic positions. In a ferroelectric phase transition, the paraelectric unit cell size is slightly distorted due to the cationic and/or anionic displacements. But in the case of

antiferroelectric phase transition, the ionic displacements occur in equal and opposite directions in pairs. Thus the unit cell of the antiferroelectric phase becomes multiple of the unit cell of the paraelectric phase giving rise to appearance of characteristic superlattice reflections in diffraction pattern. Just like ferroelectric materials, the antiferroelectric materials also show a dielectric anomaly at the paraelectric to antiferroelectric phase transition. The temperature dependence of the dielectric constant in the paraelectric phase also follows Curie-Weiss law with negative Curie-Weiss temperature (θ) [4]:

$$\varepsilon' = \frac{C}{(T+\theta)} \qquad \ldots\ldots\ldots(1.3)$$

The transition temperature for antiferroelectric materials is commonly known as Néel temperature (T_N). In an antiferroelectric material, it is possible to induce ferroelectric ordering by application of sufficiently strong electric field. This feature is manifested in the 'double' hysteresis loop shown in Fig. 1.3. However, such a switching can be observed only if the antiferroelectric to ferroelectric switching field does not exceed the breakdown strength of the material. The most common examples of antiferroelectric materials are $PbZrO_3$, $NaNbO_3$, $PbHfO_3$ [2,5,6].

1.5. Ferrielectricity:

If a material exhibits ferroelectric order along one axis and antiferroelectric order along the other axes have been termed as ferrielectric materials [7–9]. The internal distribution of ions in ferrielectric material is such that the ferroelectric and antiferroelectric orders exist simultaneously in different directions. The unit cell of ferrielectric phase is a multiple of the unit cell of the paraelectric phase. The Curie-Weiss temperature may be negative/positive for ferrielectric phase transition in close analogy with antiferromagnetic/ferromagnetic phase transitions.

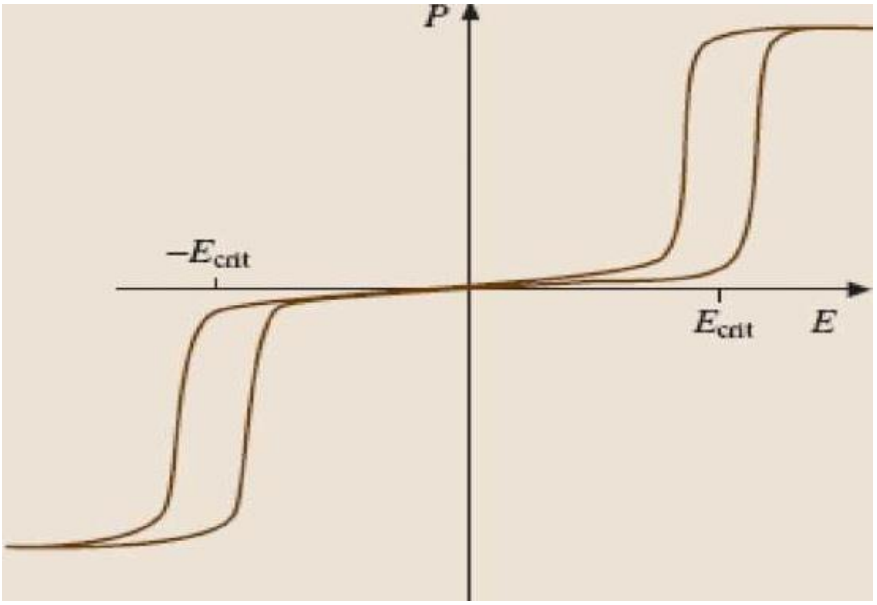

Figure 1.3: Typical hysteresis loop for antiferroelectric materials [10].

1.6. Phase transition driven by soft modes in perovskites:

In ferroelectric and antiferroelectric phase transitions, the atoms move from a high symmetry site in the high temperature phase to a low symmetry site in the low temperature phase through a small displacement. Such types of transitions are called displacive transitions. The displacive structural phase transition in perovskites can be described by soft phonon modes of the high temperature phase. This soft phonon mode is characterized by anomalous decrease in its frequency as the structural phase transition is approached. The temperature dependence of the soft phonon frequency can be expressed as

$$\omega^2 \alpha (T-T_C) \qquad \ldots\ldots\ldots(1.4)$$

A relation between the lattice dynamics and ferroelectric properties can be visualized through Lyddane-Sachs-Teller (LST) relationship [4] which relates the static dielectric constant ($\varepsilon'(0)$) and high frequency dielectric constant (($\varepsilon'(\infty)$) to the frequencies (ω) of the longitudinal optical (LO) and transverse optical (TO) phonon modes at the zone

centre (q = 0) of the Brillouin zone as:

$$\varepsilon'(0)/\varepsilon'(\infty) = (\omega_{LO}/\omega_{TO})^2 \qquad \ldots\ldots\ldots(1.5)$$

As the transverse optic mode frequency $\omega_{TO} \rightarrow 0$, the static dielectric constant shows a peak value. In fact, substituting Eq. (1.4) to Eq. (1.5) gives the well-known Curie-Weiss law for ferroelectric transition.

The structural phase transitions in perovskites are associated with soft modes corresponding to at least one of the symmetry points of the primitive cubic Brillouin zone. A schematic diagram of Brillouin zone of the ideal cubic perovskite structure is shown in Fig. 1.4 [11]. The high symmetry points of the Brillouin zone are described by the 10 symbols: Γ, Δ, Λ, Σ, R, T, M, S, X and Z. In the cubic perovskite structure containing 5 atoms, one expects 15 normal modes of vibration (12 optic and 3 acoustic). Each normal mode is characterized by an irreducible representation (Irrep). The irreps corresponding to the high symmetry points give different displacement pattern and hence play a key role in deciding the distortion of the ideal perovskite structure as a result of phase transition. The cubic to tetragonal phase transition in $BaTiO_3$ results from the freezing of the Γ_{15} soft phonon mode at q = (0, 0, 0) of the cubic Brillouin zone [12]. In $SrTiO_3$, the freezing of R_{25} mode with q = (½, ½, ½) leads to cubic to tetragonal phase transition at 105K involving anti-phase tilting of oxygen octahedra [5,13]. The freezing of the M_3 mode with q = (½, ½, 0) in $NaNbO_3$ leads to cubic to tetragonal phase transition [14].

1.7. Ferrodistortive and antiferrodistortive structural phase transitions:

The ferroelectric or antiferroelectric phase transitions in perovskites are special class of structural phase transition where the transition from the high symmetry phase to low symmetry phase is accompanied by the appearance of the spontaneous polarization or

sublattice polarization. The appearance of the long-rang polar or antipolar order is the characteristic feature of the ferroelectric or antiferroelectric transition. Based on the change in the number of formula units per unit cell, the structural phase transition may be

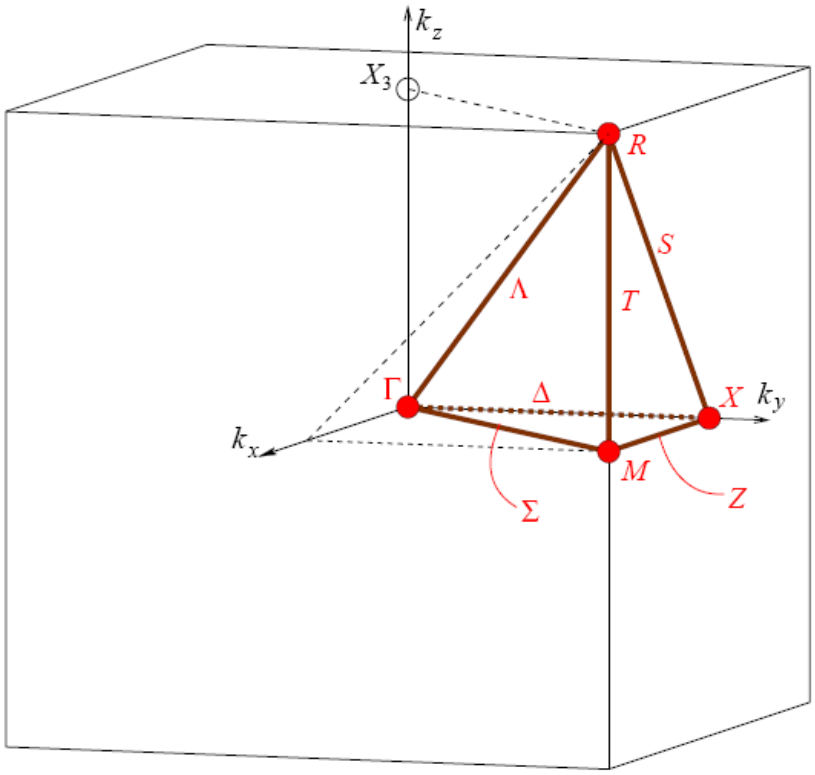

Figure 1.4: Schematic Brilloiun zone of the cubic perovskite structure showing special points [11].

classified as two categories [4]:

(1) Ferrodistortive transitions: In this type of phase transition the number of formula units per unit cell is same as that of the high temperature phase. Such type of phase transitions is always connected with the freezing of soft modes at the Brillouin zone centre (q =0). The typical examples are $BaTiO_3$, $PbTiO_3$ [15,16].

(2) Antiferrodistortive transitions: Here the number of formula units per unit cell is an

integer multiple of the high temperature phase. This type of phase transition corresponds to a freezing of the soft mode with non-zero wave vector ($q \neq 0$). The typical examples are $SrTiO_3$, $CaTiO_3$ [2,13] and also the antiferroelectric transitions [2,5,6].

1.8. Relaxor ferroelctrics:

Relaxor ferroelectrics are known to show very large value of dielectric constant (ε) with diffuse transition in the dielectric constant (ε) versus temperature (T) plot. Relaxors also shows frequency-dispersion in the ε-T plot. The peak temperatures T_m' and T_m'' corresponding to the real (ε') and imaginary (ε'') parts of the dielectric constant are not coincident but $T_m'' < T_m'$ in relaxors. Both the temperatures T_m'', T_m' shift to higher temperatures side with increasing frequency. The Lead (Pb) based perovskites with chemical formula $Pb(B'B'')O_3$ where B' = Mg^{2+}, Ni^{2+}, Zn^{2+}, Sc^{3+} and B'' = Nb^{5+}, Ta^{5+} etc., [17–19] are known to show relaxor ferroelectric behaviour. Several theoretical models such as superparaelectric [19], dipole glass [20], random field [21] random field-random bond [22] have been proposed to explain the relaxor ferroelectric behaviour. Depending upon the relaxational freezing of the polar clusters, most relaxors like $Pb(Mg_{1/3}Nb_{2/3})O_3$ (PMN) [20], $Pb(Sc_{1/2}Ta_{1/2})O_3$ (PST) [23] follow the Vogel-Fulcher law [24] for the polar dynamics:

$$\tau = \tau_0 \exp[E_a/k_B(T-T_{VF})] \qquad \text{…….(1.6)}$$

This is to be contrasted from systems which follow Arrhenius type behaviour [24].

$$\tau = \tau_0 \exp[E_a/k_BT] \qquad \text{…….(1.7)}$$

where E_a is the activation energy, τ_0 is the attempt time (inverse of the attempt frequency), k_B is the Boltzmann constant and T_{VF} is the Vogel-Fulcher freezing

temperature. The well-known examples of Arrhenius type systems are $(CoO)_{0.4}(Al_2O_3)_{0.1}(SiO_2)_{0.5}$ and $(KBr)_{0.5}(KCN)_{0.5}$ [24].

The comparisons of the normal ferroelectric with relaxors are illustrated in Fig. 1.5. Apart from the diffuse nature of the transition in the temperature dependence of the dielectric constant and the characteristics frequency dispersion of T_m' and T_m'', relaxor ferroelectrics exhibit slim P-E hysteresis loop which persist well above T_m' unlike normal ferroelectrics for which it disappears above T_C.

1.9. Ferromagnetism:

Materials which exhibit spontaneous magnetization that is stable and can be switched hysteretically by an applied magnetic field are called ferromagnetic materials. Ferromagnetism is defined as long range ordering of parallel alignment of magnetic spins (moments) resulting in net spontaneous magnetization even in the absence of magnetic field. A ferromagnetic material has domains and due to the presence of domains, magnetization is oriented in different directions. The subsequent alignment and reorientation of the domains depend on the application of a magnetic field, results in a hysteresis loop as shown in Fig. 1.6. Ferromagnetism disappears above a critical temperature T_C called Curie temperature. The magnetic susceptibility above T_C follows Curie-Weiss law as shown in Fig. 1.7 [26]:

$$\chi = \frac{C}{T - T_c} \qquad \ldots\ldots (1.8)$$

where C is the Curie constant and T_C the Curie-Weiss temperature.

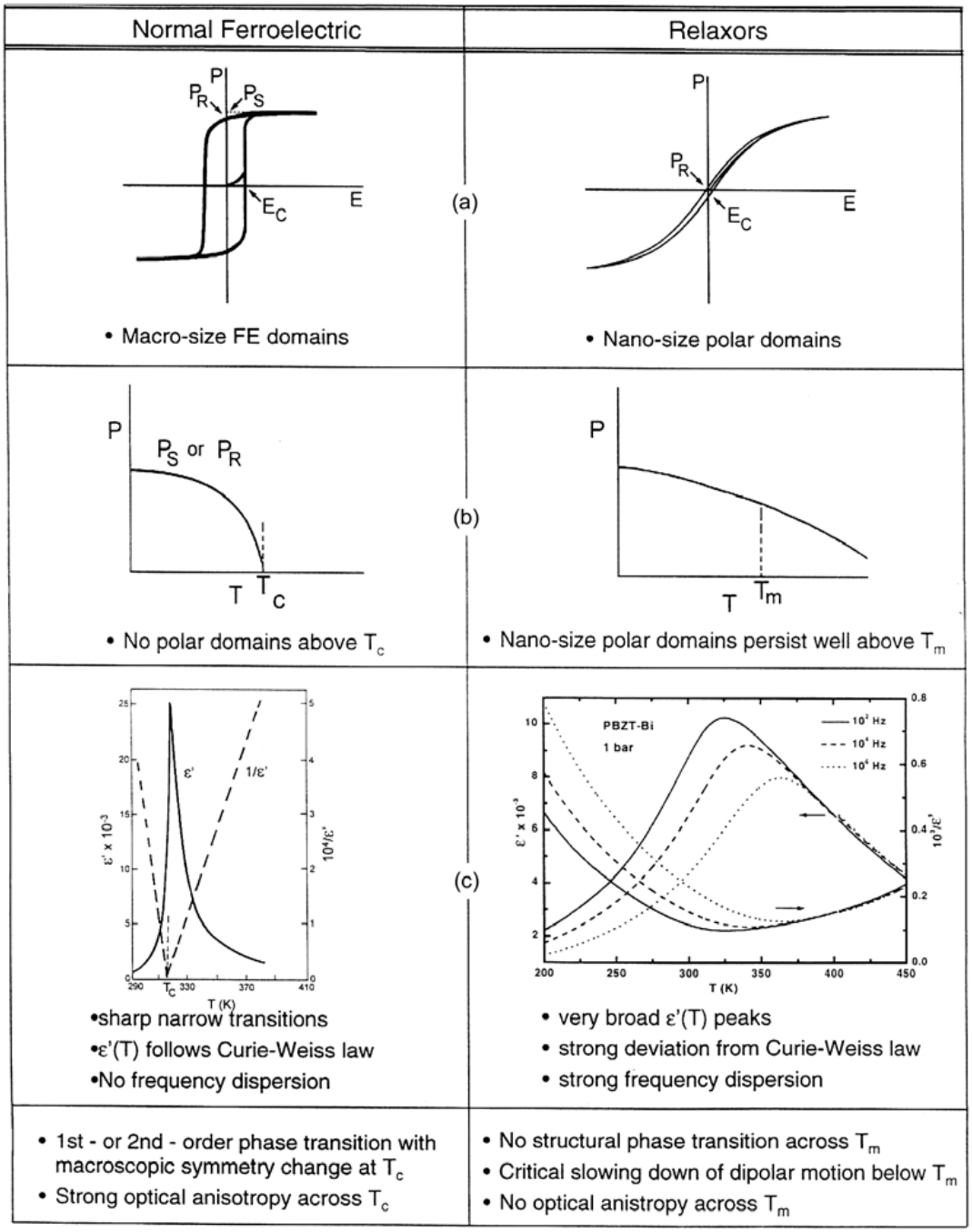

Figure 1.5: Comparison between the properties of normal and relaxors ferroelectrics behaviour [25].

The typical examples are Fe, Co, Ni, Gd, and Dy which show ferromagnetic properties but there are large number of alloys and compounds which also show ferromagnetic properties [26].

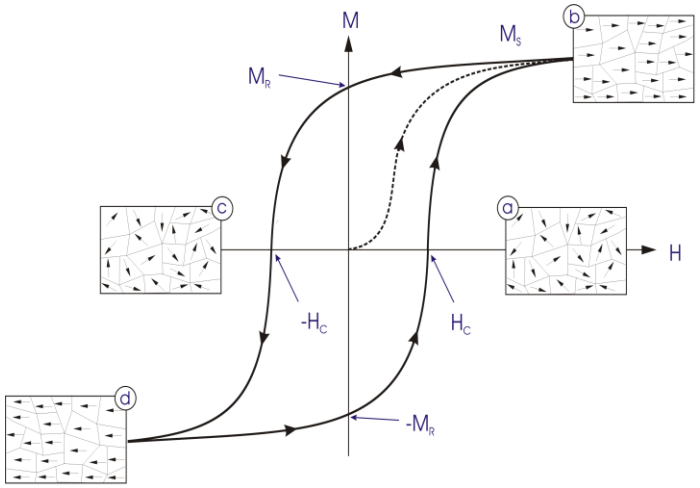

Figure 1.6: M-H Hysteresis Loop for Ferromagnetic materials. M_S is saturation magnetization, M_R is remanent magnetization at H = 0, H_C is coercivity at M = 0 [27].

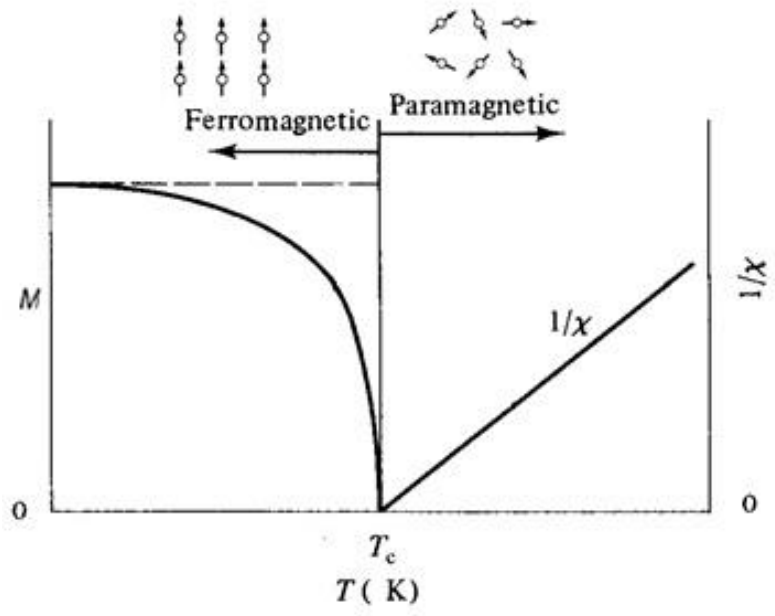

Figure 1.7: Temperature dependence of magnetization (M) and the inverse of the magnetic susceptibility ($1/\chi$) for ferromagnetic material. Reproduced from [26].

1.10. Antiferromagnetism:

In antiferromagnetic materials, the alignment of the spin moments of the neighbouring atoms is antiparallel to each other, and there is no net magnetic moment. The spin structure for the antiferromagnetic materials consists of two or more sublattices

each one of which are ferromagnetically coupled but are antiparallel to the neighbouring sublattice. Antiferromagnetic ordering exists below a critical temperature and above which materials get converted into paramagnetic material. This temperature is called as the Néel temperature (T_N). Antiferromagnetic materials also obey Curie-Weiss law but with a negative value of Curie temperature T_C and are given by the equation [26],

$$\chi = \frac{C}{T + T_c} \qquad \text{..... (1.9)}$$

where C is a Curie constant and T_C the Curie-Weiss temperature. A plot of inverse of susceptibility ($1/\chi$) versus T shown in Fig. 1.8 is a straight line above T_N and this line extrapolates to a negative temperature ($-T_C$) at $1/\chi = 0$. Although, there is no net magnetization in the antiferromagnetic materials but it may exhibit weak magnetization due to spin canting, lattice defects, and uncompensated spins at the surface in the absence of magnetic field. At sufficiently high magnetic fields, the spin direction of one of the magnetic sublattices may rotate and eventually lead to the "spin flop" where all the spins would be aligned in parallel fashion. Because of this rotation and spin flop, magnetization

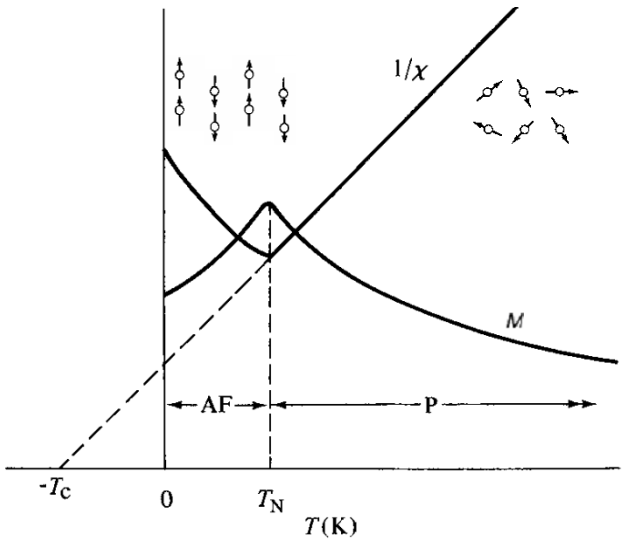

Figure 1.8: Temperature dependence of (M) and inverse of susceptibility ($1/\chi$) for antiferromagnetic material. AF: Antiferromagnetic, P : Paramagnetic [26].

can be induced by an external magnetic field. Depending on the interplane and intraplane coupling within the structure there are many types of antiferromagnetic spin orderings such as A-type, C- type and G-type or E-type shown in Fig. 1.9 [28]. The term “weak ferromagnetism” is used to explain the antiferromagnets with a small canting of spins away from antiparallel alignment. This spin canting is caused by the spin-orbit interaction.

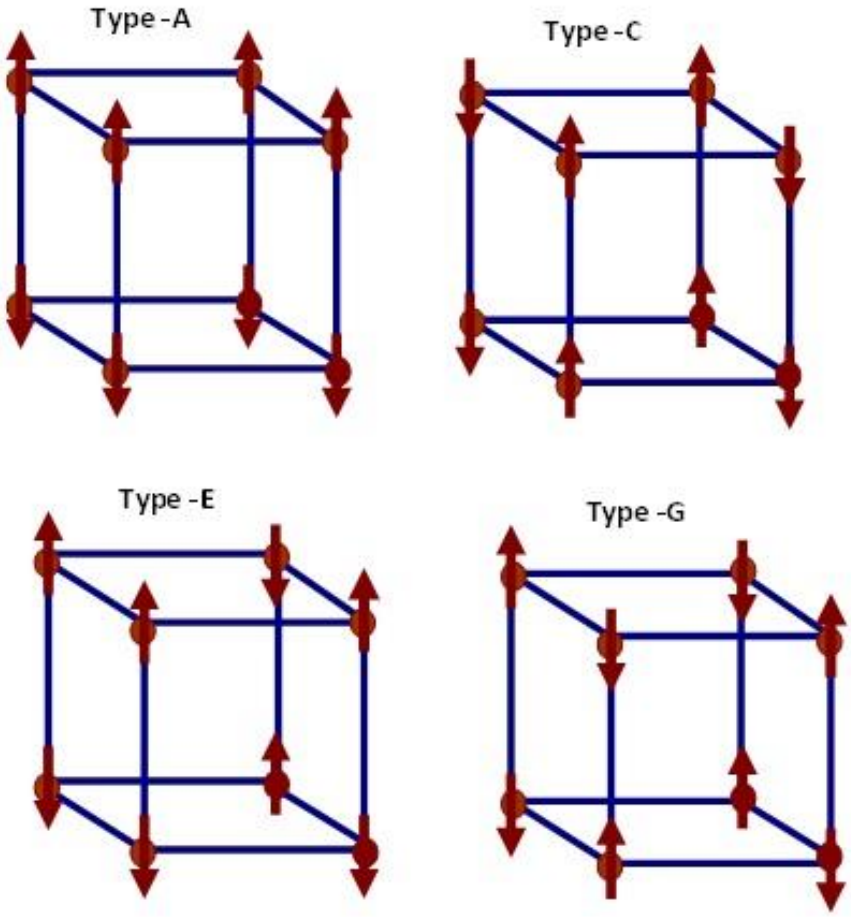

Figure 1.9: Different types of spin structure resulting in different type (A-, C-, G- or E-type) antiferromagnetic ordering [28].

1.11. Ferrimagnetism:

Ferrimagnetic materials differ from antiferromagnetics due to incomplete cancellation of the magnetic moment i.e., the adjacent spins are aligned antiparallel to each other but are unequal in magnitude. Ferrimagnetic materials exhibit spontaneous magnetization, like ferromagnetic materials. They exhibit the phenomena of magnetic saturation and also hysteresis loop. The spontaneous magnetization of a ferrimagnetic material disappears above a critical temperature T_c, with paramagnetic state (Fig. 1.10). The typical examples of ferrimagnetic materials are ferrites (Fe_3O_4), garnets ($Y_3Fe_5O_{12}$) and hexaferrites ($BaFe_{12}O_{19}$) [26]. Ferrimagnetic theory was developed by Néel, in

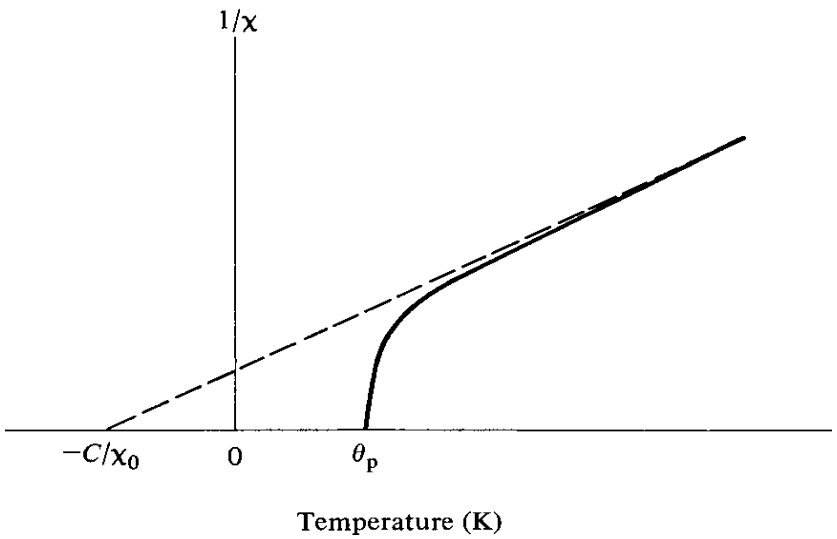

Figure 1.10: Theoretical variation of reciprocal of susceptibility with temperature for a ferrimagnetic above the Curie point [26].

continuation with the theory of antiferromagnetism. The Curie-Weiss law for ferrimagnetic materials up to T_c is given by the equation [26],

$$\chi = \frac{C}{T+\left(\frac{C}{\chi_0}\right)} \qquad \ldots.(1.10)$$

where C is Curie constant. For ferrimagnetic materials, the $(1/\chi)$ vs T plot becomes asymptotic at high temperature.

1.12. Multiferroics:

The "multiferroics" were originally defined as class of materials in which at least 2 of the 4 properties such as ferroelectricity, ferroelasticty, ferromagnetism, and ferrotoroidicity coexist in the same materials and are coupled also [29–32]. This definition has subsequently been expanded to include any for electric dipolar and magnetic spin ordering. Ferroelastics, like ferroelectrics and ferromagnets, have spontaneous strain in the absence stress that is switchable below a characteristic temperature [27–30]. Among the multiferroics, there exists a class of magnetoelectric materials where coupling between ferroelectric and magnetic order parameters occurs such that the magnetization (M) can be switched by the application of an electric field (E) and ferroelectric polarization (P) by the application of a magnetic field (H) [29,30,33]. The magnetoelectric multiferroic materials are interesting from the technological application point of view as they provide an additional degree of freedom in the designing of multifunctional sensors, actuators, storage devices, spintronics etc [30,33–36]. It also offers a challenge to theoretical physicists for understanding the physics behind the coexistence and coupling of the magnetic and ferroelectric order parameters. It has been generally believed that the ferroelectricity in ABO_3 perovskites arises due to the off-centring of the B-site cation and requires empty d-orbital (d^0) while the magnetism requires partially filled d orbitals (d^n) [37,38]. The two conditions appear to be mutually exclusive and therefore the magnetoelectric multiferroics are not so common. However, in the last two decades discovery of new multiferroic compounds like $RMnO_3$ (R=Tb, Dy, Y), $CoCrO_4$, $Ni_3V_2O_8$, $MnWO_4$, $LiCu_2O_2$, $LiCuVO_4$, CuO, $Ba_{0.5}Sr_{1.5}Zn_2Fe_{12}O_{22}$, $Ba_2Mg_2Fe_{12}O_{22}$ etc [36,39,40] in which ferroelectric polarization is induced as a result of

magnetic ordering through inverse D-M interaction. In such multiferroics, the mutually exclusiveness due to d^0 and d^n is avoided. Fig. 1.11 illustrate the various types of mechanism responsible for multiferroicity in multiferroic materials. In general, magnetoelectric multiferroics can be classified into two broad categories type- I and type-II. The difference between the two types of multiferroics is given in Table 1.1.

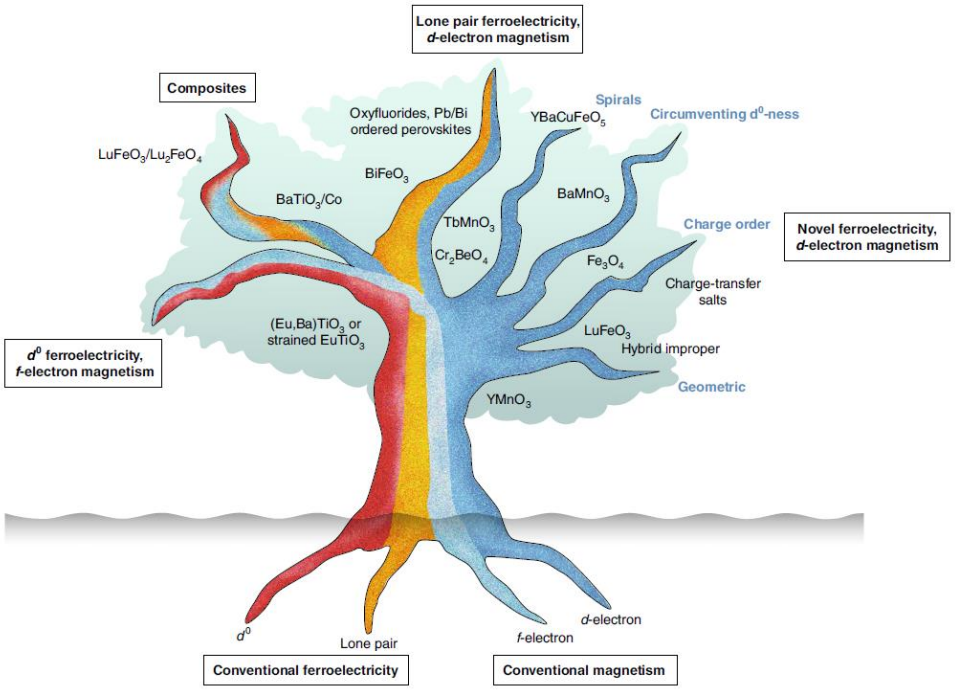

Figure 1.11: Different types of mechanism responsible for multiferroicity in a multiferroic materials [32].

1.13. Magnetoelectric coupling in multiferroics:

Magnetoelectric (ME) coupling describes the influence of a magnetic (electric) field on polarization (magnetization) of a material. ME coupling can be understood within the Landau theory framework, and can be obtained by expressing the free energy in terms of the electric field E and magnetic field H [29,33],

$$F(E,H) = F_0 - P_i^s E_i - M_i^s H_i - \frac{1}{2}\epsilon_0\epsilon_{ij} E_i E_j - \frac{1}{2}\mu_0\mu_{ij} H_i H_j - \alpha_{ij} E_i H_j$$

$$- \frac{\beta_{ijk}}{2} E_i H_j H_k - \frac{\gamma_{ijk}}{2} H_i E_j E_k + \quad \ldots\ldots\ldots(1.11)$$

where F_0 is the ground state free energy, subscript (i, j, k) represent the components of electric (E) and magnetic (H) fields, P_i^s and M_i^s are the component of spontaneous polarization and spontaneous magnetization, ϵ_0 and ϵ_{ij} are the permittivity of free space and relative permittivity (a second rank tensor), μ_0 and μ_{ij} are permeability of free space and relative permeability, α_{ij} is the linear magnetoelectric coupling. The third rank tensors β_{ijk}, γ_{ijk} represent the higher order (quadratic) magnetoelectric coefficients.

The ME effect can be easily established in the form of $P_i(H_j)$ or $M_i(E_j)$. Thus, $P_i(H_j)$ and $M_i(E_j)$ can be obtained by differentiation of the equation (1.11) with respect to E_i and H_j, respectively.

The induced polarization $P_i(H_j)$ by setting $E_j = 0$ is:

$$P_i(H_j) = -\frac{\partial F}{\partial E_i} = \alpha_{ij} H_j + \frac{\beta_{ijk}}{2} H_j H_k + \ldots\ldots \quad (1.12)$$

Similarly, The induced magnetization $M_i(E_j)$ by setting $H_j = 0$ is:

$$\mu_0 M_i(E_j) = -\frac{\partial F}{\partial H_i} = \alpha_{ji} E_j + \frac{\gamma_{ijk}}{2} E_j E_k + \ldots\ldots\ldots \quad (1.13)$$

The magnetoelectric coupling α_{ij} can be expressed by the relation,

$$\alpha_{ij}^2 \leq \epsilon_0 \mu_0 \in_{ii} \mu_{jj} \quad \ldots\ldots (1.14)$$

The magnetoelectric coupling provides an additional degree of freedom for technological applications and in designing multifunctional actuators, sensors, and memory devices. Other applications include quantum electromagnets and multiple state-logic memory elements while manipulation of the electric polarization (P) by a magnetic field (H) can create magnetically switchable devices in the visible and IR region [30,32–36].

Table 1.1: Comparison between type I and type II multiferroics

Type-I multiferroics	S. N.	Type-II multiferroics
Both ferroelectric polarization (P) and magnetization (M) are primary order parameters which emerge below ferroelectric (T_C) and magnetic (T_N) transition temperatures.	(i)	The ferroelectric polarization (P) is a secondary order parameter and an off-shoot of primary magnetic order parameter (M).
They exhibit large ferroelectric polarization and weak magnetoelectric coupling.	(ii)	These compounds result in weak ferroelectric polarization and strong magnetoelectric coupling.
The magnetic transition temperature of type-I materials is often high and even well above the room temperature.	(iii)	The magnetic transition temperature of type-II materials is well below the room temperature.
Examples: $BiFeO_3$ (T_C ~1103 K, T_N ~ 643 K, P~100$\mu C/cm^2$).	(iv)	Examples: $TbMnO_3$ (T_C ~28K, T_N ~ 41 K, P~10^{-2} $\mu C/cm^2$)

1.14. Spin glasses:

The magnetic systems with frustration, disorder, and randomness lead to spin-glass state [24,41–45]. In spin glasses, the magnetic spins freeze in random direction below a characteristic temperature called spin-glass freezing temperature (T_f). The frustration can be easily understood by considering ferromagnetic and antiferromagnetic nearest-neighbour interactions on a triangular lattice as illustrated in Fig. 1.12 (a). It can be seen from the figure that if all the nearest neighbour interactions are ferromagnetic then it is non-frustrated. However, when the nearest neighbour interactions are antiferromagnetic then frustration come into the picture and this leads to number of degenerate ground states as shown in Fig. 1.12 (b). Historically, the first spin-glass transition was reported in diluted metallic alloy systems with very small concentration of the magnetic ions, for example CuMn, AuFe, AgMn etc [24,41,42]. In such dilute magnetic alloy systems, the magnetic ions are randomly distributed over a non-magnetic metal host matrix shown in

Fig. 1.13 (a). The effective exchange interaction between the localized moments is mediated by the conduction electrons provided by the host metal. The interaction between the localized moments and conduction electrons is commonly known as Ruderman-Kittel-Kasuya-Yosida (RKKY) interaction. This RKKY interaction is a long-ranged, oscillatory in nature, and depends on separation between the magnetic moments (r) i.e. it decaying with inverse of the third power of the r.

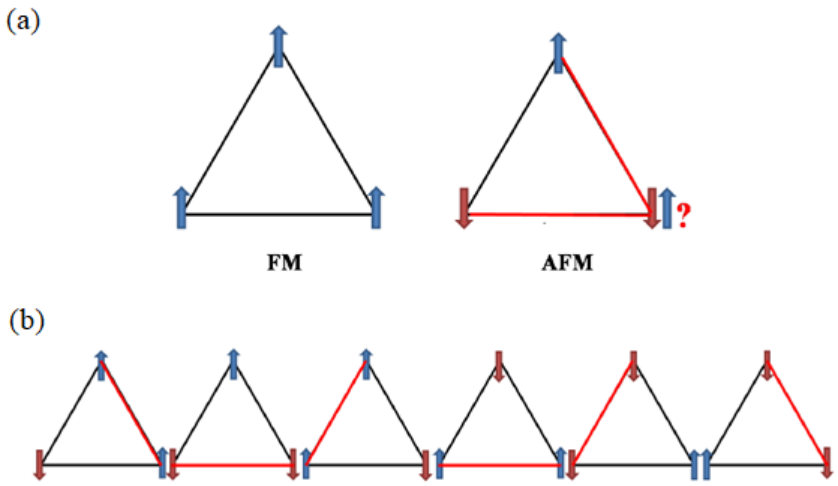

Figure 1.12: Schematic representation of magnetic ground state in a in triangular lattice by considering (a) ferromagnetic and antiferromagnetic nearest neighbour interactions and (b) shows the possible spin arrangement for nearest neighbour antiferromagnetic interactions [45].

The schematic variation of $J_{RKKY}(r)$ interaction with r is depicted in Fig. 1.13 (b). Because of the oscillatory nature, some pairs of spins will experience ferromagnetic interactions and other will experienced antiferromagnetic interaction and therefore, it leads to frustration in the system. Mathematically, the RKKY interaction can be expressed as [42]:

$$J_{RKKY}(r) \propto \cos(2k_F r)/r^3 \qquad \ldots\ldots (1.15)$$

where k_F is the Fermi wave-vector.

In addition to the diluted canonical spin glass systems, spin glass freezing has been observed in concentrated systems also by destroying long-range ordered magnetic

phase through random disorder caused by chemical substitutions [24,41,42]. Further, the compositions close to percolation threshold, the long-range ordered phase have been found to undergo re-entrant type spin-glass transition [42]. Several theories based on random field and random bond models have been proposed to explain the spin-glass transition in such concentrated systems [42].

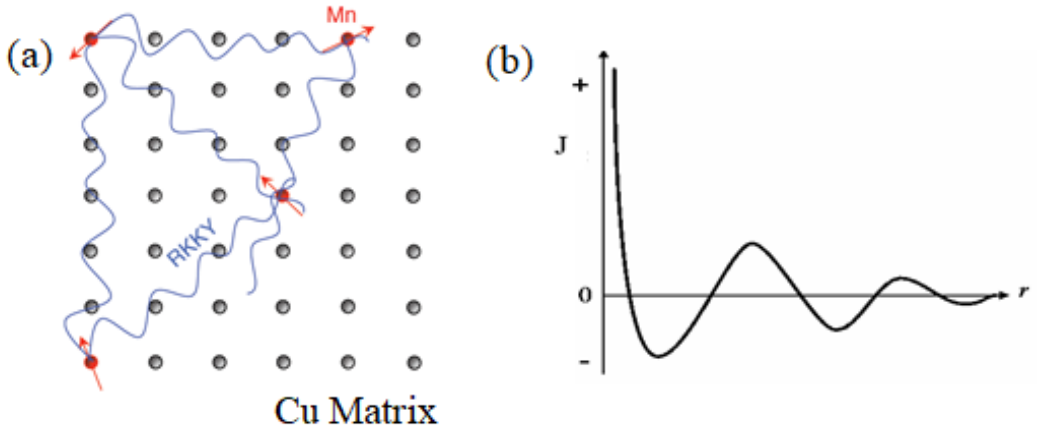

Figure 1.13: (a) Schematic representation of RKKY interactions which take place in dilute metallic spin-glass system like CuMn (b) Schematic variation of $J_{RKKY}(r)$ interaction with separation (r) between the moments.

1.15. Characteristics of spin glasses:

(**a**) The dc magnetization measurement reveals a history dependent irreversibility under zero field cooled (ZFC) and field cooled (FC) conditions below a characteristic temperature called irreversibility temperature (T_{irr}). They also show a sharp peak (cusp) in the ZFC susceptibility at the spin-glass freezing temperature (T_f) while the FC curve shows plateauing below T_f. For canonical spin glass systems like CuMn, AuFe, AgMn, the T_{irr} nearly coincides with T_f [41]. For concentrated systems, the ZFC peak is broader and $T_{irr} > T_f$. Fig. 1.14 depicts the typical dc magnetization curve for a dilute spin-glass system.

(**b**) The second criterion for the spin-glass transition is obtained from the ac susceptibility measurements. Both the dilute and concentrated systems exhibit a sharp anomaly in the ac susceptibility whose peak temperature is found to be frequency dependent i.e., it shifts towards higher temperature side with increasing frequency. This is illustrated in Fig. 1.15 for CuMn system [46]. Usually, for dilute systems the anomaly is quite sharp indicative of a thermodynamic phase transition. The spin dynamics in both dilute and concentrated systems follows critical slowing down with a characteristic spin-glass transition temperature T_{SG} at which the relaxation time diverges and the system become non-ergodic following Vogel-Fulcher or power law type dynamics [24,41–44].

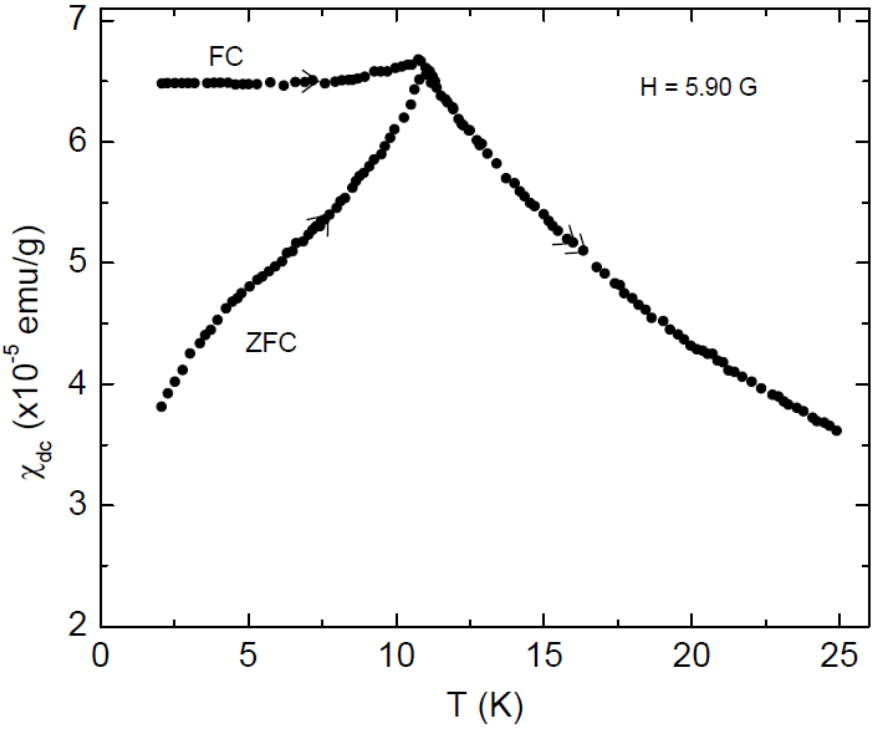

Figure 1.14: Temperature dependence of dc magnetic susceptibility curves of CuMn (3%) system measured under ZFC and FC conditions [46].

(**c**) The third characteristic feature of spin glasses can be obtained from the non-linear susceptibility data. It has been shown that the third harmonic (χ_3) diverges (see Fig. 1.16) at the spin-glass transition temperature (T_{SG}) as per a power law type behaviour [47].

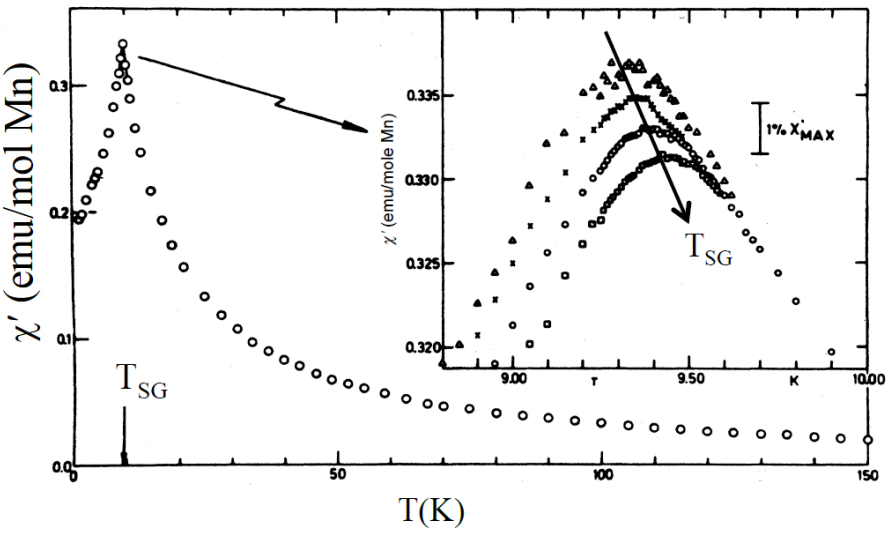

Figure 1.15: Temperature dependence of ac magnetic susceptibility curves of CuMn system showing cusp at T_{SG}. Inset depicts the frequency dispersion across T_{SG} [41].

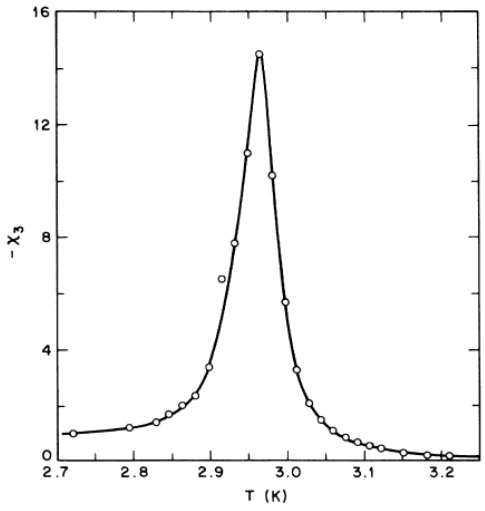

Figure 1.16: Variation of the nonlinear susceptibility (χ_3) as function of temperature across the spin-glass transition at a frequency of 10^{-2} Hz for AgMn system [47].

(**d**) The fourth criteria which are used to characterize the spin-glass state correspond to the presence of slow dynamics, aging, memory and rejuvenation effects in the spin-glass state of both the dilute and concentrated systems. The slow relaxation of magnetization in the spin-glass state follows a stretched exponential behaviour corresponding to a distribution of relaxation times [24,41–44]. The memory and rejuvenation effect in spin-glasses has been captured in dc magnetization measurements as a function of temperature at very low magnetic fields with and without intermediate wait time t_w below the T_{SG}. A hole burning dip is clearly observed at the waiting temperature T_w showing that the dc susceptibility rejuvenates to its original value. This is illustrated in Fig. 1.17 for CuMn system.

(**e**) The fifth characteristics of spin glasses is the field dependent shift of spin-glass freezing temperature T_f along de Almeida-Thouless (A-T) or Gabay-Toulouse (G-T) lines in the T-H plane [49–53]:

$$H^2 = A[1-(T_f(H)/T_f(0))]^m \qquad \text{…….(1.16)}$$

The exponent m is 3 for the A-T line and m=1 for the G-T line.

(**f**) Another criterion which is used for characterizing the spin-glass state is the magnetic contribution to specific heat (C_m). The temperature dependence of C_m shows broad maxima above the spin-glass freezing temperature (T_f) and below this temperature it shows linear behaviour for dilute metallic spin-glass systems shown in Fig. 1.18 [41]. The linear nature of C_m below T_f is explained by using a two-level tunnelling model [24,41,42,44,54]. The broad maxima above T_f can be understood in terms of the release of the magnetic entropy upto about 70-80% above T_f [41] and only 10-20% below T_f.

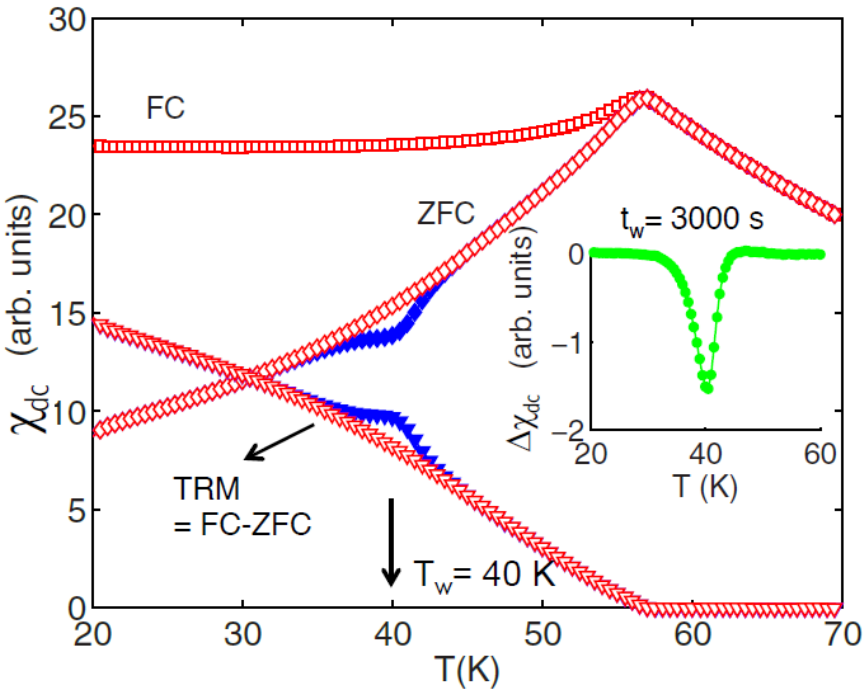

Figure 1.17: Temperature dependence of dc magnetic susceptibility of CuMn system measured at 0.5 Oe field under FC and ZFC conditions. Below T_{SG} =57K, effect of aging, memory and rejuvenation is clearly demonstrated. Inset depicts a "hole burnt" at the waiting temperature (T_w) [48].

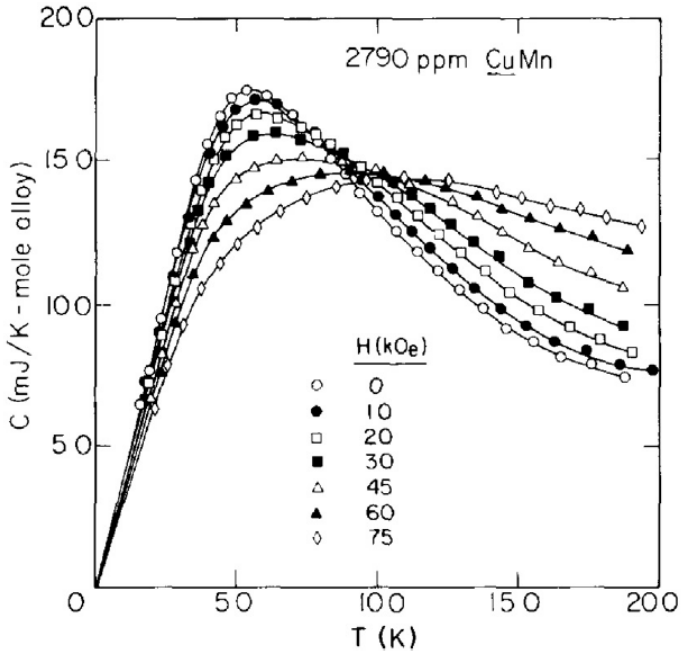

Figure 1.18: Temperature dependence of magnetic contribution to the specific heat (C_m) of CuMn system at various magnetic fields. Here, the T_f is 3.0 K and C_m exhibits maximum at 5K [41].

However, for concentrated spin-glass systems, different models have been proposed at low temperatures: (i) linear temperature dependence of C_m below T_f [55–57], (ii) C_m has been modelled using exponential functions like $C_m = aT^{1/2} \exp(-\Delta E/k_BT)$, $C_m = aT\exp(-\Delta E/k_BT)$, and $C_m = aT^{-2}\exp(-\Delta E/k_BT)$ [58–62], (iii) a power law type dependence of $C_m \sim T^{\alpha}$ with $\alpha = 1.2$ to 2 [63,64].

1.16. Literature Review:

Since in this work, we have investigated the compound bismuth ferrite ($BiFeO_3$), calcium iron niobate ($Ca(Fe_{1/2}Nb_{1/2})O_3$), and solid solution of $BiFeO_3$ with $BaTiO_3$, $Ca(Fe_{1/2}Nb_{1/2})O_3$ with $BiFeO_3$ and $LaFeO_3$, we present a brief review about the structure and properties of these compounds.

1.16.1 $BiFeO_3$ as a type-I multiferroic:

Amongst the multiferroics, $BiFeO_3$, is said to be type-I multiferroic as it not only exhibit ordering of both electric and magnetic dipoles below two different transition (ferroelectric T_C~1103K [65] and antiferromagnetic T_N~643K [66]) temperatures, but also display coupling of the electric and magnetic order. Because of their potential for designing novel multifunctional devices and data storage systems based on the possibility of manipulating magnetization (electric polarisation) by electric (magnetic) field, the interest in multiferroics continues unabetted. $BiFeO_3$ has received considerable attention over the last few decades and the last couple of years have witnessed several new findings on this compound in pure and solid solution forms.

1.16.2 Synthesis and phase diagram of $BiFeO_3$:

The $BiFeO_3$ sample is usually prepared from equimolar mixture of Bi_2O_3 and Fe_2O_3. The phase diagram for Bi_2O_3-Fe_2O_3 is shown in Fig. 1.19 [67,68]. The synthesis of single-phase $BiFeO_3$ sample is very difficult due to the narrow temperature range of the

stability of the perovskite phase and high volatility of Bi leads to formation of secondary phases like $Bi_{36}Fe_2O_{57}$ [69], $Bi_2Fe_4O_9$ [70], $Bi_{25}FeO_{39}$ [71] and $Bi_{46}Fe_2O_{72}$ [72] along with $BiFeO_3$ phase. However, these secondary phases formed during synthesis of $BiFeO_3$ can be leached out by dilute nitric acid [70,71,73]. The formation of such impurity phases has detrimental effect in the physical and magnetic properties of sample, as it increases the conductivity and leakage current of the sample.

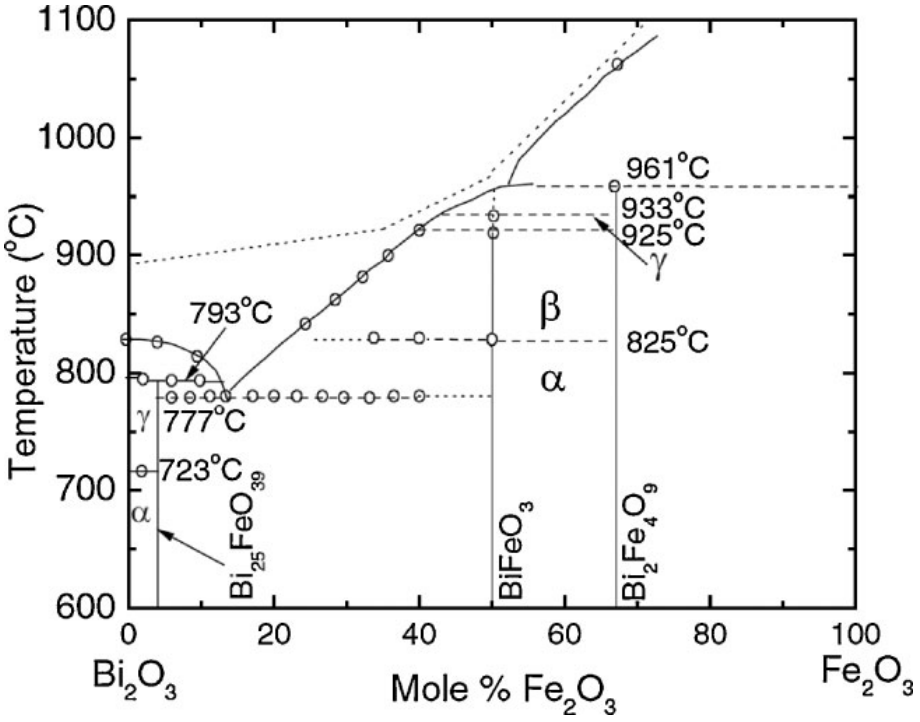

Figure 1.19: Phase diagram of $BiFeO_3$ using ingredients Bi_2O_3 and Fe_2O_3 [67].

1.16.3 Structure and multiferroic properties of $BiFeO_3$:

The room temperature crystal structure of $BiFeO_3$ corresponds to rhombohedrally distorted perovskite structure in the R3c space group [74–76] with $a^-a^-a^-$ tilt system in which the neighbouring oxygen octahedra are rotated anti-clockwise about the $[111]_{pc}$ direction. The cell parameters for R3c structure of $BiFeO_3$ were determined as a=b=5.58102(4), c=13.8757(4), $\alpha=\beta=90$ and $\gamma=120$ [77] in the hexagonal unit cell which contains six formula units (thirty atoms). The primitive unit cell, shown in Fig. 1.20 [78],

contains two formula units (ten atoms), arising from counter-rotations of neighboring oxygen octahedra about the pseudocubic $[111]_{pc}$ symmetry axis. The *R*3*c* symmetry permits the development of a spontaneous polarization along $[111]_{pc}$, and Bi, Fe, and O ions are displaced relative to one another along this threefold axis [77]. The first-principles calculations on the rhombohedral phase of $BiFeO_3$, predicted very high ferroelectric polarization 90–100 $\mu C/cm^2$ [79,80]. Experimentally, very high value of P_s = 60 $\mu C/cm^2$ has been reported along the $[010]_{pc}$ direction (i.e., 100 $\mu C/cm^2$ along the polar [111] direction) of a rhombohedral $BiFeO_3$ single crystal, with high resistivity of $6x10^{10}$ Ohm-cm at room temperature under 100V, grown from a Bi_2O_3-Fe_2O_3 flux method [81], indicating that the high value of polarization is an intrinsic property of the $BiFeO_3$ phase.

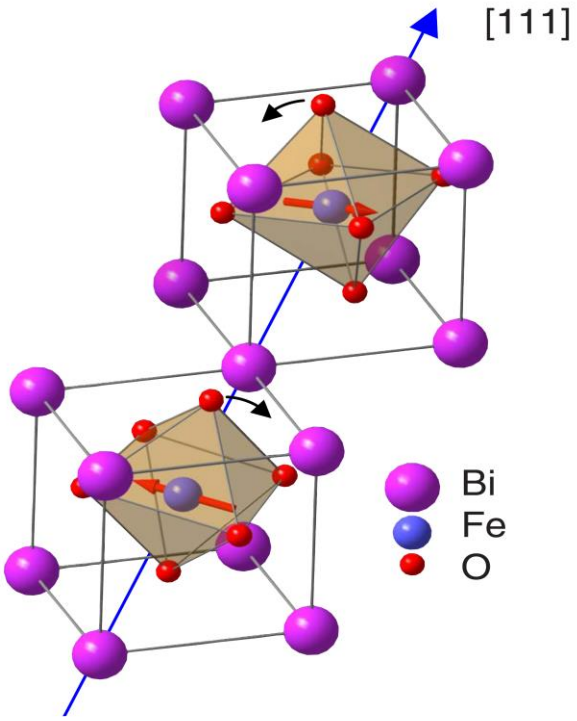

Figure 1.20: Crystal structure of $BiFeO_3$. Two simple perovskite unit cell are shown to illustrate the successive oxygen octahedra along the polar [111] axis rotate with opposite sense. Arrows on Fe atoms indicate the orientation of the magnetic moments in the (111) plane [78].

Apart from ferroelectric behaviour, $BiFeO_3$ is also known to exhibit an antiferromagnetic ordering. The magnetic structure of $BiFeO_3$ first studied by Sosnowska et al. [73] and showed that the Fe magnetic moments are coupled ferromagnetically within the pseudocubic [111] planes and antiferromagnetically between adjacent planes, leading to a G-type antiferromagnetic structure as shown in Fig 1.21 (a). If the magnetic moments are oriented perpendicular to the $[111]_{pc}$ direction (i.e. (111) plane as shown in Fig. 1.20), the symmetry also permits a canting of the antiferromagnetic sublattices resulting in a macroscopic magnetization (according to Dzyaloshinski-Moriya interaction), so-called weak ferromagnetism. However, it was also found that the there is

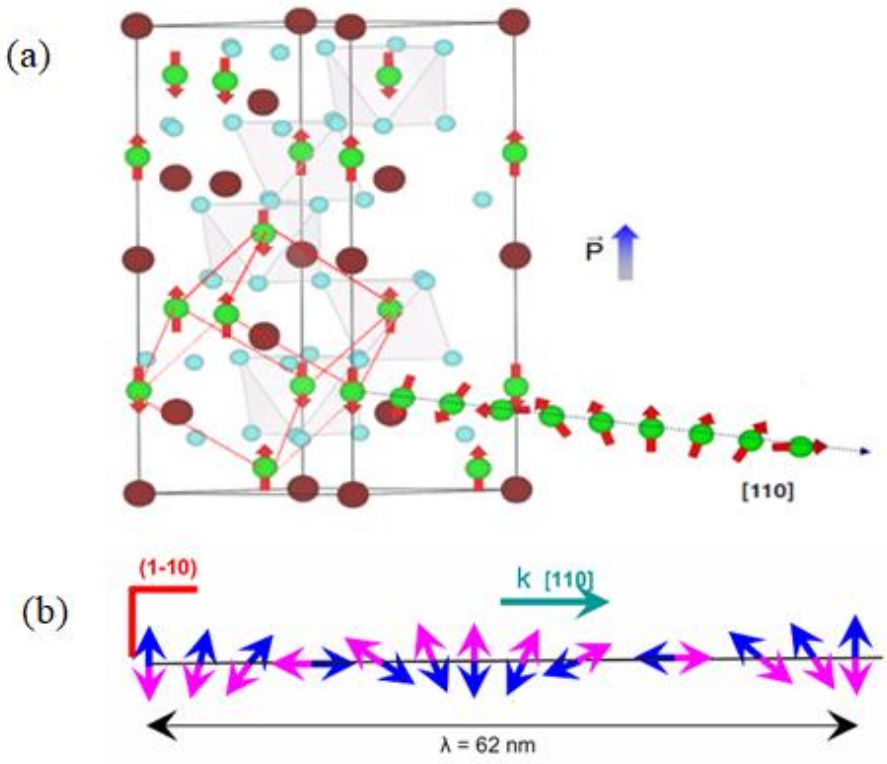

Figure 1.21: (a) Magnetic structure of $BiFeO_3$ [82] (b) The propagation wave vector **k** is along the $[110]_{hex}$ direction and lies in the plane of spin rotation (1-10) [71].

a spin cycloid structure is superimposed on the antiferromagnetic ordering. The spin cycloid propagating along $[110]_{hex}$ direction with an extremely long period of 62 nm and

lies in the plane (1-10) of spin rotation as shown in Fig. 1.21(b) [71,82]. The modulated spiral spin structure leads to cancellation of macroscopic magnetization. Owing to the presence of spiral spin structure, the field and temperature dependent magnetization measurements have been observed to exhibit pure antiferromagnetic response as shown in Fig. 1.22 [71], without any trace of weak ferromagnetism, in $BiFeO_3$ single crystals.

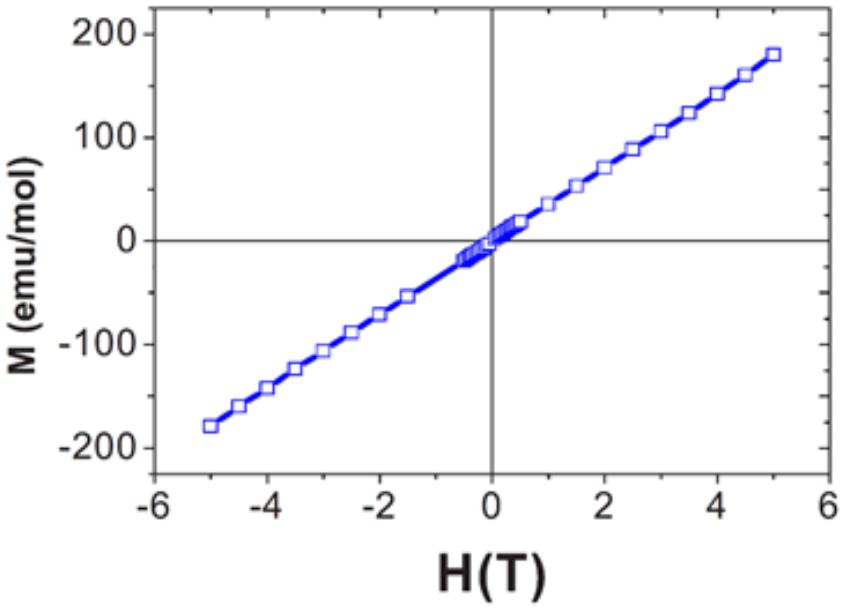

Figure 1.22: M-H hysteresis loop for $BiFeO_3$ measured at room temperature [71].

1.16.4 Magnetoelectric coupling in $BiFeO_3$:

The presence of modulated spin spiral structure in $BiFeO_3$, inhibits the linear magetoelectric coupling and shows only quadratic coupling [83]. However, it has been shown that the modulated spin spiral gets destroyed at a critical field (H_c) of 200 kOe which is illustrated in Fig. 1.23 (a). It is evident from the figure that the measured field dependence of polarization P(H) is quadratic for $H<H_c$ and has a jump at $H=H_c$ when the spiral modulated spin structure is destroyed. Above the critical field H_c, the magnetoelectric polarization changes sign and becomes linearly dependent on magnetic field [84]. The destruction of spin cycloid structure of $BiFeO_3$ by high magnetic field also

results in the release of the latent magnetization with remanent M_r ~0.30 emu/g at 10 K as shown in Fig. 1.23 (b). [84]. The application of high magnetic field greater than 20 T leads to transformation of modulated spin cycloid structure to a homogeneous magnetic structure [84].

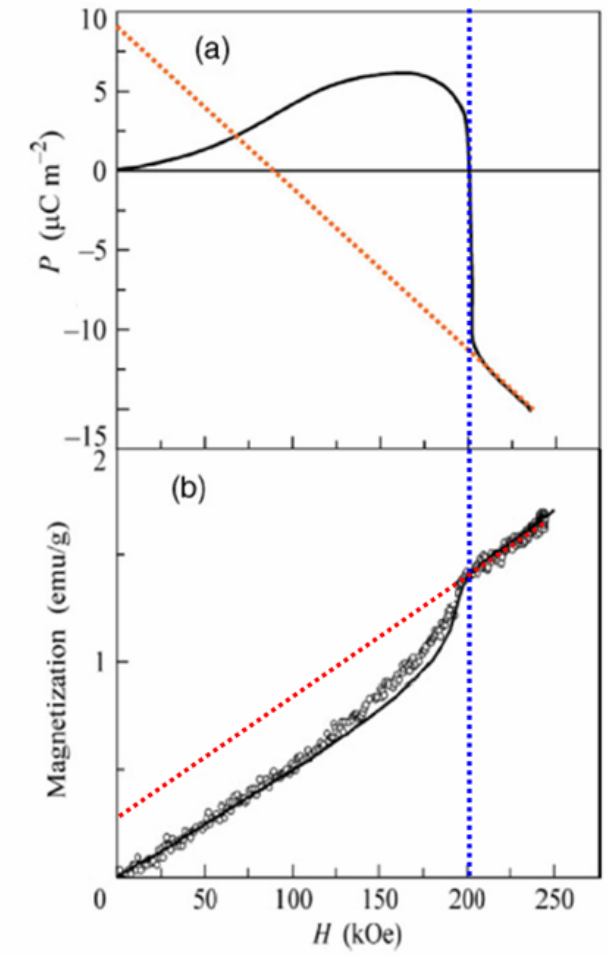

Figure 1.23: (a) Variation of longitudinal polarization with magnetic field at 10 K [84] (b) Magnetization as a function of the magnetic field for H≤25T of a $BiFeO_3$ sample at 10 K [68].

1.16.5 Ferroelectric control of magnetism in $BiFeO_3$:

High resolution neutron diffraction studies on $BiFeO_3$ by two independent groups have shown a relationship between ferroelectric polarization and

antiferromagnetism [85,86]. It is shown that the magnetic moments rotate within the plane defined by (**P**||$[111]_{pc}$) and the spiral propagation vector (**k**||$[10\text{-}1]_{pc}$) as shown in Fig. 1.24 [85]. This has profound consequences: (1) if the direction of polarization is changed by the application of voltage will also rotate the magnetic easy plane. (2) the magnetic easy plane can be switched only if the polarization changes direction, but not if it merely changes polarity, 180^0 switching of the polarization should not affect the magnetic orientation [85].

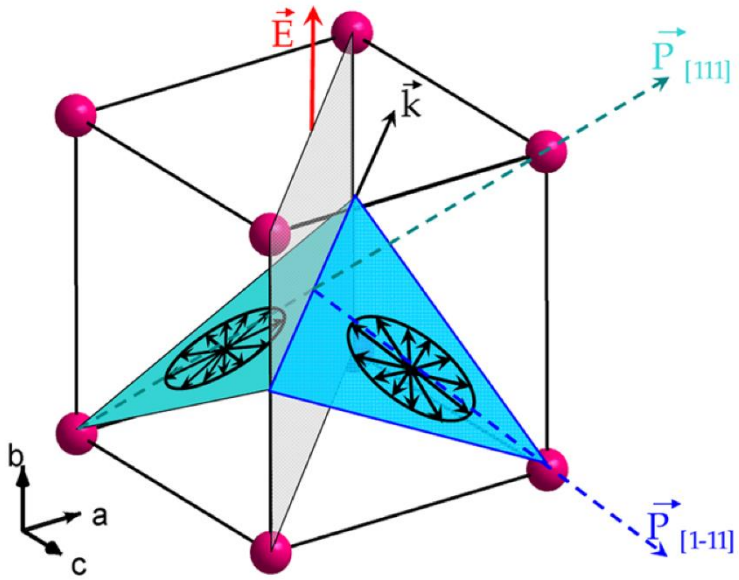

Figure 1.24: Schematic representation of the planes of spiral rotation and spin cycloids **k** vector for the two polarization domains separated by a domain wall [85].

1.16.6 Destruction of modulated spiral spin structure in $BiFeO_3$:

$BiFeO_3$ does not exhibit any macroscopic magnetization due to the presence of spin cycloid structure and thus, inhibit the linear magnetoelectric coupling. In order to observe the macroscopic magnetization and linear magnetoelectric coupling, the spin cycloid need to be destroyed. The spin cycloid of $BiFeO_3$ can be destroyed by: (i) applying high magnetic field in excess of 20T [84], (ii) reducing the particle size below the wavelength (~ 62nm, though the real magnetic structure of the cycloid is

incommensurate) of the spin cycloid [87], (iii) generating strains in epitaxial films due to lattice mismatch [88] and (iv) introducing chemical disorder in the magnetic sublattice [89–93].

The destruction of the spin cycloid due to chemical disorder in the magnetic sublattice of $BiFeO_3$ has been verified in more than one ways: (1) through the absence of the magnetic satellite peaks in the neutron diffraction patterns [90,91,94], (2) observation of weak ferromagnetism through the observation of M-H loops due to the canted G-type antiferromagnetic structure of $BiFeO_3$ [89,90] and (3) observation of linear magnetoelectric coupling [89,90] which is otherwise not permitted in pure $BiFeO_3$ due to symmetry arguments [83].

The constant wavelength and time-of-flight neutron diffraction studies on $BiFe_{1-x}Mn_xO_3$, revealed that the spin cycloid structure of $BiFeO_3$ is modified and changes to homogeneous antiferromagnetic structure beyond x=0.20 concentration (see Fig. 1.25) [76]. Also, in $(Bi_{0.8}Ba_{0.2})(Fe_{0.8},Ti_{0.2})O_3$ system, remnant magnetizations of ~0.15 emu/g, has been reported, as a result of suppression of the spin cycloid [91].

1.16.7 Low temperature magnetic transitions in $BiFeO_3$:

While the nuclear and magnetic structures as well as the multiferroic properties of $BiFeO_3$ at and above the room temperature are well settled [68,95], there exists considerable controversy about various low temperature phenomena that occurs below room temperature. Recent NMR studies suggest that the cycloidal modulation function for the magnetic phase changes from harmonic (sinusoidal) to anhormonic (sn(x, m), elliptic Jacobi function) with m, which is a measure of anhormonicity, increasing from 0.48 at room temperature to 0.95 at 4.2 K [96–99].

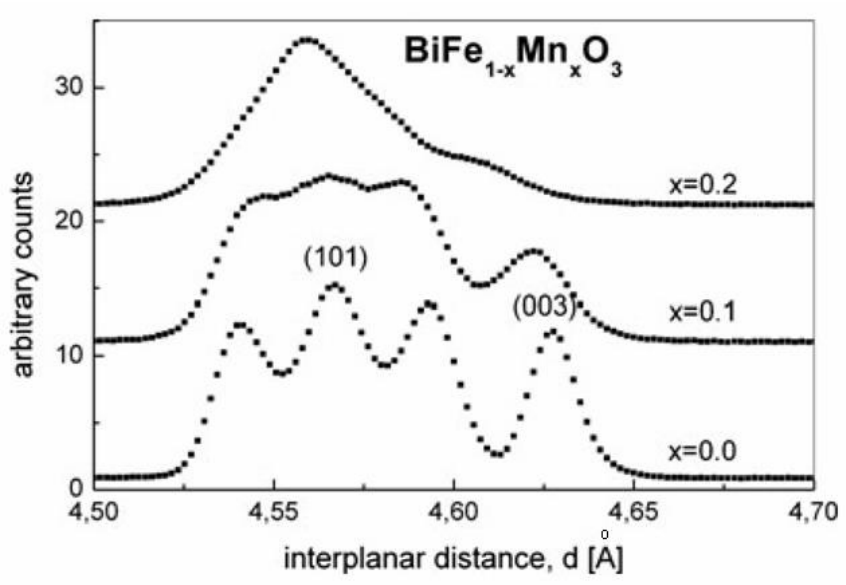

Figure 1.25: Composition dependence of magnetic satellite reflections measured using OSIRIS diffractometer at ISIS for $BiMn_xFe_{1-x}O_3$ [76].

The neutron diffraction studies, which probe the space and time averaged magnetic structure at the bulk level, have also confirmed anhormonic nature of modulation of the cycloid at low temperatures [100,101] but the anhormonicity is found to be much less, 0.50 [100] and <0.25 [101] in two independent studies using single crystals and polycrystalline samples, respectively, than that reported using a local probe like NMR. However, it is hard to imagine that the spin cycloid involving all the spins in the magnetic structure of $BiFeO_3$ will remain unaffected despite the several low temperature phase transitions that have been reported. Using a variety of measurement probes like DC magnetic susceptibility (χ_{DC}) [87,102–107], AC magnetic susceptibility ($\chi'_{AC}(\omega,T)$ and $\chi''_{AC}(\omega,T)$) [102,108], differential scanning calorimetry (DSC) [103] differential thermal analysis (DTA) [109], Raman scattering [110–116] dielectric studies [109,117] and elastic modulus spectroscopy [109,115], several low temperature magnetic transitions have been reported in the temperature range 20 to 25K [102,108], 50-60K [87], 140-150K [103,111,112,116] and 220 to 250 [103] (see Fig. 1.26). Taking into account the observations made by different experimental probes discussed above, the

transitions occurring around 50-60 K, 140–150 K and 220–250 K have been attributed to magnetic but glassy with magnetoelectric coupling, predominantly magnetic transition involving spin reorientation, and antiferromagnetic (AFM) to spin glass (SG) transition with weak coupling with polarization, respectively [103,109]. Another transition reported around 178 – 200 K has been proposed to be magnetoelastic in nature with a small coupling to polarization [109]. Finally, the transition at 20-25K has been reported to be due to a spin glass freezing [102,108]. Towards understanding the true ground state of $BiFeO_3$, it is therefore important to settle if the low temperature phase transitions reported below room temperature are intrinsic to $BiFeO_3$ or some of them could be induced due to the presence of ionic vacancies created during high temperature processing. The present work was undertaken to address this issue.

The spin-glass freezing around 25K in $BiFeO_3$ has several intriguing features in AC χ (ω, T). Firstly, the peak height of $\chi'(\omega, T)$ increases with increasing frequencies which is unusual as the susceptibility always decreases with increasing frequency except near frequencies corresponding to a resonant absorption that may be linked with the resistance, capacitance and inductance of the entire circuit rather than just the sample. Further, the imaginary part $\chi''(\omega, T)$ shows negative cusps at T_f with a peak temperature above the corresponding peak temperature for the real part $\chi'(\omega, T)$. The negative value clearly suggests that the circuit is no longer purely inductive except at very low temperatures (< ~10K). The third intriguing aspect of the $\chi''(\omega, T)$ is the presence of a tiny peak around 10K below which the imaginary part shows positive value. All these features have been tentatively attributed to the LRO AFM phase with modulated magnetic structure that coexists with the SG phase [108], as they are not observed in the conventional spin-glass systems. Further, the occurrence of a spin-glass phase in a

homogeneously ordered system like $BiFeO_3$ without any quenched impurity and randomness is equally intriguing.

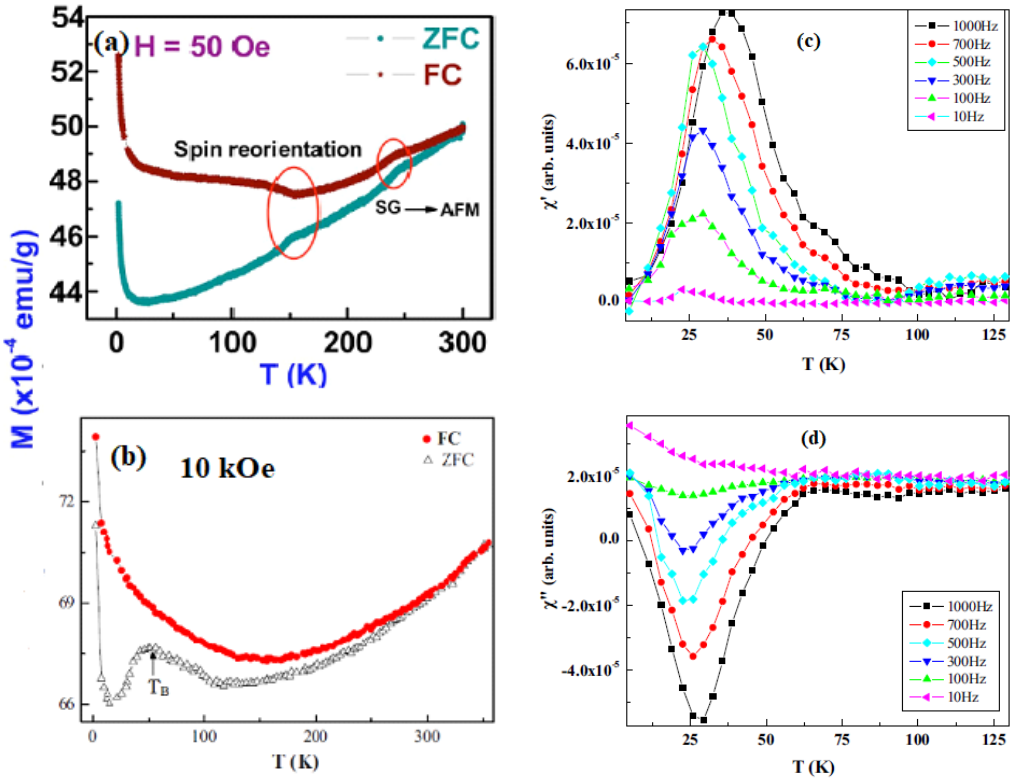

Figure 1.26: Left panel (a) and (b) show the temperature dependence of dc magnetization curves for polycrystalline and single crystals of $BiFeO_3$ measured under ZFC and FC conditions. Right panel (c) and (d) depicts the real and imaginary parts of ac susceptibility of single crystals of $BiFeO_3$ [102,103].

The existing models of spin-glass transitions are based on the concept of disorder, randomness and frustration [24,42–45] although in recent years several ordered systems like manganites h-$DyMnO_3$ [118], hydronium jarosites $(H_3O)Fe_3(SO_4)_2(OH)_6$ [119], herbertsmithite $Co_3Mg(OH)_6Cl_2$ [120], edwardsite $Cd_2Cu_3(OH)_6(SO_4)_24H_2O$ [121], and pyrochlores ($Tb_2Mo_2O_7$, $Y_2Mo_2O_7$, and $Mn_2Sb_2O_7$) [122–124] have been shown to exhibit SG transition. However, these ordered systems are different from $BiFeO_3$ as they all show frustrated interactions due to geometrical reasons. Thus more work is required to

understand the true ground state of $BiFeO_3$. We have addressed some of these issues in chapters II, III and IV.

1.16.8 $BiFeO_3$ solid solutions:

Despite the advantage of room temperature multiferroic properties of $BiFeO_3$, the use of this material for potential applications is limited due to following reasons (i) difficult to synthesize in pure phase form, (ii) low insulating resistance and (iii) weak quadratic magnetoelectric coupling as the presence of the spin cycloid does not allow linear magnetoelectric coupling to develop [84].

In recent years, attempts have been made to synthesize single phase $BiFeO_3$ based solid solutions with a view to destroy the modulated spin cycloid structure and enhance the ferroelectric and magnetic properties. The formation of solid solutions of $BiFeO_3$ with other perovskite oxides such as $BaTiO_3$ [89–91,125],$Pb(Fe_{1/2}Nb_{1/2})O_3$ [94], $PbZrO_3$ [126], $Pb(Zr_xTi_{1-x})O_3$ [127,128], $SrTiO_3$ [129], $CaTiO_3$ [130], $PbTiO_3$ [131], $BiCoO_3$ [132], $NaNbO_3$ [133] and $BiMnO_3$ [134] has been explored. Apart from the enhanced multiferroic properties when forming the solid solutions, $BiFeO_3$ solid solutions exhibit different crystallographic phases and interesting phase transitions with increasing concentration of the disorder [135]. Most importantly, the spin cycloid of $BiFeO_3$ is destroyed in most of these solid solutions leading to the release of the latent weak ferromagnetic magnetization due to spin canting locked in the spin cycloid [89,90,94]. As a result, these solid solutions exhibit linear magnetoelectric coupling.

1.16.9 $BiFeO_3$-$BaTiO_3$ solid solution:

Amongst the $BiFeO_3$ based solid solution systems, the (1-x)$BiFeO_3$-x$BaTiO_3$ or BF-xBT solid solutions have received considerable attention due to large ferroelectric polarization [89,90,136–142], large remnant magnetization [91–93,143], linear

magnetoelectric coupling [89,90] and the highest depolarization temperature for piezoelectric applications [136,139,140,144]. This system also exhibits a variety of phase transitions such as morphotropic phase transition, relaxor ferroelectric phase transition, non-relaxor type diffuse phase transition, tricritical transition, isostructural phase transition and trigger type transitions [91,135,145,146]. More recently Singh et al. presented the ferroelectric and magnetic phase diagram of $BiFeO_3$-$BaTiO_3$ system as a function of temperature and composition above room temperature [146]. It is evident from Fig. 1.27 that increasing the $BaTiO_3$ content (x) in $BiFeO_3$ leads to a structural change from the *R*3*c* phase of pure $BiFeO_3$ to an average cubic structure with the *Pm*-3*m* space group at a critical composition $x \approx 0.35$. With further increase in $BaTiO_3$ content, there is another critical composition around $x \approx 0.85$ at which this cubic phase changes to the tetragonal phase of $BaTiO_3$. The pseudocubic phase is stable in the composition range $0.35 \leq x \leq 0.85$ and show local monoclinic distortion [91,135,145]. Using MnO_2 doping [89,90,136–142], in the BF-xBT system, impressive piezoelectric coefficients have been reported. Further, the piezoelectric property persists up to T_d ~750K without any depoling characteristics in contrast to the commercial toxic Pb^{2+} based $Pb(Zr_xTi_{1-x})O_3$ ceramics which dipole below T_d ~ 400K only. Thus BF-xBT system has emerged as an important Pb-free high temperature piezoelectric material.

1.16.10 Complex perovskites and their multiferroic behaviour:

Among the disordered perovskite systems, there is a big family of $A(B'B'')O_3$ type compounds where the B-site cations may be ordered or disordered depending upon their size and charge differences but the ratio of B':B'' is fixed like 1:1, 1:2, 1:3, as in compounds [147–151]. Such site and charge disordered and ordered compounds with one of the B' site cation being a 3d transition metal element (Sc, Ti, V, Cr, Mn, Fe, Co, Ni etc) with B' and B'' in 1:1 ratio have received immense attention from the point of view of

their properties like colossal magnetoresistance (CMR) [152–154], half metallicity [155–157], metal insulator transition [158–160], superconductivity [161,162], normal ferroelectricity [150] and relaxor ferroelectricity [18,19,163–165], long-range magnetic

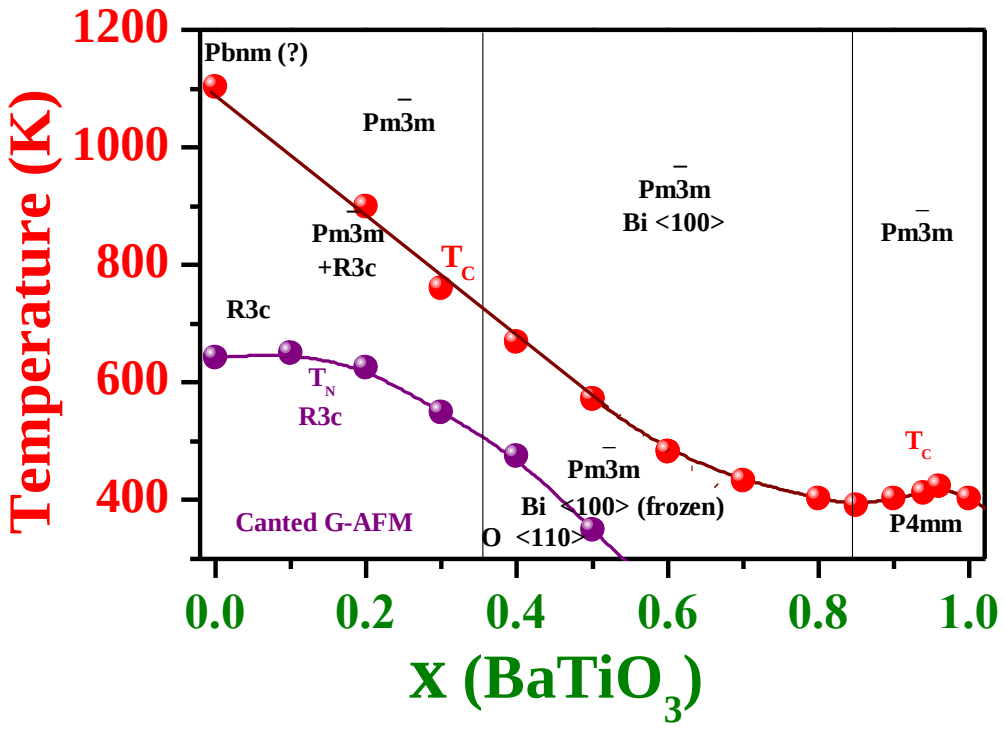

Figure 1.27: Phase diagram of (1-x)$BiFeO_3$-x$BaTiO_3$ system [146].

ordering [166–172] and spin glass (SG) transition [169,171–178], and multiferroicity [179–182]. Historically, the complex perovskites compounds with general formula A(B'B")O_3 where A = Pb, Ba, Sr, Ca and B' and B" are magnetic (Cr, Mn, Fe, Ni, Co, etc.) and non-magnetic (Nb, Ta, W, Sb etc.) transition metal elements, were first synthesized by Russian scientists nearly six decades back with the aim that these compounds can show multiferroicity [183,184]. From this approach, the lead iron niobate $Pb(Fe_{1/2}Nb_{1/2})O_3$ (PFN) emerged as a model type-I multiferroic compound [171,172,185–190].

1.16.11 Lead (Pb)-based complex perovskites:

The Pb-containing compounds like $Pb(Fe_{1/2}Nb_{1/2})O_3$ (PFN), $Pb(Fe_{1/2}Ta_{1/2})O_3$ (PFT), and $Pb(Fe_{2/3}Nb_{1/3})O_3$ (PFW) are known to exhibit relaxor ferroelectric or diffuse ferroelectric transition above room temperature [188,189], G-type antiferromagnetic order below T_N~150K [190] and a spin-glass phase below ~10K [171,172], respectively. The room temperature crystal structure along with the ferroelectric (T_c), magnetic (T_N) and spin-glass transition (T_{SG}) for these compounds are compared in Table 1.2 [171,172,174,176–178,191,192]. There is a recent report on $Pb(Fe_{1/2}Sb_{1/2})O_3$ (PFS) which reveals relaxor ferroelectric behaviour in this compound with T_c~250K and spin-glass transition around ~150K [193]. Fig. 1.28 depicts the temperature dependence of dc magnetic susceptibility measured at 100 Oe field in worming cycle under ZFC and FC conditions for PFN. The ZFC and FC curve clearly reflect the AFM phase transition T_N~144K and below 10K [171,172], the two curves diverges, which is a characteristic feature of spin glasses. Further, the AFM phase transition in PFN is manifested by jump in the temperature dependent dielectric constant [194] and anomalies in the lattice parameters [189]. Interestingly, the LRO AFM phase is found to coexist with the SG phase below T_f ~10K but there is a controversy about the exact origin of the coexistence of the two phases [171,172]. Two different models have been proposed in the literature [171,172]. According to the first model, which is based on macroscopic measurements, the LRO AFM phase results from the infinite percolative clusters of Fe^{3+} spins while the glassy phase is a consequence of the freezing of the finite size isolated clusters with uncompensated Fe^{3+} spin [171] (see Fig. 1.29(a)). This model implies that the SG and LRO AFM phases occur on two separate sublattices. In the second model based on neutron scattering and Mossbauer probes, the SG phase result from the LRO AFM sub-lattice system itself due to freezing of the transverse component of the spin in a

glassy manner [172]. We shall return to this controversy in more detailed in chapter V. The measured temperature dependence of the integrated intensity of the AFM peak at Q =(½, ½, ½) of PFN is shown in Fig. 1.29 (b). It can be seen from this figure that the below the AFM transition, the intensity of the magnetic Bragg peak increases very smoothly but a small decrease in the integrated intensity of AFM peak is observed below 50K, which has been attributed to spin-canting and transverse spin freezing [172].

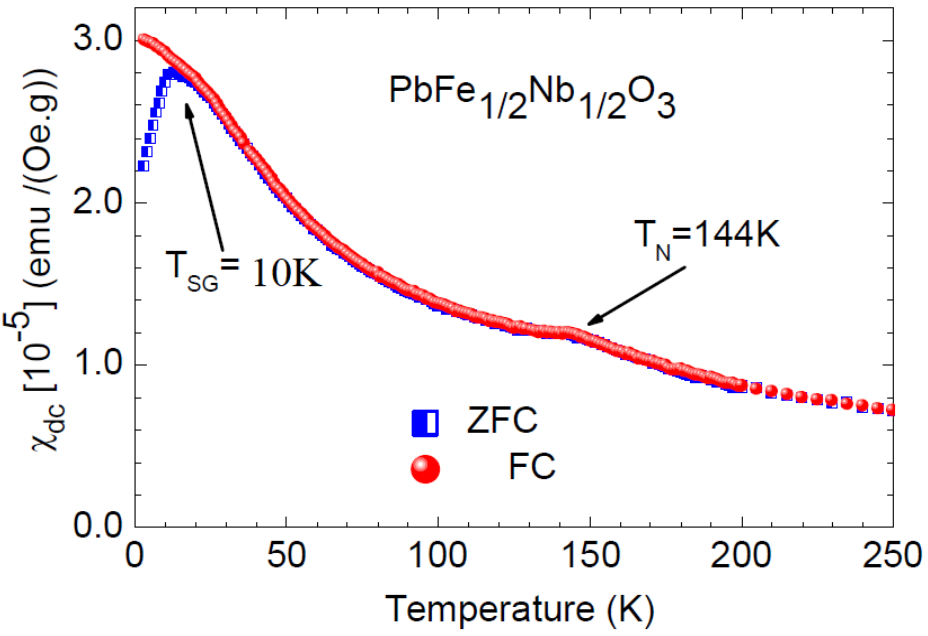

Figure 1.28: Temperature dependence of dc magnetic susceptibility curves of $Pb(Fe_{1/2}Nb_{1/2})O_3$ measured under ZFC and FC conditions [172].

1.16.12 Pb-free complex perovskites:

The Pb-free complex perovskites with a general formula of $A(Fe_{1/2}B'_{1/2})O_3$ type with A = Ba, Sr, Ca and B' = Nb, Ta, and Sb do not display LRO ferroelectric and AFM phases, despite Nb^{5+} being a ferroactive ion of $4d^0$ type [37] and the concentration of $3dFe^{3+}$ moments at the B-site being higher than the critical percolation threshold value [195–197]. However, these Pb-free complex perovskite niobates and tantalates are reported to exhibit SG freezing at low temperatures with T_f ~25K [176–178] similar to

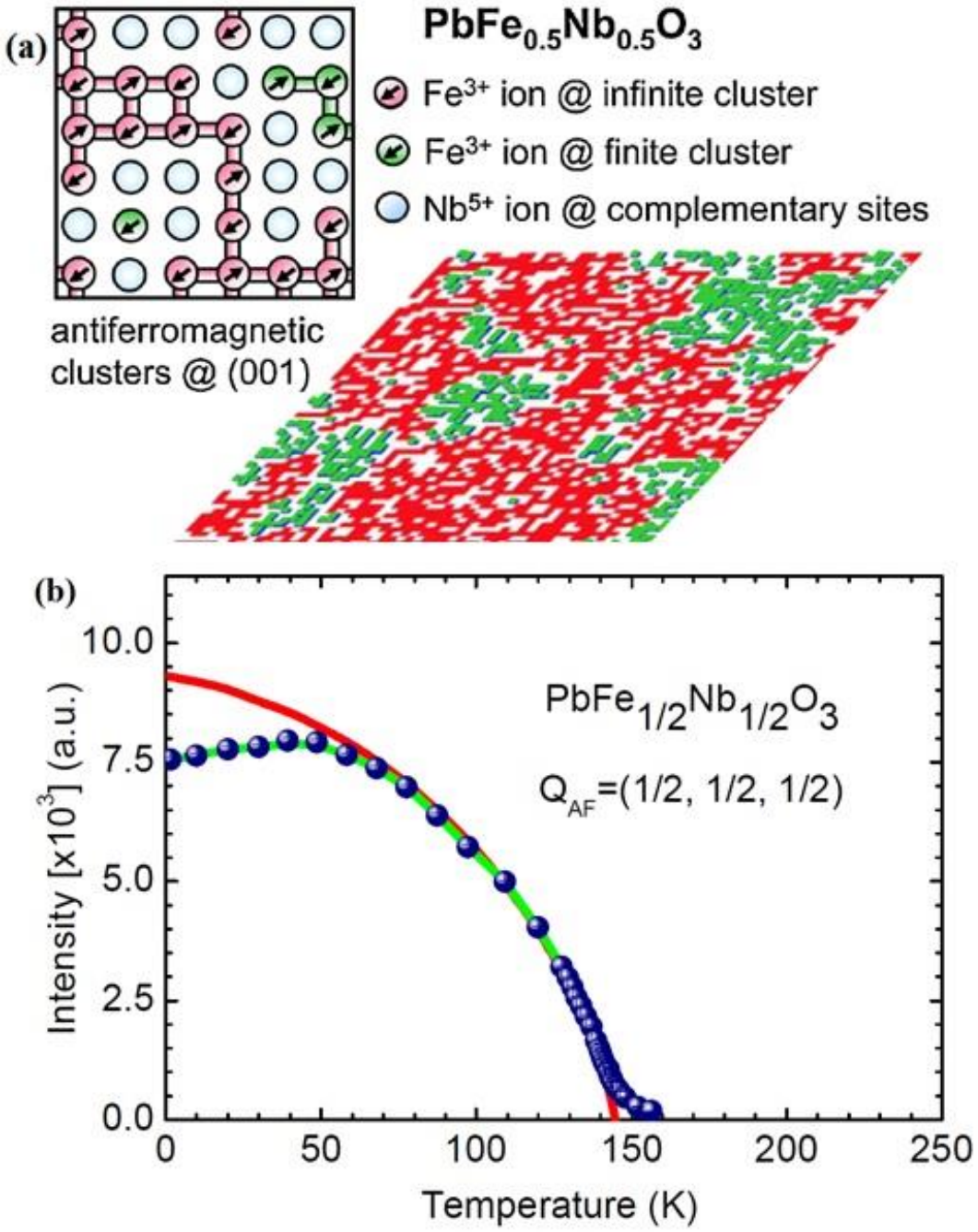

Figure 1.29: **(a)** Schematic representation of the antiferromagnetic Fe^{3+} clusters in $Pb(Fe_{1/2}Nb_{1/2})O_3$ with projections of <111>-oriented spins viewed in (001) cross sections at different scales [171] and **(b)** Temperature dependence of the integrated intensity of the antiferromagnetic (AFM) peak intensity of PFN at Q = (½, ½, ½) [172].

PFN though with a slightly higher T_f which is ~10K for PFN and PFT. Unlike the Nb and Ta based compounds, the spin glass freezing temperature T_f of Sb based complex perovskites, $Ca(Fe_{1/2}Sb_{1/2})O_3$ (CFS), $Sr(Fe_{1/2}Sb_{1/2})O_3$ (SFS), $Ba(Fe_{1/2}Sb_{1/2})O_3$ (BFS), is a little lower 17K, 20K, 16K [176,178], respectively, as compared to their niobates and tantalate counterparts.

This difference has been attributed to the partial 1:1 chemical ordering of the $Fe^{3+}$and Sb^{5+} ions at the B-site [178]. The so-called spin-glass transition in the lead-free complex perovskites has not been thoroughly investigated, except for the observation of bifurcation of the ZFC and FC dc magnetization M(T) plots with a peak in the ZFC data, and therefore the true nature of this transition may be different. Fig. 1.30 shows temperature dependence of dc susceptibility of $Ca(Fe_{1/2}Nb_{1/2})O_3$ measured at 1000 Oe field under ZFC and FC protocols [176]. It is evident from the figure that the ZFC and FC curves bifurcate below T_f~25K suggesting the spin-glass behaviour [24,41] but such a bifurcation can also occur due to superparamagnetic blocking [198]. We have carried out a comprehensive study of the spin-glass transition in $Ca(Fe_{1/2}Nb_{1/2})O_3$ using macroscopic and microscopic probes and the results are discussed in detail in chapter V. The room temperature crystal structure along with the spin-glass freezing temperature of Pb-free compounds are compared in Table 1.2 [176–178]. It is interesting to note that the Pb^{2+} and Ba^{2+} based $A(Fe_{1/2}B_{1/2})O_3$ compounds exhibit normal perovskite structure where as Ca^{2+} and Sr^{2+} based compounds exhibit tilted oxygen octahedra. As a result, the unit cell of the later is doubled giving rise to characteristic superlattice peaks [176,199,200]. Superlattice peaks in such compounds has also been reported due to cations ordering of the Fe^{3+} and Sb^{5+} at the B-site for some compounds [201,202]. It is worth mentioning that the room temperature crystal structure of $Ca(Fe_{1/2}Nb_{1/2})O_3$ is controversial as two different space group symmetries (Pbnm (orthorhombic) and $P2_1/n$ (monoclinic)) have

been reported using laboratory XRD data [176,199–202]. We have addressed this controversy using synchrotron x-ray diffraction data in chapter V. The presence of LRO AFM phase in PFN has been attributed to the presence of Pb^{2+} with $6s^2$ lone pair electrons which may mediate the next nearest neighbour superexchange pathways in pure PFN along the <111> pc directions [203]. However, this hypothesis needs to be tested by more careful analysis of the Pb-free niobate compounds like CFN around the expected AFM T_N~150K. This is subject matter of chapter VI.

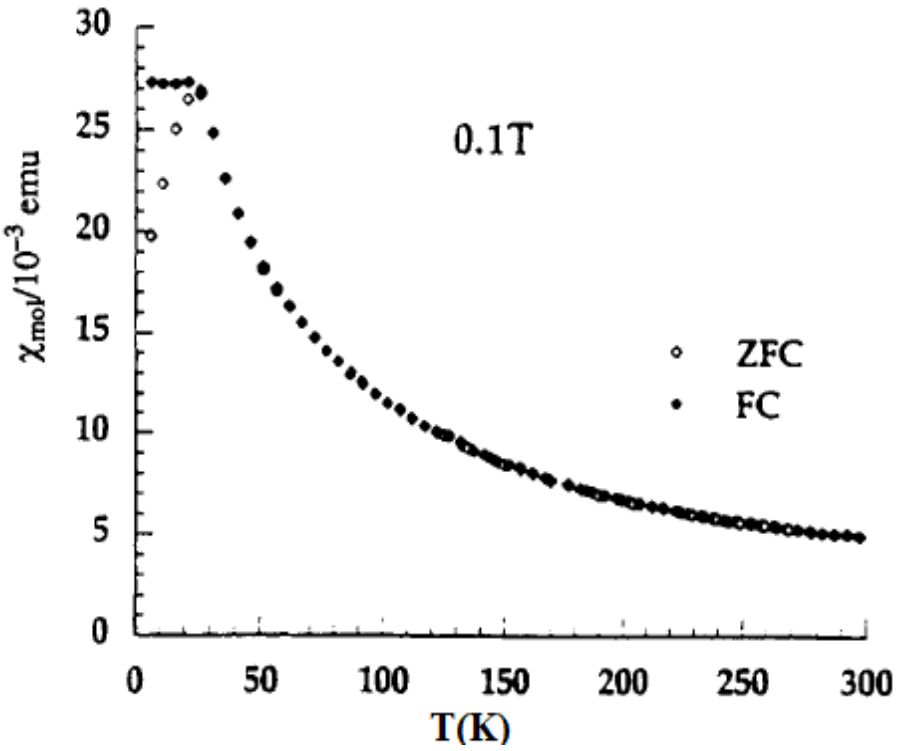

Figure 1.30: Temperature dependence of dc magnetic susceptibility curves of $Ca(Fe_{1/2}Nb_{1/2})O_3$ measured under ZFC and FC conditions [176].

Table 1.2: Comparison of room temperature crystal structure, spin-glass freezing (T_f) temperature, ferroelectric transition temperature (T_c), antiferromagnetic transition temperature (T_N) of complex perovskites.

Complex Perovskite	**Crystal Structure**	**Chemical Ordering at B-site**	**T_f /T_{SG} (K)**	**T_N (K)**	**T_c (K)**	**Reference**
$Pb(Fe_{1/2}Nb_{1/2})O_3$	Monoclinic (Cm)	Disordered	10	150	385	[171,172]
$Pb(Fe_{1/2}Ta_{1/2})O_3$	Cubic (Pm-3m)	Disordered	10	150-180	240	[174]
$Pb(Fe_{2/3}W_{1/2})O_3$	Cubic (Pm-3m)	Disordered	10	350	150	[191]
$Pb(Fe_{1/2}Sb_{1/2})O_3$	Cubic (Fm-3m)	Ordered	25	-	-	[192]
$Ca(Fe_{1/2}Nb_{1/2})O_3$ (Previous work)	Orthorhombic (Pbnm) and Monoclinic ($P2_1/n$)	Disordered/Ordered	24±1	-	-	[176,199–202]
$Ca(Fe_{1/2}Nb_{1/2})O_3$	**Orthorhombic (Pbnm)**	**Disordered**	**25**	**-**	**-**	**(Our Work)**
$Ca(Fe_{1/2}Ta_{1/2})O_3$	Orthorhombic (Pbnm)	Disordered	23±1	-	-	[176]
$Ca(Fe_{1/2}Sb_{1/2})O_3$	Orthorhombic (Pbnm)	Disordered	17±1	-	-	[176]
$Sr(Fe_{1/2}Nb_{1/2})O_3$	Tetragonal (P4/mcm)	Disordered	25±1	-	-	[176–178]
$Sr(Fe_{1/2}Ta_{1/2})O_3$	Orthorhombic (Pbnm)	Disordered	23±1	-	-	[176]
$Sr(Fe_{1/2}Sb_{1/2})O_3$	Monoclinic ($P2_1/n$)	Ordered	20	-	-	[178]
$Ba(Fe_{1/2}Nb_{1/2})O_3$	Cubic (Pm-3m)	Disordered	25±1	-	-	[176–178]
$Ba(Fe_{1/2}Ta_{1/2})O_3$	Cubic (Pm-3m)	Disordered	22±1	-	-	[176–178]
$Ba(Fe_{1/2}Sb_{1/2})O_3$	Hexagonal ($P6_3/mmc$)	Ordered	16	-	-	[178]

1.17. Objective of the present thesis:

This thesis is an attempt to understand the nature of low temperature magnetic transitions in $BiFeO_3$ (BF) and $Ca(Fe_{1/2}Nb_{1/2})O_3$ (CFN) on one hand and some of their solid solutions $(1-x)BiFeO_3$-$xBaTiO_3$ (BF-xBT), $(1-x)Ca(Fe_{1/2}Nb_{1/2})O_3$-$xBiFeO_3$ (CFN-0.10BF) and $(1-x)Ca(Fe_{1/2}Nb_{1/2})O_3$-$xLaFeO_3$ (CFN-0.10LF), on the other.

As discussed in section 1.11.7, there are several controversies about the spin-glass transition reported in $BiFeO_3$ as some workers believe that it is due to the presence of impurity phase spin clusters. Further, no attempt has been made to understand the effect of disorder on the spin-glass transitions reported in $BiFeO_3$. We have addressed these issues in chapters II, III and IV using both macroscopic (M(T), χ (ω, T), M(H), M(t), ε'(T) etc) and microscopic (neutron and x-ray diffraction) probes. We show that these spin glass transitions are intrinsic to the system based on the observation of magnetoelastic and magnetoelectric couplings at the spin-glass transitions. Our work has led to the discovery of a succession of two spin-glass transitions in BF-xBT system resulting from the freezing of the transverse and longitudinal components of the spins. We have also shown that both the spin-glass phases coexist with the LRO AFM phase in perfect agreement with the theoretical predictions for disordered Heisenberg systems. Further, we have discovered magnetoelectric and magnetoelastic character of the two spin-glass phases for the first time. We have also presented first ever evidence for phase coexistence using specific heat measurements.

The second major objective of the present thesis was to confirm the existence of spin-glass phase in Pb-free complex perovskites taking $Ca(Fe_{1/2}Nb_{1/2})O_3$ as an example using multiple criterion that are used in the literature. The spin-glass state in this system was also investigated from the point of view of the controversies related to the origin of spin-glass phase in the related compound $Pb(Fe_{1/2}Nb_{1/2})O_3$, as discussed in section

1.15.11 Chapter V of this thesis is dedicated to this aspect. We show in this chapter that $Ca(Fe_{1/2}Nb_{1/2})O_3$ undergoes cluster spin-glass freezing involving short-range ordered (SRO) AFM spin clusters.

The third major objective of this work was to go deeper into the behaviour of Pb-free complex perovskite like $Ca(Fe_{1/2}Nb_{1/2})O_3$ to get an insight into the real reason for the absence of LRO AFM state in contrast to their Pb-based counterparts like $Pb(Fe_{1/2}Nb_{1/2})O_3$. Using DC magnetization and neutron scattering studies, we show that $Ca(Fe_{1/2}Nb_{1/2})O_3$ is an incipient AFM with a potential for undergoing AFM transition around $T_N \sim 175K$. We present evidence for the stabilization of this AFM phase through 10% $BiFeO_3$ or $LaFeO_3$ substitution which enables $Ca(Fe_{1/2}Nb_{1/2})O_3$ to acquire the critical percolation threshold concentration of Fe^{3+} spins in the magnetic sublattice.

Chapter 2 Magnetic transitions in $BiFeO_3$

2.1. Introduction

Bismuth ferrite ($BiFeO_3$) is one of the most investigated magneto-electric multiferroics because of its room temperature multiferroicity with potential for applications in multifunctional devices of technological importance [29,32,34,68,95]. The room temperature ferroelectric phase of bulk $BiFeO_3$ corresponds to a rhombohedrally distorted perovskite structure in the *R*3c space group [74] in which the cations are displaced with respect to the anions along the [111] direction while the neighbouring oxygen octahedra are rotated in opposite directions (antiphase tilted structure in the $a^-a^-a^-$ tilt system [204]) about the same direction. The ferroelectric phase transition temperature is reported to be T_C ~ 1103 K [65]. The magnetic structure of $BiFeO_3$ corresponds to a non-collinear *G*-type antiferromagnetic (AFM) ordering with a superimposed incommensurate magnetic modulation below the Neel temperature T_N ~ 643 K [66]. While the nuclear and magnetic structures as well as the multiferroic properties of $BiFeO_3$ at and above the room temperature are well settled, [68,95] there exists considerable controversy about the low temperature phase transitions in this compound [87,102–104,108,109,111,112,114–117]**.**

Historically, the first low temperature magnetic transition in $BiFeO_3$ was reported by Nakamura et al. [108] using splat quenched samples. Their results showed a frequency dependent cusp in ac susceptibility ($\chi'(\omega, T)$) around T_f ~21 K with a spin-glass (SG) transition temperature T_{SG} ~ 14 K. Recent $\chi(\omega, T)$ measurements on single crystals of $BiFeO_3$ by Singh et al. [102] have also revealed frequency dependent cusp similar to that reported by Nakamura et al. [108], though with a slightly higher cusp temperature (T_f ~25 K), but with the T_{SG} ~ 29.4 K greater than T_f ~ 25 K, which is physically unrealistic as T_{SG} is the cusp temperature corresponding to the limit of $\omega (=2\pi f) \rightarrow 0$. In fact, T_{SG} in the

canonical and cluster spin glasses is invariably lower than the cusp temperature (T_f) measured at various frequencies [24,41,42]. Further, the χ (ω, T) data presented by Singh et al. [102] is also intriguing on two counts. Firstly, the peak height of χ' (ω, T) increases with increasing frequencies (see Fig. 4(a) of Ref. [102]) which is unusual as the susceptibility always decreases with increasing frequency. This anomalous frequency dependence has been attributed by Singh et al. [102] to the measuring frequency being close to the inverse of the time constant of the lumped equivalent RC circuit of the sample. The measured imaginary part of ac susceptibility, i.e. $\chi''(\omega, T)$, is also physically unrealistic as it is shown to be negative near the cusp temperature range. According to Singh et al. [102], the negative cusps at T_f in the χ'' (ω, T) may be linked with the modulated magnetic structure of $BiFeO_3$. Surprisingly, the low temperature zero field cooled (ZFC) and field cooled (FC) dc magnetization (M (T)) measurements by various workers have not revealed any signature of a spin-glass transition around 25 K and its existence has been identified by $\chi(\omega, T)$ measurements, [102] dielectric ($\varepsilon(\omega, T)$) measurements [110] and Raman studies [110] only.

In addition to the SG transition, several other transitions have been reported in $BiFeO_3$ using different measurement probes. ZFC M(T) measurements on polycrystalline powders of $BiFeO_3$ have revealed anomalies around 50 K [87], 150 K [103] and 250 K [103]. Further, the ZFC and FC M (T) curves have been reported to bifurcate below 300 K and the anomaly around 50 K does not appear under the FC condition. This has been taken as evidence for SG freezing or superparamagnetic (SPM) blocking [87,102]. The anomaly around 50 K has also been reported in the ZFC M(T) measurements on single crystals [102] as well as nanocrystalline powders [87,104].

Differential scanning calorimetry (DSC) measurements on polycrystalline $BiFeO_3$ have revealed a strong specific heat anomaly at ~250K around which an anomaly in ZFC

M (T) has also been reported [103]. The differential thermal analysis (DTA) measurements on $BiFeO_3$ single crystals, on the other hand, do not reveal any anomaly around 250 K but reveals the possibility of another phase transition in the 140 to 150 K range with a latent heat [109]. Temperature dependence of the magnetic entropy, as obtained by DSC measurements, indicates as many as five phase transitions occurring at ~38 K, ~150 K, ~178 K, ~223 K and ~250 K [103]. The ε (ω, T) measurements reveal weak anomalies around 55 K, 140 K and 215 K for single crystals [109] and around 25 K [110], 50 K [109], 200 K [109] and 220-260 K [109,117] in ceramics. Elastic modulus measurements have revealed anomalies around 140 K [109,115] and 200 K [109], respectively. Further, Raman spectroscopic studies on polycrystalline and single crystals of $BiFeO_3$ have revealed transitions at 25 K [110], 90 K [112], 140 K [111–116], 200 K [111–113] and 250 K [112]. Redfern et al. [109] have attributed the transitions occurring around 38-50 K, 140–150 K and 220–250 K to be magnetic but glassy with magnetoelectric coupling, predominantly magnetic involving spin reorientation and AFM to SG transition with weak coupling with polarization, respectively [109]. Further, the transition around 178–200 K has been proposed to be magnetoelastic in nature with a small coupling to polarization [109].

It is evident from the foregoing that no single research group has reported all the low temperature transitions in the same sample. Further, no single technique has revealed so far all the transitions. The fact that Nakamura et al. [108] did not find any cusp in χ (ω, T) around T_f ~ 50 K or signatures of other transitions above 50 K in splat quenched $BiFeO_3$ samples, supposed to be free from oxygen ion vacancies, also raises doubts about the intrinsic nature of various low temperature transitions other than the transition occurring around 25 K. In this chapter, the results of a comparative study of undoped and Mn-doped $BiFeO_3$ are presented to understand the effect of Mn-doping in small

concentration (1.5 at%) on the (1) oxygen ion vacancy concentration and the associated redox reactions, on one hand, and (2) low temperature magnetic phase transitions of $BiFeO_3$, on the other.

2.2. Sample preparation:

Both undoped and Mn-doped $BiFeO_3$ powders were prepared by the conventional solid-state route using high purity oxides as starting materials: Bi_2O_3 (Aldrich, 99.9 %), Fe_2O_3 (Aldrich, 99 %) and MnO_2 (Alfa Aesar, 99.9%). We have added 0.3 wt% MnO_2 during calcination for the preparation of doped samples. The ingredient powders were taken in stoichiometric proportions and mixed in an agate mortar pestle for 3 hours and subsequently in a planetary ball mill using a zirconia zar and zirconia balls for 6 hours with acetone as the mixing media. After drying, the mixed powders were calcined at an optimized temperature of 1063 K for 8 hours in an open alumina crucible. The calcined powder was crushed and again ball milled for 4 hours. The powder so obtained was pressed at a load of 70 KN into disks of 13mm diameter and about 1mm thickness in a hydraulic press using steel die. 2% aqueous solution of polyvinyl alcohol (PVA) was used as a binder before pressing. After binder burn-off at 773 K for 10 hours, sintering was carried out at 1093 K for 1 hour in closed alumina crucibles with calcined powder of the same composition as spacer powder for preventing the loss of Bi_2O_3 during sintering.

2.3. Characterizations tools:

The microstructure and chemical composition of the sample was obtained using Scanning Electron Microscope (SEM) (Zeiss, model no. EVO 18) and Energy Dispersive X-ray spectroscopy (EDX) attachment (Oxford, model no. 51-ADD0048). The sintered pellet was coated with conducting gold using sputter coater (Royal life Sciences, model

no. DSR1) under vacuum before taking the SEM images. The oxygen stoichiometry was determined by iodometric titration method.

The room temperature high-resolution synchrotron x-ray powder diffraction (SXRD) data were collected at P02.1 beamline of PETRA III, Hamburg, Germany, at a wavelength of 0.2079Å (~60keV). The powder sample was filled in a Kapton capillary of 0.8mm diameter and exposed for 10 s by the incident beam of cross section 0.5 mm × 0.5 mm. Two-dimensional (2D) x-ray powder diffraction (XRD) pattern was recorded using a Perkin Elmer 1621 Detector (2048 pixels × 2048 pixels, 200μm × 200μm pixel size). The sample to detector distance was set to 1310 mm. The standard LaB_6 was used to calibrate the sample to detector distance. The 2D XRD pattern was integrated using the FIT2D software. The XRD measurements were carried out using an 18-kW Cu-rotating anode based powder diffractometer (Rigaku, model no. RINT 2500/PC series) operating in the Bragg-Brentano geometry fitted with a curved crystal monochromator in the diffraction beam and a close cycle helium refrigerator based low temperature attachment. The data were collected in the 2θ range of 20 to 120 degrees at a step of 0.02 degrees. All the XRD patterns were recorded using powders obtained after crushing the ceramic pellets and annealing the crushed powder at 773 K for 10 hours for removal of stresses introduced during crushing.

X-ray photoelectron spectroscopy (XPS) measurements were performed using an Omicron energy analyzer (model no. EA-125) with Mg-K_α (1253.6 eV) lab source. The XPS data was analyzed by XPSPEAK 4.1 software.

The dc magnetization measurements were carried out using superconducting quantum interference device (SQUID) based magnetometer (Quantum Design, model no. MPMS-3) under zero filed cooled (ZFC) and field cooled (FC) conditions from 2K to 300K with low temperature attachment and ZFC M(T) from 300K to 750K using high temperature

attachment. For the ZFC measurements, the sample was first cooled from room temperature down to 2K in the absence of a magnetic field and the magnetization was measured in warming cycle after applying the magnetic field. For the FC measurements, the sample was cooled from room temperature down to 2K in the presence of magnetic field and magnetization was measured in the warming cycle under the same field.

For the resistivity and dielectric measurements, the pellets were gently polished with 0.25μm size diamond paste. After then acetone was used to clean the surfaces and then isopropyl alcohol was put on to remove the moisture on the surfaces. The electroding of the pellets on both sides was done using fired-on silver paste which is cured at 773K for 5 minutes. The DC resistivity of samples was measured using an electrometer (Keithley, model no. 6517A). The low temperature dielectric ($\varepsilon(\omega, T)$) measurements were carried out using the sample holder mounted on a variable temperature insert of a cryogen free measurement system (CFMS) (Cryogenic, model no. 7 Tesla mini CFM). Novocontrol (Alpha-A) high performance frequency analyzer was used for measuring the capacitance and loss tangent ($\tan\delta$).

2.4. Results and discussion:

2.4.1 Compositional analysis:

The composition was checked over individual grains and around grain boundaries separately. Fig. 2.1 (a-d) show the microstructure and the EDX spectra for the undoped and Mn-doped $BiFeO_3$ samples. The representative regions in the grain and at the grain boundaries are marked in the microstructures. The results of EDX analysis for the two types of samples are given in Table 2.1. Similar analyses were carried out at five randomly selected regions and the average composition is given in Table 2.2 for the undoped and Mn-doped samples. It is evident from these tables that the average composition obtained by EDX analysis is close to the nominal (expected) composition

within the limit of standard deviation for Bi, Fe and Mn. The oxygen content for the undoped sample is found to be a little less than that for the Mn-doped sample.

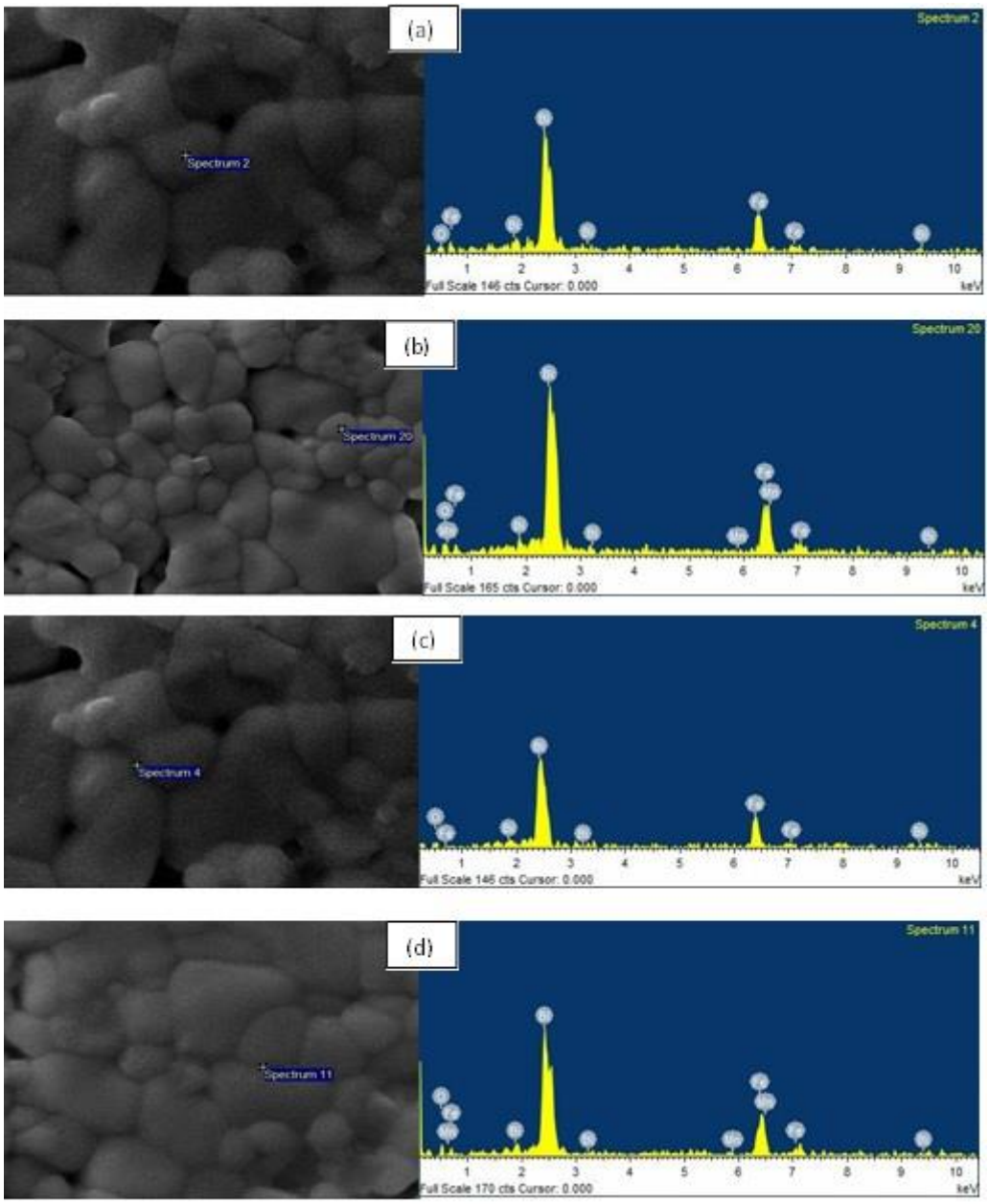

Figure 2.1: Microstructure and EDX spectra for undoped and Mn-doped $BiFeO_3$ **(a, b)** in the grain and **(c, d)** around the grain boundary.

However, it is worth mentioning that EDX is not the ideal tool for the determination of oxygen content. The oxygen content can be determined from the iodometric titration method and is found to be 2.94 ± 0.02 and 2.98 ± 0.02 for undoped and Mn-doped

$BiFeO_3$, respectively. The chemical composition formula for undoped and Mn-doped sample using EDX and iodometric titration analysis is found to be $BiFeO_{2.94\pm0.02}$ and $BiFe_{0.985}Mn_{0.015}O_{2.98\pm0.02}$, respectively.

Table 2.1: Results of EDX analysis of undoped and Mn-doped $BiFeO_3$ in weight percent and atomic percent for the microstructure and spectra shown in Fig. 2.1.

Undoped $BiFeO_3$					Mn-doped $BiFeO_3$				
	Chemical compositions					Chemical compositions			
	Grain		Grain Boundary			Grain		Grain Boundary	
Element	Weight %	Atomic %	Weight %	Atomic %	Element	Weight %	Atomic %	Weight %	Atomic %
O	11.9	52.7	11.3	51.3	O	12.6	54.5	14.6	58.0
Fe	18.7	23.8	18.8	24.4	Mn	0.3	0.4	0.3	0.4
Bi	69.4	23.5	69.9	24.3	Fe	17.6	21.9	18.5	21.2
					Bi	69.5	23.2	66.6	20.4

Table 2.2: Average composition of the undoped and Mn-doped $BiFeO_3$ samples in weight percent and atomic percent.

Undoped $BiFeO_3$			Mn-doped $BiFeO_3$		
	Average chemical compositions			Average chemical compositions	
Element	Weight %	Atomic %	Element	Weight %	Atomic %
O	13.0 ± 1.7	55.0 ± 3.5	O	13.6 ± 1.4	56.5 ± 3.1
Fe	18.6 ± 0.3	22.7 ± 1.7	Mn	0.3 ± 0.1	0.4 ± 0.2
Bi	68.4 ± 1.5	22.3 ± 1.9	Fe	17.8 ± 0.7	21.3 ± 1.6
			Bi	68.3 ± 1.3	21.8 ± 1.5

2.4.2 Room temperature synchrotron x-ray diffraction studies:

Single-phase powder and sintered ceramic samples of $BiFeO_3$ are rather difficult to prepare because of the narrow temperature range of the stability of the perovskite phase

and the volatile nature of Bi^{3+} that promotes the formation of impurity phases like $Bi_2Fe_4O_9$ [70] and $Bi_{25}FeO_{39}$ [71]. Figs. 2.2(a) and (b) compare the room-temperature SXRD patterns of undoped and Mn-doped $BiFeO_3$ powders. It is evident from the figures that both the samples are almost single phase as all the peaks correspond to the main perovskite phase of $BiFeO_3$ with only a trace amount of an impurity phase $Bi_2Fe_4O_9$ is present with a peak intensity that is 2.4 % of the strongest 220_{pc} peak of $BiFeO_3$ with respect to the doubled pseudocubic (pc) unit cell.

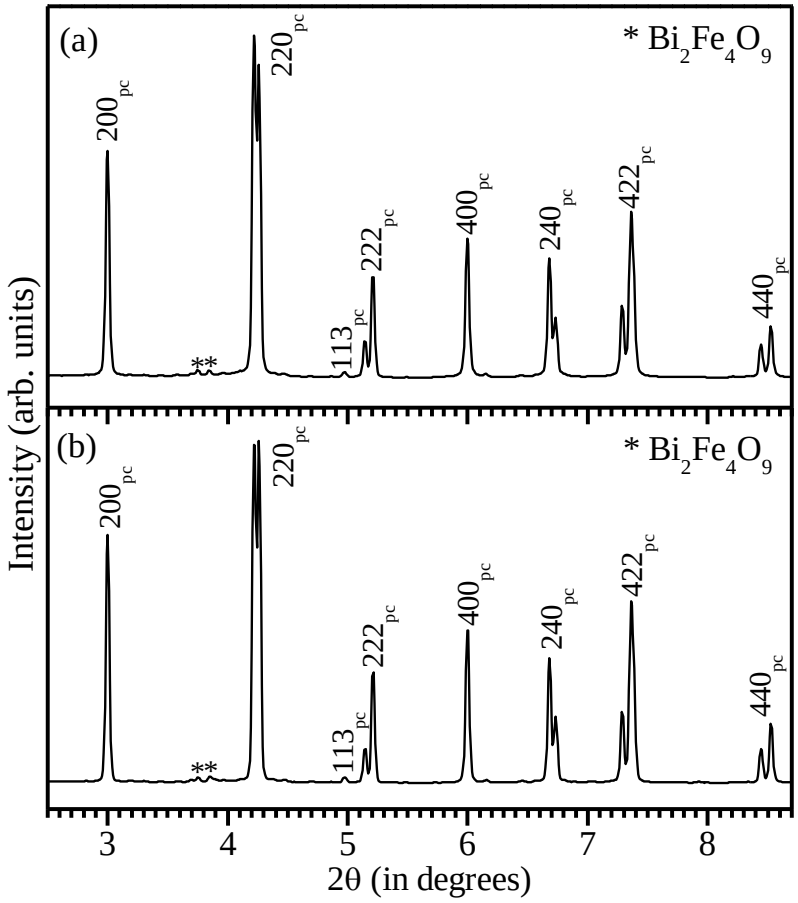

Figure 2.2: High resolution synchrotron x-ray powder diffraction patterns collected at room temperature for (a) Undoped $BiFeO_3$ and (b) Mn-doped $BiFeO_3$. All indices are with respect to a doubled pseudocubic cell.

It is also evident from Fig. 2.2(a) and (b) that the 400_{pc} is a singlet while 222_{pc} and 440_{pc} are doublets, as expected for the stable rhombohedral phase of $BiFeO_3$ in the R3c space group. The above qualitative observations for both the samples were further

confirmed by using the Rietveld refinement technique. For the Rietveld refinement of the rhombohedral phase of $BiFeO_3$ with R3c space group, we have used the hexagonal unit cell. In the asymmetric unit of $BiFeO_3$, the Bi^{3+} ions occupy the 6(a) Wyckoff site with (0, 0, 0) position and Fe^{3+} ions occupy the same 6(a) Wyckoff site with position (0, 0, z) while O^{2-} ions at the 18(b) Wyckoff site with position (x, y, z).

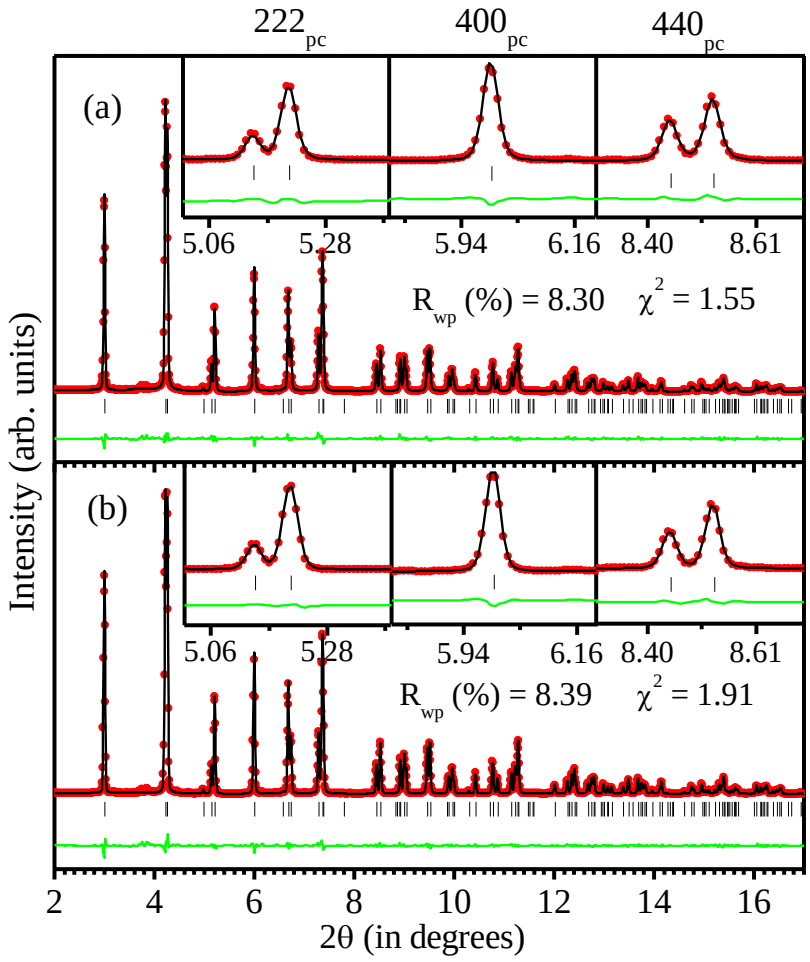

Figure 2.3: Observed (filled circles), calculated (continuous line), and difference (bottom line) profiles obtained from the Rietveld analysis of the room temperature synchrotron x-ray powder diffraction data for (a) Undoped $BiFeO_3$ and (b) Mn-doped $BiFeO_3$ sample using R3c space group. The vertical tick marks above the difference profile represent the Bragg peak positions. Insets depicts the profile fits for 222_{pc}, 400_{pc}, and 440_{pc} pseudocubic peaks.

In the refinement process the background was modelled with linear interpolation and the peak shape was modelled using pseudo-Voigt function. Occupancy of all the ions

were fixed at the nominal composition in the refinements. Zero correction, scale factor, background, lattice parameters, half width parameters (u, v and w), positional coordinates and thermal parameters were varied during the refinement. Fig. 2.3(a) and (b) depicts the Rietveld refinement of the SXRD patterns of undoped and Mn-doped $BiFeO_3$ samples at room temperature using R3c space group. It is evident from the figure that the observed (filled-circles) and calculated (continuous line) profiles show excellent fit, as can be seen from the difference (bottom line) profile given in this figure. This confirms that all the peaks in the SXRD patterns of both the samples are indexed with single phase of rhombohedral structure with R3c space group.

The refined structural parameters given in Table 2.3 are in good agreement with those reported in literature [205]. The important inference is that the unit cell parameters are not affected by Mn-doping.

Table 2.3: Structural parameters and agreement factors obtained from Rietveld refinement of SXRD data for undoped and Mn-doped $BiFeO_3$ sample using R3c space group.

Parameters	**Undoped $BiFeO_3$**	**Mn-doped $BiFeO_3$**	**Literature** [205]
a_{hex} (Å)	5.5782 (6)	5.5779 (8)	5.57874 (16)
c_{hex} (Å)	13.8665 (2)	13.8662 (3)	13.8688 (3)
v_{hex} (Å)	373.67 (8)	373.63 (1)	373.802 (17)
α, β, γ	$\alpha=\beta=90^0$, $\gamma=120^0$	$\alpha=\beta=90^0$, $\gamma=120^0$	$\alpha=\beta=90^0$, $\gamma=120^0$
Bi (x, y, z)	0	0	0
Fe (0, 0, z)	0.2208 (1)	0.2209 (2)	0.22077 (8)
O (x)	0.4481 (2)	0.4525 (1)	0.4428 (11)
O (y)	0.0179 (2)	0.0226 (2)	0.0187 (10)
O (z)	0.9536 (5)	0.9523 (6)	0.9520 (4)
β_{Bi}(Å^2)	0.64 (1)	0.64 (2)	$\beta_{11}=\beta_{22}=0.00996$ (15) $\beta_{33}=0.00641$ (14)
β_{Fe} (Å^2)	0.43 (5)	0.44 (5)	$\beta_{11}=\beta_{22}=0.00659$ (23), $\beta_{33}=0.0054$ (3)
β_O(Å^2)	0.63 (2)	0.67 (2)	$\beta_{11}=0.0112$ (14), $\beta_{22}=\beta_{33}=0.0078$ (14) $\beta_{12}=0.0052$ (12), β_{13} =-0.002(11), β_{23}= -0.0017 (11)
R_{wp} (%)	8.30	8.39	
χ^2	1.55	1.91	

2.4.3 Role of Mn-doping on oxygen ion vacancies:

It is well known that the electrical and magnetic properties of undoped $BiFeO_3$ are strongly influenced by oxygen ion vacancies created during sintering of $BiFeO_3$ [89,136,139]. Each oxygen ion vacancy leaves behind two electrons as per the following reaction written in the Kröger-Vink notation [89]:

$$O_0 \Leftrightarrow 1/2O_2 + V_0^{\cdot\cdot} + 2e' \qquad \ldots\ldots(2.1)$$

where O_o is the oxygen atom, $V_o^{\cdot\cdot}$ represents oxygen vacancies with two net positive charges and e´ stands for electron with negative charge (´). Electrons released due to oxygen ion vacancy may be captured by Fe^{3+} of $BiFeO_3$ leading to its reduction to Fe^{2+}:

$$Fe^{3+} + 1e' \Leftrightarrow Fe^{2+} \qquad \ldots\ldots\ldots (2.2)$$

The presence of Fe^{2+} and Fe^{3+} ions leads to hopping of electrons as a result of which the conductivity increases. In case of our samples, the resistivity of undoped $BiFeO_3$ at room temperature is $1.6 \times 10^7 \Omega$ cm while it increases by three orders of magnitude to $1.09 \times 10^{10} \Omega$ cm in the Mn-doped $BiFeO_3$ samples. This observation is in agreement with findings of other workers also for Mn-doping level less than 3 atom % [136–142,206–212]. Similarly, we find that the dielectric loss (tanδ) decreases quite significantly from tanδ ~ 0.969 to ~ 0.425 (at 100 kHz) as result of Mn-doping. Higher doping level (> 3 at %) leads to decrease of the resistivity due to change in the valence states from Mn^{3+} to $Mn^{2+}$of Mn ions for charge compensation and also substitution effect which creates oxygen vacancies as confirmed by XPS, leakage current and XES measurements [137,212–214]. Theoretical [215] and experimental (x-ray absorption fine structure (XAFS) spectra [216] Mössbauer and XPS [217] studies revealed that in Mn-doped $BiFeO_3$ sample the oxidation state of Mn ions is always +3. We believe that Mn^{4+} doping in low concentrations plays the role of accepter in $BiFeO_3$ and compensates the electron charge carriers generated by oxygen ion vacancies. This in turn results in redox

reaction involving capture of electron by Mn^{4+} ion reducing it to Mn^{3+}. The instability of Mn^{4+} (MnO_2 decompose to Mn_2O_3 at 923 K Ref [139]) plays a dual role through redox processes to control or reduce the oxygen ion vacancy formation as per the following redox reactions:

1. $Mn^{4+} + 1e' \rightarrow Mn^{3+}$ (capture the electrons released during oxygen ion vacancy formation)

and/ or

2. $Mn^{4+} + Fe^{2+} \rightarrow Fe^{3+} + Mn^{3+}$ (oxidize Fe^{2+} back into Fe^{3+})

Both the reactions can effectively suppress the conversion of Fe^{3+} to Fe^{2+} due to reduced concentration of oxygen ion vacancies and thereby suppress the hopping conductivity. The observed increase in the resistivity and decrease in the tanδ of the doped samples with respect to the undoped samples is therefore seem to be correlated with suppression of oxygen ion vacancy and Fe^{2+} ion concentrations.

We used XPS studies on both the undoped and Mn-doped $BiFeO_3$ samples to determine the Fe^{2+} ion concentrations. As discuss in previous section 2.4.1 that the iodometric titrations give oxygen contents of 2.94 ± 0.02 and 2.98 ± 0.02 for undoped and doped samples, respectively. Evidently, the oxygen ion vacancy concentration is lower in the doped samples. As a result of reduced oxygen ion concentration due to Mn-doping, the redox reaction given by (2) is expected to be suppressed leading to lower Fe^{2+} ion concentration. This was further verified by XPS measurements using Fe 2p core level spectra for both undoped and Mn-doped $BiFeO_3$ samples (see Fig. 2.4(a) and (b)). It is well known that due to spin-orbit coupling, the Fe 2p core level spectra split into two components $2p_{3/2}$ (located at 710.6 eV) and $2p_{1/2}$ (located at 723.5 eV) with a satellite peak located around 719 eV [218–220]. The asymmetry in the peaks towards the lower binding energy in Figs. 2.4(a) and (b) reveals the presence of Fe^{2+} in both the undoped and Mn-doped $BiFeO_3$ samples. In order to quantify the ratio of Fe^{3+}/Fe^{2+}, we have

carefully analyzed the $2p_{3/2}$ peak for both undoped and Mn-doped $BiFeO_3$ samples and the best fits are shown in the insets to Fig. 2.4(a) and (b). The $2p_{3/2}$ peak in the inset consists of two components corresponding to Fe^{2+} (708.5-709.3 eV) and Fe^{3+} (710.6 eV).

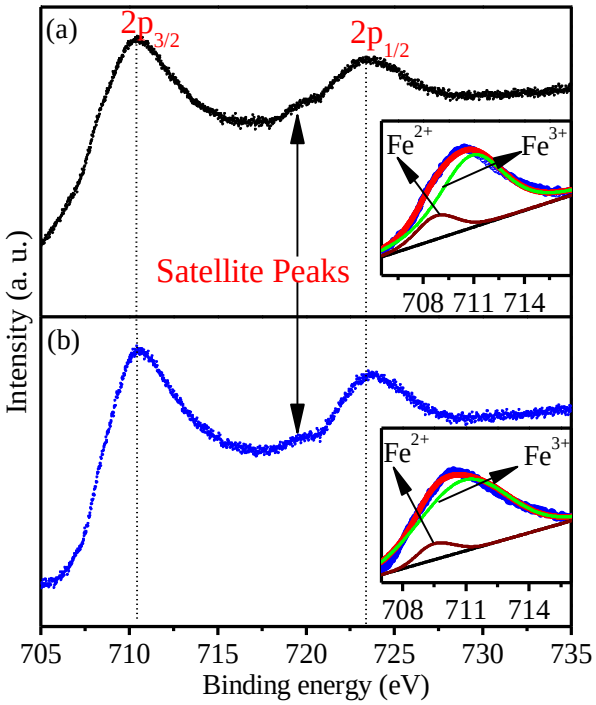

Figure 2.4: XPS Fe 2p core level spectra for **(a)** undoped $BiFeO_3$ **(b)** Mn-doped $BiFeO_3$. Insets to figure 3**(a)** and **(b)** depict the fitted profile of $2p_{3/2}$ peak.

The ratio of Fe^{3+}/ Fe^{2+} for undoped $BiFeO_3$ was found to be 85/15 and for the Mn-doped sample this comes out to be 92/08. The larger concentration of Fe^{2+} ions in undoped $BiFeO_3$ sample is attributed to redox reaction caused by the capture of electron released during oxygen ion vacancy formation as per reaction (1) at high temperatures during sintering. These results along with EDX and iodometric titration analysis give the overall formula as $BiFe^{3+}_{0.88}Fe^{2+}_{0.12}O_{2.94}$ and $BiFe^{3+}_{0.925}Fe^{2+}_{0.06}Mn^{3+}_{0.015}O_{2.98}$, respectively, for the undoped and doped sample assuming that all of Mn has gone into the Fe sites. The ratio of Fe^{3+}/ Fe^{2+} by XPS study show very close proximity with the electronic configuration of our samples as determined by taking charge neutrality and oxygen stoichiometry into the consideration. Thus, our results

clearly reveal a close correlation between Mn-doping and oxygen ion vacancy and Fe^{2+} ion concentrations leading to three order of magnitude increase in the resistivity and significant decrease in tanδ value of the Mn-doped samples with respect to the undoped samples. We now proceed to show the effect of Mn-doping with reduced oxygen ion vacancy and Fe^{2+} concentrations on the low temperature magnetic transitions of $BiFeO_3$.

2.4.4 Effect of Mn doping on the low temperature magnetic phase transitions:

Fig. 2.5 shows the variation of dc magnetization (M (T)) with temperature under ZFC and FC conditions for the undoped and doped samples, respectively, for an applied field of 500 Oe. The ZFC and FC magnetizations bifurcate above 300 K for the undoped samples whereas for the doped samples it begins around 270 K. The bifurcation of the M (T) plots under ZFC and FC conditions increases with decreasing temperature suggesting spin-glass or superparamagnetic behaviour in $BiFeO_3$ at low temperatures as proposed by previous workers also [102,108]. The ZFC and FC magnetization curves of both the samples in the 300 to ~150 K range are consistent with conventional antiferromagnetic (AFM) behaviour in which magnetization is expected to decrease with decreasing temperature below T_N which is close to~650 K for both undoped and doped samples (see Fig. 2.5(b) and (d)). However, both types of samples show an upturn in magnetization below ~150 K. This can happen as a precursor effect to an impending phase transition and accordingly a spin reorientation transition [111,112,116], similar to that in orthoferrites [221,222], with the involvement of electromagnons [111,116], has been proposed [102]. Such a spin reorientation transition has recently been reported in monoclinic compositions of solid solutions of $BiFeO_3$ with $PbTiO_3$ but the transition temperature is well above the room temperature and just below the T_N [223]. In pure $BiFeO_3$, the situation is quite different as spin reorientation has been proposed well below room temperature.

In addition to the transition around 150K due to electromagnon [111,116], the M(T) measurements clearly reveal another anomaly around 260 K in the doped samples (see Fig. 2.5(b)) which is less clear in the undoped samples. A similar anomaly has been

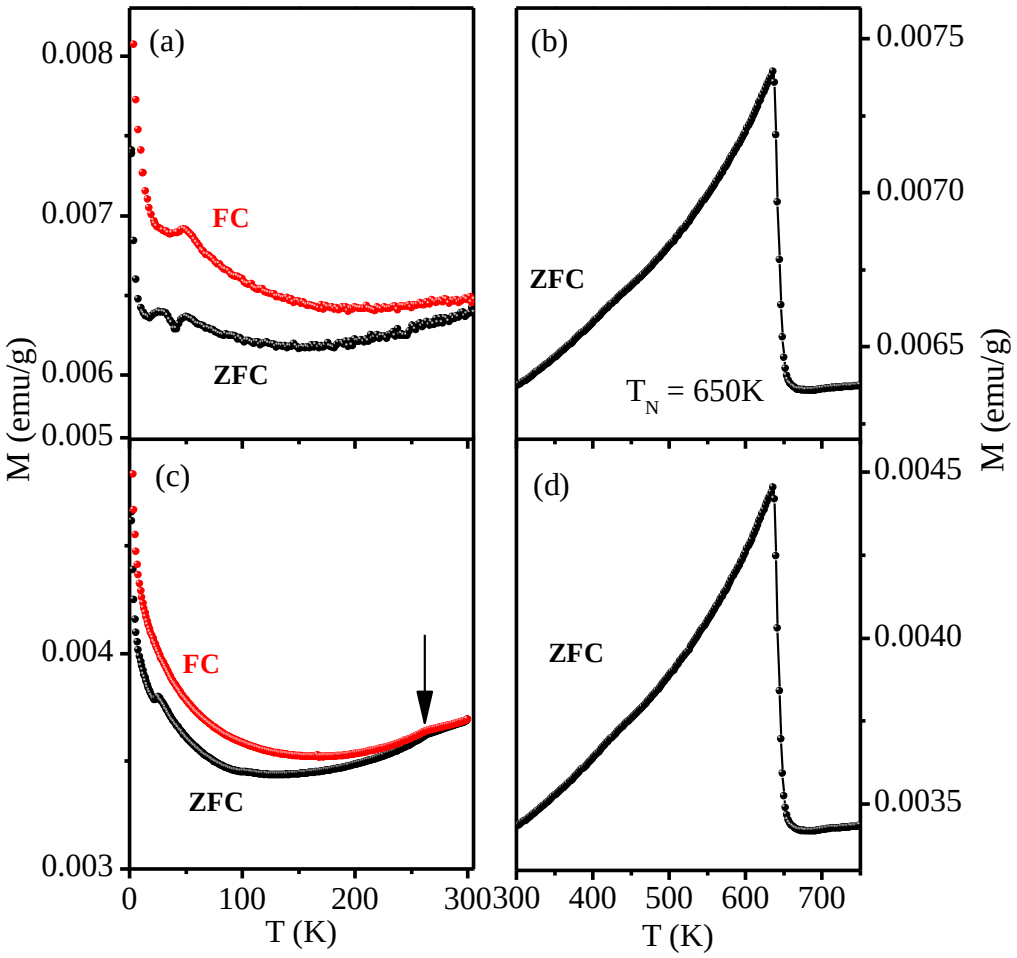

Figure 2.5: Temperature dependence of dc magnetization for **(a-b)** Undoped $BiFeO_3$ and **(c-d)** Mn- doped $BiFeO_3$ at an applied field of 500 Oe in two separate measurements from 2-300K and 300 to 750K range.

reported by Ramachandran et al. [103] also who attributed it to spin-glass transition. We shall discuss the nature of this transition further in the next chapter in more detail. On cooling below 150 K, the ZFC M(T) of undoped samples shows a very prominent peak around 50K but this transition is absent in the doped samples. This transition has been reported by a few workers in the past [87,102] and has been proposed to be due to spin-

glass freezing or superparamagnetic (SPM) blocking since the FC M(T) plot shows clear bifurcation around the peak temperature (~50K) in the ZFC plot of the undoped samples. The peak around 25 K in the ZFC M(T) of both types of sample is not present in the FC M (T) plots of these samples suggests that it could be due to spin glass freezing or superparamagnetic blocking. Below 10 K, both ZFC and FC curves for both types of samples show increase in the magnetization indicating a weak ferromagnetic behaviour of $BiFeO_3$ at such low temperatures, as noted by previous workers also [102,103].

A frequency dependent peak in ac susceptibility (χ' (ω, T)) has been reported around 25K in the literature [102] which has been attributed to spin-glass freezing. Accordingly, we also carried out ac susceptibility measurements χ (ω, T). Fig. 2.6 (a, b) and (c, b) show the real (χ' (ω, T)) and imaginary (χ'' (ω, T)) parts of χ(ω, T) measured

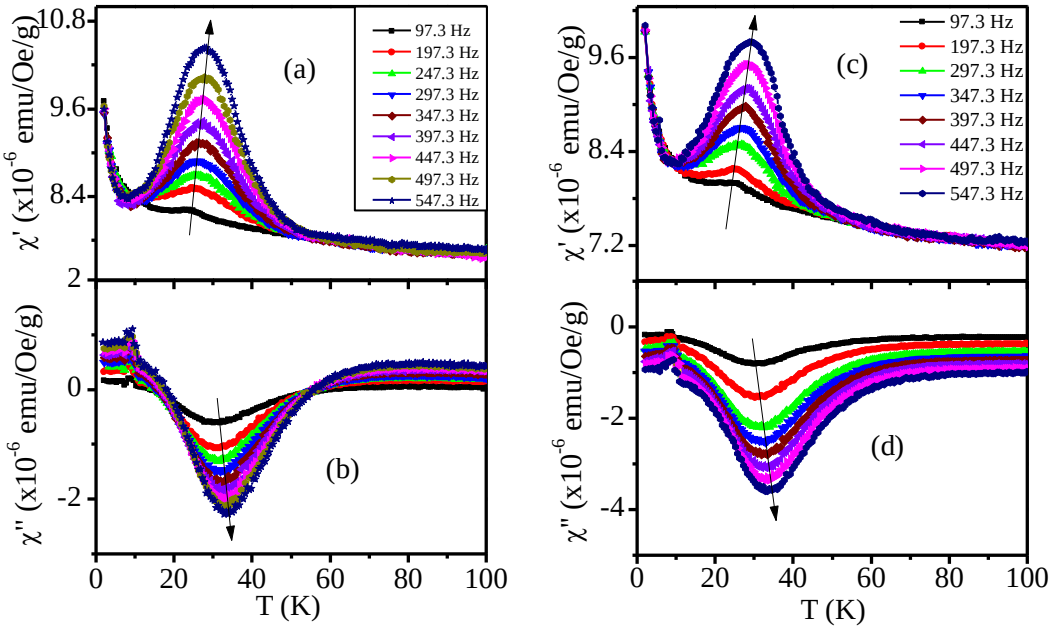

Figure 2.6: Temperature dependence of the real and imaginary parts of the ac susceptibility at various frequencies at an applied ac field of 5 Oe for (**a**, **b**) undoped $BiFeO_3$ and (**c**, **d**) Mn-doped $BiFeO_3$.

with an applied ac drive field of 5 Oe in the frequency range 97.3 Hz to 547.3 Hz for undoped and doped $BiFeO_3$, respectively. It is evident from the figures that the peak temperatures corresponding to the χ' (ω, T) and χ'' (ω, T) shift towards higher temperatures with increasing frequency which can be due to SG freezing or SPM blocking. For SPM blocking, ln τ versus 1/T plot should be linear as per Arrhenius law [224] ($\tau = \tau_0 \, exp\left(\frac{E_a}{k_B T}\right)$ where E_a is activation energy). The spin relaxation time τ can be determined from the measurement frequency (ω =2πf) at the peak temperature (T_f) of χ' (ω, T). The non-linear nature of the plots shown in the insets of Fig. 2.7 (a) and (b) rules out SPM blocking in $BiFeO_3$ at low temperatures. The power law [225] ($\tau = \tau_0 \left(\frac{T_f - T_{SG}}{T_{SG}}\right)^{-z\nu}$ type critical dynamics provides excellent fit for both the undoped and doped samples, as can be seen from Fig. 2.7 (a) and (b), confirming the SG freezing with a T_{SG} ≈ (20±1)K. Our results thus confirm unambiguously that the anomaly observed around T_f ~ 25 K in $BiFeO_3$ is due to SG freezing with a T_{SG} ≈ (20±1)K at which the ergodicity is broken. Our results also show that the earlier report [102] of $T_{SG} > T_f$ in $BiFeO_3$ is not correct and may be an artifact of numerical fit. By definition also, the T_{SG} cannot be higher than $T_f(\omega)$ as it corresponds to the value of $T_f(\omega)$ in the limit of ω tending towards zero at which the slowest spin dynamics diverges. The difference between the M(T) behaviour of the undoped and doped $BiFeO_3$ samples is the absence of the 50K transition and clearer evidence for another transition around 260K in the doped samples. Some weak signatures of a possible transition around 260K has been reported by the previous workers also in undoped samples [103] but it becomes very clear in the doped sample (see Fig.2.5(a) and (c)). The fact that the signatures of these two transitions could be observed unambiguously in M(T) plots of the doped samples highlights the role of Mn-doping and associated decrease in the oxygen ion vacancy and Fe^{2+} ion concentrations in

capturing this transition as discussed in section 2.4.5, both doped and undoped samples exhibit a dielectric step around the 260K with a peak in the loss tangent (tanδ) suggesting

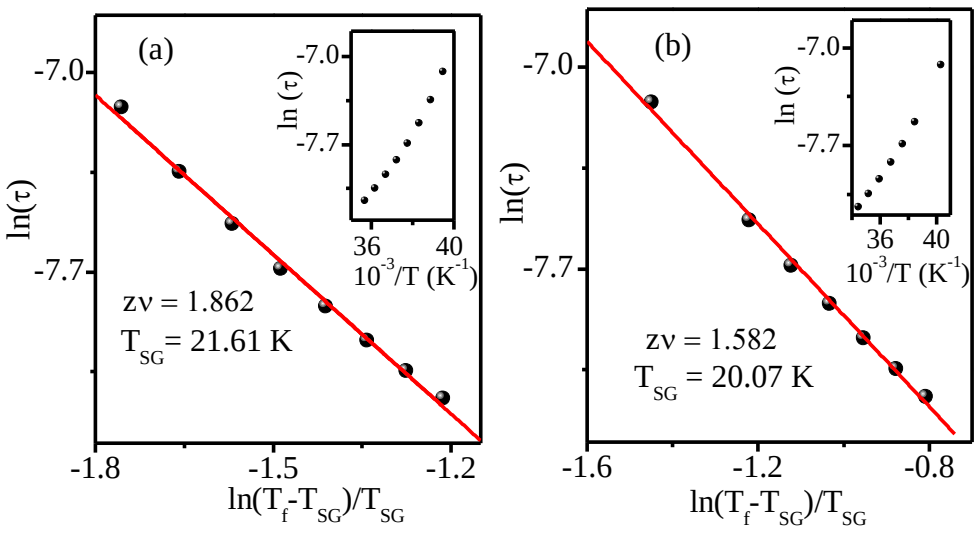

Figure 2.7: ln(τ) vs ln(T_f-T_{SG}/T_{SG}) plot. The solid line is the fit for the power law for **(a)** undoped $BiFeO_3$ **(b)** Mn-doped $BiFeO_3$. Insets depicts ln(τ) vs 1/T plot.

the presence of this transition in both the samples with magnetodielectric couplings. Our magnetization measurements thus suggest that the transition around 25, upturn around 150K and the step around 260 K observed in the ZFC M (T) plot of the doped sample are intrinsic to $BiFeO_3$.

What could be responsible for the 50K transition in the undoped samples and its absence in the doped samples. The iodometric and XPS studies on undoped and doped samples clearly reveal the difference in the defect chemistry of the two samples in terms of decrease in oxygen ion vacancy and Fe^{2+} ion concentrations, respectively, in the doped samples with respect to the undoped samples. The three orders of magnitude increase in the resistivity and decrease in tanδ of the doped sample as compared to that of the undoped samples provides additional credence to the possible role of Mn-doping through reduction in the oxygen ion vacancy and Fe^{2+} ion concentrations. Hence, we believe that

the absence of the 50 K transition in the doped samples of $BiFeO_3$ is most likely due to the neutralization of charged oxygen ion vacancies through Mn-doping.

Defect-induced magnetism is well known phenomenon in solids, in general, and the role of oxygen ion vacancies, in particular, in magnetic as well as non-magnetic materials has been investigated extensively, both experimentally [226–230] and theoretically [231–234]. The oxygen ion vacancies have been reported to influence the magnetic behavior of oxides in several ways. For example, the Fe^{3+} to Fe^{2+} redox reaction has been proposed to create local ferromagnetic clusters via double exchange mechanism that may enhance the magnetization. Using first principle calculations, [232] showed that intrinsic oxygen ion vacancies indeed lead to the formation of Fe^{2+}, as evident from the qualitative differences in the local density of states and promote ferromagnetism. The fact that the magnetization of the undoped samples shown in Fig. 2.5(a) is higher than that of the doped sample (see Fig. 2.5(c)) agrees well with this picture.

2.4.5 Evidence for change in dielectric constant around the magnetic transitions:

The appearance of an anomaly in the dielectric constant and/or loss tangent around a magnetic transition is a signature of magnetoelectric coupling [68,89], in the absence of space charge contribution coming of Fe^{2+}/Fe^{3+} redox reaction [117]. The space charge effect is minimized at higher frequencies [89] in $BiFeO_3$ based samples. The variation of the real part of the dielectric constant (ε') and loss tangent ($\tan\delta$) for undoped and Mn-doped $BiFeO_3$ as a function of temperature is shown in Figs. 2.8 (a, b) and 2.9 (a, b) at 20 kHz. The real part of ε' shows a change of slope around 25 K for both undoped and Mn-doped $BiFeO_3$ samples as shown in the inset of Figs. 2.8 (a) and 2.9(a) for the undoped and Mn-doped $BiFeO_3$ samples at 20 kHz. This suggests that the transition around 25 K, observed by M(T) measurement may involve magnetoelectric coupling also. Also, since the Mn-doping reduces oxygen ion vacancies, it would lead to suppression of

space charge dipole. This indeed is reflected in the lower values of ε′ and tanδ of the doped sample shown in Fig. 2.9. One also observes a prominent dielectric step around 260K transition [117] with a peak in the tanδ plot in both the doped and undoped samples. This not only suggests the presence of magneto-dielectric coupling for 260K transition

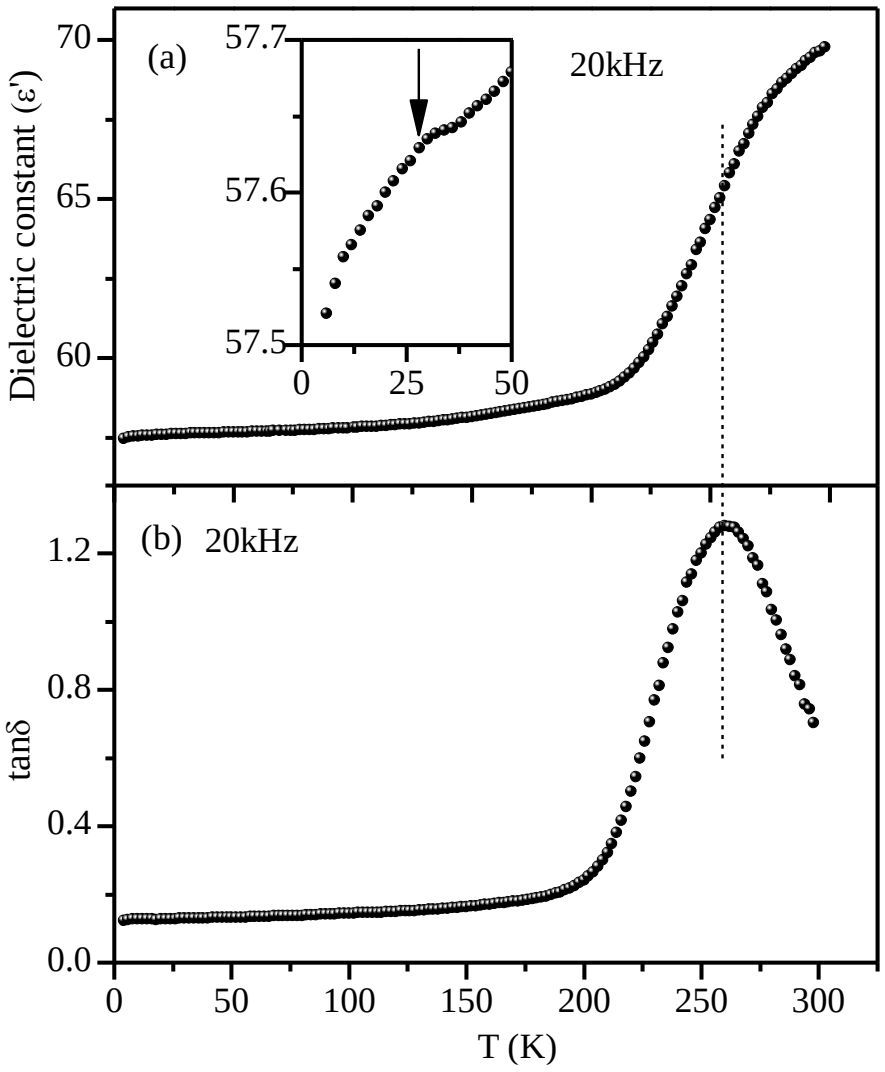

Figure 2.8: Dielectric constant and dielectric loss as a function of temperature for undoped $BiFeO_3$ at 20 kHz frequency. Inset to figure show the anomaly around 25K.

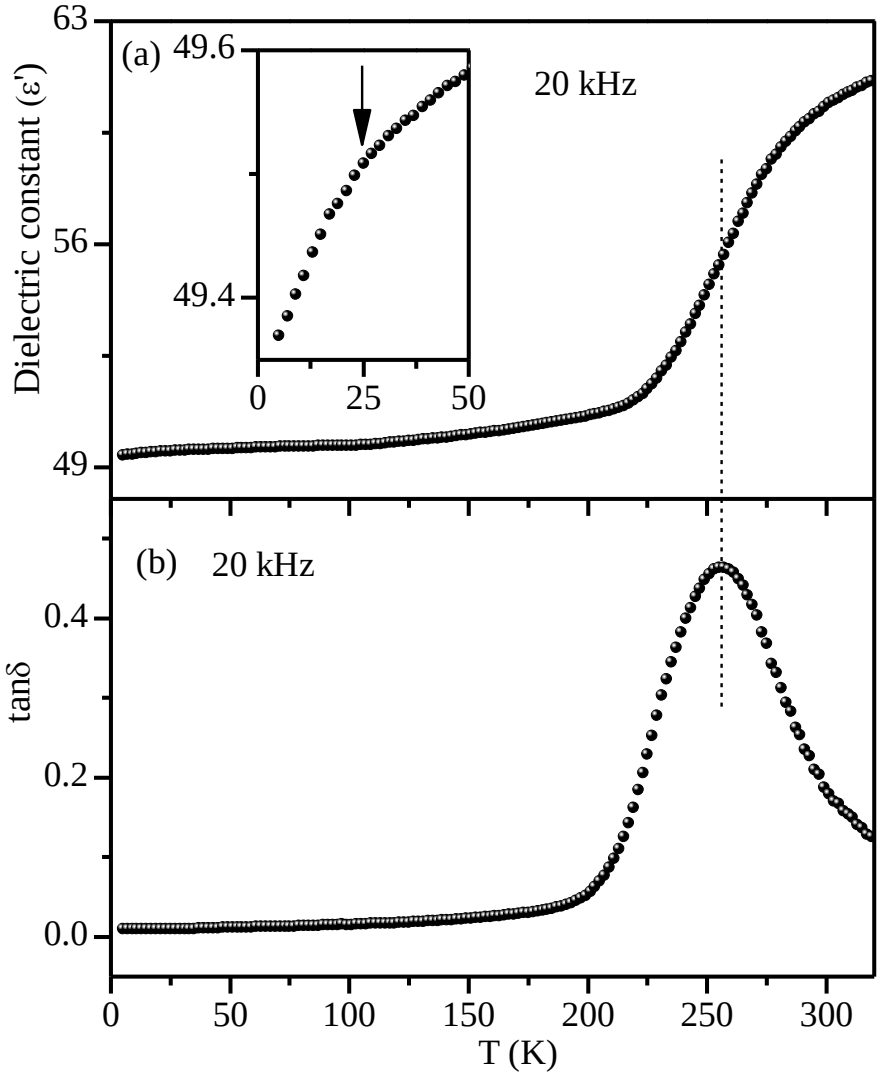

Figure 2.9: Dielectric constant and dielectric loss as a function of temperature for Mn-doped $BiFeO_3$ at 20 kHz frequency. Inset to figure show the anomaly around 25K.

but also provides indirect support to the presence of this transition in undoped sample, not clearly revealed in the M (T) plot (see Fig. 2.5(a)). The observation of a relaxation step and a change of slope 260K and 25 K, transitions in both types of samples suggests magneto-dielectric coupling.

2.4.6 Evidence for change in unit cell parameters around the magnetic transitions:

In order to verify if any one of the low temperature magnetic transitions involves a structural change, we carried out XRD studies in the 300 to 13 K temperature range. Fig.

2.10 and 2.11 shows the temperature dependent evolution of XRD profiles of a few selected peaks (222_{pc}, 400_{pc} and 440_{pc} reflections) after stripping off the $K_{\alpha 2}$ contribution

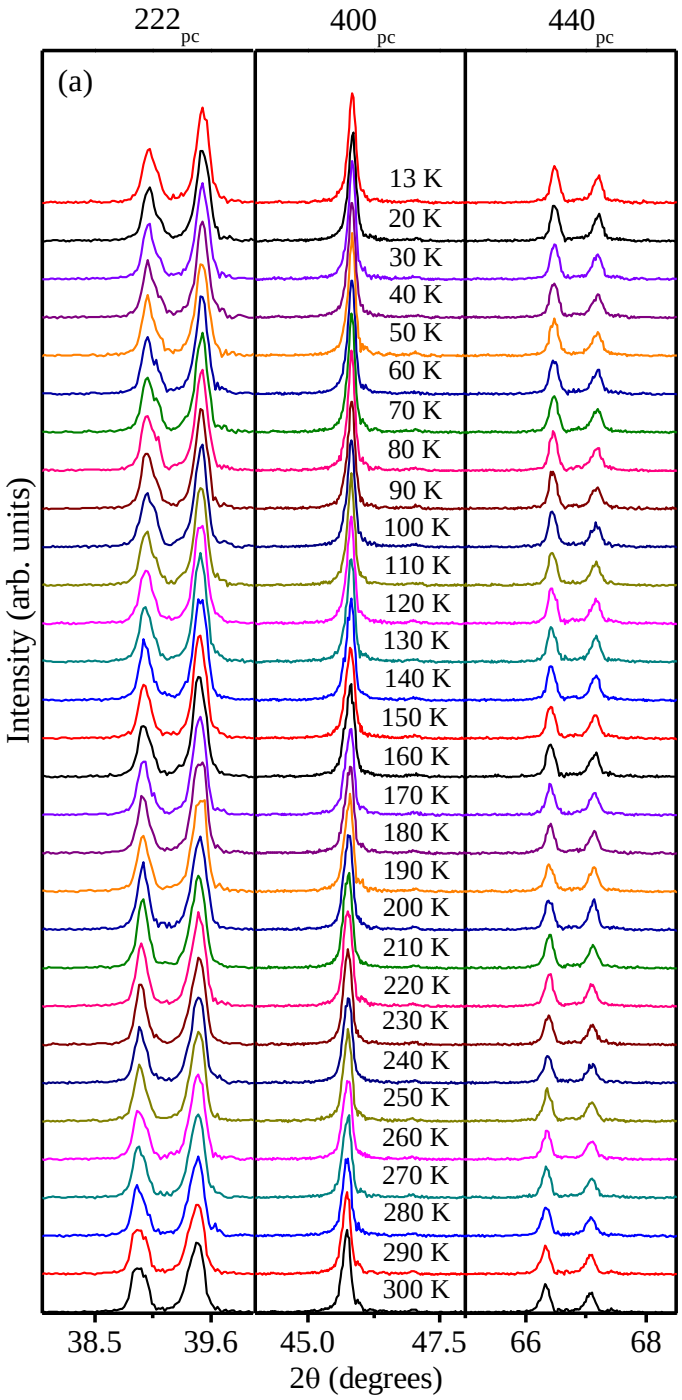

Figure 2.10: The evolution of x-ray powder diffraction profiles of the $(222)_{pc}$, $(400)_{pc}$ and $(440)_{pc}$ reflections of pure $BiFeO_3$ sample with temperature showing the absence of any structural phase transition. The Miller indices are written with respect to a doubled pseudocubic cell.

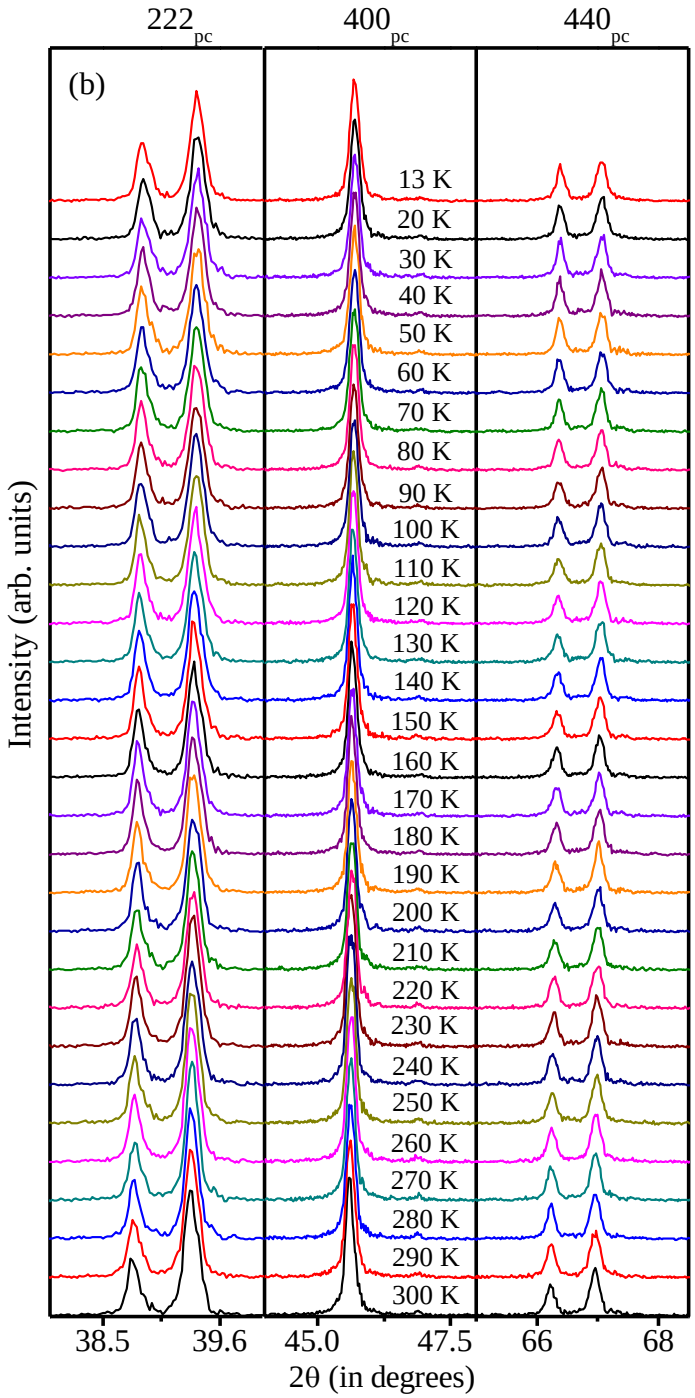

Figure 2.11: The evolution of x-ray powder diffraction profiles of the $(222)_{pc}$, $(400)_{pc}$ and $(440)_{pc}$ reflections of Mn-doped $BiFeO_3$ sample with temperature showing the absence of any structural phase transition. The Miller indices are written with respect to a doubled pseudocubic cell.

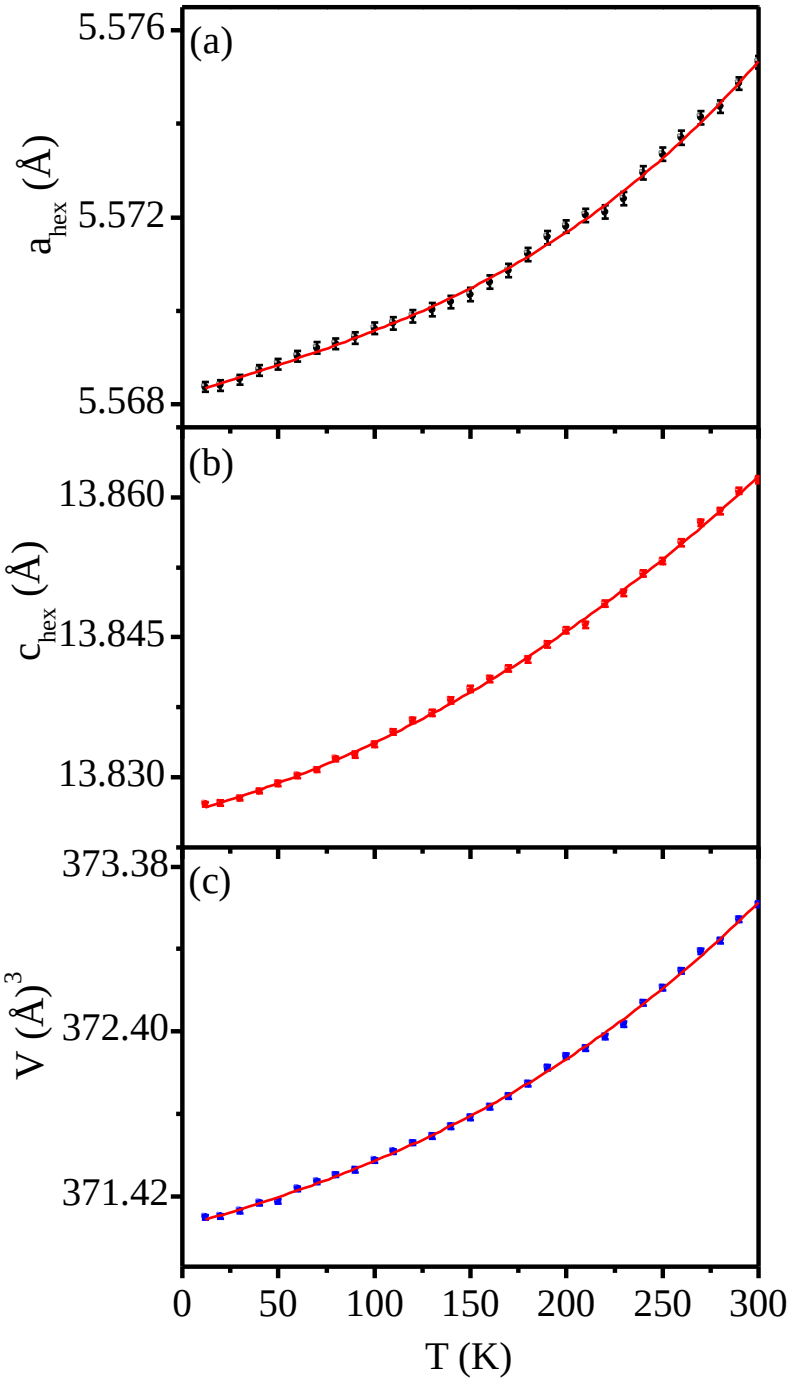

Figure 2.12: Variation of unit cell parameters (a_{hex}, c_{hex} and V_{hex}) with temperature obtained from the LeBail refinement of the x-ray powder diffraction data for pure $BiFeO_3$ sample.

for both the undoped and Mn-doped $BiFeO_3$. It is evident from the figures that no new peaks appear or disappear in the investigated temperature range 13 K-300 K. This implies that the crystal structure remains rhombohedral in the R3c space group and that there is no structural phase transition in the temperature range from 13 K to 300 K. The variation

of lattice parameters (a_{hex} and c_{hex}) and unit cell volume (V_{hex}) of the hexagonal unit cell, as obtained from the LeBail analysis of XRD data, with temperature is shown in Figs. 2.12 (a-c) and 2.13(a-c) for undoped and Mn-doped samples, respectively.

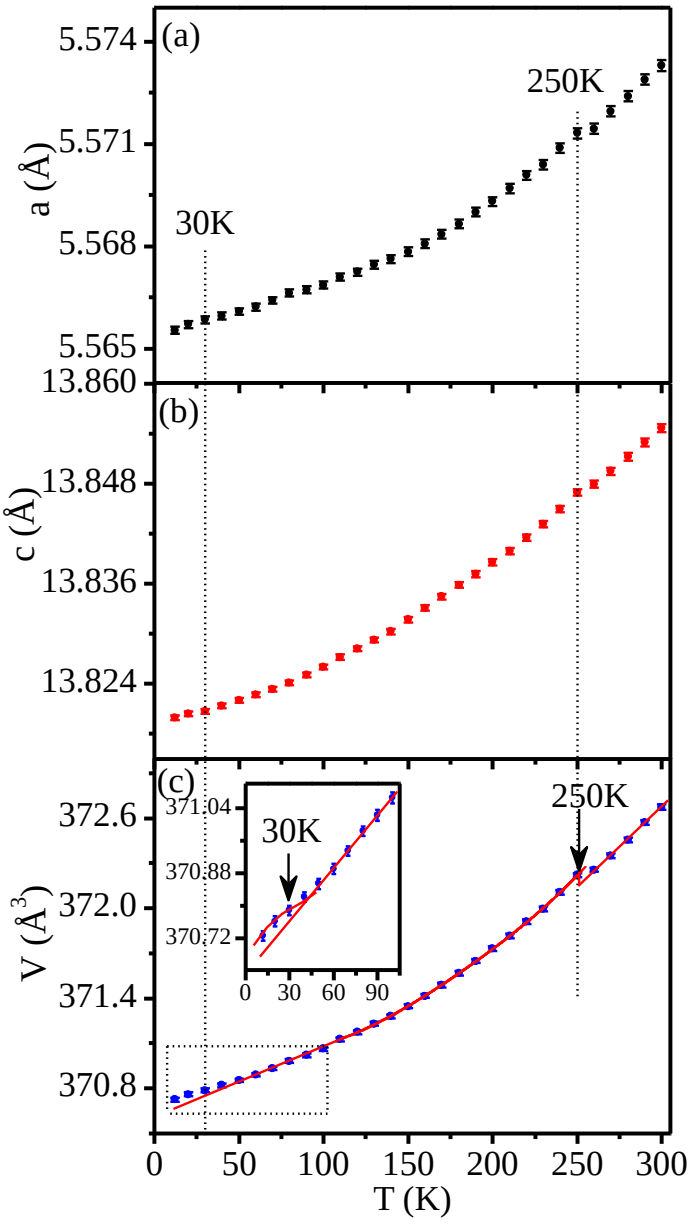

Figure 2.13: Variation of unit cell parameters (a_{hex}, c_{hex} and V_{hex}) with temperature obtained from the LeBail refinement of the x-ray powder diffraction data for Mn doped $BiFeO_3$ sample.

The unit cell parameters gradually decrease with decreasing temperature for both types of samples. However, the temperature variation of cell parameters and unit cell volume of Mn-doped $BiFeO_3$ sample shows a clear change of slope around 30 K and

250K. In case of undoped sample, this change of slope is not clear. Thus Mn-doping helps in revealing these weak anomalies in the unit cell parameters while in the undoped samples these transitions are masked due to higher oxygen in vacancies. The observation of anomaly in the unit cell parameters around the two magnetic transitions suggests magneto-elastic coupling [189,235,236].

2.4.7 Anomalous ac susceptibility response of $BiFeO_3$:

Having established the existence of a spin glass freezing around 25K in both types of samples of $BiFeO_3$, we now turn to some intriguing aspects of ac susceptibility $\chi(\omega, T)$ around this transition. Firstly, the peak height of $\chi'(\omega, T)$ increases with increasing frequencies which is unusual as the susceptibility always decreases with increasing frequency except near frequencies corresponding to a resonant absorption that may be linked with the resistance, capacitance and inductance of the entire circuit rather than just the sample. In principle, it is possible to push the resonance frequencies to higher side by reducing the capacitance and inductance of the circuit by reducing the sample quantity. However, this was not possible in $BiFeO_3$ due to very weak signal for the $\chi'(\omega, T)$. A similar anomalous ac magnetic susceptibility data has been reported even in single crystal samples of $BiFeO_3$ [102]. It is also important to note that the imaginary part $\chi''(\omega, T)$ shows negative cusps at T_f with a peak temperature above the corresponding peak temperature for the real part $\chi'(\omega, T)$. The negative value clearly suggests that the circuit is no longer purely inductive except at very low temperatures (< ~10K). The third intriguing aspect of the $\chi''(\omega, T)$ is the presence of a tiny peak around 10K below which the imaginary part shows positive value. All these features require further study, as some of these anomalous features have also been tentatively attributed to the coexisting modulated magnetic structure of $BiFeO_3$ [102], not observed in the conventional spin glass systems. We shall return to the possible role of spin cycloid in causing this

anomalous frequency dependence of $\chi(\omega, T)$ in the next chapter. What is even more intriguing is the occurrence of a spin-glass phase in a homogeneously ordered system like $BiFeO_3$ without any quenched impurity and randomness as the existing models of spin-glass transitions are based on the concept of disorder, randomness and frustration [24,41–45]. In recent years, several compounds with geometrical frustration have been reported to exhibit spin glass transition in the absence of any apparent disorder [118–124]. But source of frustration in $BiFeO_3$ is not obvious. We believe that the spin glass transition may be caused by competing nearest and next-nearest neighbour interactions. But the existing density functional theory (DFT) give very small value J_2 (0.29 meV) as compared to J_1 (6.48 meV) [237]. The calculations need to be revisited in future.

2.4.8 Ground state of $BiFeO_3$:

$BiFeO_3$ shows non-collinear AFM ordering with Heisenberg spins with an incommensurately modulated cycloidal spin structure superimposed on it. Recent neutron scattering [73–75,100,101] and NMR studies [96–99] suggest that this spin cycloid is stable down to the lowest temperature (~5K). Considering these observations in conjunction with the present results, the most likely scenario for the ground state of $BiFeO_3$ is the coexistence of the spin glass phase and the long range ordered spin cycloid. The coexistence of LRO AFM and spin glass state has been a subject of extensive theoretical and experimental investigations for both Ising and Heisenberg systems [49–53]. In some of the Heisenberg systems, it has been predicted theoretically [51–53] and verified experimentally [172,238–243] that the coexistence is due to the freezing of the transverse component of the spins. An alternative proposal in disordered systems like $PbFe_{0.5}Nb_{0.5}O_3$ (PFN) whereby the two phases result from two different magnetic sublattices, one (LRO) with percolative path ways and the other due to isolated Fe-O-Fe clusters, has also been proposed [171]. In $BiFeO_3$ has no quenched disorder per say,

except for the possibility of Fe^{2+} ions in the magnetic sublattice replacing some of the Fe^{3+} sites due to redox reaction caused by oxygen vacancies and raising the possibility of local ferromagnetic interactions via double exchange. In the absence of disorder in the magnetic sublattice or any frustrated interaction between the spins, the most likely possibility for the emergence of the spin glass phase is due to the freezing of the transverse component of the spins. Local magnetic probe like NMR [96–99] and the global probes like neutron scattering [73–75,100,101] have revealed the possibility of distortions in the long range ordered magnetic modulated structure even though the extent of distortion from harmonic modulation is much less for the average structure, probed by the bulk techniques like neutron scattering, than that reported by local probe like NMR. Whether this anhormonicity is linked with the gradual transverse freezing of the spins or not needs further investigation using neutron scattering studies on single crystals. We shall return to transverse freezing aspect in the next chapter at greater length.

2.5. Conclusions:

$BiFeO_3$ samples were synthesized by conventional solid-state route with and without 0.3wt% MnO_2 doping and characterized for their phase purity and crystal structure, microstructure and composition using synchrotron x-ray diffraction, SEM and EDX techniques. A comparative iodometric titration and XPS study of undoped and Mn-doped $BiFeO_3$ reveals that the oxygen ion vacancy and Fe^{2+} ion concentrations decrease significantly as a result of Mn doping. Based on the results of dc magnetization M(T), AC susceptibility χ (ω, T), dielectric constant ε' (ω, T) and XRD studies in conjunction with iodometric titration and XPS studies on the undoped and doped samples, we conclude that the low temperature transitions of $BiFeO_3$ occurring around 25 K, 150 K and 260 K are intrinsic to $BiFeO_3$ as they are present in both the samples. Our results show that the

magnetic transition around 50 K reported by earlier workers, is absent in Mn-doped $BiFeO_3$ and results in the undoped sample due to oxygen vacancies.

Chapter 3 Spin-glass transitions in BF-xBT solid solutions

3.1. Introduction

Study of phase transitions in disordered magnetic systems has been a time honoured problem in the field of solid state and materials sciences [24,41–44]. In dilute magnetic systems (e.g. Cu-Mn), the ground state is known to be a spin glass (SG) state [24,42]. However, controversies still abound in the case of concentrated systems. Theoretically, it is known that the disordered concentrated magnetic systems can still lock into a long-range ordered (LRO) magnetic ground state if the disorder content (c) is less than a percolation threshold (c_p) for the exchange pathways, except that there is disorder induced broadening of the phase transition leading to the rounding of the susceptibility peak at the transition temperature (T_c) [24,195,244]. However, when the disorder content is close to the percolation threshold, the LRO percolative phase for both the Ising [238–241,245] and Heisenberg [242,243,246] systems has been reported to undergo another transition to the SG state. The pertinent questions that arise in relation to such systems are: (1) What is the true ground state? (2) Does the LRO phase coexist with SG phase in the ground state? (3) If both the phases do coexist, what is the proof that the SG phase has resulted from the same magnetic sublattice that led to the LRO phase? (4) Is the coexistence of SG phase with the LRO phase due to coexistence of isolated short range ordered (SRO) superparamagnetic (SPM) clusters with LRO clusters on two different magnetic sublattices as a result of segregation and clustering?

The theoretical treatments for such concentrated Ising as well as Heisenberg systems predict that the SG state can result from freezing of either the longitudinal or transverse components of the spin in the LRO phase and that it can coexist with the LRO phase on the same magnetic sublattice [49–53]. These theoretical predictions cannot be verified using macroscopic measurements (DC and AC susceptibilities) alone and require

microscopic tools (neutron scattering, Mössbauer spectroscopy etc.) which have been used for a few systems in support of the longitudinal/transverse freezing model in both the Ising and Heisenberg systems [238–243,245,246]. More interestingly, yet another interesting situation has been predicted theoretically for concentrated Heisenberg systems with small single ion anisotropy (D) as compared to the magnetic exchange interaction (J), where both the longitudinal and transverse components can freeze successively leading to two SG transitions below the so-called Almeida-Thouless (A-T) and Gabey-Toulose (G-T) lines, respectively [49–53]. Although most of these theoretical treatments are for concentrated ferromagnetic (FM) systems, these theories have been applied to disordered antiferromagnetic (AFM) systems as well [238]. While evidence for two SG transitions has been obtained in several systems using macroscopic measurements [247–250], the results are rather controversial as it is not clear if the LRO and the SG phases are formed on the same or separate magnetic sublattices. Unambiguous evidence confirming the occurrence of two SG transitions and coexistence of the two SG phases (SG1 and SG2) with the LRO phase on the same magnetic lattice using microscopic tools are rather sparse [e.g. Ref. [248]] in such systems.

Spin-glass phase has been reported in several multiferroic systems also [102,103,171,172,251]. Unlike the conventional SG systems, the multiferroic SG systems offer the possibility of verifying the theoretical predictions for concentrated systems through a study of the change in ferroelectric polarization and strain as a result of magnetoelectric and magnetoelastic couplings across the SG transition using diffraction techniques. A transition from LRO AFM phase to SG phase at low temperatures with coexistence of LRO and SG phases in the ground state has been reported in the multiferroic systems like pure [102,103] and disordered [251] $BiFeO_3$ and some site-disordered compounds like $Pb(Fe_{1/2}Nb_{1/2})O_3$ [171,172]. The origin of coexistence of SG

and LRO AFM phases at low temperatures in such multiferroics is still controversial as experimental evidences for and against both the phase segregation [171] and transverse freezing models [172] have been advanced in the literature. Further, there is no experimental report for LRO to LRO+SG1 to LRO+SG2 transitions in a disordered multiferroic systems. In this context, it is interesting to note that the single ion anisotropy (D) of $BiFeO_3$, a canonical Heisenberg system, is rather small as compared to exchange interaction (J) D/J ~0.00 [237] which falls within the range where two SG phases have been reported in non-multiferroic disordered systems like MgMn [52].

In this chapter, we present first experimental evidence in support of theoretical predictions for two SG phases below the A-T and G-T lines in coexistence with the LRO phase on the same magnetic sublattice in the multiferroic solid solution $(Bi_{1-x}Ba_x)(Fe_{1-x}Ti_x)O_3$ (BF-xBT) system using a combination of macroscopic (DC M(H,T), M(t), AC susceptibility (χ (ω, T)) and specific heat (C_p)) and microscopic (x-ray and neutron scattering) measurements. We have selected $BaTiO_3$ based solid solution of $BiFeO_3$ for this study as it has received considerable attention in recent years due to large ferroelectric polarization [89,90,136], highest depolarization temperature for piezoelectric applications [136,140,144] and destruction of spin cycloid [87,89–91,93,143] leading to large remnant magnetization [87,89–91,93,143] as well linear magnetoelectric coupling [89,90]. From the analysis of neutron and x-ray diffraction data on BF-0.20BT, we demonstrate two distinguishing features of SG transitions in disordered multiferroics: (1) very strong and moderate magnetoelastic couplings associated with the SG1 and SG2 transitions, respectively, as revealed by the change in the unit cell volume (ΔV) with respect to the theoretically predicted values, that scales quadratically with the spontaneous magnetization (M_s^2) and (2) strong magnetoelectric coupling at both the SG transitions as revealed by the large change in spontaneous polarization (ΔP_s), calculated

from the atomic coordinates obtained by Rietveld refinements of the nuclear structure and the Born effective charges (BEC), at the two SG transitions. After presenting the results on BF-0.20BT, we also discuss the effect of dopant ($BaTiO_3$) concentration on the magnetic transitions in BF-xBT and construct a phase diagram showing all the magnetic phases.

3.2. Sample preparation:

Polycrystalline samples of $(Bi_{1-x}Ba_x)(Fe_{1-x}Ti_x)O_3$ (BF-xBT) solid solutions were synthesized by solid state route for x = 0.10 to 0.60 at $\Delta x = 0.10$ interval using high purity oxides of Bi_2O_3, Fe_2O_3, $BaCO_3$, TiO_2, MnO_2 (Aldrich and Alfa Aesar). The starting materials were carefully weighed in stoichiometric ratio and mixed in an agate mortar and pestle for 3 hours and then ball milled for 6 hours in acetone as mixing media using zirconia jar and zirconia ball. After drying, the mixture was calcined at optimized temperatures in the range 1073 K-1173 K depending upon the composition for 8 hours in open alumina crucible. The calcined powders were mixed with 0.3 wt % MnO_2 and ball milled again for 4 hours to break the agglomerates formed during calcination. MnO_2 doping reduces the leakage current as discussed in the literature [136–142,252] and also the previous chapter for $BiFeO_3$. We used 2 % polyvinyl alcohol as a binder to press the calcined powder into pellets of 12 mm diameter and 1 mm thickness at an optimized load of ~70 kN. After the binder burn-off at 773 K for 12 hours, sintering were carried out at optimized temperatures in the range 1173 to 1273 K, in closed alumina crucible with calcined powder of the same composition as spacer powder for preventing the loss of Bi_2O_3 during sintering. The sintering time was increased with increasing $BaTiO_3$ content from 1 hour for x = 0.10 to 4 hours for x = 0.60.

3.3. Characterizations:

The microstructure and chemical composition of the sample was obtained using Scanning Electron Microscope (SEM) (Zeiss, model no. EVO 18) and Energy Dispersive X-ray spectroscopy (EDX) attachment (Oxford, model no. 51-ADD0048). The sintered pellet was coated with conducting gold using sputter coater (Royal life Sciences, model no. DSR1) under vacuum before taking the SEM images. The composition analysis was also checked using Electron Probe Micro Analyzer (EPMA) (CAMECA SXFive instrument). The sintered pellet was coated with 20 nm thin layer of carbon using LEICA-EM ACE200 sputtering system. Natural silicate mineral andardite was used as internal standard to verify positions of crystals (SP1-PET, SP2-LiF and SP4-LPC0) with respect to corresponding wavelenght dispersive spectrometers in CAMECA SX-Five instrument. The following X-ray lines were used in the analyses: O-Kα, Ti-Kα, Mn-Kα, Fe-Kα, Ba-Lα & Bi-Mα. Natural mineral standards: hematite and pure metal standards (Mn & Bi) supplied by CAMECA-AMETEK were used for calibration and quantification. Routine calibration, acquisition, quantification and data processing were carried out using SxSAB version 6.1 and SX-Results softwares of CAMECA.

X-ray powder diffraction (XRD) measurements in the temperature range 12 K to 350 K were carried out using an 18-kW Cu rotating anode powder diffractometer (Rigaku, model no. RINT 2500/PC series) operating in the Bragg-Brentano geometry and fitted with a curved crystal monochromator in the diffraction beam. Sample environment was varied using a close cycle helium refrigerator based low temperature attachment on this diffractometer. The data in the 2θ range 20 to 120° were collected using annealed powders (10 hours at 773 K) obtained after crushing the sintered pellets at a step of 0.02 degrees.

High resolution synchrotron x-ray powder diffraction (SXRD) data were also collected at P02.1 beamline of PETRA III, Hamburg, Germany, at a wavelength of 0.2079Å (~60keV) for a few selected temperatures. The sample was filled in a quartz capillary of 0.8mm diameter. The temperature of the sample was adjusted by blowing a cold stream of N_2 gas produced by the Oxford CryoStream 700 cryocooler. At each temperature, the sample was exposed for 10 s by an incident beam with a cross section of 0.5 mm × 0.5 mm. Two-dimensional (2D) XRD pattern was recorded using a Perkin Elmer 1621 Detector (2048 pixels × 2048 pixels, 200μm × 200μm pixel size). The sample to detector distance was set to 1310 mm. The standard LaB_6 was used to calibrate the sample to detector distance. The 2D XRD pattern was integrated using the FIT2D software.

Temperature dependent neutron powder diffraction (NPD) data in the range 300 K to 2.8 K was collected at Druva reactor, BARC, Mumbai at a wavelength of 1.48 Å using high-resolution powder diffractometer PD-3. A close cycle helium refrigerator (CCR) (Cryogenic, A S Scientific UK) with variable temperature insert (VTI) was used for sample temperature variation. The powder sample was filled in a vanadium can of 6mm diameter and attached to the sample rod of the VTI. The nuclear and magnetic structures were refined by Rietveld techniques using FULLPROF suite [253].

DC magnetization (M(T, H)) measurements were carried out on a superconducting quantum interference device (SQUID) based magnetometer (Quantum Design, MPMS-3) in the temperature range 2 K to 900 K at 500 Oe applied dc field in two separate measurements from 2 to 400K and 300K to 900K range. The ac susceptibility (χ (ω, T)) measurements were carried out in the temperature range 2 K to 300 K on the same machine using an ac drive field of 2 Oe.

3.4. Results and discussion:

3.4.1 Microstructure and compositional analysis:

Fig. 3.1(a) depicts the scanning electron micrograph of BF-0.20BT solid solution. The average grain size of the ceramic sample obtained by linear intercept method is found to be ~2.5μm. The EDX spectra shown in the right panel reveal the presence of bismuth (Bi), iron (Fe), barium (Ba), titanium (Ti), manganese (Mn) and oxygen (O) atoms in our sample. The results of the quantitative analysis of the chemical composition of the atoms averaged over 10 different regions are given in Table 3.1. We have also confirmed the average composition of the ceramics through EPMA analysis, which gives the average composition more accurately. Results of average composition of Bi, Fe, Ba, Ti, Mn and O obtained by EPMA are given in Table 3.1. It is evident from the table that the values obtained by EDX and EPMA analysis are close to the expected (nominal) composition within the standard deviation except for the oxygen atom. Since, the accuracy of determining oxygen content is rather low due to its low atomic number, the average weight % of oxygen atoms can not be determined accurately from the EDX and EPMA.

Table 3.1: Quantification of BF-0.20BT by EDX and EPMA analysis

Average Chemical Composition in Weight %			
		EDX Analysis	EPMA Analysis
Element	Expected	Average	Average
Bi	56.3	56.5 ± 1.8	56.2 ± 0.5
Fe	15.1	15.2 ± 2.3	15.0 ± 0.2
Ba	9.2	9.4 ± 1.4	8.9 ± 0.2
Ti	3.2	3.7 ± 0.9	3.1 ± 0.05
Mn	0.3	0.3 ± 0.1	0.22 ± 0.04
O	16.2	15.0 ± 2.2	15.2± 0.5

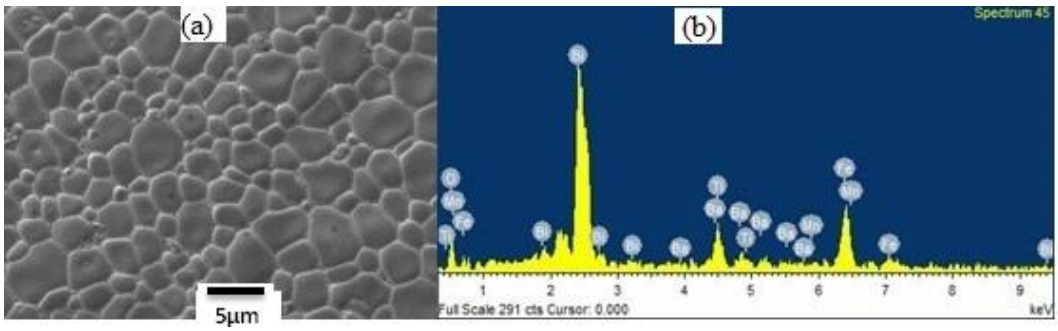

Figure 3.1: Left panel depicts the scanning electron micrograph of BF-0.20BT sample. Right panel show the EDX spectrum.

3.4.2 Room temperature crystal structure of BF-xBT:

Fig. 3.2 depicts the synchrotron x-ray diffraction (SXRD) patterns of sintered and well annealed powders of BF-xBT samples at room temperature over a limited 2θ range of 2.5-8.7 degrees for the composition (x) range $0.10 \leq x \leq 0.60$. It is evident from the figure that all the compositions exhibit pure perovskite peaks and no trace of any impurity phase is observed. This confirms that all the samples of BF-xBT correspond to a single phase. In order to study the room temperature crystal structure of BF-xBT samples as a function of composition qualitatively, we first plot the evolution of profiles of selected reflections 400_{pc}, 440_{pc} and 444_{pc}, (here all indices are with respect to a pseudocubic (pc) doubled perovskite cell) in the range $0.10 \leq x \leq 0.60$ in Fig. 3.3. It is evident from this figure that for the composition range $x \leq 0.30$, the 400_{pc} is a singlet, while 440_{pc} and 444_{pc} are doublets, which is expected for the stable rhombohedral structure of $BiFeO_3$ with R3c space group. It is also evident from the figure that the peak splitting of 440_{pc} and 444_{pc} pseudocubic reflections decreases with increasing x. This suggests that the rhombohedral distortion of $BiFeO_3$ gradually decreases with $BaTiO_3$ substitution. For the composition range $0.40 \leq x \leq 60$, all the peaks in Fig. 3.3 appear to be singlet which is a characteristic of a cubic-like phase with $Pm\bar{3}m$ space group. It is, however, known that these cubic-like compositions are not truly cubic as they possess local monoclinic distortion [91,135,145].

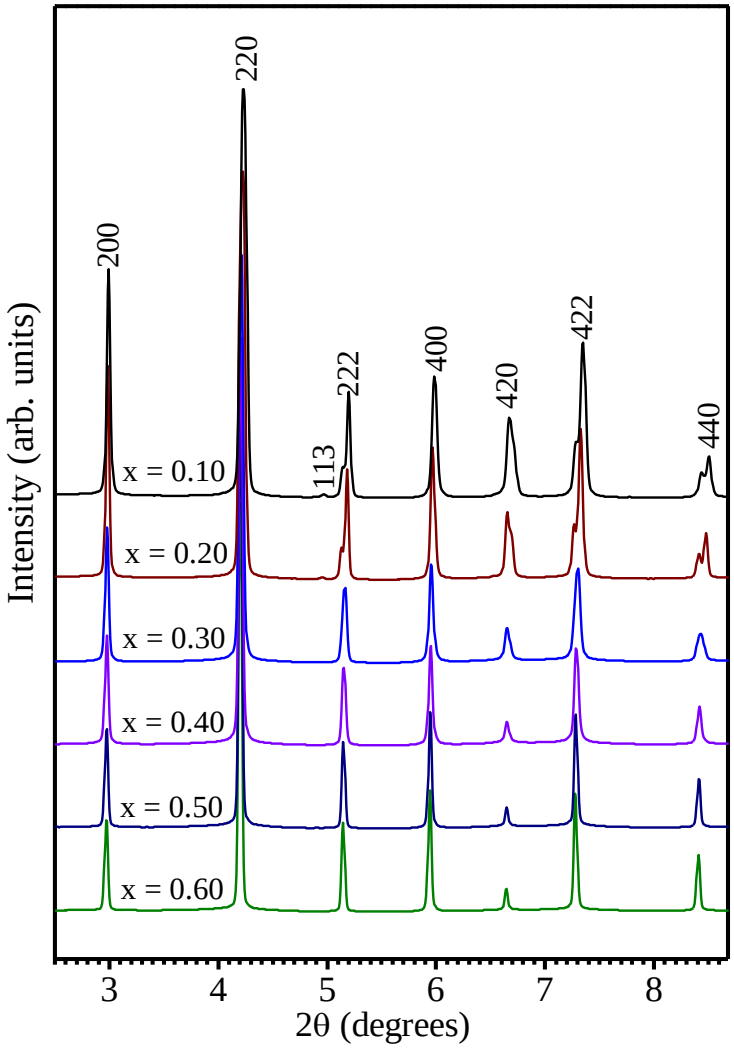

Figure 3.2: Synchrotron x-ray diffractogram of sintered and annealed powder of BF-xBT solid solutions for $0.10 \leq x \leq 0.60$. All indices are with respect to a pseudocubic (pc) doubled perovskite cell. The 113 reflection is a superlattice peak due to the anti-phase tilting of the oxygen octahedra about the trigonal $[111]_{pc}$ axis that doubles the unit cell size.

Thus, there are two different crystal structure regions corresponding to change of evolution of selected reflections 400_{pc}, 440_{pc} and 444_{pc} of SXRD profiles.

In order to confirm the above qualitative observations, we have carried out Rietveld analysis of SXRD data using the FULLPROF package [253]. For the refinement of rhombohedral phase with R3c space group, we have used the atomic positions in

hexagonal cell given by Megaw and Darlington [254]. The coordinates of atoms in the asymmetric unit can be expressed as a function of displacement parameters s, t, d and e

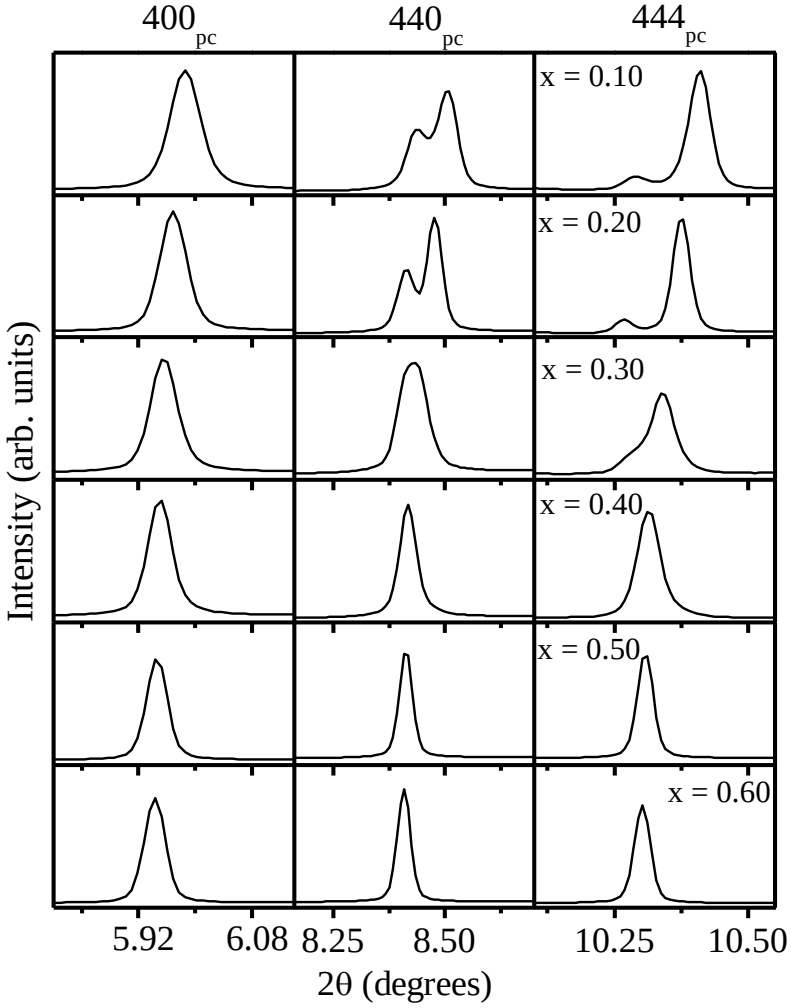

Figure 3.3: Composition evolution of selected profiles of 400_{pc},440_{pc} and 444_{pc} reflection for BF-xBT in the composition range $0.10 \leq x \leq 0.60$.

as: Bi^{3+}/Ba^{2+} (0,0,1/4+s), Fe^{3+}/Ti^{4+} (0,0,t), O^{2-} (1/6-2e-2d,1/3 -4d,1/12). The parameters 's' and 't' describe the polar displacement of cations Bi^{3+}/Ba^{2+} and Fe^{3+}/Ti^{4+} along $[111]_{pc}$ direction. The parameter 'e' gives the displacement of oxygen O^{2-} from its ideal position and is related to tilt angle by the expression $\omega = \tan^{-1}(4e\sqrt{3})$ [254] whereas parameter 'd'

is related to the distortion of octahedra BO_6 (B: Fe^{3+}/Ti^{4+}) parallel to the $[111]_{pc}$ axis. The z coordinate of the oxygen atom was fixed and the remaining atomic positions were refined. The asymmetric unit of the cubic phase with $Pm\bar{3}m$ space group consists of three atoms: one A-site atom (Bi^{3+}/Ba^{2+}) at (0, 0, 0), B-site atom at (0.5, 0.5, 0.5) and one oxygen atom O at (0.5, 0.5, 0.0), respectively. All the atomic coordinates correspond to special positions in the cubic phase. Fig. 3.4 shows the observed (filled circles), calculated (continuous line) and difference (bottom line) profiles obtained after the Rietveld analysis of the SXRD patterns for selected compositions x = 0.20, 0.40, and 0.60 using space groups R3c, $Pm\bar{3}m$ and $Pm\bar{3}m$, respectively. Excellent fit between the observed and calculated profiles confirms the average crystal structures. In order to compare the unit cell parameters of rhombohedral and cubic phases as a composition, we have first calculated equivalent elementary perovskite cell parameters from the refined hexagonal 'c' and 'a' parameters of the rhombohedral phase for $x \leq 0.30$ using the following relationships: $a=a_H/\sqrt{2}$ and $c=c_H/2\sqrt{3}$. The variation of the elementary perovskite cell parameters for the composition range $0.10 \leq x \leq 0.60$, obtained from the Rietveld refinements, is shown in Fig. 3.5. It is evident from the figure that the structural phase boundary occurs around the composition $x_c = 0.40$ from rhombohedral (R3c space group) to cubic phase ($Pm\bar{3}m$ space group). The unit cell volume (see Fig. 3.5 (b)) shows a change of slope across the structural phase boundary. The observed structural phase boundary is in agreement with the previous reports [90,91]. The refined structural parameters for all compositions of BF-xBT are given in Table 3.2.

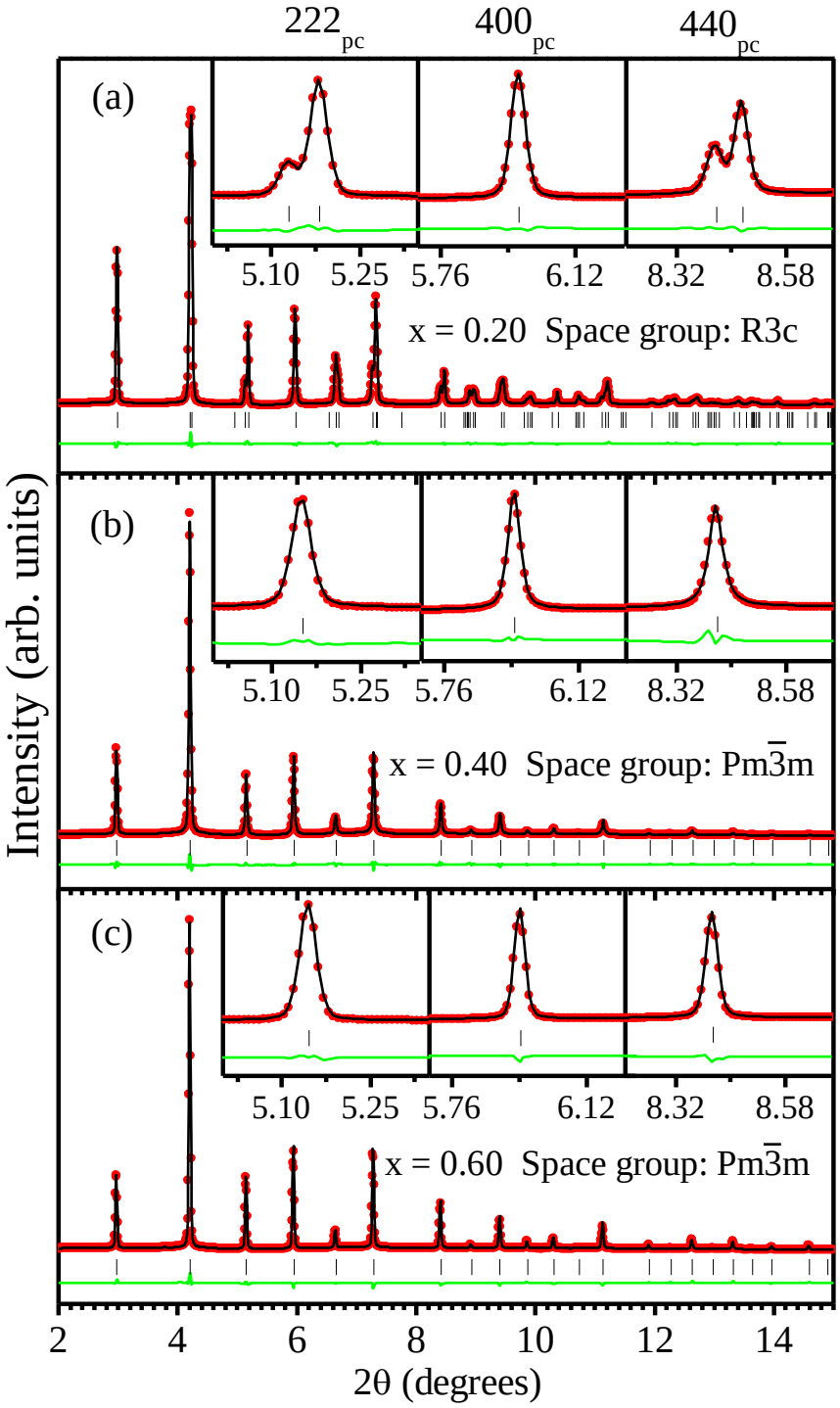

Figure 3.4: Rietveld refinement using synchrotron x-ray diffractogram of (1-x)$BiFeO_3$-x$BaTiO_3$ powders for representative compositions x = 0.20, 0.40, 0.60 using **(a)** Rhombohedral R3c space group **(b)** Cubic $Pm\bar{3}m$ space group and **(c)** Cubic $Pm\bar{3}m$ space group. Inset depicts the fits for the pseudocubic reflections 222_{pc}, 400_{pc} and 440_{pc}.

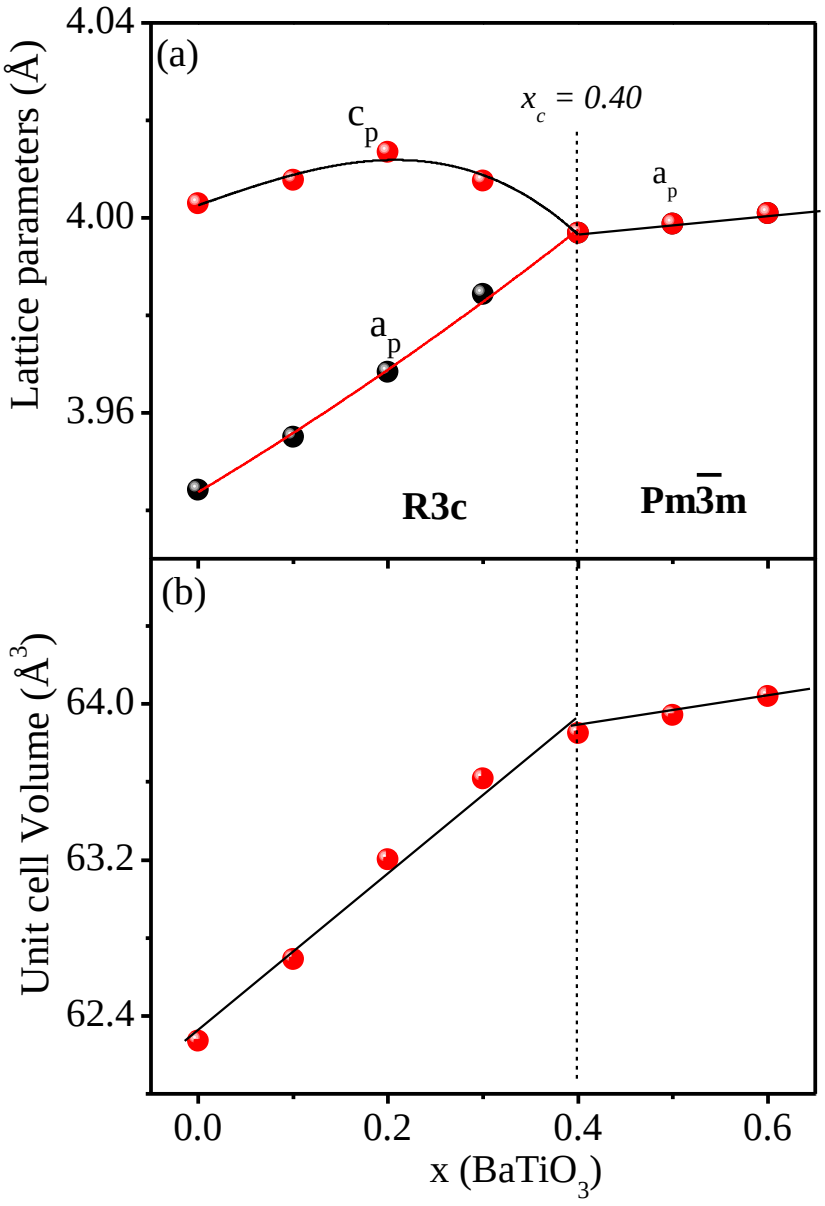

Figure 3.5: Variation of elementary perovskite (a) cell parameters (b) unit cell volume of BF-xBT as a function of composition (x) at room temperature. The structural parameters for x = 0.0 i.e. $BiFeO_3$ was taken from the previous chapter's analysis.

Table 3.2: Refined structural parameters for various compositions of BF-xBT (for $0.10 \leq x \leq 0.60$)

x	0.10	0.20	0.30	0.40	0.50	0.60
Space group	R3c $a = b \neq c$, $\alpha = \beta = 90^0$, $\gamma = 120^0$			$Pm\bar{3}m$ $a = b = c$, $\alpha = \beta = \gamma = 90^0$		
a(Å)	5.5932 (8)	5.6125 (3)	5.6346 (5)	3.9968(5)	3.9987 (1)	4.0008 (9)
c(Å)	13.8691 (5)	13.9016 (6)	13.8828 (4)	-	-	-
Bi (z)	0.2952 (6)	0.2889 (6)	0.2668 (9)	0	0	0.5
Fe/Ti (z)	0.0189 (6)	0.0146(6)	0.0996 8)	0.5	0.5	0.5
O (x)	0.2285 (2)	0.2030 (8)	0.1873 (1)	0.5	0.5	0.5
O(y)	0.3506 (2)	0.3405 (3)	0.336 (2)	0.5	0.5	0.5
B(Bi/Ba)	1.03 (2)	β_{11}= 0.0242(3) β_{33}=0.0035(1) B_{eq}=3.44	β_{11}= 0.041(7) β_{33}=0.007(2) B_{eq}=5.9	4.99(1)	4.51(4)	4.47 (4)
B (Fe/Ti)	0.43 (6)	1.19 (9)	1.1 (1)	1.54 (6)	1.26 (5)	0.85 (4)
B(O)	1.15 (2)	3.8 (3)	5.1 (5)	4.26 (1)	2.6 (2)	1.7 (1)
$R_{wp\,(\%)}$	8.14	9.26	10.8	9.92	9.73	9.41
$R_{p\,(\%)}$	7.68	8.97	9.91	8.65	7.62	8.69

3.4.3 Magnetic transitions in BF-0.20BT:

3.4.3.1 The Néel transition:

The antiferromagnetic (AFM) Néel transition in pure $BiFeO_3$ (BF) occurs at T_N ~650K. As a result of 20% substitution of $BaTiO_3$ in BF, i.e. in BF-0.20BT, T_N decreases due to dilution of the magnetic sublattice. Fig. 3.6 depicts the variation of DC magnetization (M(T)) with temperature on a zero-field cooled (ZFC) sample of BF-0.20BT recorded during sample worming under an applied field of 500 Oe in the temperature range 300 to 900K. It is evident from the figure that a long-range ordered (LRO) magnetic phase emerges below T_N ~608K in agreement with the previous reports [91]. The nature of ZFC M(T) response of BF-0.20BT is, however, not like a typical AFM transition seen in pure BF but is rather like a ferromagnetic (FM) transition.

The FM type transition is due to the destruction of the spin cycloid, superimposed on the canted G-type AFM arrangement of spins in BF, that releases the latent FM component of the spins in the magnetic sublattice. This was confirmed through M-H hysteresis loop measurements, Curie-Weiss plot and neutron diffraction patterns.

The M-H hysteresis loop of BF-0.20BT is shown in Fig. 3.7. It reveals weakly ferromagnetic behaviour (see Fig. 3.7) in contrast to linear M-H characteristic of AFM phase in pure BF. However, even in pure BF, the M-H loop opens up with a remanant magnetization $M_r \sim 0.3$ emu/g at 10 K on destruction of the spin cycloid in the presence of external magnetic field in excess of ~20T [84]. The opening of the hysteresis loop in BF-0.20BT even at moderate fields thus indicates the destruction of the spin cycloid of $BiFeO_3$ as noted by previous workers also in various solid solutions of BF [91–93,143]. The remanant magnetization $M_r \approx 0.13$ emu/g of our samples is close to the value of ~0.15 emu/g reported by Singh et al. [91]. The fact that the magnetization does not saturate even at 7T field clearly suggests weakly FM behaviour due to canted AFM structure.

The ZFC M (T) of BF-0.20BT shows Curie-Weiss behaviour $\chi = C/(T-\theta_W)$ above T_N~608K, where C and θ_W are Curie constant and Curie-Weiss temperature, respectively. Fig. 3.6(b) shows the temperature dependence of the inverse DC susceptibility (χ^{-1}) whose linear behaviour at high temperatures (T > 700 K) clearly confirms to Curie-Weiss law with θ_W = -873.6 K. The large negative value of θ_W indicates strong antiferromagnetic interactions and a LRO AFM state below T_N~608K. The effective magnetic moment (μ_{eff}) of Fe^{3+} ion, calculated from the Curie constant C, comes out to be 4.98 μ_B which is nearly 80% of the magnetic moment of Fe^{3+} ions in the high spin configuration (S = 5/2), as expected for BF-0.20BT due to 20% Ti substitution at the Fe site. AFM structure of BF-0.20BT was further confirmed by neutron powder diffraction (NPD) studies.

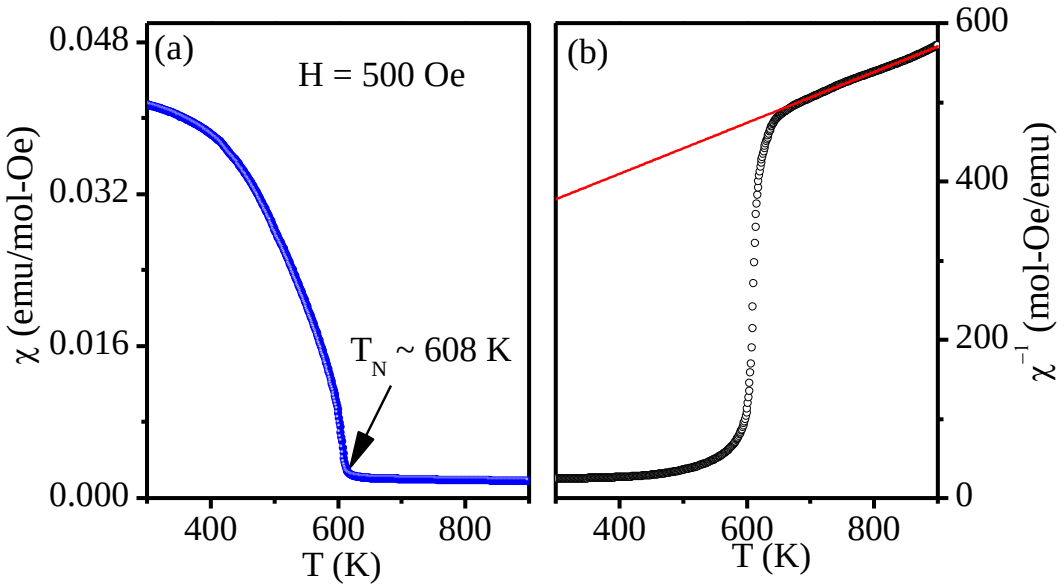

Figure 3.6: **(a)** ZFC DC magnetization versus temperature plot of BF-0.20BT for an applied field of 500 Oe **(b)** depicts the Curie-Weiss plot for BF-0.20BT above T_N**.**

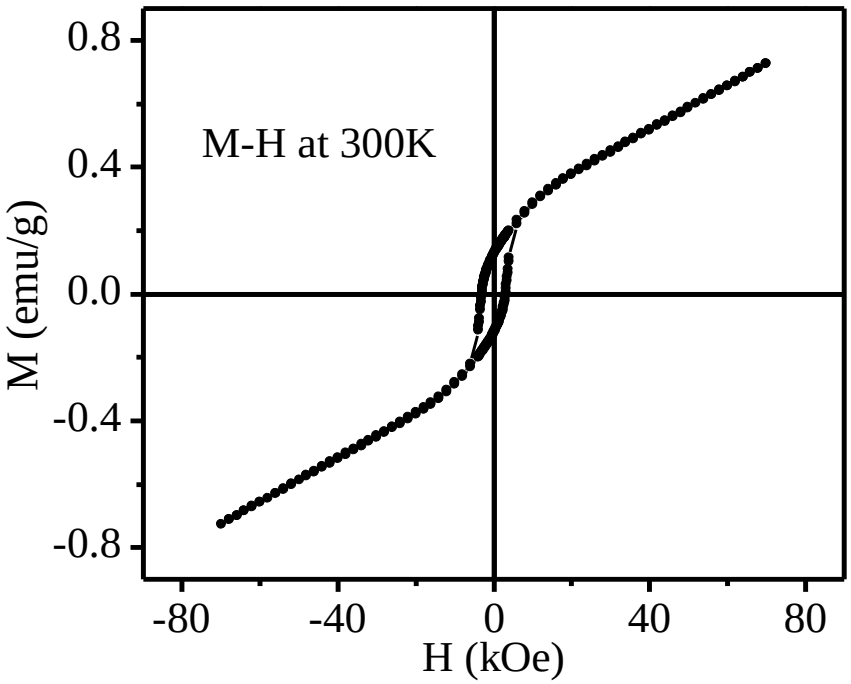

Figure 3.7: The M-H hysteresis loop at 300K for BF-0.20BT.

Fig. 3.8 shows the NPD pattern of BF-0.20BT at room temperature in the limited 2θ range of 15º -57º. This pattern contains main perovskite reflections as well as some superlattice reflections which arise either due to antiferromagnetic ordering or tilting of

oxygen octahedra. All the reflections could be indexed with respect to a doubled perovskite unit cell. The 111_{pc} (pc stands for pseudocubic unit cell) magnetic superlattice peak at $2\theta = 18.6^{o}$ (marked with an arrow) is not allowed in the rhombohedral R3c space group and arises due to AFM ordering of the Fe spins. Thus, the transition at T_N ~608K in Fig. 3.6 (a) is linked with the appearance of a LRO AFM phase.

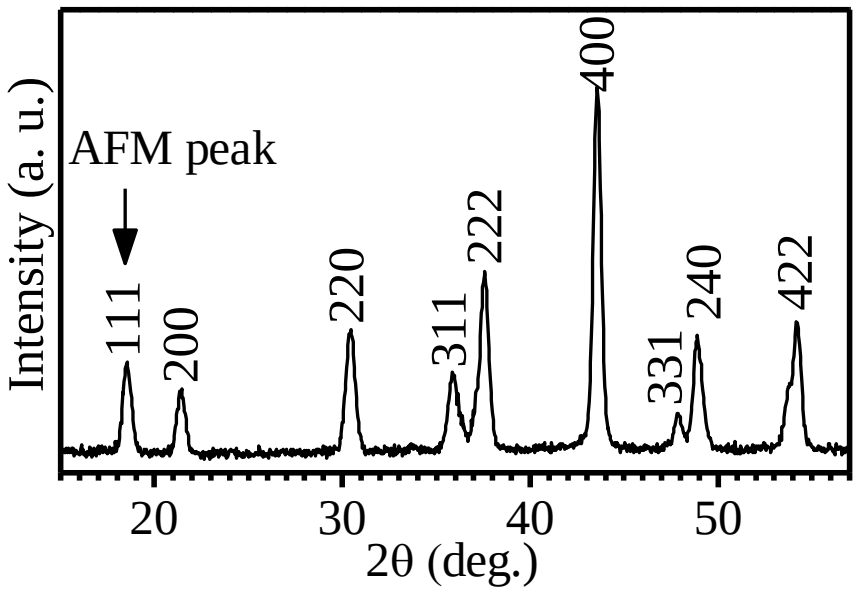

Figure 3.8: Neutron powder diffraction pattern of BF-0.20BT at room temperature. Arrow marks the antiferromagnetic peak. All the indices are written with respect to a doubled pseudocubic cell.

3.4.3.2 The low temperature magnetic transitions:

Below room temperature, the ZFC M(T) of BF-0.20BT clearly reveals three anomalies near 240K, 135K and 30K as can be seen from Fig. 3.9. In addition, the ZFC and FC M(T) curves show bifurcation due to history dependent effects. Such a bifurcation has been reported in spin glass and superparamagnetic (SPM) systems [24,41–43]. In canonical spin glasses, ZFC M(T) shows a cusp at T_{max} and the bifurcation of FC and ZFC M(T) occurs close to the cusp temperature [41]. However, unlike the canonical systems, the peak around ~240 K in M(T) of BF-0.20BT is quite smeared out and the

bifurcation starts well above T_{max}. While smeared peaks have been reported in several cluster glass and SPM systems due to occurrence of freezing/blocking over a wide range of temperatures as a result of large distribution of cluster sizes [255–257], the peak around 240K is much more broad and the bifurcation of ZFC and FC M (T) curves occurs well above the peak temperature (T_{max}). The extent of broadening of the 240K peak in the ZFC M(T) measurements is dependent on the field strength as discussed in a later section. As shown in next section, the AC susceptibility peak is rather relatively sharper (see inset of Fig. 3.10(b)) than the peak in the ZFC M(T) for the 240K transition. Obviously, the time scales associated with different measuring probes give different widths for the 240K transition as expected for a glassy phase in a concentrated system with larger distribution of cluster sizes. What is significant is that the two different measurement probes, i.e. M(T) and AC susceptibility, clearly confirm that a transition is indeed taking place around 240K.

Below the 240K transition, the ZFC M(T) plot shows a kink around 135 K followed by a nearly temperature independent plateau upto ~30K. On further cooling below 30K, ZFC M(T) starts decreasing. The FC M(T) also shows a kink around 135K but below this temperature it keeps on increasing without any anomalous decrease around 30K. In polycrystalline $BiFeO_3$ sample [103] and single crystals of $BiFeO_3$ [102], two transitions around 260K and 30K, respectively, have been observed as discussed in previous chapter. Further, the transition around 140K has been investigated in great detail in $BiFeO_3$ and has been linked with electromagnons [111,114,116]. The electromagnons are collective spin and lattice excitations that can be excited by electric field. The electromagnons have been reported using terahertz [258] and Raman [111,114,116] spectroscopy as well as inelastic neutron scattering studies [237]. The first experimental evidence of electromagnons was demonstrated in $RMnO_3$ (R = Tb, Gd) using terahertz

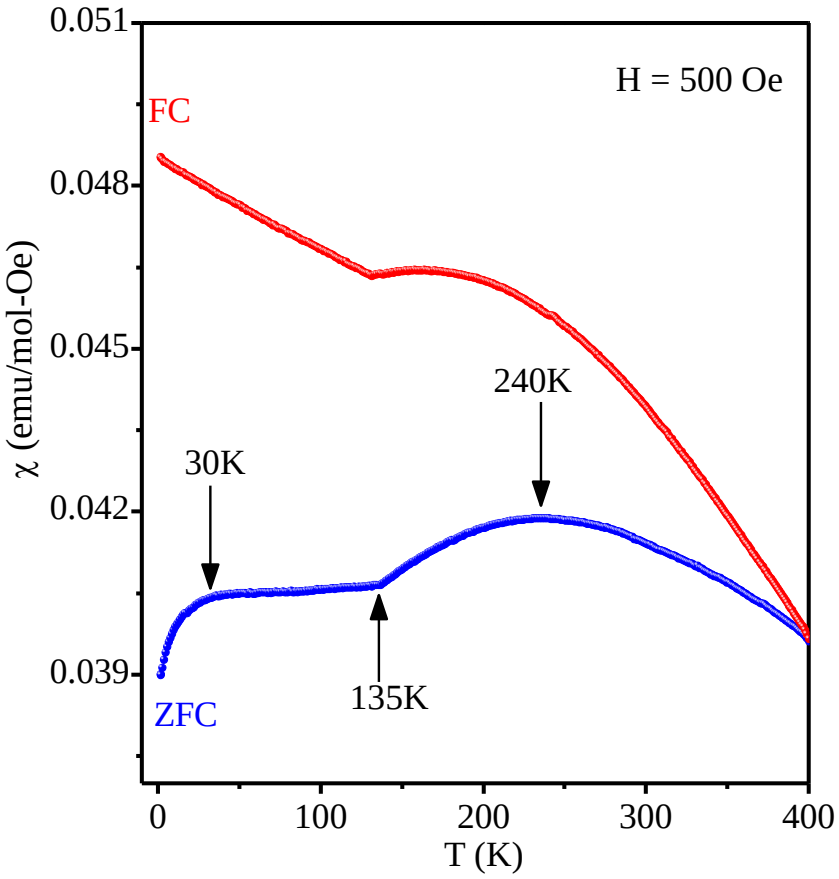

Figure 3.9: Temperature dependence of DC magnetization of BF-0.20BT under ZFC and FC conditions for an applied field of 500 Oe.

spectroscopy [258] whereas in $BiFeO_3$, the electromagnons were first reported using Raman spectroscopy [111,114,116] where the intensity and frequency of magnon modes appearing around 140K was shown to change on application of external electric field. The theoretical work of de Sousa and Moore [259] and Fishman et al. [260] have confirmed the existence of electromagnons in Raman scattering studies on $BiFeO_3$. In case of BF-0.20BT, the M(T) measurement reveals strong signature of 135K transition and shows an anomaly in the integrated intensity of the AFM peak in the neutron diffraction pattern (discussed later in section). We believe that this transition is also linked with electromagnons although, Raman scattering, THz spectroscopy and inelastic neutron

scattering studies are required to confirm this. As this is beyond the scope of the present work, we keep our focus on the other two transitions occurring around 240K and 30K in what follows hereafter.

3.4.4 Evidence for two spin-glass transitions in AC susceptibility of BF-0.20BT:

We carried out frequency dependent AC magnetic susceptibility ($\chi(\omega, T)$) measurements to understand whether the bifurcation of the ZFC and FC M(T) is associated with spin-glass freezing or SPM blocking. Figs. 3.10 (a) and (b) depict real ($\chi'(\omega, T)$) and imaginary ($\chi''(\omega, T)$) parts, respectively, of $\chi(\omega, T)$ of BF-0.20BT measured at various frequencies for a drive field of 2 Oe in the temperature range 2-300K. The $\chi'(\omega, T)$ shows two peaks at T_{f1} and T_{f2} corresponding to the two anomalies around ~240 and ~30K revealed in ZFC M(T) plot as can be seen from the insets (i) and (ii) of Fig. 3.10(a). It is noteworthy that the temperature dependence of $\chi''(\omega, T)$ for the 240K anomaly exhibits normal freezing behavior whereas it shows anomalous behavior with negative cusp for the 30K anomaly. The negative cusp is in agreement with that reported in single crystals of $BiFeO_3$ as well as in polycrystalline samples of $BiFeO_3$ [102]. The anomalous frequency dependence of the lowest temperature SG phase (SG2) has been discussed in detail in the context of pure $BiFeO_3$ where the role of cycloidal magnetic structure has been highlighted [102]. However, the spin cycloid of $BiFeO_3$ is known to be destroyed in the presence of disorder, such as 20% $BaTiO_3$ substitution in the present case. This has been confirmed by neutron scattering and magnetization measurements [90,91]. Suffice is to say that the opening of the M-H loop in our samples (see Fig. 3.7) rules out the presence of spin cycloid and therefore there is no correlation between the anomalous frequency dispersion [see Ref. [102] for more details] of the 30K anomaly and the spin cycloid. We believe that this anomalous behaviour is linked with

the LCR circuit resonance frequency as pointed out in Ref. [102] and discussed in the previous chapter.

The peak corresponding to the 240K transition is relatively less broad in χ' (ω, T) and χ'' (ω, T) as compared to that in the ZFC M(T) (see Fig. 3.9) indicating the role of time scales associated with the spin freezing/blocking process and the measurement time for different probes. The temperatures T_{f1} and T_{f2} corresponding to the two peaks in χ' (ω, T) shift towards higher side on increasing the measuring frequency. Such a frequency dependent shift may be due to either SG freezing or SPM blocking [24,41–43]. The shift of the χ' (ω, T) peak temperature has been analyzed in terms of an empirical frequency sensitivity parameter $K = \Delta T_f / (T_f \Delta(\ln \omega)$, the so-called Mydosh parameter [42], which lies in the range 0.003-0.08 [42] and 0.1 to 0.3 [42] for spin-glass freezing and SPM blocking, respectively. In the case of BF-0.20BT, K is found to be ~0.04 for both the transitions which supports the spin-glass freezing rather than SPM blocking.

For SPM blocking, the relaxation time (τ) should follow the typical Arrhenius type dependence without any critical slowing down behaviour [198]:

$$\tau = \tau_0 \exp(E_a / k_B T), \qquad \ldots\ldots (3.1)$$

where τ is the relaxation time, E_a the activation energy, k_B the Boltzmann constant, and τ_0 the inverse of the attempt frequency. The ln (τ) vs 1/T plots derived from the frequency dependent peak positions $T_f(\omega)$ of χ' (ω, T) for the transitions around 240 K and 30 K are therefore expected to be linear for SPM blocking. The fact that this plot is non-linear in BF-0.20BT, as can be seen from Figs. 3.11(a) and (b)), rules out the SPM blocking being responsible for the two peaks in χ' (ω, T). For spin glass freezing, one observes critical slowing down of the relaxation time (τ) due to ergodicity breaking. This has been modelled using a power law [261]:

$$\tau = \tau_0 [(T_f - T_{SG})/T_{SG}]^{-z\nu}, \qquad \ldots\ldots\ldots (3.2)$$

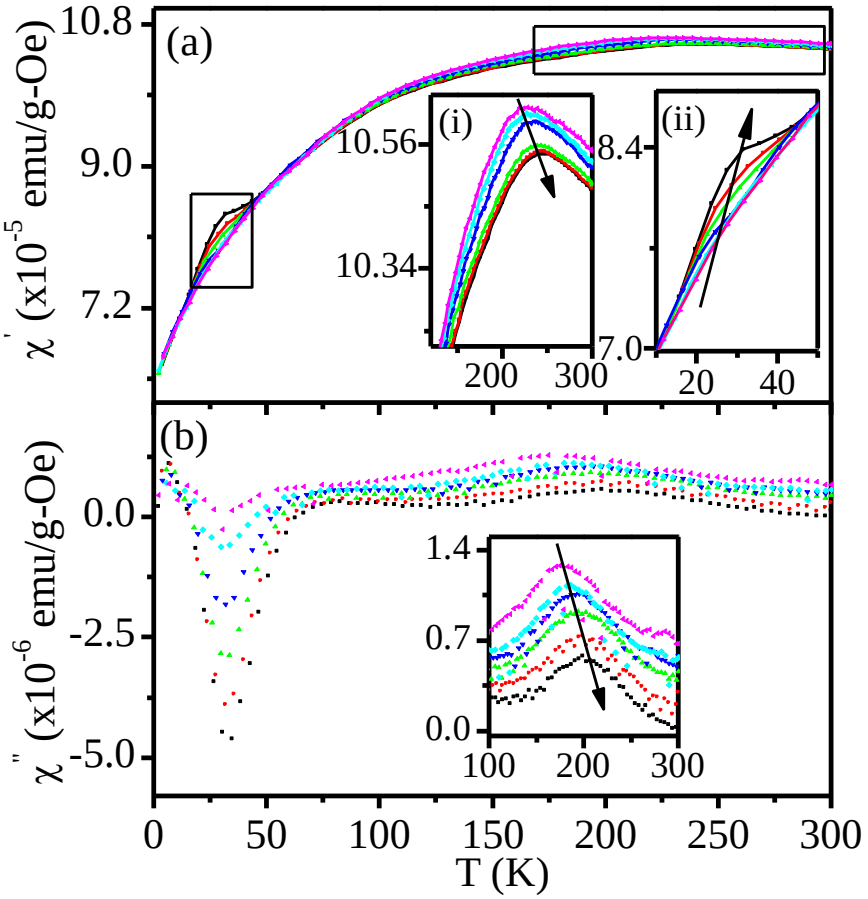

Figure 3.10: Variation of χ' (ω, T) and χ'' (ω, T) in the temperature range 2-300K at various frequencies [47.3 Hz (►), 97.3 Hz (◄), 197.3 Hz (▼), 297.3 Hz (▲), 397.3 Hz (●), 497.3 Hz (■)]. Insets (i) and (ii) depict χ' (ω, T) on a zoomed scale for SG 1 and SG 2, respectively.

where, T_{SG} is the SG transition temperature, ν the critical exponent for the correlation length (ξ) and z the dynamical exponent relating τ to ξ. In some spin glass systems [224], the frequency dependent shift of the χ' (ω, T) peak temperature has been modelled using the empirical Vogel–Fulcher (V-F) law also [224]:

$$\tau = \tau_0 \exp(E_a / k_B (T_f - T_{SG}), \qquad \ldots\ldots(3.3)$$

where E_a is the activation energy. Both the power law and V-F law type critical dynamics provide excellent fits for the two transitions, as can be seen from Figs. 3.11 and 3.12, respectively. The continuous line in Figs. 3.11(a) and (b) are the fits for the V-F law. Both the fits are excellent. The least squires fitting parameters for the two transitions are:

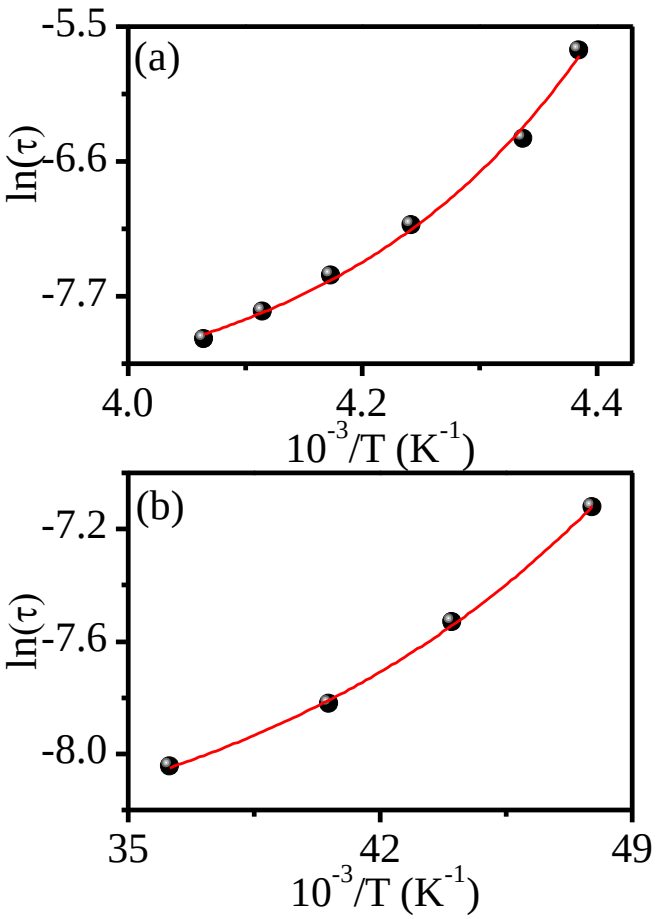

Figure 3.11: ln(τ) versus 1/T plot for (a) SG1 and (b) SG 2 transitions. Solid line is the least squares fit for Vogel-Fulcher law.

T_{SG1}~ (218.6±0.8) K, $z\nu_1$ = 2.09 s, τ_{01} = 3.87x10^{-6} s and T_{SG2} = (18.6±0.4) K, $z\nu_2$ = 0.69, and τ_{02} = 1.92x10^{-4}s for power law and T_{SG1} ~(214±2) K, E_{a1} = 4.89 meV, and τ_{01} = 5.64x10^{-6}s and T_{SG2} ~(15.9±0.1) K, E_{a2} = 0.65 meV, and τ_{02} =1.64x10^{-4} s for V-F law. The values of T_{SG1} and T_{SG2} as well as τ_{01} and τ_{02} obtained by V-F law and power law type critical dynamics are comparable. Thus, both the power law and V-F dynamics confirm the glassy nature of the two frequency dependent anomalies in $\chi'(\omega, T)$. The magnitude of τ_{01} and τ_{02} for both the power law and V-F law type dynamics falls in the typical cluster glass (CG) category (10^{-5}-10^{-10}s) for concentrated systems [24] [42] and not the

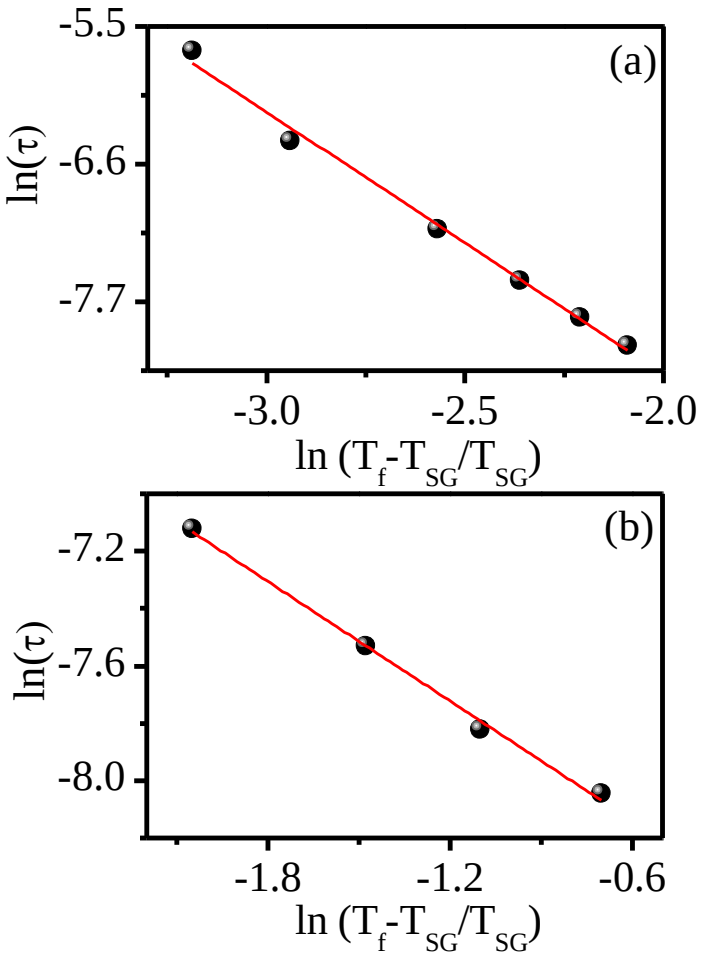

Figure 3.12: ln(τ) versus ln(T-T_{SG}/T_{SG}) plot for (a) SG1 and (b) SG2 transitions. Solid line shows the least squares fit for power law.

canonical spin glasses in dilute systems [24,42] which is much smaller due to involvement of atomic spins in the glassy freezing.

3.4.5 Evidence for de Almeida-Thouless and Gabay-Toulouse lines in BF-0.20BT:

The existence of two spin-glass phases, which we shall label as SG1 and SG2 hereafter, was further confirmed by the presence of the so-called de Almeida-Thouless (A-T) [49] and Gabay-Toulouse (G-T) [50–53] lines. For Ising systems, it has been shown by de Almeida and Thouless [49] that the peak temperature (T_{max}) of the ZFC M (T) plot shifts to lower temperature side on increasing the magnetic field (H) as a result of

replica symmetry breaking [49]. For low fields, this shift shows the following H dependence:

$$H^2 = A[1- T_{max}(H)/T_{max}(0)]^3, \qquad \ldots\ldots(3.4)$$

where $T_{max}(H)$ and $T_{max}(0)$ are the field dependent and zero-field freezing temperatures, respectively. Eq. (3.4) sets the boundary between ergodic paramagnetic and non-ergodic spin-glass phases and is commonly known as the A-T line [49]. For the Heisenberg systems also, it has been shown that the A-T line is present and T_{max} follows $H^{2/3}$ dependence at low fields [50–53]. However, it can occur due to freezing of either the longitudinal (q_{ll}) or the transverse ($q_{\perp}$) components of the spin, depending on whether the single ion anisotropy (D/J) is positive or negative. For low values of D/J, a second SG transition whose T_{max} decreases as H^2 at low fields is predicted to occur due to the freezing of the second component of the spin. For small but positive values of D/J, as is the case with $BiFeO_3$ [237], the first SG transition (i.e. SG1) is expected to be due to the freezing of q_{ll} component while the second one (i.e. SG2) due to freezing of $q_{\perp}$ as per the theoretical predictions [50–53]. The H dependence of the q_{ll} and $q_{\perp}$ freezing temperatures should thus fix the A-T and G-T lines in the T_{max} versus H phase diagram for the SG1 and SG2 phases, respectively.

To verify the existence of A-T and G-T lines in BF-0.20BT, we carried out ZFC M (T) measurements at different fields and the results are depicted in Fig. 3.13 for both the transitions. It is evident from the figure that the peak corresponding to SG1 transition is prominent, even though broad, while no such peak, except a step, is observed for SG2 transition up to a field of 500 Oe. With increasing field, the peak corresponding to SG2 transition also starts taking a prominent shape (see insets), while the peak corresponding to the SG1 transition starts getting smeared out and suppressed after initial sharpening

upto 800 Oe. We find that the T_{max} for both the transitions decreases with increasing magnetic field as expected theoretically. The linear nature of the T_{max} versus $H^{2/3}$ and T_{max}

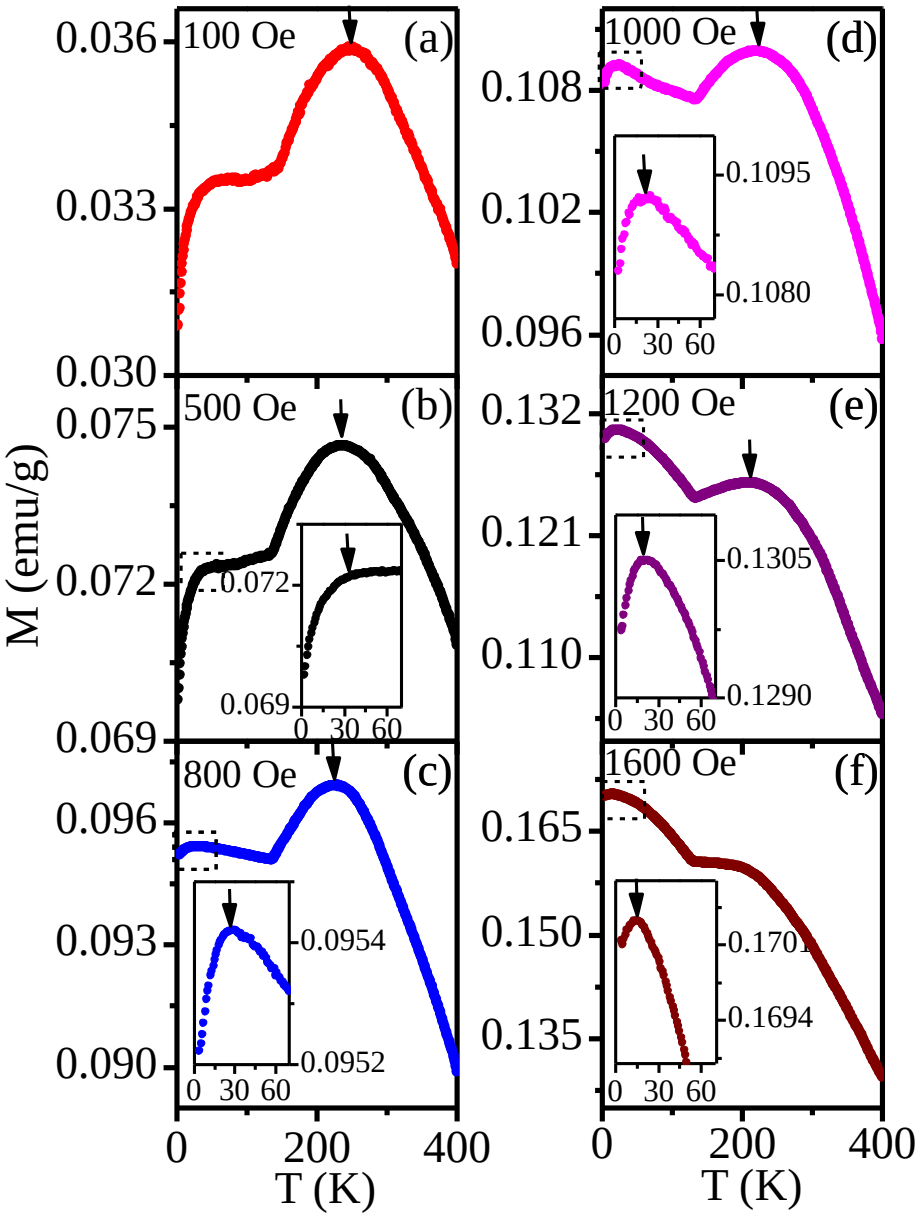

Figure 3.13: ZFC DC magnetization vs temperature plots of BF-0.20BT measured at different applied fields. Insets depict the magnified view around SG2 transition.

vs H^2 plots shown in Figs. 3.14(a) and 3.14(b) for the SG1 and SG2 transitions confirms the existence of A-T and G-T lines, respectively, in the T_{max} versus H phase diagram. Thus our results confirm the theoretical predictions [50–53] for two spin-glass transitions in Heisenberg systems with low D/J.

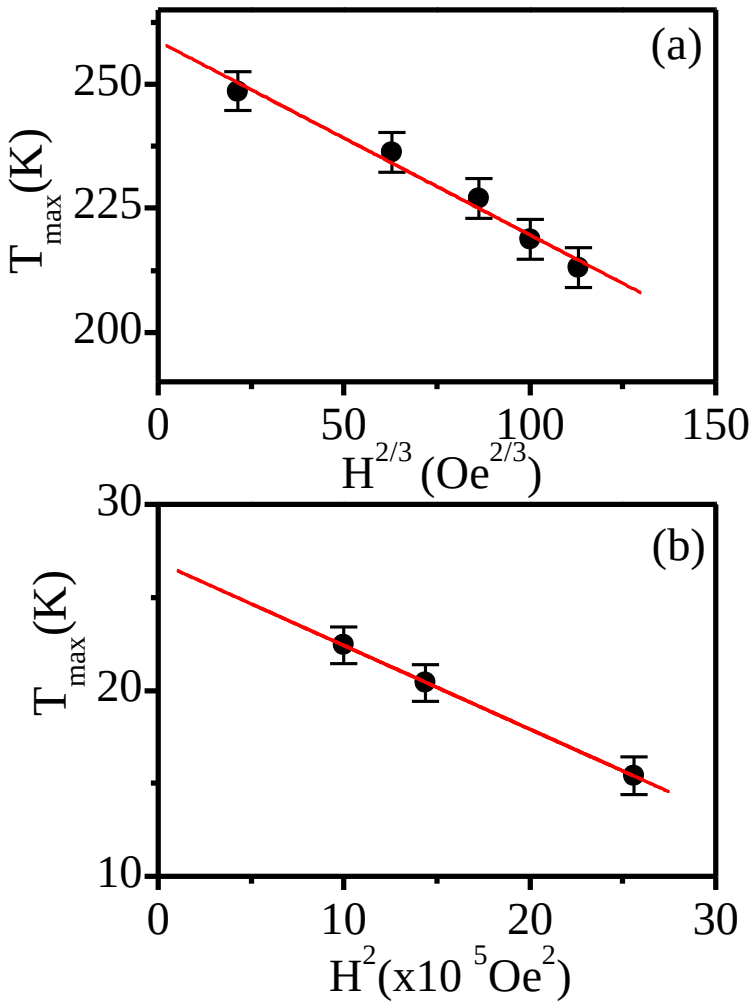

Figure 3.14: (a) de Almeida-Thouless (A-T) line for SG1 transition and (b) Gabay-Toulouse (G-T) line for SG2 transition.

3.4.6 Relaxation of thermoremanent magnetization for the spin glass phases of BF-0.20BT:

Spin glass state is known to exhibit slow relaxation of thermoremanent magnetization which has been modelled using stretched exponential function [262,263]:

$$M(t) = M_0 + M_r \exp[-(t/\tau)^{1-n}] \qquad \text{…….(3.5)}$$

where M_0 is the intrinsic ferromagnetic component, M_r the glassy component, τ the characteristic relaxation time and n the stretched exponential exponent. To study the slow

relaxation of the thermoremanent magnetization, we cooled the sample under a field of 1T from 300 K to 200K for the SG1 phase. After reaching the set temperatures, the sample was allowed to age without switching off the field for a waiting time of t_w = 500s. After a waiting time of t_w=500s, the field was switched off. For the SG2 phase, the sample was first annealed at 773 K above T_N to remove any remanent magnetization introduced during the first cycle and then cooled to 10K under 1T field. This was followed by the protocol identical to that adopted for the SG1 phase. The thermoremanent magnetizations so measured as a function of time are shown in Figs. 3.15(a) and (b) at

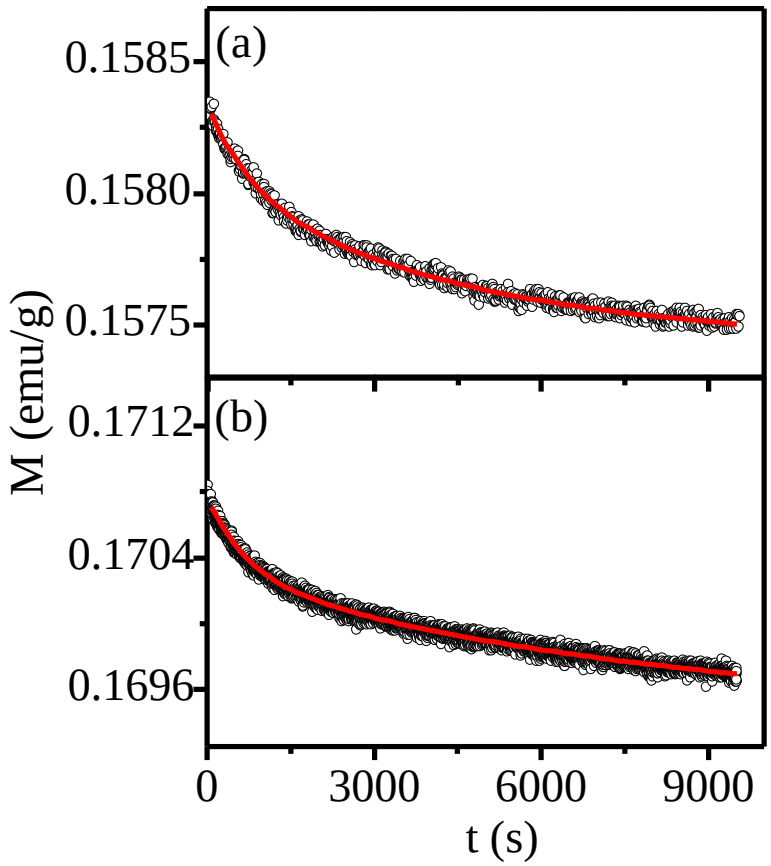

Figure 3.15: Variation of thermoremanent remnant magnetization (M (t)) with time at (a) 200 K and (b)10 K for BF-0.20BT.

200K and 10K, respectively. The continuous line in the two figures depicts the best fit for Eq. (5). These fits yield n, M_0, M_r and τ as 0.55, 0.1575 emu/g, 0.0008 emu/g, (1207±15)s for the SG1 phase and 0.53, 0.1697 emu/g, 0.0009 emu/g, (1661±14)s for the SG2 phase, respectively. The observed exponent (n) and relaxation time (τ) are in agreement with the reported values for cluster glasses and super spin glasses [263]. Thus, relaxation behaviour of thermoremanent magnetization also favours the existence of two SG phases in BF-0.20BT.

3.4.7 Evidence for magnetoelastic coupling at spin-glass transitions in BF-0.20BT:

In order to verify if the two SG transitions and the intervening transition driven by electromagnons involve any structural phase transition, we carried out XRD studies in the temperature range 12K to 350K. Fig. 3.16 depicts the temperature evolution of the XRD profiles of a few selected pseudocubic (pc) peaks (222_{pc}, 400_{pc} and 440_{pc} reflections) of BF-0.20BT after stripping off the $K_{\alpha 2}$ contribution. It is evident from this figure that the 222_{pc} and 440_{pc} peaks are doublets, whereas 400_{pc} is a singlet, as expected for the rhombohedral structure, down to 12K which implies absence of any structural phase transition below room temperature. This was further confirmed by Rietveld refinements at different temperatures. The excellent fits confirm the R3c space group for BF-0.20BT at all temperatures. Fig. 3.17 depicts the observed, calculated and difference profiles obtained after the Rietveld analysis of the XRD patterns at selected temperatures 300K, 200K, 100K and 12K, respectively, for BF-0.20BT using R3c space group. Thus, our Rietveld refinements also confirm that there is no structural phase transition down to 12K. While the magnetic measurements clearly indicate the existence of SG1 and SG2 transitions in BF-0.20BT, the reason for the broad nature of the peak in the ZFC M(T) of the SG1 transition needs to be understood. In order to rule out the role of a structural phase transition, which might have been missed in the medium resolution rotating anode

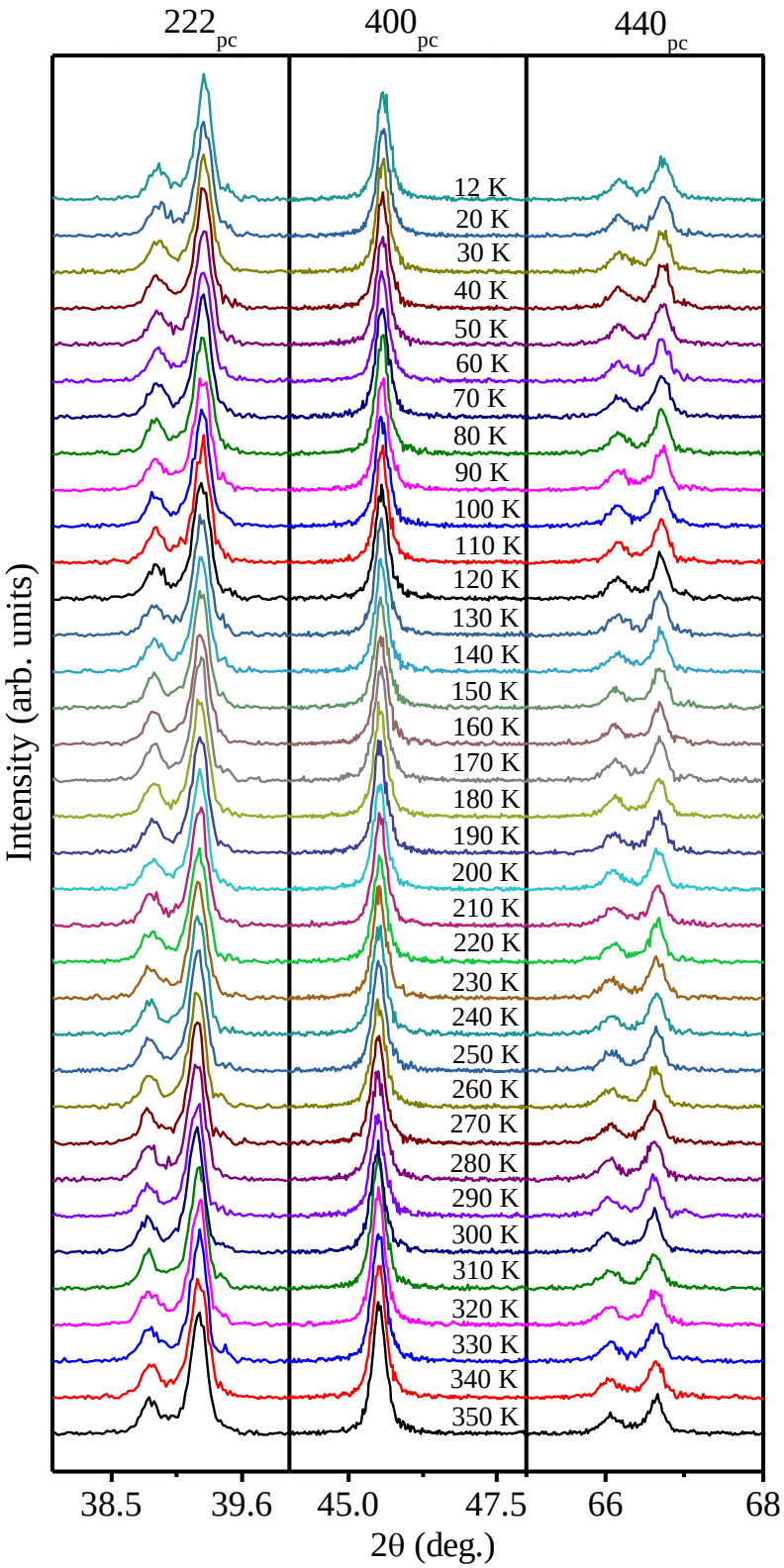

Figure 3.16: The evolution of x-ray powder diffraction profiles of the $(222)_{pc}$, $(400)_{pc}$ and $(440)_{pc}$ reflections of BF-0.20BT with temperature showing absence of any structural phase transition.

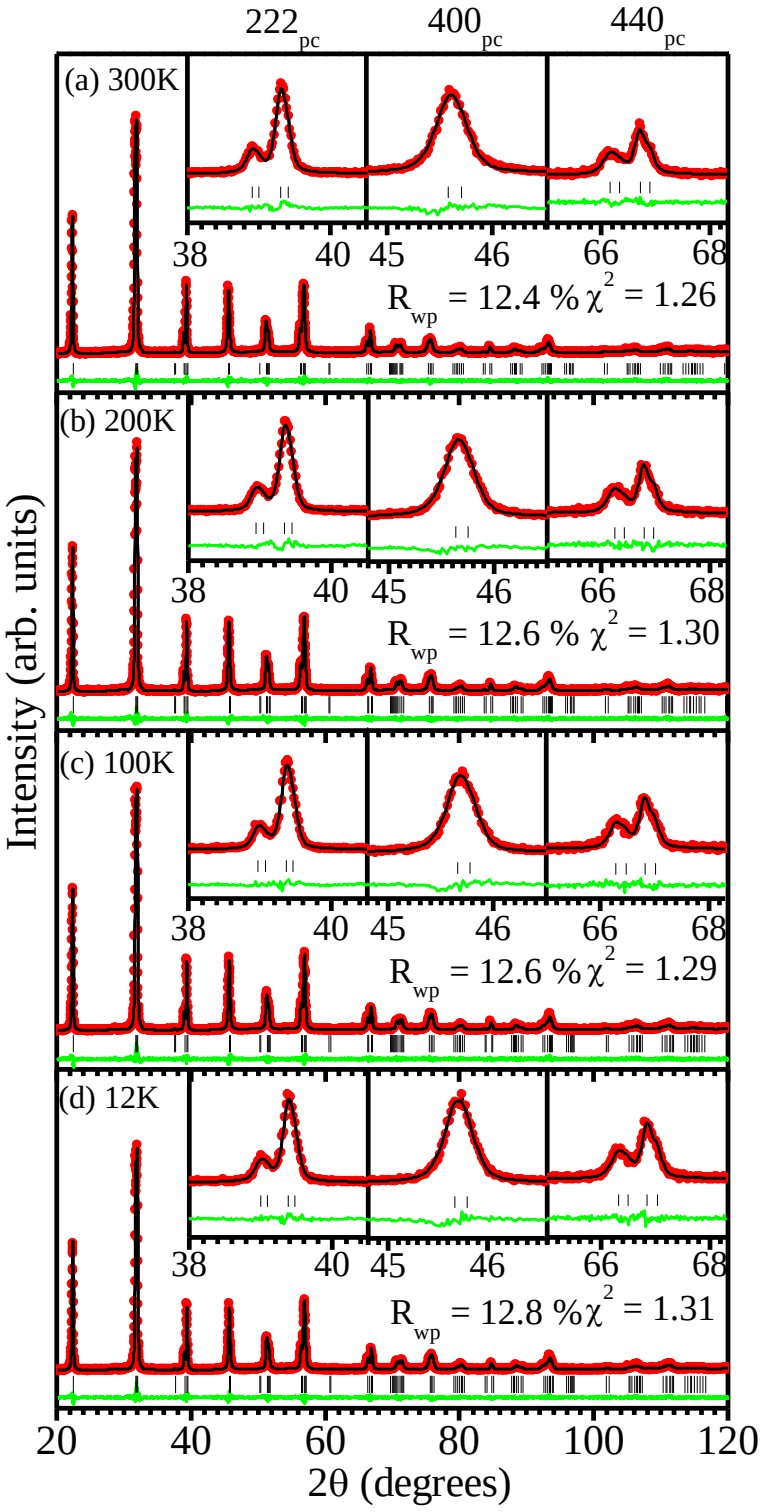

Figure 3.17: Observed (filled circles), calculated (continuous line), and difference (bottom line) profiles obtained from Rietveld refinement using R3c space group at (a) 300K (b) 200K (c)100K and (d) 12K. The vertical tick marks correspond to the position of all allowed Bragg reflections.

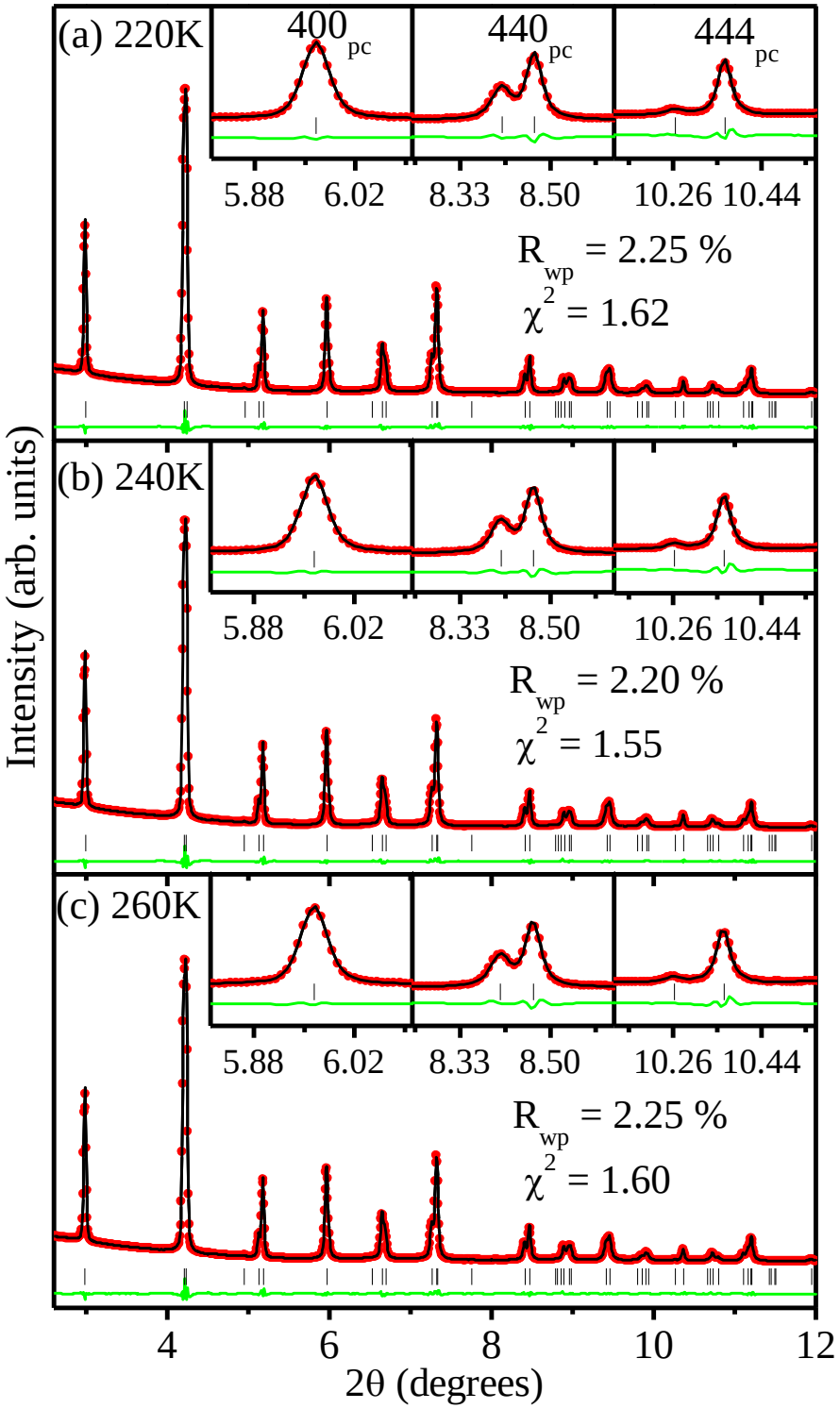

Figure 3.18: Observed (filled circles), calculated (continuous line), and difference (bottom line) profiles obtained from the Rietveld refinement using SXRD data at (a) 220K (b) 240K and (c) 260K using R3c space group for BF-0.20BT. The vertical tick marks above the difference profile represents the Bragg peak positions.

based XRD data, we also carried out Rietveld refinement using high resolution synchrotron x-ray diffraction (SXRD) patterns at three selected temperatures 260K, 240K and 220K. Fig. 3.18 depicts the observed, calculated and difference profiles obtained after the Rietveld analysis of the SXRD patterns at 260K, 240K and 220K, respectively, for BF-0.20BT using R3c space group. The excellent fit between observed and calculated profiles confirms that the R3c space group for BF-0.20BT at room temperature does not change across the SG1 transition. We can thus conclusively rule out the role of any structural phase in the broad SG1 transition.

Even though there is no structural phase transition, the temperature dependence of unit cell volume (V_{hex}), as obtained from the Rietveld refinements, shows anomalies around the three magnetic transitions (see Fig. 3.19). It is interesting to note that the slope of the experimental V_{hex} versus T plot changes prominently around the SG1 transition without any discontinuous change in the value of V_{hex}. After the initial change of slope, the experimental V_{hex} values decrease smoothly with temperature below SG1 transition upto~150K. Small changes in volume around 140K and SG2 transitions are also observed as shown in the inset of Fig. 3.19.

The large change of slope around the SG1 transition suggests strong magnetoelastic coupling associated with this transition. It is possible to separate out the magnetic (magnetoelastic) contribution from the anharmonic lattice part at least for the SG1 transition because of the large slope change. For this, the temperature dependence of V_{hex} above T_{SG1} was modeled using the Debye-Grüneisen equation [264]:

$$V \cong V(0) + \frac{9\gamma N k_B}{B} T \left(\frac{T}{\Theta_D} \right)^3 \int_0^{\Theta_D/T} \frac{x^3}{e^x - 1} dx \quad \ldots\ldots\ldots (3.6),$$

where V(0), Θ_D, γ and B are the unit cell volume at 0K, the Debye temperature, the Grüneisen parameter and the bulk modulus, respectively. Continuous solid line in the figure shows the results of least squares fit to the observed unit cell volume in the temperature range 260K <T≤ 350K using Eq. (3.6). The fitting parameters so obtained are: V (0) = (375.86 ± 0.01) Å^3, Θ_D = (594 ± 10) K, and $9\gamma Nk_B/B$ = (0.071 ± 0.003) Å^3/K. The difference ΔV between the experimentally observed values of V_{hex} and the theoretically calculated anharmonic lattice contribution increases with decreasing temperature. It is interesting to note that the bulk strain ($\Delta V/V$) vs M_s^2 plot corresponding to the shaded region in the figure is linear in the temperature range 240 to 150K as can be seen from Fig. 3.20. This linear dependence confirms that the slope change is due to

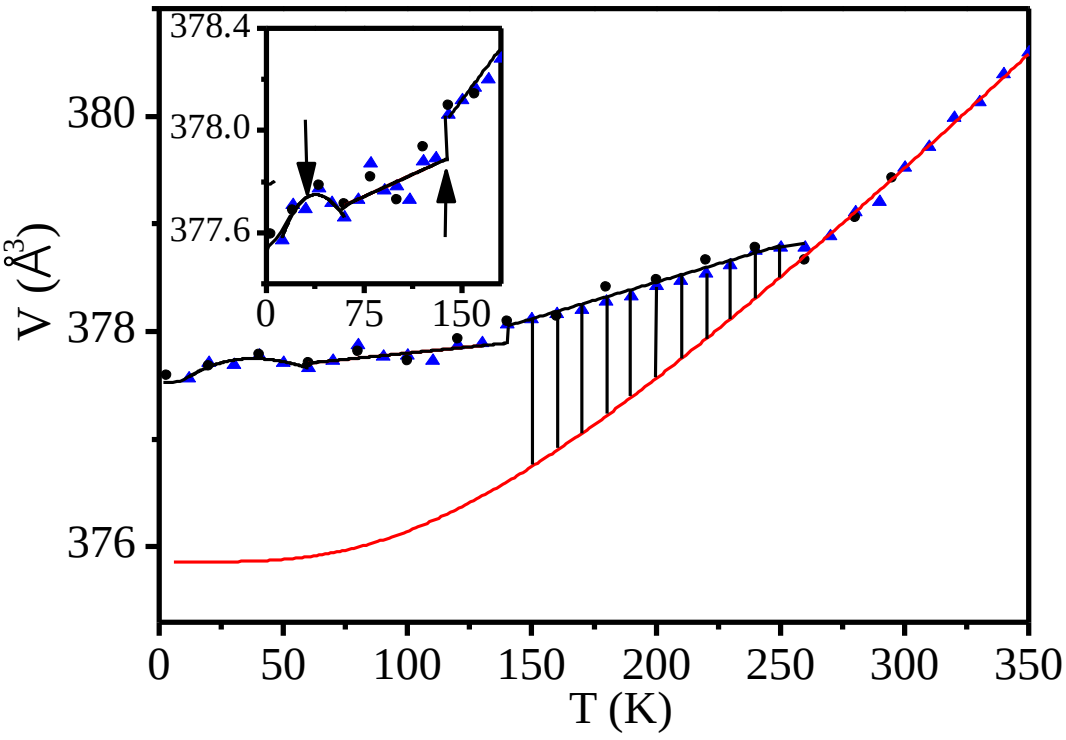

Figure 3.19: Variation of unit cell volume with temperature: XRD (▲) and NPD (●) data. Solid line (—) is fit for Debye Grüneisen equation T_{SG1}. Inset shows the zoomed view around 140K and SG2 transitions.

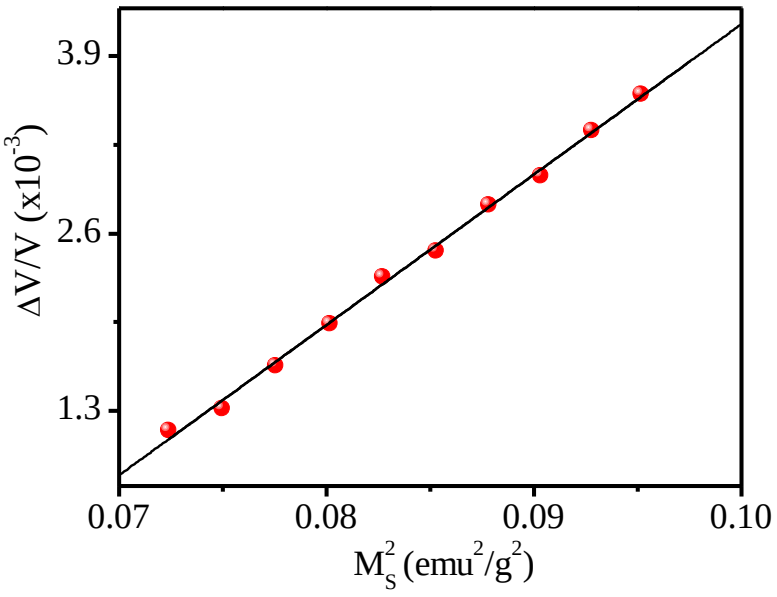

Figure 3.20: Variation of volume strain (ΔV/V) against square of magnetization (M_S^2) obtained by M-H loop.

quadratic spin-lattice coupling [264]. The fact that the change of slope is much more pronounced around SG1 as compared to that around 140 and SG2 transitions suggests that the spin-lattice coupling for the other two transitions is rather weak as compared to that for the SG1 phase.

3.4.8 Evidence for coexistence of LRO AFM and spin-glass phases in BF-0.20BT:

We now turn towards neutron diffraction studies to understand whether the LRO, SG1 and SG2 transitions occur on the same magnetic sublattice or not. Fig. 3.21 depicts the temperature evolution of the neutron powder diffraction patterns of BF-0.20BT in the limited 2θ range of 15-57º. It was verified by Rietveld refinement that neither the nuclear nor the magnetic structure changes down to the lowest temperature of measurement. The asymmetric unit of rhombohedral structure with R3c space group is already given in section 3.4.2. All the nuclear structure peaks are well indexed with respect to the nuclear unit cell of the R3c space group except the magnetic peaks. No evidence for any magnetic impurity phase was found in the neutron data. The magnetic peaks are indexed by

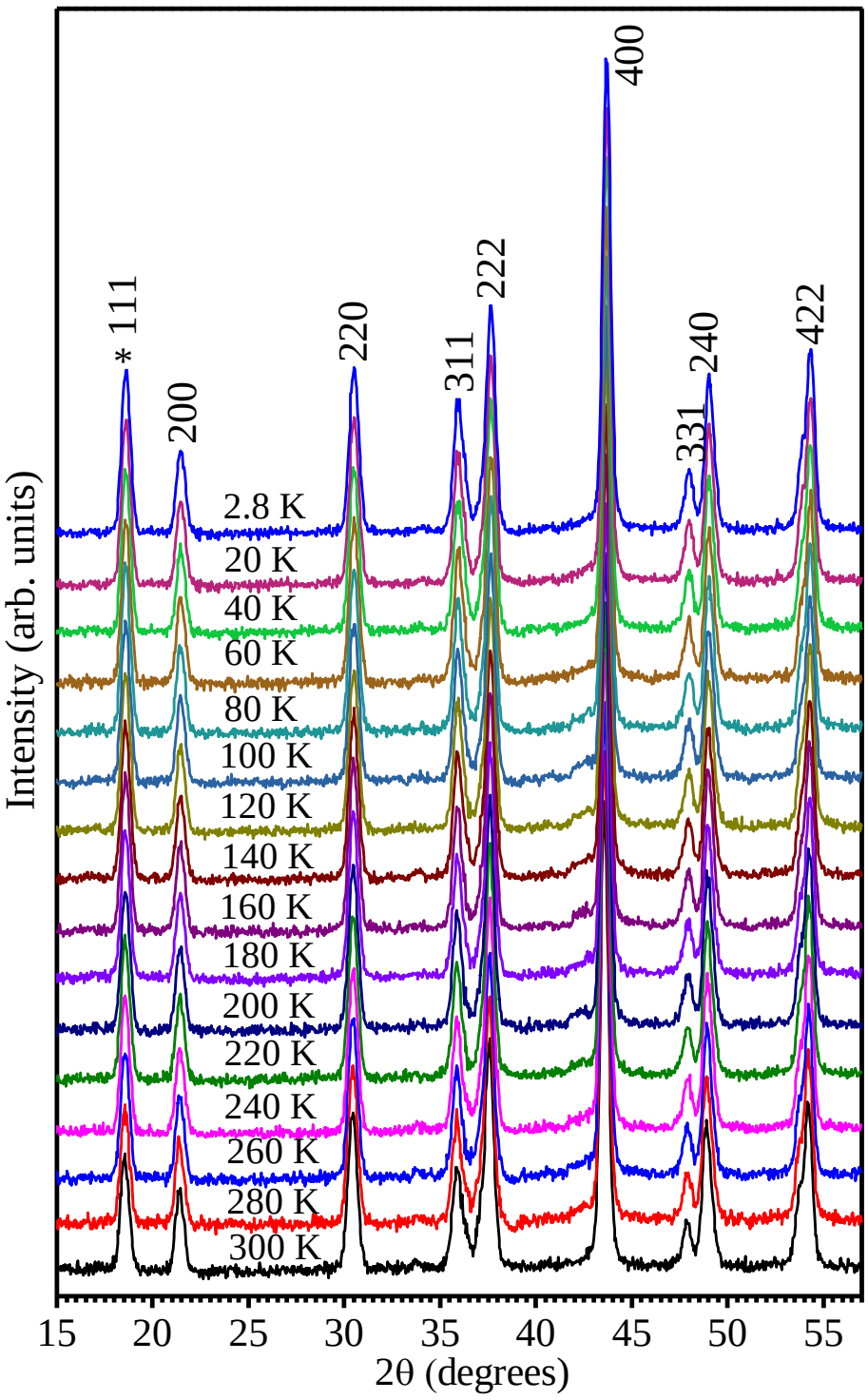

Figure 3.21: The evolution of the neutron powder diffraction patterns with temperature in the limited 2θ = 15º-57º range. The first peak is due to AFM ordering. The Miller indices are written with respect to a doubled pseudocubic cell.

considering additional phase in the nuclear structure refinement of neutron powder diffraction (NPD) data. We use the representation analysis to determine the magnetic structure of BF-0.20BT. For propagation vector k = (0,0,0), the little group G_k formed by those elements of space group that leave k invariant or only changed by a translation of the reciprocal lattice coincide with the space group R3c. The irreducible representations corresponding to propagation vector k = (0,0,0) are given in Table 3.3. In hexagonal unit cell with R3c space group, the magnetic ions Fe^{3+} occupy the 6(a) Wyckoff site with general positions (0, 0, z) and (0, 0, z+1/2). The magnetic reducible representation Γ_{mag} for the 6(a) Wyckoff site can be decomposed as direct sum of three irreducible representations,

$$\Gamma\ (6a/\ Fe) = 1\Gamma_1^1 + 1\Gamma_2^1 + 2\Gamma_3^2 \qquad \text{.....(3.7)}$$

The basis vectors associated with each irreducible representation are given in Table 3.4. The Γ_1 and Γ_2 representations are one dimensional whereas the representation Γ_3 is two dimensional. Γ_1 and Γ_2 correspond to single basis vector magnetic structures while Γ_3 corresponds to four basis vector magnetic structure. Following Singh et al. [90], the magnetic structure of BF-0.20BT corresponds to the representations Γ_1 and Γ_3 since the magnetic structure corresponding to the representation Γ_2 fails to model the magnetic reflections. The representations Γ_1 and Γ_3 gives similar values for structural as well as magnetic parameters within the standard deviation. Following Singh et al. [90], we use the Γ_1 representation for the magnetic structure analysis of BF-0.20BT. All the magnetic peaks were well indexed with propagation vector $\vec{k} =$ (0,0,0) and Γ_1 representation. The initial input parameters for Rietveld refinement of nuclear structure were taken from the Rietveld refinement using SXRD data. Both the nuclear and magnetic structures were refined, and the refinement converged successfully after a few

cycles. The observed (filled-circles) and calculated (continuous line) profiles show excellent fits at all temperatures and some selected fits obtained after Rietveld refinement at 300 K, 200K, 100K and 2.8K are shown in Fig. 3.22 (a) (b) (c) and (d), respectively. The refined lattice parameters, positional coordinates, thermal parameters, and magnetic

Table 3.3. Irreducible representation of the little group G_k for propagation vector is k = (0,0,0).

Irreps	Symmetry operators of G_k					
	1	3+ 0,0,z	3- 0,0,z	c x,-x,z	c x,2x,z	c 2x,x,2z
Γ_1	1	1	1	1	1	1
Γ_2	1	1	1	-1	-1	-1
Γ_3	$\begin{pmatrix}1 & 0\\0 & 1\end{pmatrix}$	$\begin{pmatrix}a & 0\\0 & b\end{pmatrix}$	$\begin{pmatrix}b & 0\\0 & a\end{pmatrix}$	$\begin{pmatrix}0 & 1\\1 & 0\end{pmatrix}$	$\begin{pmatrix}0 & b\\a & 0\end{pmatrix}$	$\begin{pmatrix}0 & a\\b & 0\end{pmatrix}$

Table 3.4: The basis vectors of the irreducible representations of the space group R3c appearing in the magnetic representation at the Wyckoff position 6a for the wave vector k = (0, 0, 0).

Irreps	Basis vector	Atom 1 (0, 0, z)			Atom 2 (0, 0, z+½)		
		m_x	m_y	m_z	m_x	m_y	m_z
Γ_1	ψ_1	0	0	3	0	0	-3
Γ_2	ψ_2	0	0	3	0	0	3
Γ_3	ψ_3	$\frac{3}{2}-i\frac{\sqrt{3}}{2}$	$-i\sqrt{3}$	0	0	0	0
	ψ_4	0	0	0	$-\frac{3}{2}-i\frac{\sqrt{3}}{2}$	$-\frac{3}{2}+i\frac{\sqrt{3}}{2}$	0
	ψ_5	0	0	0	$-\frac{3}{2}+i\frac{\sqrt{3}}{2}$	$-\frac{3}{2}-i\frac{\sqrt{3}}{2}$	0
	ψ_6	$\frac{3}{2}+i\frac{\sqrt{3}}{2}$	$i\sqrt{3}$	0	0	0	0

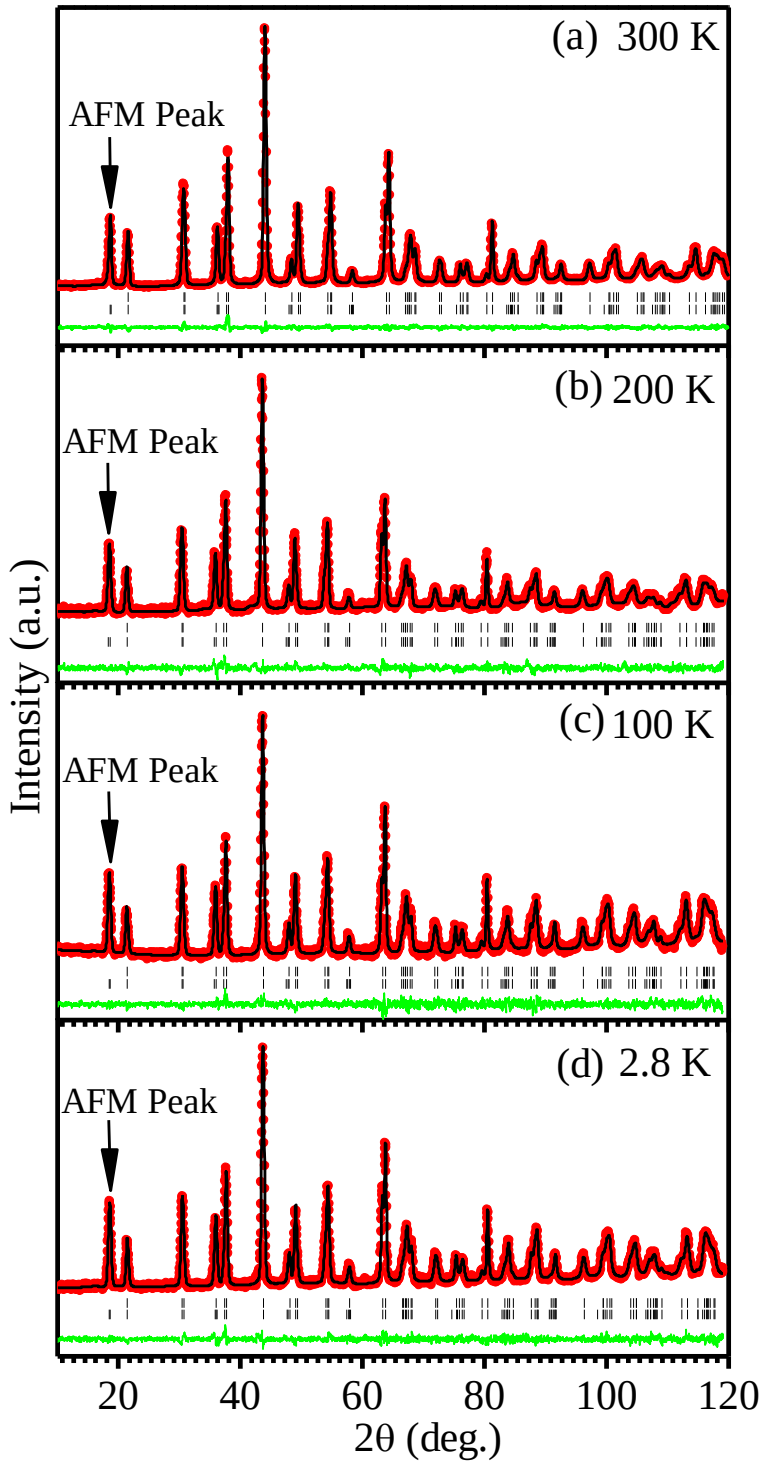

Figure 3.22: Observed (filled circles), calculated (continuous line), and difference (bottom line) profiles obtained from Rietveld refinement using R3c space group at (a) 300K (b) 200K (c) 100K and (d) 2.8K. Arrow indicates the AFM peak. The vertical tick marks correspond to the position of all allowed Bragg reflections for the nuclear (top) and magnetic (bottom) reflections.

moment, listed in Table 3.5, are in good agreement with those reported in the literature [90]. The Rietveld refinement results confirm that both the nuclear structure with R3c space group and the magnetic structure do not change down to the lowest temperature as a result of the magnetic transitions. The fact that the AFM peak, marked with arrow in the figure, persists down to 2.8K clearly suggests that the LRO AFM phase coexists with the SG phases. We modelled the temperature dependence of the integrated intensity of the AFM peak using the molecular-field theory according to which the magnetic moment should follow the following temperature dependence [265],

$$\frac{\mu}{\mu_0} = B_J(x), \text{ where } x = \left(\frac{3J}{J+1} \frac{T_C}{T} \frac{\mu}{\mu_0} \right) \qquad \text{.....(3.8)}$$

Here, J is the total angular momentum of the system, μ/μ_0 is the ratio of the magnetic moment at temperature T to that at T= 0K, and B_J is the Brillouin function

$$B_J(x) = \frac{2J+1}{2J} \coth\left(\frac{2J+1}{2J} x \right) - \frac{1}{2J} \coth\left(\frac{1}{2J} x \right) \qquad \text{.....(3.9)}$$

We fitted the square of the ordered magnetic moment to the experimentally measured integrated intensity of the AFM peak as a function of temperature and the results are shown in Fig. 3.23. Solid line in the figure is the fit for the square of the Brillouin function behaviour. Evidently, the observed variation of the integrated intensity of the AFM peak deviates from the molecular field behavior around the two SG transition temperatures. This decrease in the integrated intensity around T_{SG1} and T_{SG2} clearly suggests that some spin components are being removed from the LRO AFM phase regions and transformed to the glassy phase. This proves that the two SG phases are

Table 3.5: Refined nuclear and magnetic structural parameters and agreement factors using NPD data at 300K, 200K, 100K and 2.8K with R3c space group.

Parameters	**NPD 300 K**	**NPD 200 K**	**NPD 100 K**	**NPD 2.8 K**
a_{hex} (Å)	5.6132 (5)	5.6084 (5)	5.6052 (5)	5.6051 (4)
c_{hex} (Å)	13.9078 (2)	13.8939 (1)	13.8825 (1)	13.8813 (1)
v_{hex} (Å)	379.42 (6)	378.48 (6)	377.73 (6)	377.59 (5)
α, β, γ	$\alpha=\beta=90^0$, $\gamma=120^0$	$\alpha=\beta=90^0$, $\gamma=120^0$	$\alpha=\beta=90^0$, $\gamma=120^0$	$\alpha=\beta=90^0$, $\gamma=120^0$
Bi/Ba (z)	0.2854 (5)	0.2865 (4)	0.2862 (4)	0.2859 (4)
Fe/Ti (z)	0.0110 (6)	0.0119 (4)	0.0110 (5)	0.0115 (4)
O (x)	0.2116 (8)	0.2117 (6)	0.2171 (6)	0.2159 (6)
O (y)	0.3468 (4)	0.3466 (7)	0.3488 (6)	0.3487 (6)
O (z)	1/12	1/12	1/12	1/12
$\beta_{Bi/Ba}$(Å^2)	$\beta_{11}=\beta_{22}=2\beta_{12}$ = 0.0363 (2) β_{33} = 0.0031 (3)	$\beta_{11}=\beta_{22}=2\beta_{12}$ = 0.0313 (2) β_{33} = 0.0029 (4)	$\beta_{11}=\beta_{22}=2\beta_{12}$ = 0.0250 (2) β_{33} = 0.0026 (3)	$\beta_{11}=\beta_{22}=2\beta_{12}$ = 0.031 (2) β_{33} = 0.0024 (2)
$\beta_{Fe/Ti}$ (Å^2)	1.33 (9)	1.30 (5)	1.27 (9)	1.27 (8)
β_O(Å^2)	β_{11}= 0.057 (3) β_{22} = 0.019 (1) β_{33} = 0.002 (3) β_{12} = 0.025 (2) β_{13} = 0.003 (9) β_{23} = 0.006 (4)	β_{11}= 0.048 (5) β_{22} = 0.011 (3) β_{33} = 0.002 (3) β_{12} = 0.019 (7) β_{13} = 0.003 (6) β_{23} = 0.006 (5)	β_{11}= 0.039 (3) β_{22} = 0.004 (13) β_{33} = 0.003 (2) β_{12} = 0.014 (2) β_{13} = 0.002 (7) β_{23} = 0.005 (3)	β_{11}= 0.046 (3) β_{22} = 0.008 (14) β_{33} = 0.003 (2) β_{12} = 0.017 (1) β_{13} = 0.004 (7) β_{23} = 0.006 (4)
μ_{Fe} (μ_B)	3.25 (8)	3.55 (7)	3.75 (8)	3.82 (7)
R_{wp} (%)	9.15	9.89	9.87	9.03
R_{mag} (%)	4.63	4.21	3.39	3.36
χ^2	7.58	8.35	9.80	8.38

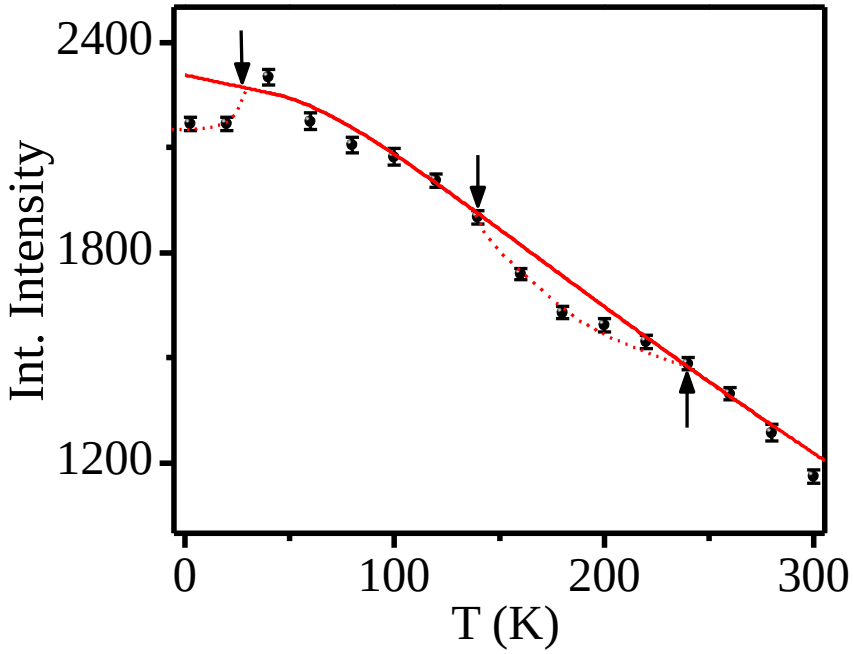

Figure 3.23: Temperature dependent variation of the integrated intensity of the AFM peak (111) of BF-0.20BT (The miller indices are with respect to a doubled pseudocubic cell). Solid line is fit for Brillouin function.

formed on the same magnetic sublattice [172] that gives rise to the LRO AFM phase and that they are not due to nanosized impurity phases, proposed in the context of the low temperature SG phase of pure $BiFeO_3$ [88,266,267] or smaller SPM clusters in a segregated magnetic microstructure proposed in the context of $Pb(Fe_{1/2}Nb_{1/2})O_3$ [171].

3.4.9 Evidence for isostructural phase transitions and polarization changes across the spin-glass transitions in BF-0.20BT:

Even though the space group symmetry of BF-0.20BT does not change in the 300 to 2.8K temperature range, the fractional coordinates of $z_{Bi/Ba}$ and $z_{Fe/Ti}$, obtained by Rietveld refinements using neutron diffraction data, change discontinuously around the two spin-glass transition temperatures as shown in Fig. 3.24. Further, the coordinates of the two oxygen positions (x_O and y_O) show anomalies around the third transition driven by electromagnons. This change of atomic positions (fractional coordinates) can be explained in terms of one of the irreducible representations (Irrep) of the R3c space group corresponding to an optical phonon mode at k= (0,0,0) point of the Brillouin zone, as discussed in the supplemental information of Ref. [89]. Such a change of atomic positions

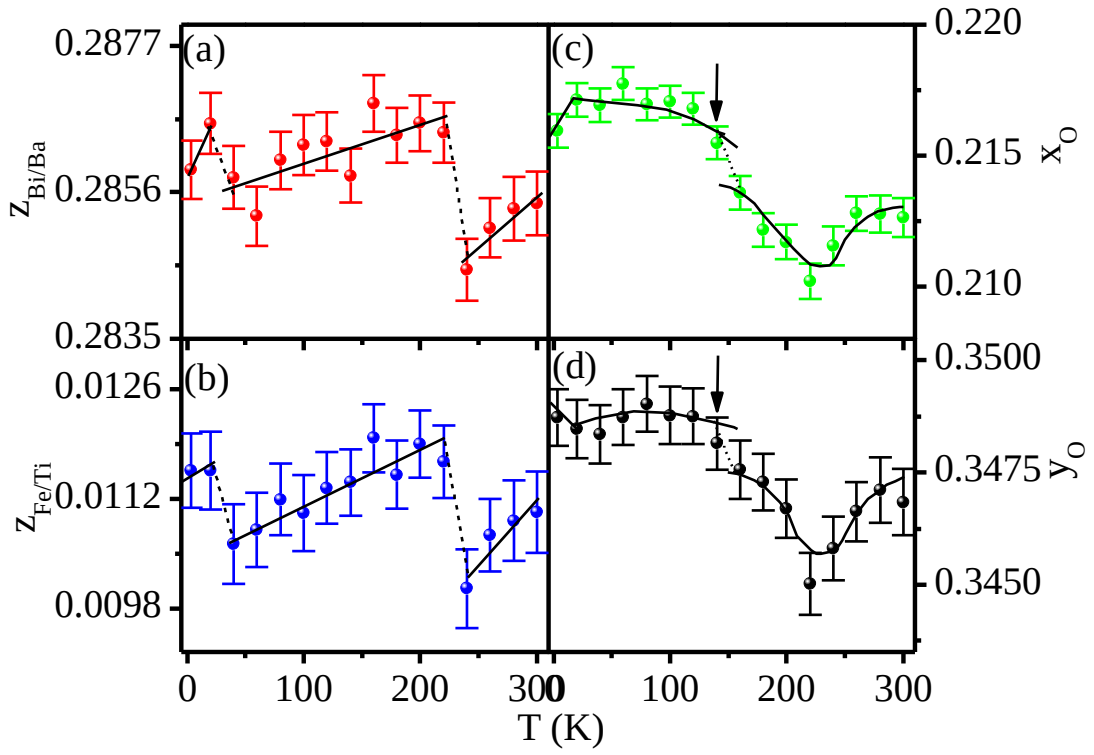

Figure 3.24: Temperature dependence of the fractional z coordinates of (a) Bi/Ba and (b) Fe/Ti. The x and y coordinates of O are shown in (c) and (d). All these coordinates were obtained from the Rietveld refinements using neutron powder diffraction data.

without any change in the space group symmetry has previously been observed in $BiFeO_3$ solid solutions across T_N where it has been attributed to an isostructural phase transition (ISPT) [89,90,94]. We believe that the anomalies in atomic positions across the three low temperature magnetic transitions in BF-0.20BT are due to similar ISPTs driven by spin-polar phonon coupling (SPC). In literature [268], the origin of SPC effect has been attributed to the electronic structure which may suggest that the low temperature transitions in BF-0.20BT could be of electronic origin.

As a result of change in the atomic positions due to the ISPT, the ferroelectric polarisation (P_s) is known to change significantly by about 2 to 3 $\mu C/cm^2$ at T_N revealing magnetoelectric coupling in $BiFeO_3$ solid solutions including BF-0.20BT [89,90,94].

We have also calculated P_s below room temperature from Rietveld refined coordinates, unit cell parameters and first principles derived Born Effective Charges (BEC) taken from the literature [79] using the following relationship:

$$P = e/V \sum_k z'_k \Delta(k), \qquad \text{.....(3.10)}$$

where the sum runs over all the ions inside the unit cell while $\Delta(k)$ is the displacement of the k^{th} ion from its ideal cubic perovskite position, z'_k the Born effective charge for k^{th} ion and V the volume of the primitive unit cell. The temperature variation of P_s so obtained is shown in Fig. 3.25 which reveals distinct changes across the two SG transitions. The change in P_s observed by us around T_{SG1} and T_{SG2} is (5±1)μC/cm^2 and (2±1)μC/cm^2, respectively, which are of similar order of magnitude as reported at the T_N for BF-0.20BT [90]. The observation of large change in P_s (ΔP_s) at the two SG transitions not only reveals strong magnetoelectric coupling but also provides additional microscopic evidence for the coexistence of the SG and the LRO phases on the same magnetic sublattice at the two spin glass transition temperatures due to multiferroic nature of the two SG phases.

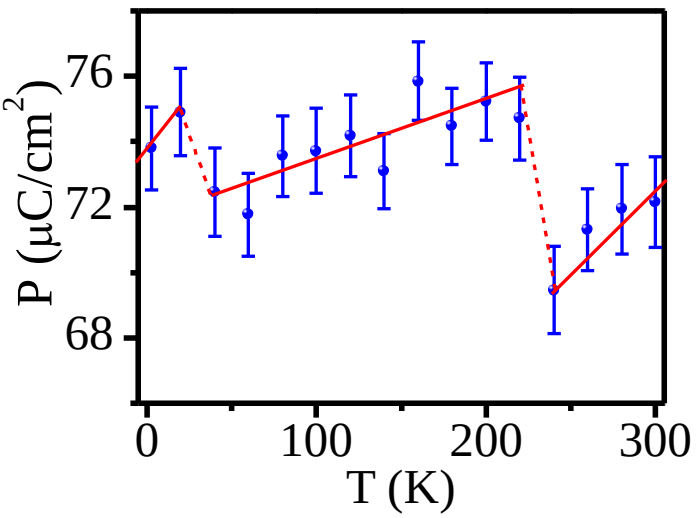

Figure 3.25: Temperature dependent variation of the spontaneous polarization calculated from the positional coordinates.

3.5. Magnetic phase diagram of BF-xBT:

In this section, we briefly discuss the effect of $BaTiO_3$ concentration (x) on the low temperature phase transitions of $BiFeO_3$ with the objective of constructing a magnetic phase diagram of BF-xBT system using the transition/freezing temperatures obtained from ZFC M(T) and AC susceptibility measurements (see Figs. 3.26-3.28). Fig. 3.26 depicts the plot of ZFC M(T) for various compositions (x). Signature of a transition to a LRO magnetic state is clearly seen upto x=0.40. For x=0.50 also, a diffuse transition is seen in the figure but for x = 0.60 there is no signature of this transition in the M(T) plot. Disorder induced gradual broadening of the transition is seen quite clearly in this figure for higher x values. The LRO transition temperature T_N was determined from the first derivative of M(T) shown in Fig. 3.26(b). It shows clear dips for all the compositions including x = 0.50 due to the Néel transition (see also the inset of Fig.3.26(b)). The composition dependence of T_N shown in Fig. 3.29 could be described using $(x-x_c)^n$ type dependence with n = 0.30±0.02 and x_c = 0.55±0.01. In the previous neutron diffraction studies [91], AFM peak was observed for x = 0.50 but not for x=0.60 which also suggests that x_c lies in the range $0.50 \leq x_c \leq 0.60$. We believe that x_c = 0.55 is the percolation threshold limit for the LRO phase to emerge in the presence of disorder introduced by $BaTiO_3$ substitution in the $BiFeO_3$ matrix.

To investigate the effect of disorder (x) on the SG1 and SG2 transitions, we show in Fig. 3.27 the χ' (ω, T) plots at 497.3 Hz for various compositions of BF-xBT. The variation of χ' (ω, T) for x = 0.10, 0.20 and 0.30 are similar where the peaks corresponding to SG1 and SG2 transitions are clearly seen. While two peaks in the χ' (ω, T) plot are also seen for x= 0.40, the magnitude of the susceptibility below the SG1 transition shows a slightly increasing trend with decreasing temperature whereas it shows a decreasing trend

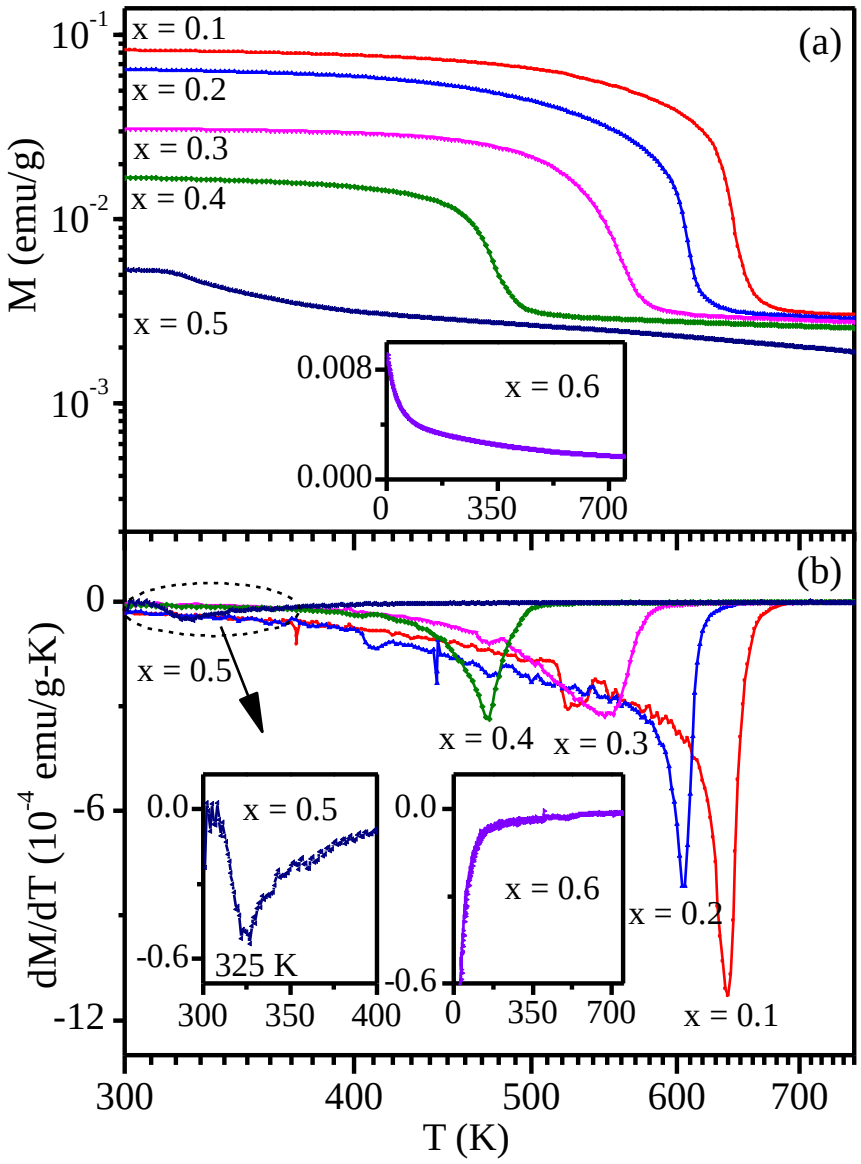

Figure 3.26: (a) The variation of ZFC magnetization with temperature measured at a field of 500 Oe for various compositions in the range $0.10 \leq x \leq 0.60$. (b) shows first derivative of M (dM/dT) with respect to temperature for these compositions.

for x = 0.10, 0.20 and 0.30 showing that the disorder affects the two transitions differently. For x= 0.50, only one peak corresponding to the SG2 transition is seen clearly. There is, however, an inflection point around 51K which could possibly be linked with the SG1 transition. The composition dependence of the SG1 and SG2 transition temperatures are shown in Fig. 3.29. The SG1 transition temperatures for various

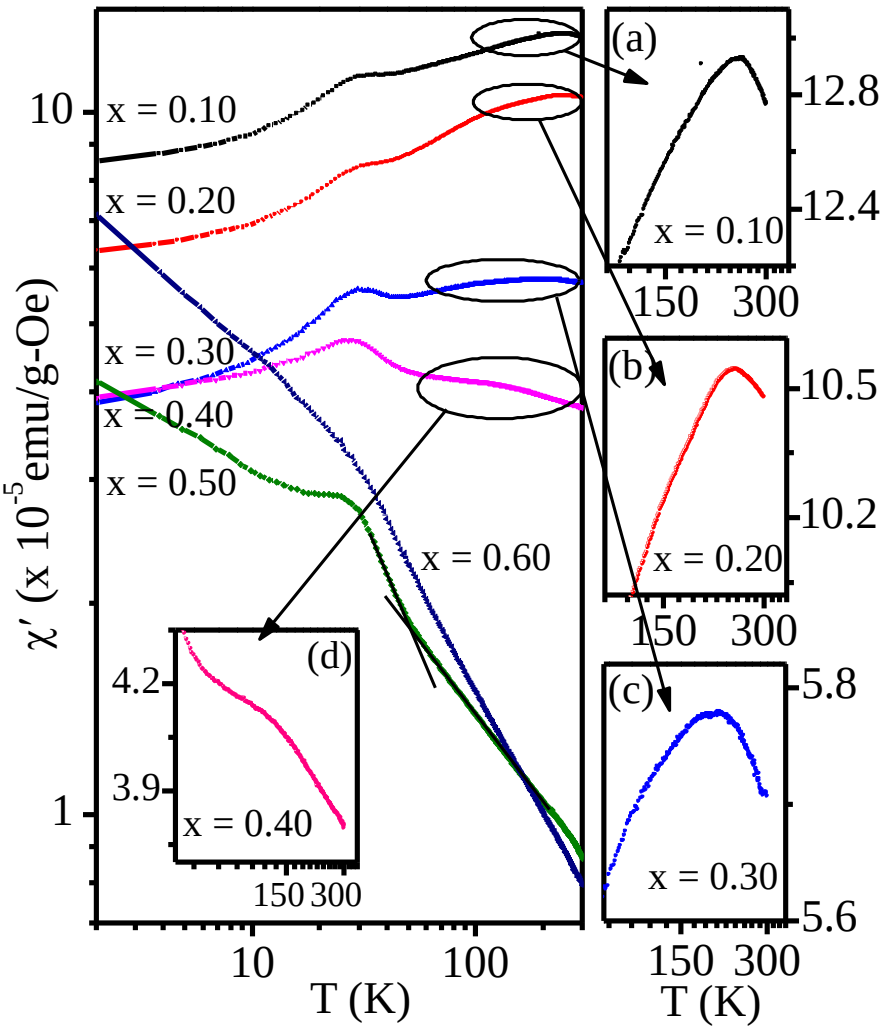

Figure 3.27: Left panel shows the variation of χ' (ω, T) of BF-xBT with temperature at 497.3 Hz frequency for various compositions in the range $0.10 \leq x \leq 0.60$. Right panel (a-c) as well as panel (d) depict the zoomed view around the SG1 transition.

compositions, including x= 0.40 and 0.50, also show $T_c \sim (x-x_c)^n$ type dependence with x_c =0.55±0.01 but with an exponent n = 0.49±0.07. This exponent (n ~½) is reminiscent of a quantum phase transition [269,270] and the possibility of the existence of a quantum critical point corresponding to the percolation threshold composition x_c= 0.55 for the SG1 transition needs to be investigated carefully in a future work. Further, the extrapolation of the curve for SG1 transition to x = 0 predicts a transition around 260K for $BiFeO_3$.

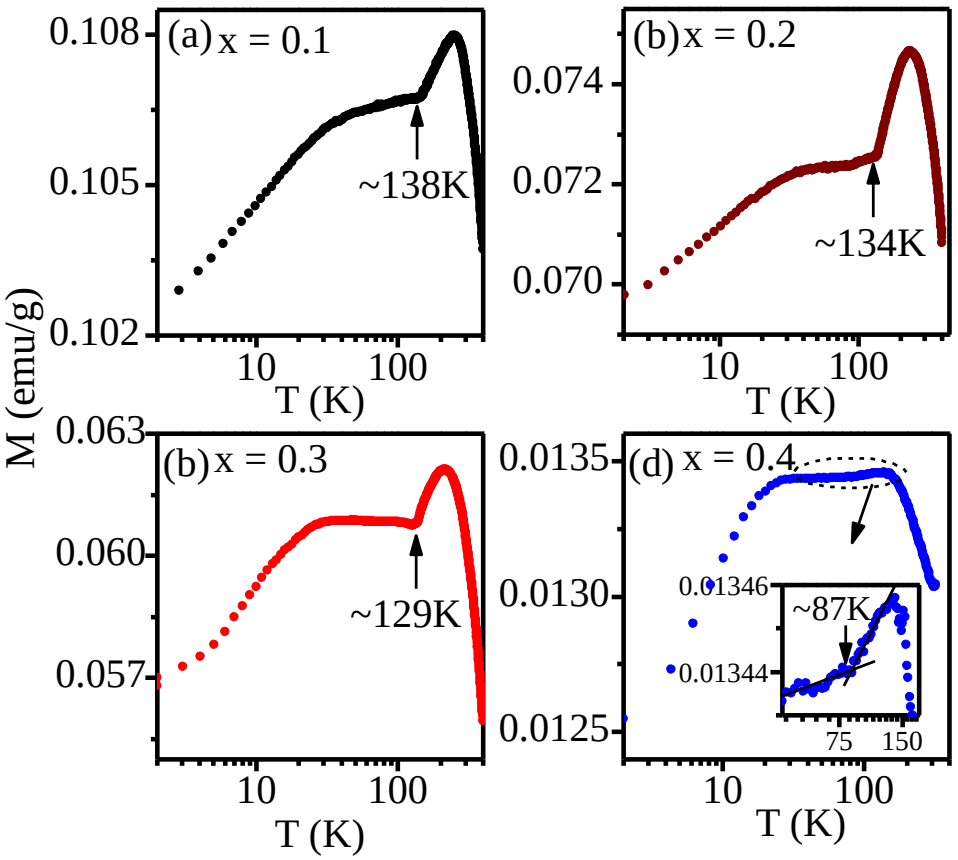

Figure 3.28: The variation of ZFC magnetization of BF-xBT with temperature below 300K measured at field of 500 Oe for compositions (a) x= 0.10, (b) x = 0.20, (c) x = 0.30 and (d) x = 0.40.

This transition was presented in the previous chapter. It is likely that this transition in $BiFeO_3$ may also have a spin glass character as predicted in the literature [103]. In contrast to the SG1 transition, the SG2 transition temperature shows weak composition dependence upto about x= 0.40 but significant decrease is seen for x=0.50. From the least squares fit to the observed T_{f2} values using $(x-x_c)^n$ type dependence, the critical composition limit for this transition is also found to be close to x_c=0.55 but with an exponent n =0.08. We have also examined the composition dependence of the intermediate transition, that occurs between the SG1 and SG2 transitions and is known to be driven by electromagnons in pure $BiFeO_3$, using ZFC M(T) plot below room

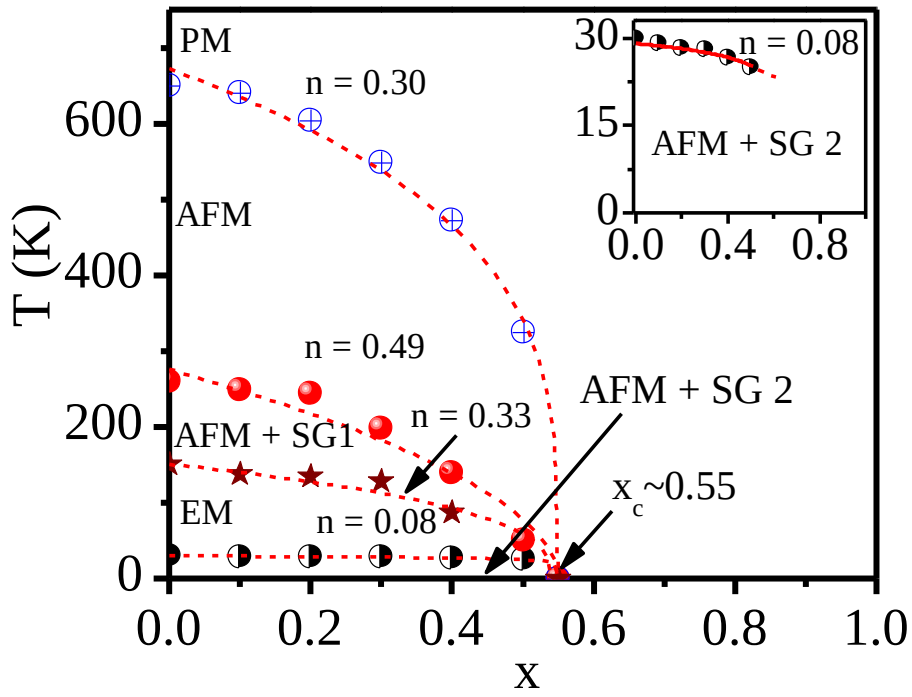

Figure 3.29: Phase diagram of BF-xBT. PM: Paramagnetic, SG: Spin glass, AFM: Antiferromagnetic, EM: Electromagnon. The SG2 transition temperatures (see the inset) shows the weakest composition dependence. The dotted lines through the data points depict the least squares fit for $T_c \sim (x-x_c)^n$ type dependence with x_c = 0.55 giving n = 0.30, 0.49, 0.33 and 0.08 for the AFM, SG1, electromagnon driven and SG2 transitions, respectively. The exponent n ~ ½ indicates the possibility of a quantum critical point at $x_c \sim 0.55$.

temperature shown in Fig. 3.28 for four different compositions of BF-xBT. The M(T) plot shows a peak corresponding to the SG1 transition whereas the SG2 transition is signalled by a step like decrease in the magnetization value at low temperatures. As a result of dilution of the magnetic sublattice due to disorder, magnetization decreases and the peak corresponding to the SG1 transition becomes less prominent for x= 0.40. The electromagnon transition is signalled by a kink (for $x \leq 0.30$) or a dip (x=0.40) at the foothill of the SG1 peak. The corresponding transition temperature shows a rather weak composition dependence upto x= 0.30. The composition dependence of this transition temperature (T_c) was also fitted to $(x-x_c)^n$ type function which gave us n = 0.33±0.06 and x_c = 0.55±0.02. The phase diagram presented in Fig. 3.29 clearly shows the SG1 and SG2

transitions as well as the intervening third transition supposedly driven by electromagnons for all the compositions with $x < x_c$. This intermediate transition was not envisaged in the existing theories of a succession of two spin-glass transitions in Heisenberg system [50–53] and needs to be looked into in a future work.

3.6. Conclusions:

Excellent quality samples of (1-x)$BiFeO_3$-x$BaTiO_3$ (BF-xBT) solid solutions with x = 0.10, 0.020, 0.30, 0.40, 0.50, and 0.60 were synthesized by the conventional solid state route and characterized by laboratory source and synchrotron based XRD, SEM, EDX and EPMA for their phase purity, crystal structure, microstructure and composition. The low temperature magnetic transitions were investigated using DC magnetization measurements as a function of temperature (M (T)), time (M(t)), field (M (H)) and sample history (ZFC and FC conditions), AC susceptibility measurements as a function of frequency (ω) and temperature (T) (χ (ω,T)), as well as low temperature XRD and neutron diffraction measurements.

We have presented evidence for two spin-glass transitions (SG1 and SG2) in the BF-xBT system using a series of bulk measurements revealing history dependent effect, critical slowing down of the spin dynamics due to ergodicity breaking, existence of A-T and G-T lines due to freezing of the longitudinal and transverse components of the spins and stretched exponential type decay of the thermoremanent magnetization. Using neutron and x-ray diffraction measurements, which provide evidence on microscopic scales, we have shown that the two spin-glass transitions are not only intrinsic to the BF-xBT system but also occur on the same magnetic sublattice in coexistence with the long range ordered antiferromagnetic phase. Our results show for the first time that the spontaneous polarization (P_s) and unit cell volume (V) show significant variation across the SG1 and SG2 transitions confirming the presence of magnetoelectric and

magnetoelastic couplings, respectively. These couplings, and possibly the presence of electromagnons, constitute unique features of a multiferroic spin-glass system like BF-xBT that distinguish it from the conventional spin glass systems. While the existence of the A-T and G-T lines confirms that the SG1 and SG2 transitions result from the freezing of the longitudinal and transverse components of spins, as predicted theoretically for Heisenberg systems with small single ion anisotropy (D), there are a few unexplained aspects of our observations. First and foremost is whether the smeared SG1 transition could have a structural origin, rather than magnetic. Although the SG1 transition is not found to be linked with any change in the space group symmetry, the occurrence of isostructural phase transition (ISPT) has been confirmed by us which indicates spin-phonon coupling. Secondly, the temperatures for the two spin-glass transitions are far too apart whereas the difference between the two-successive spin-glass transitions in conventional spin glasses is rather modest (<50K). Thirdly, the two spin-glass transitions are not successive as there is another transition, possibly driven by electromagnons, in between the two spin glass transitions. Any plausible theory of spin-glass transitions in a multiferroic system requires consideration of magnetoelastic and magnetoelectric couplings as well as electromagnons, if present. The mechanism of spin-phonon coupling (electronic or otherwise) needs to be investigated for each multiferroic system since it differs from compound to compound [268]. We hope that our results would stimulate future theoretical work to consider the effect of these couplings and electromagnons in the mean field theories as well as Monte Carlo simulation studies of SG transitions in insulating magnetoelectric multiferroics like $BiFeO_3$.

Chapter 4 Specific heat studies on $BiFeO_3$ and its solid solution with $BaTiO_3$

4.1. Introduction

Ever since its discovery in 1970's, studies on spin-glass (SG) transitions continue to receive tremendous interest in condensed matter and materials physics, till date [24,41,42,123,271–278]. The SG transition in the dilute magnetic systems has been the focus of initial studies in the field leading to development of theoretical tools to capture the essential physics underlying history dependent effects, divergence of third order (χ_3) non-linear susceptibility, critical slowing down of spin dynamics and ergodicity breaking, extremely slow non-Debye relaxation of magnetization on switching off the field [24,41,42,198,262,271], and memory and rejuvenation effects [198,279]. In this context, the role of frustrated interactions and randomness due to disorder has been identified as the key ingredients leading to SG states. A similar approach for concentrated magnetic systems, especially for compositions near the percolation threshold, predict coexistence of long-range ordered (LRO) and SG phases for both Ising and Heisenberg spins [24,42]. As discussed in the previous chapter, the experimental verification of such a coexistence has been quite controversial as similar phenomenon can also occur due to extrinsic factors like phase separation and segregation of impurities [171,238,239,242,243]. As a result, the initial reports on re-entrant SG transition below the LRO FM/AFM transition temperature (T_c/T_N) were taken with disbelief [171,238,239,242,243]. It is generally believed that the intrinsic nature of such a phase coexistence cannot be verified using macroscopic measurements alone and require microscopic probes such as neutron scattering, muon spin rotation (μSR) and Mössbauer technique [172]. In the preceding chapter, we showed using neutron scattering measurements that in disordered $BiFeO_3$, such a phase coexistence occurs due to the

detachment of small longitudinal/transverse components of the $3dFe^{3+}$ spins from the LRO phase which freeze into the SG state. More interestingly, we demonstrated for the first time that SG transitions in such disordered multiferroics is accompanied with magnetoelectric and magnetoelastic couplings leading to change in ferroelectric polarization and unit cell volume, respectively. In this chapter, we use specific heat measurements to provide additional evidence for the coexistence of LRO AFM and SG phases at low temperatures.

Specific heat studies have been very useful in studying the role of electrons, phonons, magnons, Schottky defect, hyperfine splitting etc. to the total specific heat measured experimentally in various types of phase transitions, especially in ferroics and multiferroics [24,42,60–62,280,281]. In the context of SG transition, a characteristic linear dependence of the magnetic contribution to the specific heat (C_m) below the SG freezing temperature T_f was reported experimentally [42,55–57,282,283] and explained theoretically using two level tunnelling model in dilute systems [54,284]. In concentrated systems, there is no unanimity about the temperature dependence of the magnetic contribution to the specific heat below T_f. Different empirical and theoretical models involving linear [55–57], exponential [58–62] and power law [63,64] type dependence of magnetic contribution to the specific heat have been proposed in the literature for the concentrated systems. Although most of these specific heat studies on concentrated systems are on compositions which show coexistence of LRO and SG phases, the low temperature specific heat behaviour has been modelled as if the entire contribution to the magnetic contribution C_m is essentially due to the SG phase only. The present investigation was undertaken to seek the signatures of phase coexistence in the temperature dependence of specific heat of $(Bi_{1-x}Ba_x)(Fe_{1-x}Ti_x)O_3$ [BF-xBT] system where coexistence of the LRO AFM phase with SG phase was established using

macroscopic as well as microscopic probes as described in the preceding chapter (chapter-III). We show here that the low temperature behaviour of the magnetic contribution to the specific heat below the Boson peak (C_p/T^3 versus T plot) temperature cannot be modelled using SG phase exclusively. We also show that the coexistence model explains the low temperature specific heat behaviour quite precisely. We believe that this is the first evidence for the coexistence of LRO and SG phases in a concentrated system using specific heat studies.

4.2. Sample preparation and characterization details:

Polycrystalline samples of $(Bi_{1-x}Ba_x)(Fe_{1-x}Ti_x)O_3$ or BF-xBT with x = 0.0 to 0.60 at a step of 0.10 prepared by standard solid-state route using high purity oxides were used in this study. The details of sample preparation and characterizations are given in the preceding two chapters. The specific heat at constant pressure (C_p) was measured using a physical properties measurement system (PPMS) (Dynacool, Quantum Design). The thermal relaxation of calorimeter is employed to extract the value of specific heat. A small piece of the sintered pellet (~12mg) with smooth surface is attached to the specific heat platform using apiezone N-grease. Before each sample measurement, measurement was carried out on the addenda (platform + apiezone N-grease) also. The apiezone N-grease is used for better thermal conduction between sample and platform of the puck. The absolute value of the specific heat of sample was obtained by subtracting the value of specific heat of addenda from the total measured specific heat.

4.3. Results and discussion:

4.3.1 Different contributions to total specific heat:

It is well stablished that the measured total specific heat of a material at constant pressure has various contributions which can be expressed as [280]:

$$C_{total} = C_{electronic} + C_{phonon} + C_{magnon} + C_{spin\text{-}glass} + C_{hyperfine\ splitting/schottkey}$$

The electronic and phonon contributions are of non-magnetic origin and are given by the Eqs. (4.1) and (4.2) below [280]:

$$C_{electronic} = \gamma T \quad \ldots\ldots\ldots\ldots\ldots\ldots\ldots\ldots\ldots\ldots \quad (4.1)$$

and

$$C_{phonon} = 9N_A k_B \left(\frac{T}{\Theta_D}\right)^3 \int_0^{\Theta_D/T} \frac{x^4 e^x}{(e^x-1)^2} dx \ , \quad \ldots\ldots\ldots\ldots\ldots\ldots (4.2)$$

Here, N_A is the Avogadro number, k_B is the Boltzmann constant, Θ_D the Debye temperature and $x = \hbar\omega/k_BT$, where $\hbar$ is the Planck's constant and ω the phonon frequency.

The magnon contribution to specific heat for antiferromagnetic ordering is given by [280]:

$$C_{magnetic} = \frac{4\pi k_B^4}{(\gamma D\hbar)^3\hbar} T^3 \int_0^{\Theta_m/T} \frac{x^3}{e^x-1} dx \quad \ldots\ldots\ldots\ldots\ldots (4.3)$$

where $x = \hbar\omega/k_BT$, γ is Gyromagnetic ratio and D is proportionality constant.

The hyperfine splitting/Schottky contribution is usually modelled as [281]:

$$C_{hyperfine\ splitting/Schottky} = \frac{R}{T^2} \frac{\sum_i \sum_j (\Delta_i^2 - \Delta_i\Delta_j)\ exp[-(\Delta_i+\Delta_j)/T]}{\sum_i \sum_j exp\ [-(\Delta_i+\Delta_j)/T]} \ldots\ldots (4.4)$$

where $\Delta_i = \varepsilon_i/k_B$ and ε_i is i^{th} energy level, R is universal gas constant (8.314 $Jmol^{-1}\ K^{-1}$). The hyperfine splitting or nuclear contribution may be neglected in our case as it is known to dominate at very low temperatures (i.e. millikelvin range) whereas our data is from 1.8K to 300K. Low temperature measurements in the millikelvin temperature range is needed to precisely determine whether it is present or not in BF-xBT samples. Further, our samples are insulators, so the electronic contribution to specific heat can also be

neglected. So, we shall focus on the phonon, antiferromagnetic magnon and glassy contributions to the specific heat.

The magnetic contribution (C_m) to the specific heat for long-range ordered (LRO) ferromagnetic (FM)/antiferromagnetic (AFM) magnons at low temperatures varies as $C_m \sim T^{d/n}$, where d is the dimensionality and n is the exponent of wave vector k in the magnon dispersion curve. Typically, LRO AFM and LRO FM states give T^3 and $T^{3/2}$ type dependence at low temperatures. Moreover, detailed calculations by Cooper and Mackintosh [58] have shown that some magnetic contributions to specific heat may also follow exponential behaviour at low temperatures $C_m = f(T)\exp(-\Delta E/k_BT)$, where ΔE is an energy gap. This type of exponential behaviour has been attributed to the gapped magnons which can arise due to D-M interaction and single-ion anisotropies [58] and have been postulated in spin glasses also [59–62].

As said earlier, for dilute spin-glass systems, a characteristic linear dependence of the magnetic contribution to the specific heat below the SG freezing temperature T_f has been observed experimentally and explained theoretically using two level tunnelling model [54]. For concentrated systems, different empirical and theoretical models of magnetic contribution to the specific heat have been proposed in the literature. (1) linear temperature dependence of C_m below T_f [55–57], (2) C_m modelled using exponential functions ($C_m = aT^{1/2}\exp(-\Delta E/k_BT)$, $C_m = aT\exp(-\Delta E/k_BT)$, $C_m = aT^{-2}\exp(-\Delta E/k_BT)$) [58–62] and (3) C_m modelled by a power law $C_m \sim T^{\alpha}$, where α = 1.2 to 2 at low temperatures [63,64]. Power law has been mostly used for geometrically frustrated AFM systems.

Before proceeding to model the low temperature behaviour of magnetic contribution (C_m) to the total specific heat (C_p) of BF-xBT for spin-glass and LRO AFM contributions, it is worth summarizing the status of the modelling of C_m behaviour at low

temperatures in dilute and concentrated spin-glass systems. In the canonical (dilute) spin-glass systems, like CuMn, AuFe, the magnetic contribution to specific heat shows linear dependence at low temperature and a broad maximum above the spin glass freezing temperature T_f at nearly 1.5 times the freezing temperature ($1.5T_f$). No anomaly is observed in the vicinity of T_f [41]. The numerical calculations by Walker and Walstedt [285] have also confirmed this linear dependence of C_m in dilute (metallic) spin-glass systems [282]. The concentrated cluster spin glass systems, like $Eu_xSr_{1-x}S$ (x = 0.40, 0.54), display smeared rounded peak in C_m around T ~$2T_f$, and the decrease in C_m is faster than the canonical (dilute) spin glass systems. Towards higher temperature side, the magnetic specific heat data of CuMn roughly follows 1/T dependence as expected on the basic of scaling theories [282] while in cluster spin-glass systems, the thermal disorder rapidly destroys the short-range magnetic ordering and thus leads to faster return of the C_m value to zero [55,56]. For $Eu_xSr_{1-x}S$ with x = 0.40, the lattice contribution is less than 0.3 % of the measured specific heat below 10K and hence negligible [56]. These compositions are reported to display the characteristic spin-glass type linear variation of C_m with temperature below T_f, a broad maximum well above T_f and no singularity at T_f. However, at very low temperatures (below 0.45K) a distinct deviation from this linear behaviour is observed and the data is adequately represented by $C_m = AT + B/T^2$ type function [55,56]. The first term is the well-known spin-glass term and the second term B/T^2 is due to the Schottky anomaly or hyperfine splitting of the ^{151}Eu and ^{153}Eu nuclei [55,56]. However, in the presence of field (1T), the low temperature spin-glass phase is suppressed and induces a ferromagnetic ordering [55]. For x= 0.54, a deviation of spin-glass specific heat from strictly linear behaviour is observed for $T<T_f$. A better fit has been reported by adding a T^2 term: $C_m = AT + B/T^2 + CT^2$ [55,56]. Such a T^2 term has been frequently used to describe the small deviation from the linear dependence [55,56].

The most convincing interpretation of the C_m at low temperatures in $Eu_xSr_{1-x}As_3$ with x= 0.24 and x= 0.30, showing freezing of the transverse and longitudinal components at successively lower temperatures, like BF-xBT discussed in the previous chapter, has been found in terms of an exponential function C_m= aTexp(-ΔE/k_BT) corresponding to a gapped magnon [58–62].

4.3.2 Low temperature specific heat behaviour of BF-xBT:

After setting the necessary background, we now proceed to discuss our experimental observations. In order to probe the nature of ground state and magnetic transitions in the multiferroic BF-xBT system with x = 0.0 to 0.60, we carried out specific heat measurements under zero-magnetic field in the temperature range 1.8-300 K and the results are shown in Fig. 4.1. We first examine the data qualitatively towards the higher temperature side. As per Dulong-Petit law, the value of specific heat at constant volume (C_v) having n atoms per formula unit should approach asymptotically the value 3nR J/mol-K, where R is the gas constant. In our case n = 5 and therefore the maximum value of C_v is ~124.7 J/mol-K. Further, the specific heat at constant pressure (C_p) is always higher than the specific heat at constant volume which should approach 3nR J/mol-K well above the Debye temperature (Θ_D). Our C_p data shown in Fig. 4.1 for x = 0, 0.10, and 0.20 are consistent with the expected behaviour. It is also in excellent agreement with the reported values measured experimentally and predicted theoretically for pure (x =0) $BiFeO_3$ [286–289].

Towards understanding the phase transition and true ground state of the multiferroic system BF-xBT using specific heat measurements, there are challenges in separating out the phonon contributions from the total specific heat. There is no standard protocol to subtract the phonon contributions to obtain the magnetic specific heat. For

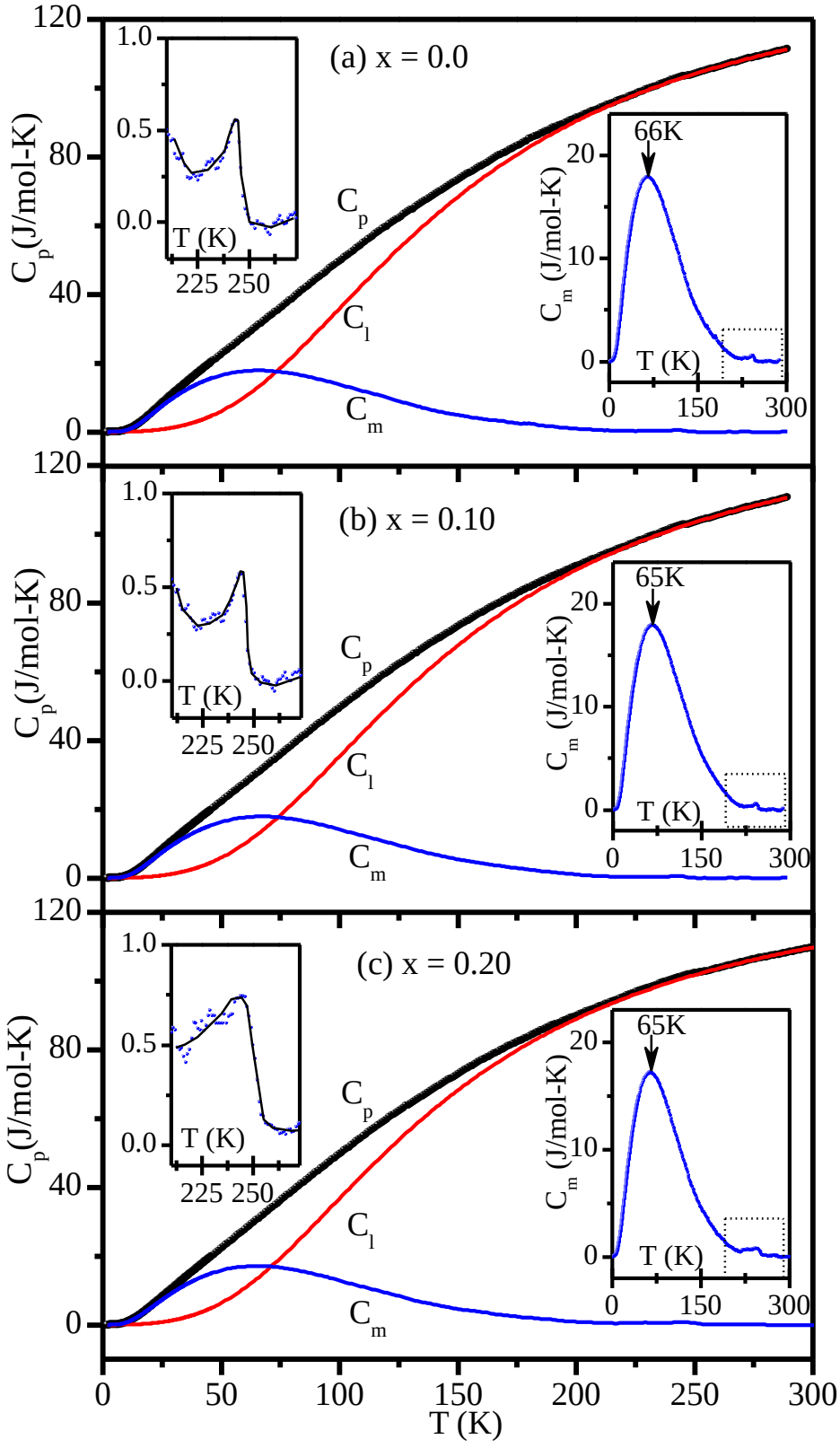

Figure 4.1: Temperature dependence of total specific heat (C_p), phonon contribution (C_l) and magnetic contribution (C_m) of BF-xBT for (a) x = 0 (b) x =0.10 and (c) x =0.20.

BF-xBT system, there is also no non-magnetic analogue which has identical crystal structure and whose specific heat can be used to subtract the phonon contribution for obtaining the magnetic contribution as has been done in some other systems. Further, this subtraction becomes a nearly impossible task with antiferromagnetic long-range ordering as both the phonon and magnon contributions have the same T^3 dependence at low temperatures. To the best of our knowledge, no specific heat study has been performed on BF-xBT system, except for x = 0 [286–289], in the literature. Further, no attempt has been made to separate out the magnetic contribution. In order to subtract the phonon contribution, we used the Debye temperature (Θ_D), determined from the thermal expansion data discussed in chapter III, as the initial input value for obtaining the most plausible value of Θ_D through successive refinements until a self-consistent value of Θ_D was obtained such that it explains the observed value of specific heat at high temperatures (260 to 295K range) and also gives T^3 dependence at low temperatures as per Debye theory of specific heat. After the determination of the Θ_D, we calculated the phonon contribution (C_l) from 1.8K to 300K using the Debye expression given by Eq. (4.2). This is shown in Fig. 4.1 for BF, BF-0.10BT and BF-0.20BT samples along with the total specific heat. It can be seen from this figure that the calculated phonon contribution using Eq. (4.2) is in excellent agreement with the measured specific heat data towards higher temperature side. The best fit is obtained for Θ_D = (609±10)K, (607±10)K, (585±10)K for BF, BF-0.10BT and BF-0.20BT samples. The best fit value for $BiFeO_3$ (Θ_D =609±10) is in close agreement with the reported value (577K) by Park et al. [82], determined from the thermal expansion behaviour of the XRD data, and also the predicted value by the density functional theory (DFT) calculations (Θ_D =554K) [287]. The value obtained from thermal expansion data of BF-0.20BT in chapter III also falls in a similar range.

To obtain the magnetic contribution to specific heat C_m, we subtracted the calculated phonon/lattice contribution (C_l) from total specific heat (C_P). The magnetic contribution to the specific heat (C_m) of BF, BF-0.10BT and BF-0.20BT so obtained is also shown in Fig 4.1. Two anomalies around 250K and 66K are clearly discernible in the magnetic contribution to the specific heat which we attribute to the two spin-glass phases SG1 and SG2. The peak around 66K in the C_m vs T plot is quite diffuse and rules out long-range magnetic ordering transition [42]. The absence of sharp peaks in the C_m is a well-known characteristic feature of the existence of disordered spin configurations [55,56,59].

Now we proceed to interpret the results of BF-xBT in the context of spin-glass phase in coexistence with the LRO AFM phase at low temperatures. It is well known that at very low temperatures, typically in the range 2-30K, several crystalline and glassy materials exhibit larger specific heat than predicted by Debye model. This excess specific heat manifests itself as a peak in the C_p/T^3 versus T plot and is generally attributed to local low energy excitation modes observed in Raman spectra and inelastic neutron scattering [272,278,290–293]. This peak is called as Boson peak and has been observed in several glasses [272,278,290–293], both magnetic and non-magnetic. The strong Boson peak is observed in strong glasses and weak Boson peak occurs in fragile glasses [292]. Boson peak has also been attributed to Van Hove singularities where the vibrational density of states crosses the Debye density of states, leading to a flattening of the phonon dispersion curve [294]. As per Debye T^3 law, the lattice contribution to C_p/T^3 versus T plot should be constant at low temperatures. Therefore, the C_p/T^3 vs T plot shown in Figs. 4.2 (a), (b), (c) and Fig. 4.3(b) for BF-xBT samples can be used to determine whether the Boson peak results from magnetic contributions or some other contributions present in the samples. The C_p/T^3 vs T plot shown in Figs. 4.2(a), (b), (c) and Figs. 4.3 (b), reveals a

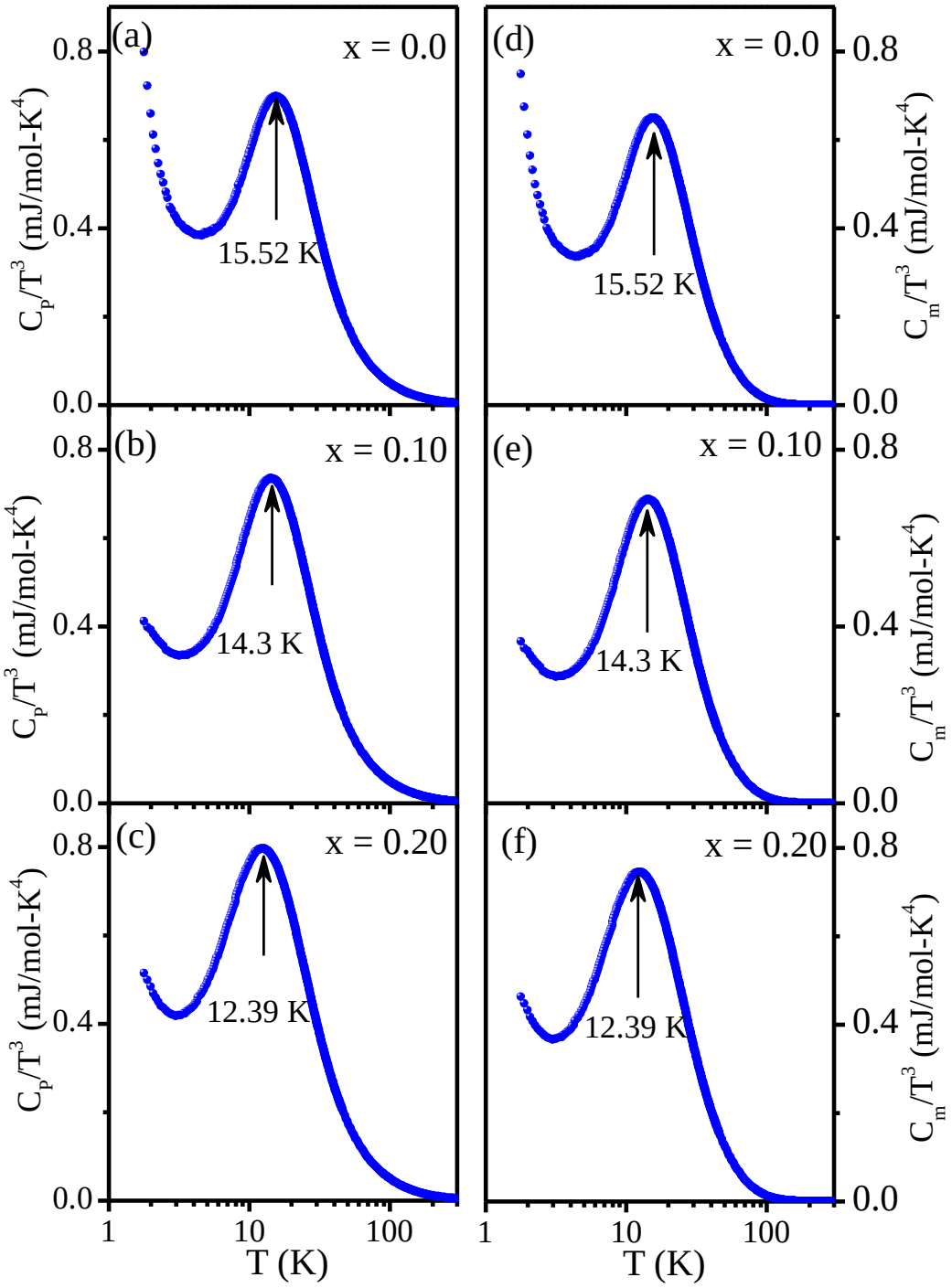

Figure 4.2: Left panel (a-c) shows the temperature evolution of Boson peak in the C_p/T^3 versus T plot of BF-xBT as a function of composition (x). Right panel (d-f) depicts the temperature variation of magnetic Boson peak in the C_m/T^3 versus T plot of BF-xBT as a function of x.

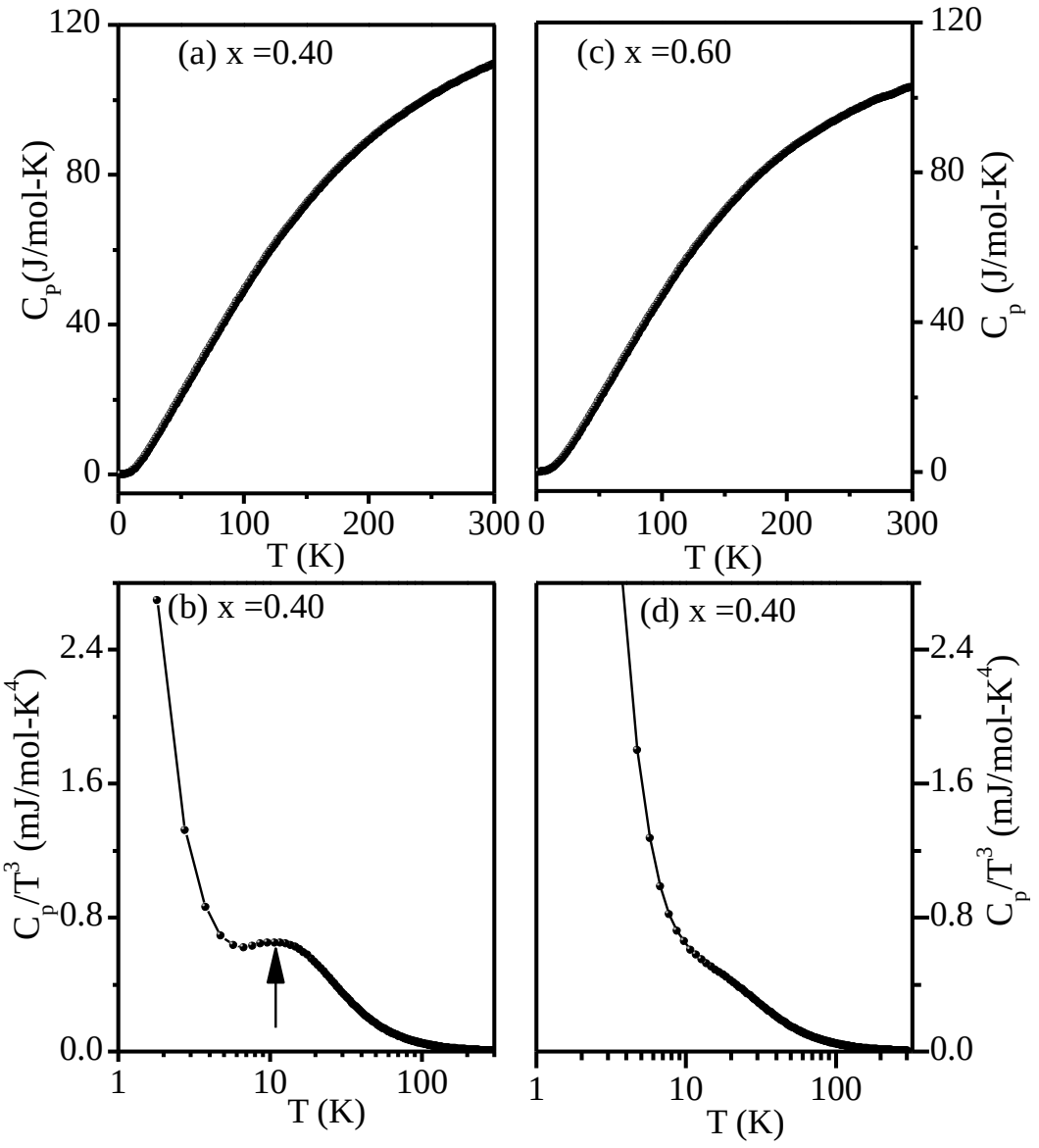

Figure 4.3: Left panel (a) and (b) shows the temperature dependence of total specific heat (C_p) and Boson peak of BF-xBT for x 0.40. Right panel (c) and (d) shows the temperature dependence of total specific heat (C_p) and Boson peak for x = 0.60.

Boson peak around 15.52K, 14.3K, 12.39, and 9.64K for x= 0.0, 0.10, 0.20 and 0.40, respectively. For x = 0.60, the signature of Boson peak is too weak to be compared with other BF-xBT composition (see Fig. 4.3(d)). For this composition, we do not observe spin glass transition at low temperatures. Thus the existence of Boson peak in BF-xBT is clearly linked with the spin glass transition at low temperatures. It is interesting to note that even after subtracting the phonon contribution,

the plot of C_m/T^3 vs T continues to show the Boson peak at the same peak temperature (see Figs. 4.2 (d), (e), and (f)). This suggests that this peak is predominantly of magnetic origin. The observation of Boson peak in C_m / T^3 vs T plot of BF-xBT is close to the gapped magnon mode observed at 1.1 meV by inelastic neutron scattering studies on $BiFeO_3$ [237]. Boson peak has been reported in several spin glass systems below the spin-glass transition temperature [272,278,294], as is the case with BF-xBT compositions. It is important to note that in several spin-glass systems, the specific heat starts increasing again well below the Boson peak temperature. We have also observed such an increasing trend for BF-xBT as can be seen from Fig. 4.2. Interestingly, there is a small but systematic composition dependence of the Boson peak temperature and it follows $T_{Boson\ peak} \sim(x-x_c)^n$ type dependence with an exponent n= 0.47±0.02 for x_c= 0.55±0.01 (see Fig. 4.4). The exponent being close to n = ½ is reminiscent of a quantum phase transition and the possibility of the existence of a quantum critical point corresponding to the percolation threshold composition x_c= 0.55±0.01 cannot be ruled out. But this aspect requires further investigation on several compositions close to x_c. Above x_c, neither LRO AFM nor spin-glass transitions are observed in BF-xBT system as can be seen from the phase diagram given in chapter III. We note that the exponent for the lower temperature spin-glass transition temperature is found to be n=0.08 while the exponent for Boson peak corresponds to n=0.47±0.02. The reason for this difference is not obvious to us but may be due to the fact that T_f used in the phase diagram of chapter III was measured at 497.3 Hz. For spin-glasses this temperature is frequency dependent and $T_f(\omega)$ in the limit of ω tending towards zero is the real spin glass transition temperature T_{SG} below which the ergodicity symmetry is broken. The Boson peak temperature, on the otherhand, is not affected by frequency and may therefore be more reliable estimate for a characteristic temperature associated with the spin glass phase.

The temperature dependence of the magnetic contribution to specific heat (C_m vs T plot) for BF-xBT shown in the insets of Fig. 4.1 for x = 0, 0.10, and 0.20 show features similar to those observed in concentrated insulating spin glasses. In case of BF-xBT, the broad peak in C_m occurs at ~65K which corresponds to ~$2T_f$. The peak temperature 65K for C_m vs T plot corresponds to an energy gap of 6 meV reported by Lui et al. for $BiFeO_3$ [286]. The magnetic contribution starts decreasing above 65K but shows a small increase around 225K corresponding to the second spin-glass transition discussed in Chapter III. The small peak around 240K is relatively sharp in $BiFeO_3$ and BF-0.10BT but becomes diffuse for BF-0.20BT, as can be seen from the insets of Fig. 4.1, which depict this peak on a magnified scale. Because of the dominant contribution of phonons as compared to the magnons at high temperatures, no meaningful analysis could be

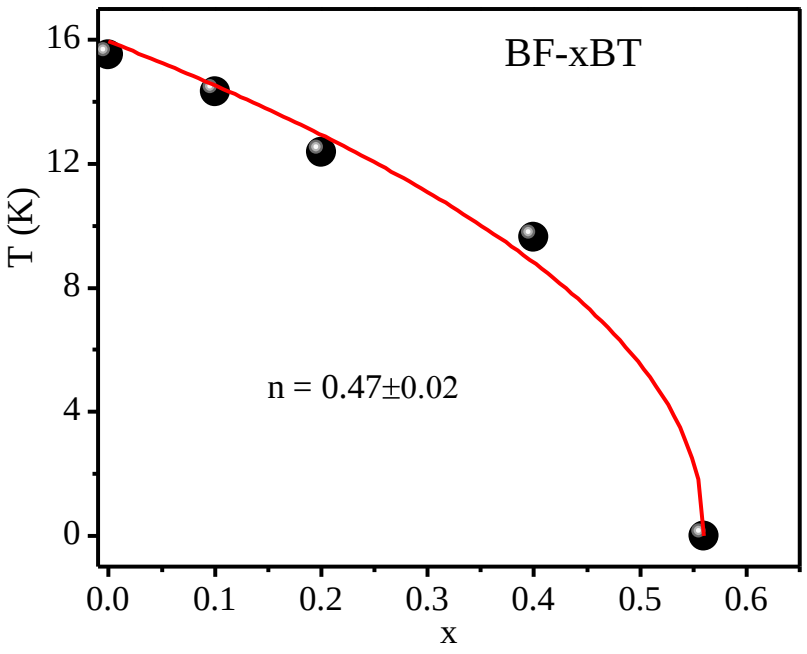

Figure 4.4: Variation of Boson peak temperature with composition. It follows $(x-x_c)^{1/2}$ type dependence suggesting possibility of a quantum critical point at $x_c \approx 0.55\pm0.01$.

carried out for this anomaly except for noting that it has become diffuse for BF-0.20BT. On decreasing the temperature, the magnetic contribution starts increasing below 225K and peaks around 65K. We believe that this rapid increase in C_m is due to multimagnon contributions as has been noted in the context of pure $BiFeO_3$ also [286]. Raman scattering studies have revealed presence of magnon modes at 18 cm^{-1} (25.8K), 22 cm^{-1} (31.5K), 28cm^{-1} (~40K) and 32cm^{-1} (~46K) [111]. Further, inelastic neutron scattering studies have revealed two gapped magnons corresponding to 1.1±0.2 meV (~13K) and 2.5±0.2 meV (~29K) of which the latter is quite broad while the former is sharper [237]. Since there is a coexistence of LRO and SG phases in the ground state of BF-xBT, as discussed in chapter III, we have attempted to model the low temperature specific heat behaviour using both the contributions taking first BF-0.20BT composition. Figs. 4.5, 4.6 and 4.7 depict the magnetic part of specific heat in the temperature range 1.8-40K and the

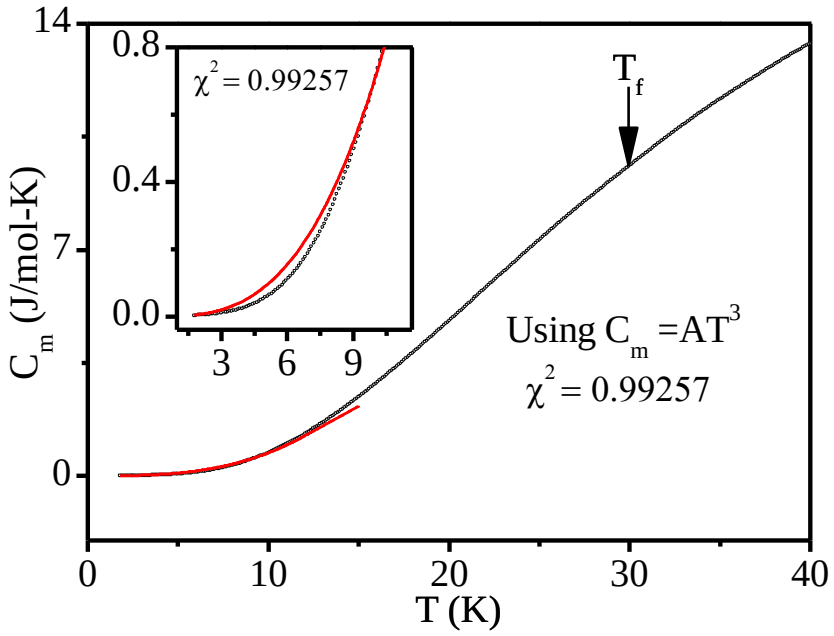

Figure 4.5: Temperature dependence of magnetic contribution to specific heat for BF-0.20BT in the range 1.8-40K. Solid line is the fit using AT^3-type dependence of C_m. Inset depicts the fit on a magnified scale.

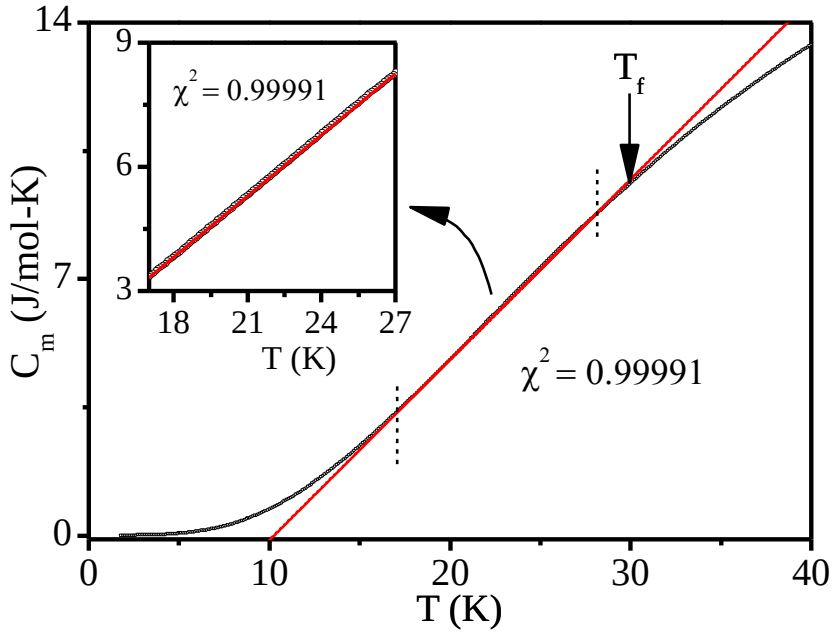

Figure 4.6: Temperature dependence of magnetic contribution to specific heat for BF-0.20BT in the range 1.8-40K. Solid line is the fit using C_m =AT-type dependence. Inset depicts the fit on a magnified scale.

fits using various models discussed in the previous section. It is found that the C_m cannot be modelled satisfactorily using LRO AFM magnon term (T^3) alone. This can be seen from the fit shown in the inset of Fig. 4.5. This clearly suggests another contribution which we believe is of glassy origin. This is also corroborated by the fact that at low temperatures C_m/T^3 vs T plot is not horizontal as expected for a typical AFM system (see Fig. 4.2(f)). It is found (not shown in the figure) that the fit between observed C_m and calculated C_m using T^3 dependence in the 5 to 10K range becomes worse with increasing BT contribution. To model the spin glass contribution, we first considered the most widely used linear temperature dependence of C_m as reported in the dilute systems [282,283] and also in some concentrated systems [56,59,295]. In this context, we note that C_m indeed follows linear dependence below T_f in the temperature range ~17K to ~28K whose extrapolation cuts the temperature axis at ~10K, as shown in Fig. 4.6. However, this model cannot explain the specific heat behaviour below 17K. The

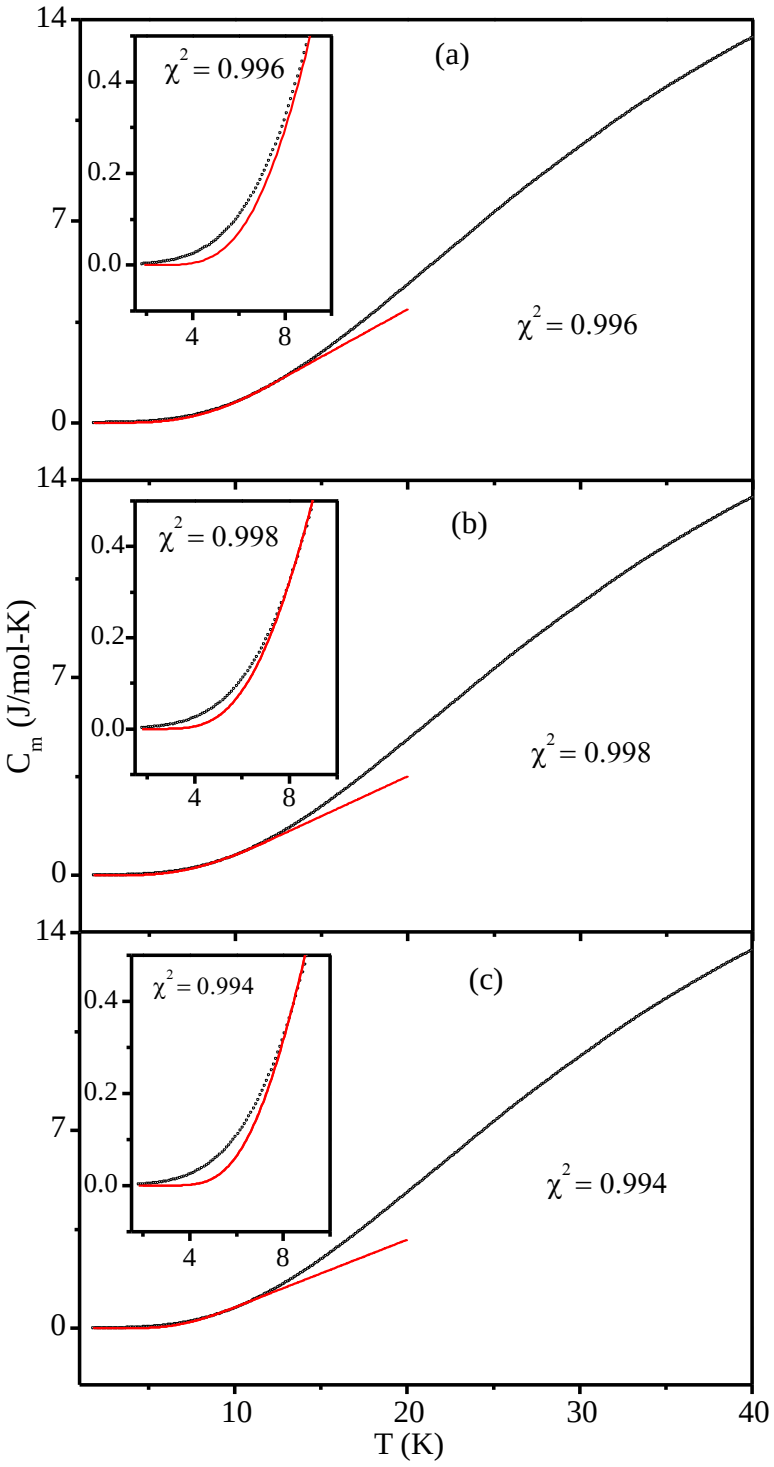

Figure 4.7: Temperature variation of magnetic contribution (C_m) to specific heat for BF-0.20BT in the range 1.8 to 40K. Solid line is the fit corresponding to different model (a) $C_m = aT^{1/2}\exp(-\Delta E/k_BT)$, (b) $C_m = aT\exp(-\Delta E/k_BT)$ (c) $C_m = aT^{-2}\exp(-\Delta E/k_BT)$ below the Boson peak temperature.

decrease in the C_m with temperature below 17K suggests exponential decay. Accordingly, we considered the following models used in the literature (i) $C_m = aT^{1/2}exp(-\Delta E/k_BT)$ [61], (ii) $C_m = aTexp(-\Delta E/k_BT)$ [58,59,61], (iii) $C_m = aT^{-2}exp(-\Delta E/k_BT)$ [62], and the corresponding fits for BF-0.20BT below the Boson peak temperature (i.e., 1.8 to 12K range) are shown in Figs. 4.7 (a), (b) and (c), respectively. It is evident from the magnified views given in the insets of Fig. 4.7 that none of these models can provide satisfactory fit.

Since the low temperature specific heat behaviour in the 1.8 to 12K range cannot be modelled either by LRO AFM gapless magnon mode ($C_m \sim T^3$) or by gapped magnon modes ($C_m = f(T)exp(-\Delta E/k_BT)$), we considered coexistence of LRO AFM and spin-glass phases. We tried all possible combinations, but the best fit was obtained for the following functional dependence $C_m = AT^3 + BTexp(-\Delta E/k_BT)$. The corresponding fit shown in Fig. 4.8(a) (see the inset for the quality of the fit) is excellent. For comparison, we also give a fit corresponding to $C_m = AT^3 + BT$ type dependence in Fig. 4.8(b). This fit is rather poor as can be seen from the inset of Fig.4.8 (b) as compared to the fit shown in the inset of Fig 4.8(a). The fits for C_m versus T plots of BF and BF-0.10BT using $C_m = AT^3 + BT$ $exp((-\Delta E/k_BT)$ type dependence below the Boson peak temperature are shown in Fig. 4.9. The excellent quality of the fits can be seen from the insets of Fig. 4.9 where a magnified view is plotted. To summaries, the best and most reliable fit for the temperature dependence of the magnetic contribution to the specific heat of BF-xBT in the 1.8 to 12K range was obtained for $C_m = AT^3 + BTexp(-\Delta E/k_BT)$ type functional dependence, where the first term is attributed to the LRO AFM magnons (gapless) and the second term is due to gapped magnons (non-propagating) of the SG phase [237]. This functional form gives gap energy of 3.1, 2.69, and 2.3 meV for x = 0, 0.10 and 0.20, respectively, The gap energy is close to the experimentally observed broad peak at ~2.5 ±0.2 meV (~29K) in

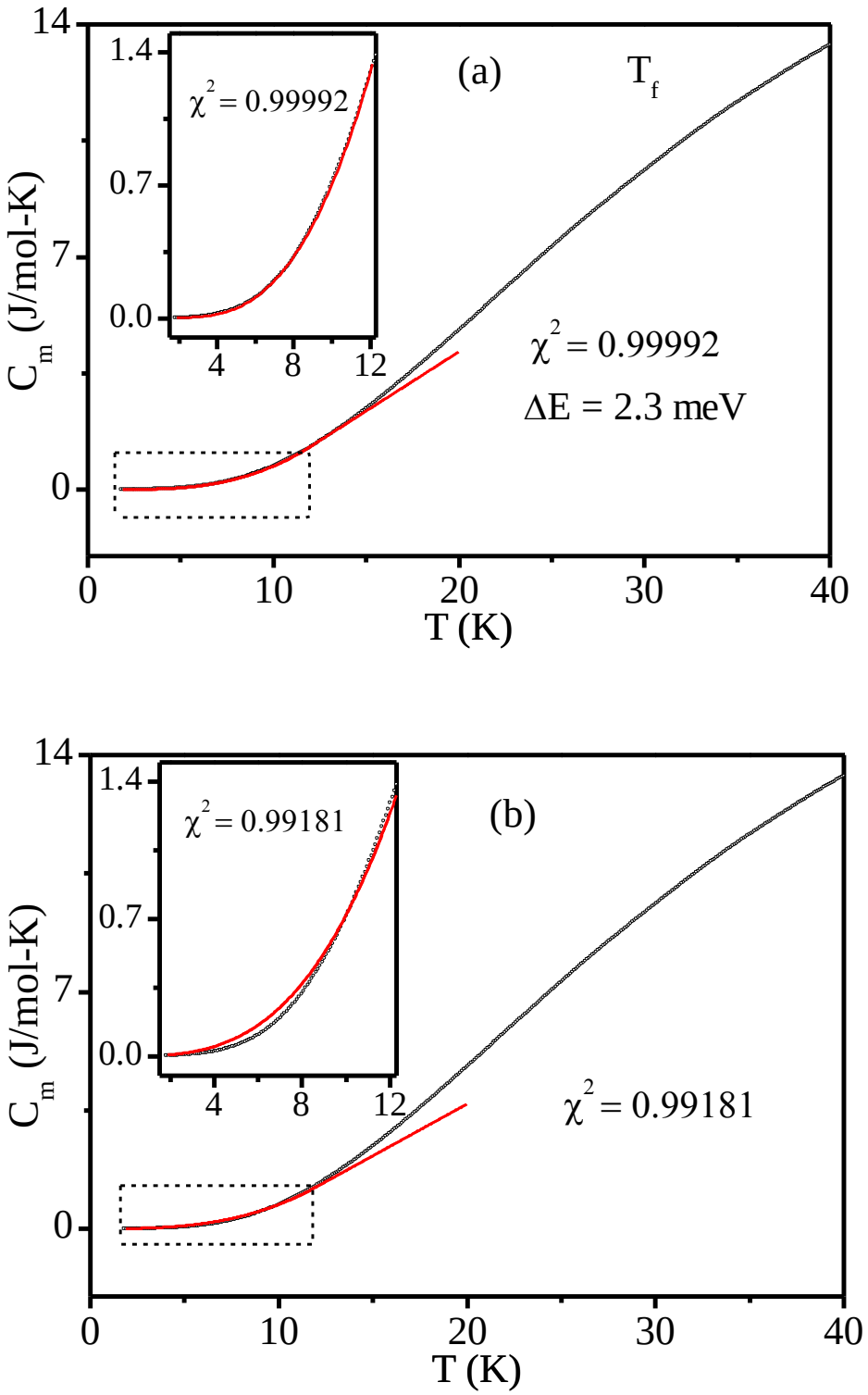

Figure 4.8: The fit to C_m versus T plot of BF-0.20BT using (a) $C_m = AT^3 + BTexp(-\Delta E/k_BT)$ and (b) $C_m = AT^3+BT$ type function dependence. The quality of the fits can be seen from the insets where a magnified view is plotted. In contrast, $C_m = AT^3 + BT$ type dependence gives poor fit as can be seen from the inset of bottom panel (b) given on the left-hand corner. The goodness of fit χ^2 is better for the $AT^3 + BTexp(-\Delta E/k_BT)$ dependence.

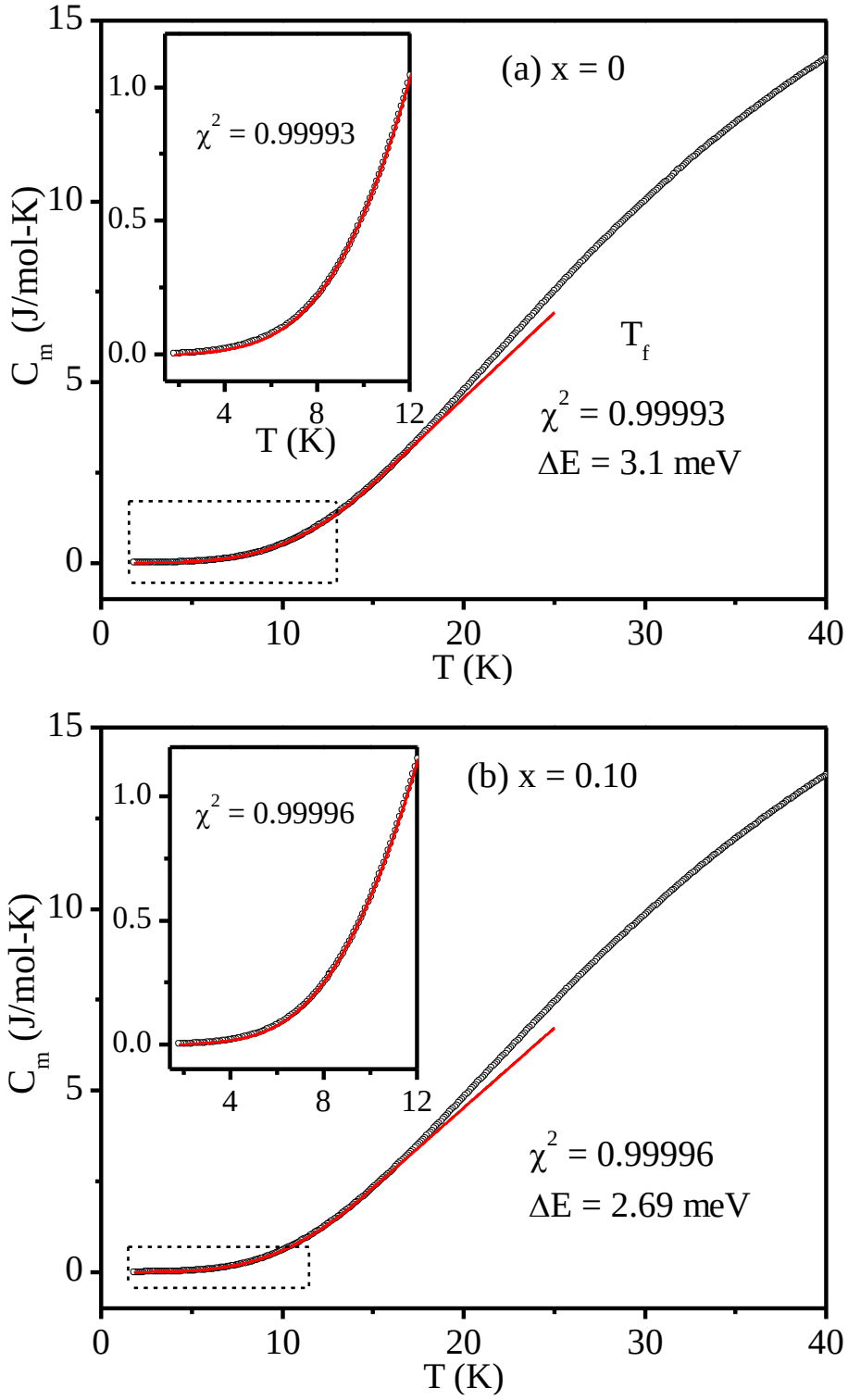

Figure 4.9: The fit to C_m vs T plot of BF-xBT using $C_m = AT^3 + BTexp(-\Delta E/k_BT)$ type function for (a) x =0, (b) x = 0.10. The quality of the fits can be seen in the insets where a magnified view is plotted.

inelastic neutron scattering studies on BF (x=0) [237] due to gapped magnons. We believe that many non-propagating gapped magnons contribute to the specific heat due to the coexisting spin glass phase because of which the inelastic peak shows an unusually large broadening. The experimental measured gap energy in specific heat and inelastic neutron scattering corresponds to some average value for several non-propagating magnons.

4.4. Conclusions:

We have investigated the temperature dependence of specific heat (C_p) in the temperature range 1.8 to 300K. Both the total specific heat and the magnetic contribution (C_m) of BF-xBT, obtained after subtracting phonon contributions, show the presence of a Boson peak in the C_p/T^3 or C_m/T^3 vs T plots whose peak temperature various as $T_{Boson} \sim (x - x_c)^{1/2}$ suggesting the possibility of a quantum critical point and $x_c \sim 0.55$. The magnetic specific heat (C_m) below the Boson peak temperature cannot be explained without considering coexistence of spin glass and LRO AFM phases. It is shown than C_m in the temperature range 1.8 to 12 K is best described using a functional dependence $C_m = AT^3 + BT\exp(-\Delta E/k_BT)$ where the AT^3 term is due to the long-range ordered (LRO) antiferromagnetic (AFM) phase and the exponential term is due to gapped magnons in the spin-glass (SG) phase. We believe that this is the first evidence for the coexistence of LRO and SG phases in concentrated systems using specific heat studies.

Chapter 5 Cluster spin-glass transition in $Ca(Fe_{1/2}Nb_{1/2})O_3$

5.1. Introduction

As discussed in chapter I, complex perovskites with a general formula $A(B'B'')O_3$, where A is an alkaline metal ion Pb^{2+}, Ba^{2+}, Sr^{2+}, Ca^{2+}, B' is a transition metal ion Fe^{3+}, Ni^{2+}, Co^{2+} with partially filled 3d orbital and B'' is a ferro-active ion like Nb^{5+}, Ta^{5+}, W^{6+} with $4d^0/5d^0$ configuration were synthesized by Russian scientist to exhibit magnetoelectric multiferroic characteristics [147,183,184]. These compounds have both site as well as charge disorder at the B-site occupied by B' and B'' cations randomly. Despite the presence of magnetic and ferro-active ions at the B-site in 1:1 proportion, only the Pb^{2+} based compounds, like $Pb(Fe_{1/2}Nb_{1/2})O_3$ (PFN) [171,172], $Pb(Fe_{1/2}Ta_{1/2})O_3$ (PFT) [174], and $Pb(Fe_{2/3}W_{1/3})O_3$ (PFW) [191] exhibit long range ordered (LRO) antiferromagnetic (AFM) and ferroelectric (FE)/relaxor ferroelectric (RFE) transitions at T_N~150K, 150-180K and 350K and T_c at 385K, 240K and 150K, respectively. The Pb^{2+} free compounds do not exhibit either LRO AFM or FE/RFE states [176–178]. However, all these complex perovskites exhibit a spin glass (SG) like transition at low temperature. The SG freezing temperature T_f for Pb^{2+} based and Pb^{2+} free compounds are around 10 and 25K, respectively [171,172,176–178]. While the SG transition has been properly investigated using macroscopic (DC and AC susceptibilities (χ_{DC}, $\chi(\omega, T)$) and microscopic (neutron, Mössbauer, μSR) and local probes like (NMR, EPR, EXAFS and PDF) techniques only in Pb^{2+} based compounds [171,172], especially PFN, the so-called evidence for SG transition in Pb^{2+} free complex perovskites has been limited to the observation of irreversibility of the field cooled (FC) and zero-field cooled (ZFC) magnetization M(T). Since such an irreversibility occurs in superparamagnetic systems [198] also, there is a need to test the existence of SG transition using other criterion also discussed in chapter III in relation to disordered $BiFeO_3$ system.

Despite the extensive literature, the origin of the SG phase in the well-known multiferroic PFN is still controversial as discussed in chapter I. Two different models have been proposed in the literature [171,172]. According to one of these models based on macroscopic measurements, the LRO AFM phase of PFN results from the infinite percolative clusters of Fe^{3+} spins while the glassy phase is a consequence of the freezing of the finite size isolated clusters with uncompensated Fe^{3+} spin [171]. This model implies that the SG and LRO AFM phases occur on two separate sublattices. In the second model, which is based on microscopic measurements (neutron and Mössbauer techniques), on the other hand, the SG phase is argued to result from the LRO AFM sub-lattice system itself due to freezing of the transverse component of the spins in a glassy manner [172]. Since the controversy in this compound is due to the complications introduced by the coexistence of SG and LRO AFM phases, the Pb-free compounds can provide an ideal platform to resolve this controversy as they do not exhibit any LRO AFM transition. Taking this objective in mind, we present in this chapter results of a comprehensive study of the spin-glass state of $Ca(Fe_{1/2}Nb_{1/2})O_3$ using both macroscopic and microscopic measurements.

5.2. Sample preparation:

Polycrystalline $Ca(Fe_{1/2}Nb_{1/2})O_3$ (CFN) was synthesized by standard solid-state route using high purity carbonate ($CaCO_3$) and oxides (Fe_2O_3, Nb_2O_5) supplied by Sigma Aldrich. The stoichiometric powders were first mixed in an agate mortar and pestle for 2 hours. The mixture was then ball milled (Retsch GmbH, Germany) for 6 hours in the presence of acetone as the mixing media in a zirconia jar using zirconia balls. After evaporation of the acetone, the mixed powder was calcined at 1423 K for 10 hours in an open alumina crucible. The calcined powder was crushed into fine powder and again ball milled for 4 hours, dried and then pressed into pellets (diameter 12mm, thickness ~1mm)

using cylindrical steel die of 12mm diameter and a uniaxial hydraulic press at an optimized load of 70 kN. A 2% polyvinyl alcohol (PVA) aqueous solution was used as a binder for making the green pellets. After binder burn-off at 773 K for 10 hours, sintering of the green pellets was carried out at 1523 K for 3 hours in open air. Powders obtained after crushing the sintered pellets were annealed at 773K for 10 hours to remove any strains developed during crushing. The annealed powders were used in all the measurements.

5.3. Characterizations:

Microstructure of the $Ca(Fe_{1/2}Nb_{1/2})O_3$ pellet was obtained using a Carl-Zeiss Scanning Electron Microscope (SEM), model no. EVO 18. The chemical compositions were checked by Energy Dispersive X-ray spectroscopy (EDX) attachment (Oxford, model no. 51-ADD0048) in the above-mentioned SEM and Electron Probe Micro Analyzer (EPMA) using CAMECA SXFive instrument. The sintered pellet was coated with conducting gold using sputter coater (Royal life Sciences, model no. DSR1) under vacuum before taking the SEM images. For EPMA analysis, the sintered pellet was coated with 20 nm thin layer of carbon using LEICA-EM ACE200 instrument. Natural silicate mineral andardite as internal standard used to verify positions of crystals (SP1-PET, SP2-LiF and SP4-LPC0) with respect to corresponding wavelenght dispersive spectrometers in CAMECA SX-Five instrument. The following X-ray lines were used in the analyses: O-$K\alpha$, Ca-$K\alpha$, Fe-$K\alpha$, and Nb-$L\alpha$. Routine calibration, acquisition, quantification and data processing were carried out using SxSAB version 6.1 and SX-Results softwares of CAMECA.

X-ray powder diffraction (XRD) measurement was carried out using an 18-kW Cu rotating anode powder diffractometer (Rigaku, model no. RINT 2500/PC series) operating in the Bragg-Brentano geometry and fitted with a curved crystal

monochromator in the diffraction beam. The data were collected in the 2θ range 20 to 120° at a step of 0.02 degrees.

High-resolution synchrotron x-ray powder diffraction (SXRD) data at room temperature was also collected at P02.1 beamline of PETRA III, Hamburg, Germany, at a wavelength of 0.2079Å (~60keV) to determine the phase purity and crystal structure. The powder sample was filled in a Kapton capillary of 0.6mm diameter and exposed to the incident beam of cross section of 0.5 mm × 0.5 mm for 10 s. Two-dimensional (2D) XRD pattern was recorded using a Perkin Elmer 1621 Detector (2048 pixels × 2048 pixels, 200μm × 200μm pixel size). The sample to detector distance was set to 1310 mm. The standard LaB_6 was used to calibrate the sample to detector distance. The 2D XRD pattern was integrated using the FIT2D software.

High-resolution neutron powder diffraction (NPD) patterns were collected in the temperature range 5-300K using structure powder diffractometer SPODI at FRM-II research reactor in Garching, Germany . The incident neutron wavelength was 1.5482Å as obtained from germanium (551) reflection of vertically focussed monochromator at a take-off angle of 155°. Approximately 12g powder sample was kept in a cylindrical vanadium (V) can of diameter 4mm which was cooled to different temperatures using close cycle helium refrigerator. The data were recorded at a step of 0.05° in the 2θ range from 5 to 150°. The nuclear structure was refined by Rietveld technique using software package “FULLPROF” [253].

DC magnetization M (T, H) and AC susceptibility (χ (ω, T)) measurements were carried out on a superconducting quantum interference device (SQUID) based magnetometer (Quantum Design, MPMS-3).

5.4. Results and discussion:

5.4.1 Microstructure and chemical composition analysis:

The scanning electron microscopic image of the microstructure of CFN is shown in Fig. 5.1(a). The average grain size calculated by linear intercept method is found to be approximately 1.4 μm. The EDX spectra of CFN are shown on the right panel (see Fig. 5.1(b)). The chemical composition of the sample was determined through a quantitative analysis of the EDX spectra. The average composition of the ceramic sample was confirmed through EPMA analysis also as its results are more accurate. The results of EDX and EPMA are compared in Table 5.1 which confirms that the composition of the samples corresponds to the nominal composition within the standard deviation.

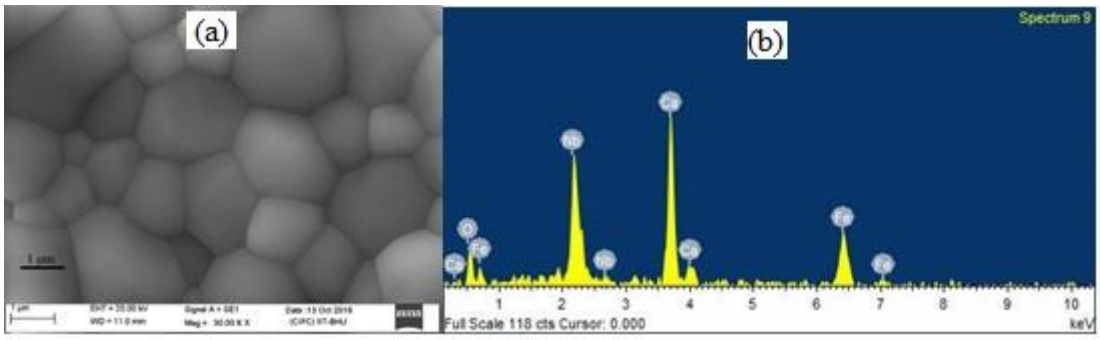

Figure 5.1: Scanning electron micrograph and EDX spectra of $Ca(Fe_{1/2}Nb_{1/2})O_3$.

Table 5.1: Quantification of $Ca(Fe_{1/2}Nb_{1/2})O_3$ by EDX and EPMA analysis

Average chemical composition in weight %			
Element	Expected	Observed by	
		EDX	EPMA
Ca	24.7	24.1 ± 1.0	23.8 ± 0.5
Fe	17.2	17.3 ± 1.0	16.7 ± 0.2
Nb	28.6	29.8 ± 0.5	28.9 ± 0.8
O	29.5	28.7 ± 0.8	28.3 ± 0.5

5.4.2 Phase purity and crystal structure:

The x-ray powder diffraction (XRD) pattern of $Ca(Fe_{1/2}Nb_{1/2})O_3$ (CFN) along with those of calcium carbonate ($CaCO_3$), iron oxide (Fe_2O_3) and niobium oxide (Nb_2O_5) are shown in Fig. 5.2. All the peaks in the diffraction patterns of CFN could be indexed with an orthorhombic unit cell. The absence of the strongest peaks of the $CaCO_3$, Fe_2O_3 and Nb_2O_5 in the CFN pattern confirms that the powder does not contains any impurity phases. The very small peaks, marked with arrows in the diffraction pattern of CFN, are not due to any unreacted ingradients or some unwanted phases but are the superlattice reflection arising from unit cell doubling. The phase purity was further confirmed by the high-resolution synchrotron x-ray powder diffraction (SXRD) data shown in Fig. 5.3. It is evident from the figure that all the peaks in the SXRD patterns of the sintered powder of CFN could be indexed with the orthorhombic phase and no trace of any impurity phase is observed.

The superlattice reflections can arise due to cation ordering at the B-site of the perovskite structure. The differences in the charges that occupy the same site in the unit cell can promote the ordering of the cations to minimize the electrostatic energy [19,151]. Further, the significant size difference of the cations occupying the same site in the unit cell can also promote the cations ordering to minimize the elastic strain energy [151]. The most common ordering at the B-site in these complex perovskites compound is the (111) or rock-salt ordering that leads to a doubling of the unit cell in every direction [147]. The ordering of the cations leads to change in the space group symmetry also [201,202]. In case of CFN, the significant charge difference in the B-site of Fe^{3+} and Nb^{5+} may promote the ordering of the cations to minimize the electrostatic energy. Since the size difference of the Fe^{3+} = 0.645 Å, and Nb^{5+} = 0.64 Å ions at the B-site is small (0.005Å), it may not promote ordering of the cations. Another common source of unit cell doubling in

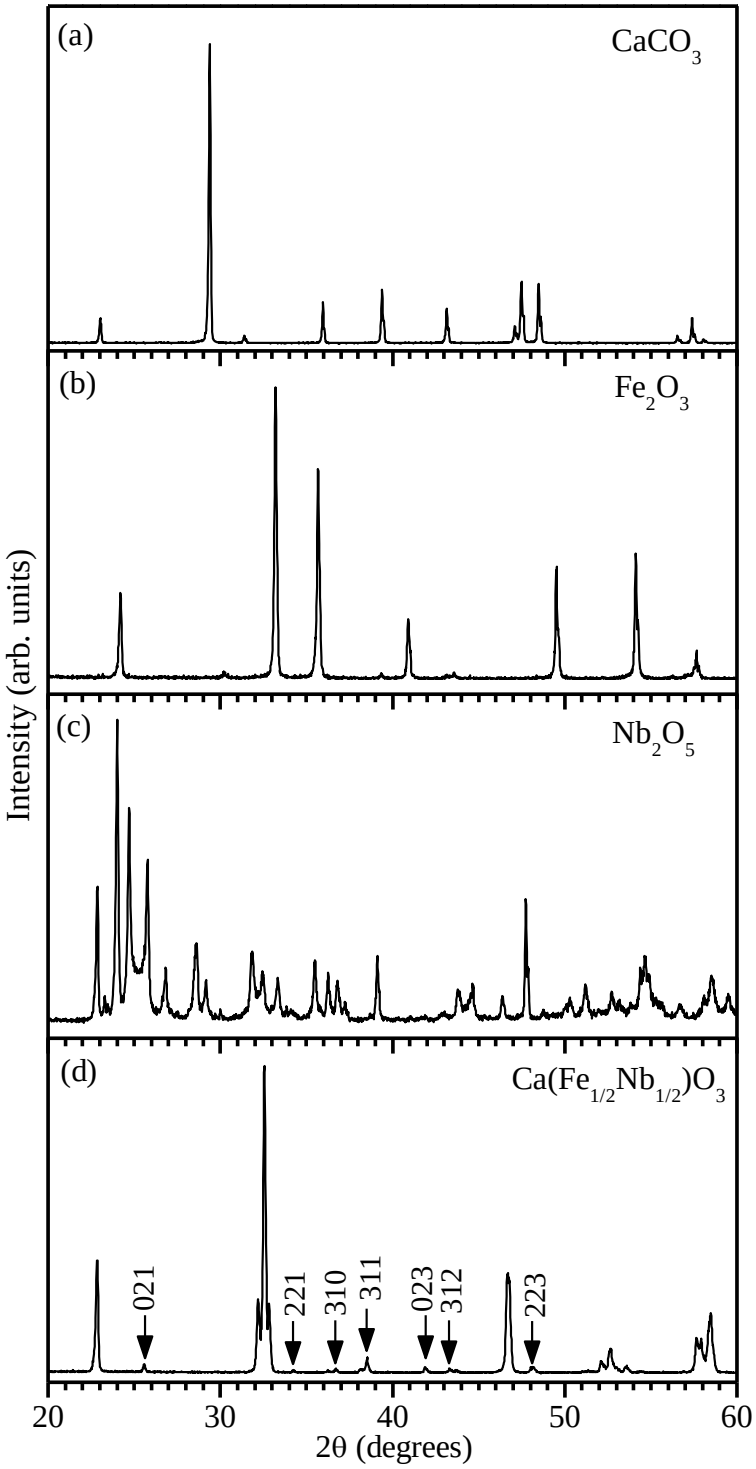

Figure 5.2: X-ray powder diffraction patterns of (a) $CaCO_3$ (b) Fe_2O_3 (c) Nb_2O_5 and (d) $Ca(Fe_{1/2}Nb_{1/2})O_3$. The positions of superlattice reflections for the orthorhombic structure with the Pbnm space group, are marked by arrows. All the indices are written with respect to the double cubic perovskite cell.

complex perovskites is the tilting of the BO_6 octahedra. According to Glazer, the tilts can be described by three components about the three tetrad axes namely a, b, c of the elementary perovskite unit cell. Each tilt about a given axis forces tilt of opposite sense about the other two tetrad axes leading to the doubling of the corresponding unit cell parameters. In addition, the octahedra along the tilt axis in the neighbouring unit cells may be tilted in-phase or anti-phase. For anti-phase tilting, the unit cell will be doubled along the tilt axis also. In Glazer's notation [204], aaa means equal tilts about all the three axes and abc means three unequal tilts. Thus aac means equal tilt about [100] and [010] but unequal tilt about [001]. The in-phase tilt is denoted by '+' sign as superscript while the anti-phase tilt is denoted by '-' sign as superscript. The absence of tilt is denoted by '0' in the superscript. Thus $a^0a^0c^-$ means that the structure has antiphase tilting about the pseudo-cubic c axis and no tilt about the a and b axes. Thus, the cation ordering, in-phase and anti-phase octahedral tilting may give rise to a set of superlattice reflections which may be indexed with respect to a doubled perovskite cell. The fundamental perovskite reflections acquire Miller indices (hkl) which are all even (eee-type) integers while the reflections that arise from either B-site cation ordering or anti-phase octahedral tilting have Miller indices that corresponds to h, k and l being all odd (ooo-type). The anti-phase octahedral tilt is known to be linked with phonon instability at the R (q =½ ½ ½) point of the Brillouin zone of the elementary perovskite unit cell, as was first confirmed in $SrTiO_3$ [5]. The superlattice reflections that arise from the in-phase tilting of the octahedra have two odd integer indices and one even integer (ooe-type) and is known to be associated with M (q = ½ ½ 0) point phonon instability [14]. Further, the antiparallel A-site cation displacements also results in the unit cell doubling and leads to superlattice reflections of the even-even-odd (eeo-type) observed in the orthorhombic $CaTiO_3$ [14]. Jahn-Teller distortion can also distort the shape of the octahedra which may lead to

doubling of the unit cell and hence produce superlattice reflections [14] but the complex perovskite under present discussion do not have a John-Teller active ion at the B-site. In CFN, we observe three types of superlattice reflections having indices odd-odd-odd and odd-odd-even and even-even-odd with respect to the doubled perovskite cell. The presence of odd-odd-odd and odd-odd-even types of superlattice reflection in CFN confirms the anti-phase and in-phase tilts in CFN.

The room temperature crystal structure of CFN is controversial as both orthorhombic (disordered) Pbnm space group based on $a^-a^-c^+$ tilt system with B-site cation ordering [176,199,200] and monoclinic (ordered) $P2_1/n$ space group [200–202] with $a^-a^-c^+$ tilt as well as B-site cation ordering have been proposed in the literature [201,202]. In order to resolve the existing controversy about the room temperature crystal structure of CFN, we have performed the Rietveld refinement using SXRD pattern using space group symmetries $P2_1/n$ and Pbnm corresponding to ordered monoclinic and B-site disordered orthorhombic structures. The asymmetric unit of the orthorhombic structure of CFN consists of Ca^{2+}, Fe^{3+}/Nb^{5+}, O^{2-}_{I} and O^{2-}_{II} at (x, y, 1/4), (1/2, 0, 0), (x, y, 1/4) and (x, y, z) corresponding to the Wyckoff sites 4c, 4b, 4c and 8d, respectively. The asymmetric unit of monoclinic phase, consists of Ca^{2+} at the 4e sites and x, y, z general positions, Fe^{3+} at 2d site with 1/2, 0, 0 special position, Nb^{5+} at 2c site with 0, 1/2, 0 special position, and the three oxygen (O_1 O_2 and O_3) at 4e sites with x, y, z general positions. In the Rietveld refinement, the background and peak shape were modelled with linear interpolation and pseudo-Voigt function, respectively while the occupancy was fixed at the nominal composition. Zero correction, scale factor, background, lattice parameters, half width parameters (u, v, w), positional coordinates and thermal parameters were varied during the refinement which converged after a few cycles. Figs. 5.3(a) and (b) depict the comparison of observed and calculated SXRD

profiles obtained by Rietveld refinement using monoclinic ($P2_1/n$) and orthorhombic (Pbnm) space group symmetries, respectively. It is evident from the figures that the observed (filled-circles) and calculated (continuous line) profiles show excellent fit for the orthorhombic phase with Pbnm space group as can be seen from the nearly flat difference profile (bottom line) in the same figure. The superlattice reflections expected from the cation ordering as well as octahedral tilt for the monoclinic $P2_1/n$ space group, on the otherhand, are not observed (see the reflections marked with arrows in the insets of Fig. 5.3(a)). Thus, rules out the chemical ordering in $Ca(Fe_{1/2}Nb_{1/2})O_3$. The Rietveld refinement using SXRD data thus confirms that CFN belongs to orthorhombic phase in the Pbnm space group in agreement with the previous reports [176,199,200] and rejects the monoclinic $P2_1/n$ space group proposed by other workers [200–202]. This was possible simply because of the use of high resolution SXRD data in the present work which revealed very weak superlattice reflections, not observable unambiguously in the laboratory source data used by previous workers [200–202].

The refined structural parameters using Pbnm space group for CFN are given in Tables 5.2. The unit cell parameters, positional coordinate and thermal parameters are in good agreement with those reported in literature [176,199,200]. Thus, CFN belongs to the $a^-a^-c^+$ tilt system in Glazer's notation with orthorhombic crystal structure in the Pbnm space group. Fig. 5.3(c) depicts the orthorhombic crystal structure of CFN along with the tilted oxygen octahedra. After setting the controversies about the structure and space group symmetry of CFN at room temperature, we now proceed to analyse the low temperature magnetic transition in CFN.

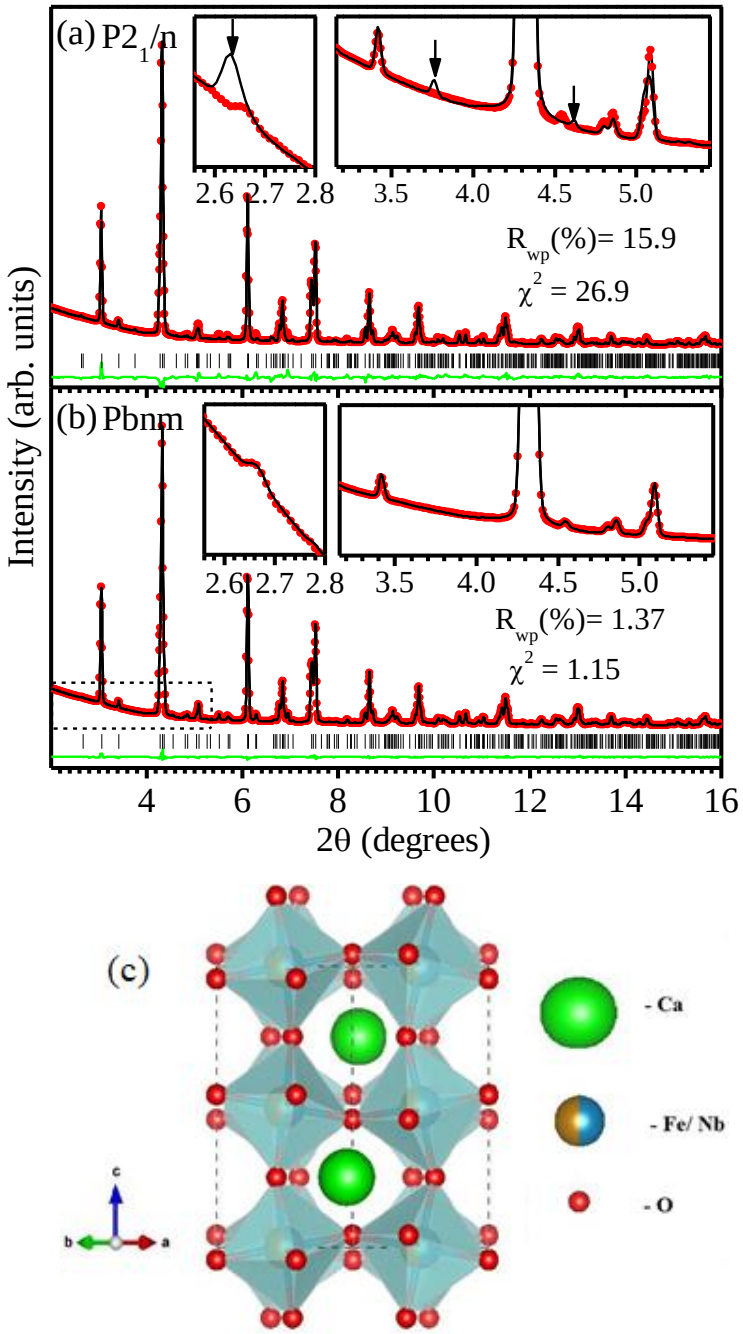

Figure 5.3: Observed (red dots), calculated (black continuous line) and difference (green continuous line) profiles obtained by Rietveld refinement using synchrotron x-ray data of $Ca(Fe_{1/2}Nb_{1/2})O_3$ at room temperature using (a) monoclinic $P2_1/n$ (b) orthorhombic Pbnm space groups. Vertical tick marks above the difference profile represent the Bragg peak positions. Arrow marked the expected positions of superlattice peak at 2.63, 3.75 and 4.62 degree for the monoclinic phase. The absence of these peaks rules out the monoclinic structure. (c) depicts the crystal structure of $Ca(Fe_{1/2}Nb_{1/2})O_3$ along with tilted octahedra.

Table 5.2: Structural parameters obtained from the Rietveld analysis of the SXRD pattern of $Ca(Fe_{1/2}Nb_{1/2})O_3$ using orthorhombic Pbnm space group.

Atoms	x	y	z	B ($Å^2$)
Ca^{2+}	0.0083 (5)	0.0439 (2)	¼	1.01 (2)
Fe^{3+}/Nb^{5+}	½	0	0	0.89 (9)
$O^{2-}{}_1$	0.9170 (7)	0.4471 (6)	¼	1.02 (7)
$O^{2-}{}_2$	0.2953 (5)	0.2916 (4)	0.0425 (4)	0.77 (5)
A_o= 5.4480(1) Å, B_o = 5.5499 (1) Å, C_o = 7.7573 (2) Å: α = β = γ= 90°				

5.4.3 Evidence for history dependent irreversibility in DC magnetization studies:

The temperature dependence of dc magnetization M(T) of CFN measured during warming under a magnetic field of 100 Oe after zero-field cooling (ZFC) of the sample shows a peak at T_f ~25 K (see Fig. 5.4) in agreement with previous reports on CFN [56]. The disordered complex perovskites like $Sr(Fe_{1/2}Nb_{1/2})O_3$ (SFN), $Ba(Fe_{1/2}Nb_{1/2})O_3$ (BFN), $Ca(Fe_{1/2}Ta_{1/2})O_3$ (CFT), $Sr(Fe_{1/2}Ta_{1/2})O_3$ (SFT), and $Ba(Fe_{1/2}Ta_{1/2})O_3$ (BFT) also show T_f around 25K [176–178]. Pb-based disordered complex perovskites, like PFN, $Pb(Fe_{1/2}Ta_{1/2})O_3$ (PFT), $Pb(Fe_{2/3}W_{1/3})O_3$ (PFW), on the otherhand, show lower T_f ~10K [171,172,174,175,191]. As discussed in the next chapter, the Curie-Weiss temperature (θ_{CW}) obtained from high temperature DC susceptibility (χ_{dc}) data is –(113.7±0.8)K. Thus large negative value of θ_{CW} reveals predominant antiferromagnetic interactions in CFN but there is no signature of any AFM transition in the ZFC M(T) plot of CFN in marked contrast to PFN and PFT which show a small anomaly at T_N ~150K [171,172,174,175]. The ZFC and FC M(T) plots at 100 Oe, shown in Fig. 5.4 reveal bifurcation of the two curves at the irreversibility temperature T_{irr} ~27K, which is a characteristic of SG freezing [24,41–43]. However, such a bifurcation is known to occur in an ensemble of non-interacting SPM spin clusters also due to the onset of blocking

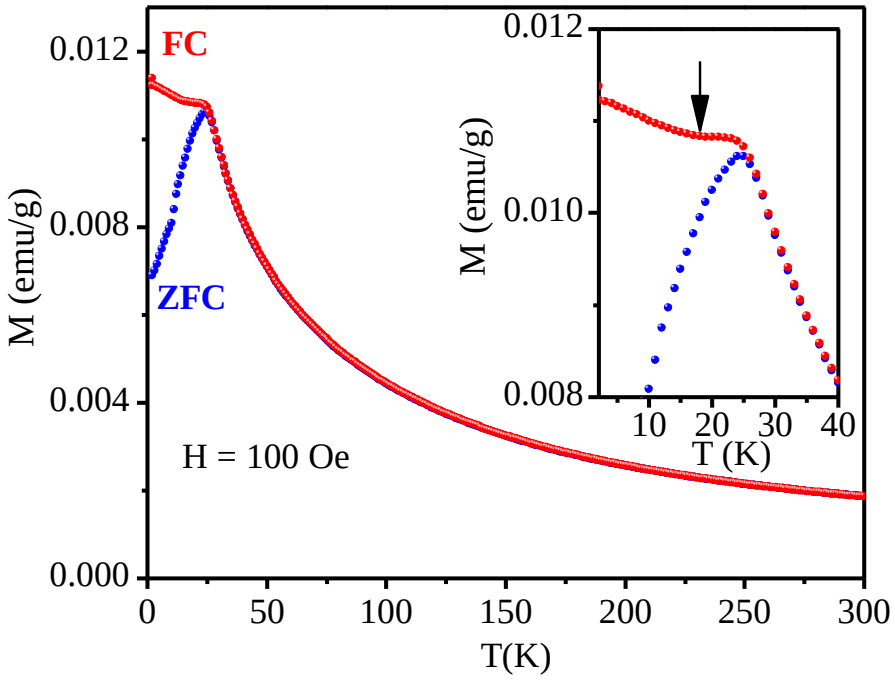

Figure 5.4: Temperature dependence of dc magnetization of $Ca(Fe_{1/2}Nb_{1/2})O_3$ measured at 100 Oe field in warming cycle for both zero-field cooled (ZFC) and field cooled (FC) conditions. The inset gives a magnified view of the M(T) to reveal a small dip (marked with an arrow) in the FC M(T) below T_f.

dynamics at T_{irr} [198]. The FC M(T) curve for non-interacting SPM systems is known to increase continuously below T_B, whereas in our case the FC M(T) curve shows a small dip just below the peak temperature over a narrow temperature range before it begins to rise again. Such a behaviour is known to occur in cluster spin-glass (CSG) systems with interacting spin clusters [198].

5.4.4 Evidence for critical slowing down of the spin dynamics: AC susceptibility studies:

The analysis of the dc magnetisation data presented in the previous section suggests the existence of SG freezing with T_f ~25K. In order to rule out the possibility of SPM blocking leading to the peak in ZFC dc M(T) and bifurcation of ZFC and FC M(T),

we carried out a study of the spin/cluster dynamics using frequency and temperature dependent ac magnetic susceptibility ($\chi(\omega, T)$) measurements. Fig. 5.5(a) depicts the variation of the real ($\chi'(\omega, T)$) part of ac susceptibility of CFN measured at various frequencies for an applied ac drive field of 1 Oe. It is evident from the figure that the temperature corresponding to the peak in the $\chi'(\omega, T)$) plot shifts to higher temperatures side with increasing frequency. Although a frequency dependent shift of $T_f(\omega)$ is known for both SG freezing and SPM blocking [24,41–43,198], a distinction between the two can be made using the empirical Mydosh parameter (*K)* [42] discussed in chapter III:

$$K=\frac{1}{T_f(\omega)}\frac{\Delta T_f(\omega)}{\Delta(ln\,\omega)} \qquad \ldots\ldots\ldots\ldots (5.1)$$

where $\Delta T_f(\omega)$ is the difference between the peak temperatures of $\chi'(\omega, T)$ at low and high frequencies. For SG/CSG freezing, the Mydosh parameter lies in the range 0.005-0.09 whereas it usually lies in the 0.1 to 0.3 range for SPM blocking [24,42]. In the present case, the Mydosh parameter comes out to be 0.045 which suggests that the frequency dispersion of $T_f(\omega)$ is due to SG/CSG freezing and not SPM blocking.

As discussed in chapter III, the frequency dependence of the SG freezing temperature ($T_f(\omega)$) in the scaling theories of spin-glasses has been modelled using a power law behaviour which predicts critical-slowing down of the spin dynamics and its divergence at T_{SG} at which the ergodic symmetry is broken [261]:

$$\tau = \tau_0 \left(\frac{T_f(\omega) - T_{SG}}{T_{SG}}\right)^{-z\nu} \qquad \ldots\ldots\ldots(5.2)$$

Here, τ_0 the inverse of the attempt frequency (i.e. attempt time), T_{SG} the SG transition temperature at which τ diverges, ν the critical exponent of the correlation length $\xi = (T_f/T_{SG}-1)^{-\nu}$ and z the dynamic exponent $\tau \sim \xi^z$. The relaxation time τ corresponding to the peak temperature $T_f(\omega)$ for each measuring frequency $\omega=2\pi f$ was determined using τ =

$1/2\pi f$. A least-square fit to the $\ln(\tau)$ versus $\ln(T_f/T_{SG}-1)$ plot shown with solid line in Fig. 5.5(b) gives $T_{SG} = (23.9 \pm 0.4)$ K, $\tau_0 = 1.47\text{x}10^{-6}$ s and $z\nu = (2.01 \pm 0.04)$. The large value of τ_0 reveals slow dynamics as expected for cluster spin glasses for which τ_0 typically lies in the range $\sim 10^{-6}$-10^{-10}s [24,42]. Such high τ_0 values have been reported in several CSG systems [296–298]. For canonical SG systems, like Cu:Mn, the value of τ_0 is of the order of $\sim 10^{-13}$s which is several orders of magnitude smaller than that for the cluster spin-glasses [24,42].

In order to cross-check the CSG dynamics, we modelled $T_f(\omega)$ using the Vogel-Fulcher (V-F) law also which has been used to describe the critical spin dynamics in some spin glasses [224], as discussed in chapter III:

$$\tau = \tau_0 \, exp\left(\frac{E_a}{k_B(T_f(\omega) - T_{VF})}\right) \qquad \text{.....(5.3)}$$

Here, E_a is the activation energy, k_B the Boltzmann constant and T_{VF} (which is equivalent of T_{SG} in Eq. (5.2)) is called Vogel-Fulcher freezing temperature at which the spin dynamics diverges. SPM blocking dynamics, unlike the SG critical dynamics, does not show critical slowing down of the relaxation time but exhibits Arrhenius type of non-critical behaviour with $T_{VF} = 0$ in Eq. (5.3). The $\ln(\tau)$ vs $(1/T)$ plot for Arrhenius dynamics should obviously be linear. The non-linearity of this plot shown in the inset of Fig. 5.5(b) clearly rules out SPM blocking process to be responsible for the peak in the ZFC dc magnetization M(T) or ac susceptibility $\chi'(\omega, T)$. On the otherhand, V-F law provides excellent fit as shown with continuous line through the data points in the inset. The least squares fitting parameters for V-F law are: $T_{VF} = (23.3 \pm 0.1)$ K, $E_a = 0.495$ meV and $\tau_0 = 2.51\text{x}10^{-6}$s. The T_{SG} and τ_0 values obtained using power law and V-F law are comparable. It is worth mentioning here that the value of activation energy $E_a = 0.495$

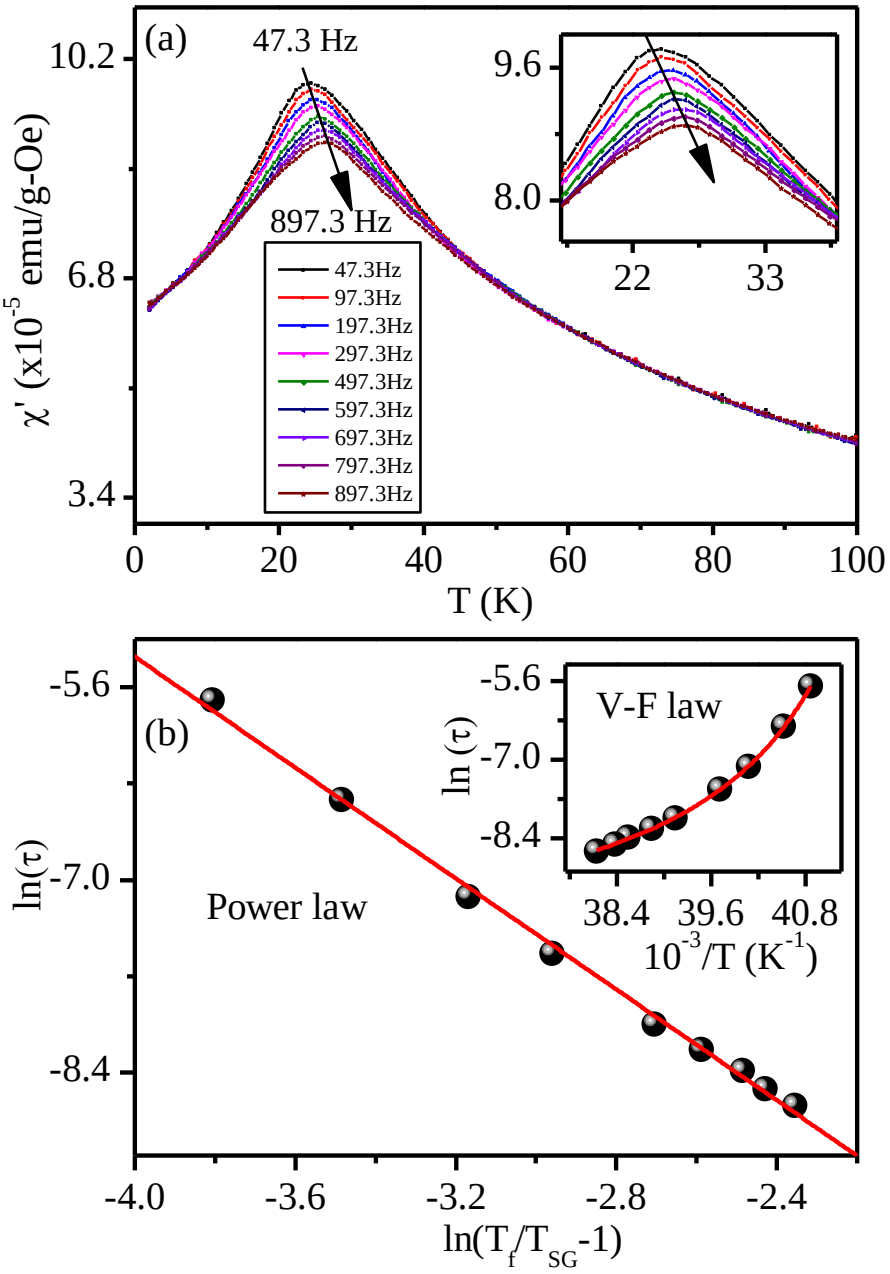

Figure 5.5: Temperature dependence of the real part ((χ' (ω, T)) of ac magnetic susceptibility of $Ca(Fe_{1/2}Nb_{1/2})O_3$ measured at various frequencies as labelled in the plot for an applied ac drive field of 1 Oe. The main panel **(b)** depict ln(τ) versus $\ln(T_f/T_{SG}-1)$ plot, where $\tau = 1/(2\pi f)$. Inset to panel (b) depict the ln(τ) versus 1/T plot. The solid line represents the least-squares fit for critical power law and Vogel-Fulcher law.

meV (i.e., 5.74 K) is comparable to the activation energies reported for frustrated CSG systems (e.g., $Eu_xSr_{1-x}S$) but lower than those for the canonical Ruderman-Kittel-Kasuya-

Yosida type spin glasses [224]. Thus, both the power law and Vogel-Fulcher fits confirm CSG freezing in CFN with T_{SG}~24±1 K and $\tau_0 = (2\pm0.5)x10^{-6}$s.

5.4.5 Evidence for the existence of de Almeida-Thouless line in the H-T plane:

Using the concept of replica symmetry breaking [299], it has been shown theoretically that the irreversibility temperature T_{irr}, which nearly coincides with T_f for canonical SG systems [42], would shift towards lower temperatures in the presence of magnetic field for both the Ising and Heisenberg systems [24,42]. The field dependence of T_{irr} / T_f (i.e., $T_{irr}(H)$ / $T_f(H)$) is predicted to follow the following relationship at low fields:

$$H(T) \propto \left(1 - \frac{T_f(H)}{T_f(0)}\right)^m, \qquad \ldots\ldots(5.4)$$

where the characteristic exponent m takes the value 3/2 or 1/2 for de Almeida-Thouless (A-T) [49] or Gabay-Toulouse (G-T) lines [51,52] in the H-T plane, as discussed in chapter III also. To verify the stability of the SG phase of CFN in the presence of magnetic field, we depict the ZFC and FC M(T) plots of CFN at various fields in Fig. 5.6. It is evident from the figure that the irreversibility temperature $T_{irr,}$ marked with an arrow pointing downwards, shifts to the lower temperature side on increasing the magnetic field in agreement with the theoretical predictions [49,51,52]. Unlike CFN where the irreversibility temperature clearly observed, in the BF-0.20BT system T_{irr} is not obvious probably due to large variation in the size of the spin clusters taking part in the SG freezing process. The SG freezing temperature T_f (H), shown with an arrow pointing upwards in the same figure, corresponding to the peak in the ZFC M(T) also decreases with increasing magnetic field, similar to that observed in BF-0.20BT system. Fig. 5.7 depicts a plot of T_{irr} versus $H^{2/3}$ as well as T_f(H) versus $H^{2/3}$. It can be seen from

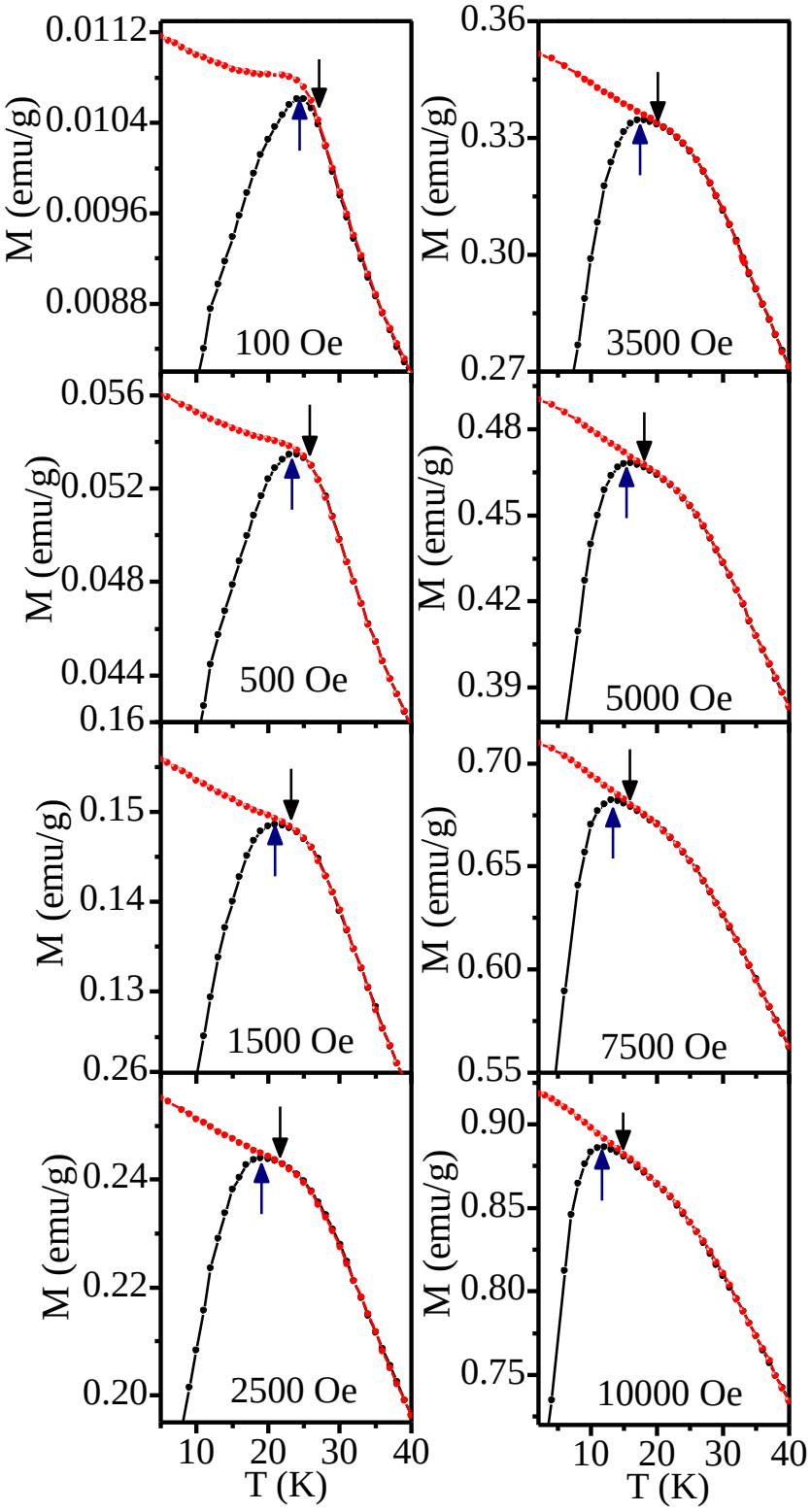

Figure 5.6: Temperature dependence of the zero-field cooled (ZFC) and field-cooled (FC) dc magnetization plots of $Ca(Fe_{1/2}Nb_{1/2})O_3$ at various applied magnetic fields. The arrow pointing downwards represents the irreversibility (T_{irr}) temperature while the arrow pointing upwards corresponds to the peak (T_f) in the ZFC M(T).

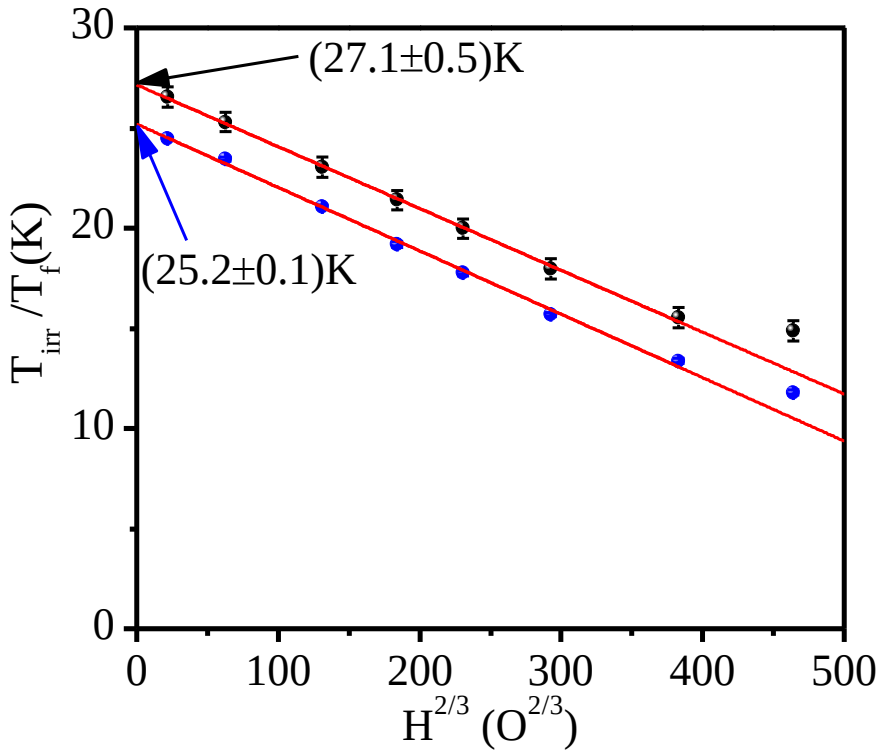

Figure 5.7: Plot of T_{irr} versus $H^{2/3}$ as well as T_f versus $H^{2/3}$ showing the presence of de Almeida-Thouless (A-T) line.

this figure that both the plots are linear below 7500 Oe confirming A-T type field dependence of $T_{irr}(H)$ as well as $T_f(H)$. The extrapolation of the A-T line to H = 0 gives the SG transition temperature T_{SG} ~27.1K and 25.2 K, using $T_{irr}(H)$ and $T_f(H)$ temperatures, respectively. The difference between $T_{irr}(H)$ and $T_f(H)$ at each field is about 2K which is also reflected in the T_{SG} temperature obtained from these two characteristic temperatures. We note that the value of T_{SG}~25.2K obtained from $T_f(H)$ versus $H^{2/3}$ plot is closer to that obtained from power law/Vogel-Fulcher spin dynamics.

The A-T line has been reported for both the canonical SG as well as CSG systems using field dependence of either $T_{irr}(H)$ [300–302] or $T_f(H)$ [303–305] and represents the boundary between the high temperature ergodic and low temperature non-ergodic phases. While the original formulation for the A-T line was for Ising spins [49], subsequent

theoretical papers have shown that it can occur in Heisenberg systems also if the single ion anisotropy is low and positive [52]. It is therefore not possible to comment on the nature of the spins (Ising versus Heisenberg) in CFN on the basis of Fig. 5.7.

5.4.6 Other characteristic features of the spin-glass phase of CFN:

Having confirmed the existence of CSG freezing with T_f ~25K in CFN, we now proceed to examine the characteristic properties of glassy state, namely slow relaxation of the thermoremanent magnetization [24,42,262], memory and rejuvenation effects [198]. The slow relaxation of thermoremanent magnetization (TRM) below T_{SG} in SG and CSG systems has been a subject matter of theoretical and experimental investigations by several workers [171,262,300]. Palmer et al. [262] have presented a generalised theory for strongly interacting SG systems, including spin clusters, in terms of a hierarchically constrained dynamics and have shown that the time dependence of TRM should exhibit a stretched exponential behaviour [171]:

$$M(t)=M_0\exp[-(t/\tau)^{\beta}] \qquad \ldots.(5.5)$$

where M_0 is the initial magnetization at t = 0, τ the characteristic relaxation time and β the exponent for the stretched exponential function. The value of β usually lies between 0 and 1 for different class of SG systems [24,42,198]. In this context, β =1 means, the system has monodispersive Debye like relaxation while β =0 implies absence of any relaxation. The intermediate values of β in the range $0< \beta <1$ implies a non-Debye behaviour with distribution of relaxation times due to the presence of a large number of degenerate states in the frozen state. We investigated the slow relaxation of the TRM in the glassy phase of CFN using the stretched exponential function given by Eq. (5.5). For this, the sample was first cooled in an applied magnetic field of 1000 Oe from 300 K to 15 K (i.e., below the SG freezing temperature T_f) and then allowed to age for a wait time $t_w = 10^3$s with field

applied. After the waiting time, the field was switched off to zero and magnetization was measured as a function of time for 10^4s. The results are shown in Fig. 5.8 where the continuous line shows the best fit to the stretched exponential function of Eq. (5.5) with $M_0 = 0.035$, $\tau = (40166 \pm 77)$s and $\beta = 0.10$. The value of the exponent $\beta = 0.10$ not only lies in the typical range for spin glasses and cluster spin glasses but also indicates strongly polydispersive non-Debye relaxation, characteristic of the strongly interacting glassy systems in general [171]. It is interesting to compare the relaxation behaviour of TRM of CFN with that of BF-0.20BT discussed in chapter III. In BF-0.20BT system, due to the coexistence of LRO AFM phase with SG phase a nearly time independent constant TRM value was also required besides the stretched exponential function for fitting the observed relaxation behaviour. In contrast, because there is no coexisting LRO phase in CFN, only the stretched exponential term was sufficient to account for the relaxation behaviour.

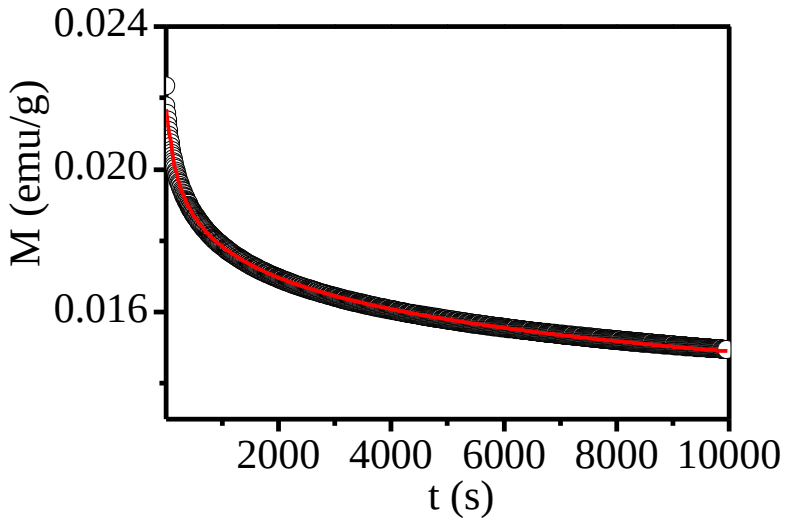

Figure 5.8: Time dependence of thermoremanent magnetization of $Ca(Fe_{1/2}Nb_{1/2})O_3$ sample at 15 K for 1000 Oe cooling field and wait time of 1000s. The solid line is the best fit for stretched exponential function to the data.

Both spin glasses and cluster spin glasses are known to exhibit aging, memory and rejuvenation effects [198,279,300,306] due to chaotic ground state of the SG phase [307]. Towards understanding the important characteristic of glassy phase, two different models have been proposed to describe the spin-glass state. In the Droplet model [308], only one spin configuration exists in the free energy landscape at a given temperature whereas in the case of Hierarchical model [309] multi-valleyed spin configurations have been postulated which split into new sub-valleys on decreasing temperature and merge on increasing the temperature. We followed three different protocols to verify the aging, memory and rejuvenation effects in the CSG phase of CFN.

In the first protocol, the sample was initially cooled under zero field (ZFC) from T = 300K which is greater than T_f to a wait temperature T_w=15K, which is less than T_f ~25K, at which the sample was allowed to age for a wait time of $t_w=10^4$s. After ageing for $t=t_w$, the sample was allowed to cool further in zero field down to 2K. After such a zero-field cooling with an intermediate wait at T_w=15K for $t_w=10^4$s, the magnetization (M_{wait}^{ZFC}(T)) was measured during the heating cycle under 100 Oe field (see Fig. 5.9(a)). This magnetization curve (M_{wait}^{ZFC}(T)) was compared with a reference curve M_{ref}^{ZFC}(T) which was obtained by measuring magnetization during heating cycle under identical field (i.e., 100 Oe) after the sample was cooled in zero field up to 2K without any intermediate stop /wait at 15K. Fig. 5.9(b) depicts the difference ΔM (T) = M_{wait}^{ZFC}(T) - M_{ref}^{ZFC}(T) vs temperature (T) plot from which it is evident that a sharp dip occurs exactly at the waiting temperature (T_w). Such a "hole burning" in the difference plot clearly demonstrates memory and rejuvenation effect in the CSG phase of CFN [198].

The second protocol involves FC condition [279]. Here, the sample was first cooled in 100 Oe magnetic field from 300 K to 2 K at a constant rate of 2K/min and then

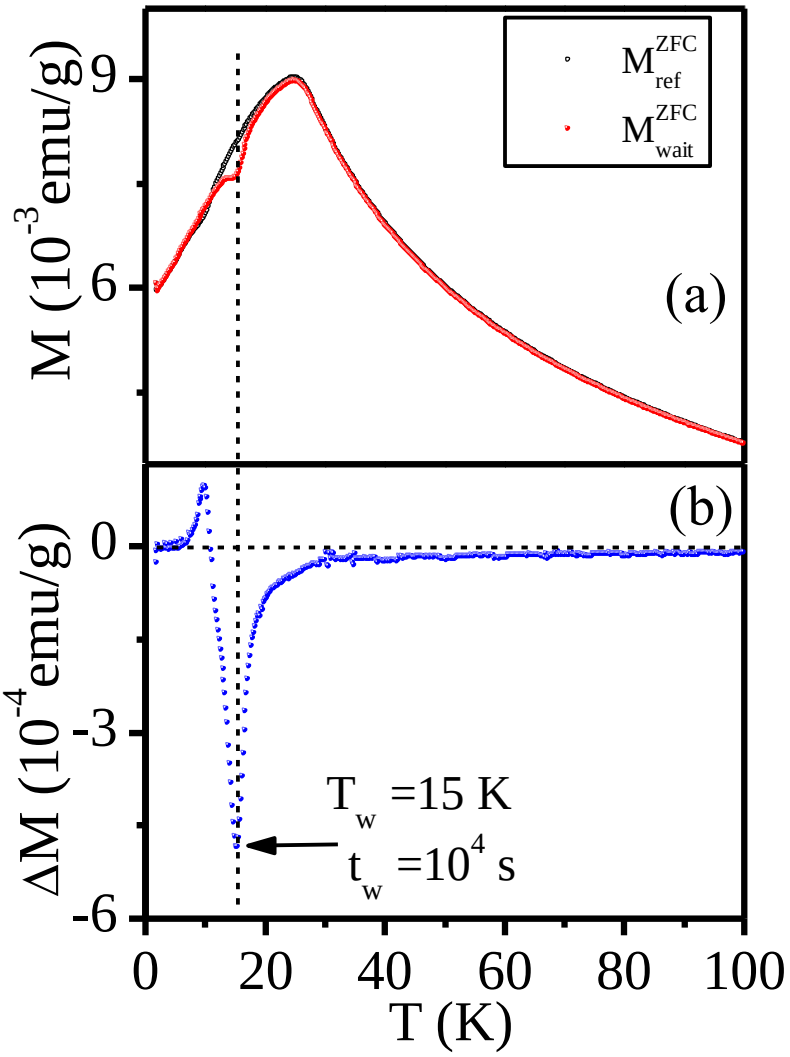

Figure 5.9: Temperature dependence ZFC magnetization of $Ca(Fe_{1/2}Nb_{1/2})O_3$ recorded at 100 Oe field with (●) and without (o) intermediate stop at T_w=15K for a wait time (t_w) of 10^4s. **(b)** depicts the difference ΔM (T) = M^{ZFC}_{wait}(T) - M^{ZFC}_{ref}(T) vs temperature (T) plot from which it is evident that a sharp dip occurs exactly at the waiting temperature (T_w).

heated back continuously at the same rate and magnetization M(T) was recorded under the same field. This gives the reference curve (M^{FCW}_{ref}(T)) shown with continuous line in Fig. 5.10. This sample was cooled again from 300K to 2K at the same rate of cooling (2K/min) and under identical field (i.e., 100 Oe) but the sample was allowed to wait at two intermediate temperatures T =50 and 15 K, which are above and below T_f,

respectively, for a wait time t_w = 3 hours each. The field was set to zero during the wait time at both the temperatures. After the completion of the wait time, the field was reapplied and the measurement was resumed during further cooling. The M(T) curve so obtained is labelled as M^{FCC}_{wait}(T) and is shown with plus (+) symbol in Fig. 5.10. After cooling the sample to the lowest temperature 2K in this way, the magnetization (M^{FCW}_{mem}(T)) measurement was carried out during heating cycle maintaining the same rate (i.e., 2K/min) and the same field (i.e., 100 Oe). The results are shown with open (o) circles in Fig. 5.10. It is evident from the figure that the M^{FCC}_{wait}(T) curve shows a step at the wait temperature T_w =15K below T_f. However, no such step is observed at the other wait temperature T_w = 50K greater than T_f ~25K. Further, all the three curves merge above T_f. This protocol based on measurements done during both heating and cooling

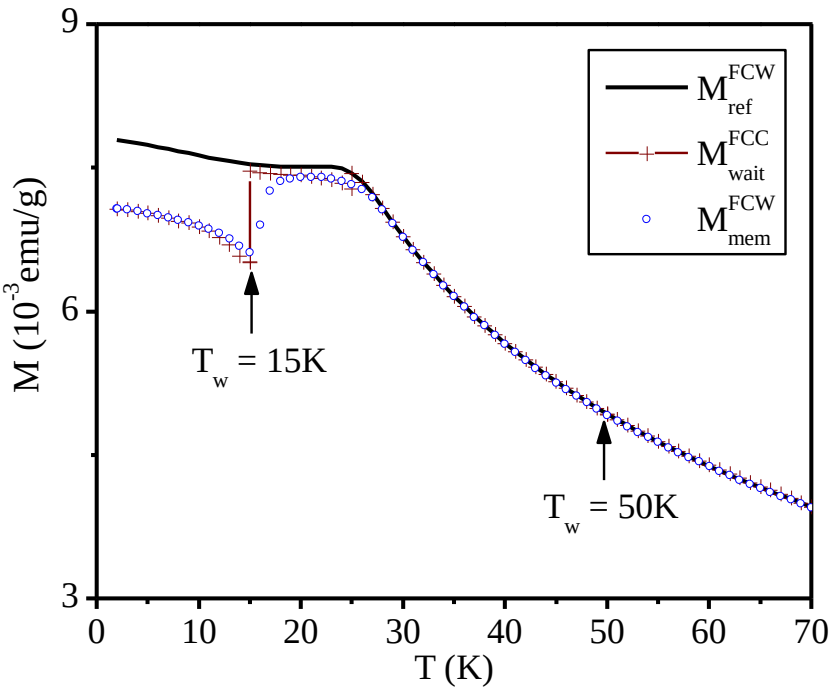

Figure 5.10: Temperature dependence dc magnetization of $Ca(Fe_{1/2}Nb_{1/2})O_3$ recorded at 100 Oe field in three different cycles as labelled in the plot. The field is set to zero during the intermittent wait of cooling temperature T_w = 50K, 15K for 3 hours. The cooling and heating rate of measurement is 2K/min. The pronounced steps in the cooling curve occurs at 15K and no such step is seen above the spin-glass freezing temperature (i.e. at 50K).

cycles further confirm that the sample remembers the measurement history. The observation of memory and rejuvenation effect rules out SPM blocking and confirms the existence of the glassy phase below T_f ~25K.

We followed a third protocol proposed by Sun et al. [279] for memory effect as this protocol enables to make a distinction between the Droplet [308] and Hierarchical [309] models of the spin glass state. As per the ZFC protocol, sample was first cooled under zero magnetic field from 300K to 15K at the rate of 2K/min and then the growth of M(t) was recorded on application of a 100 Oe field from time t=0 to $t=t_1$ =4000s (see Figs. 5.11(a)). After time $t=t_1$, the sample was quenched down to 10K and the growth of magnetization was measured again for the time $t=t_2$ =4000s as shown in the same figure. Finally, the sample temperature was raised to 15K quickly under the same field (i.e. 100 Oe) and the growth of magnetization was recorded for time $t=t_3$ = 4000s at 15K which is also shown in Fig. 5.11(a). It is evident from this figure that the M(t) curve measured during time $t=t_3$ is a continuance of the same curve measured during the time $t=t_1$ which is shown more clearly in the inset of the same panel. This protocol clearly suggests that when sample is cycled back to 15K, i.e. the initial temperature, the state of the system is recovered. For the FC condition, the sample was cooled down from 300 to 15 K under 100 Oe magnetic field at the rate 2K/min. Immediately the field was set to zero and magnetization was measured for the time $t=t_1$=4000s. After the elapse of time t $=t_1$, the sample was quenched down to 10K (here the field was still zero) and the evolution of magnetization M (t) was measured for the time $t=t_2$ = 4000s. Finally, the sample was heated back again to 15K and the evolution of magnetization was recorded for time $t=t_3$=4000s. It is evident from panel (b) of Fig. 5.11 that the state of the system is recovered when the temperature returns to initial 15K. Further, the relaxation of magnetization M(t) curve during the time t_3 is a continuance of $t = t_1$ as shown more

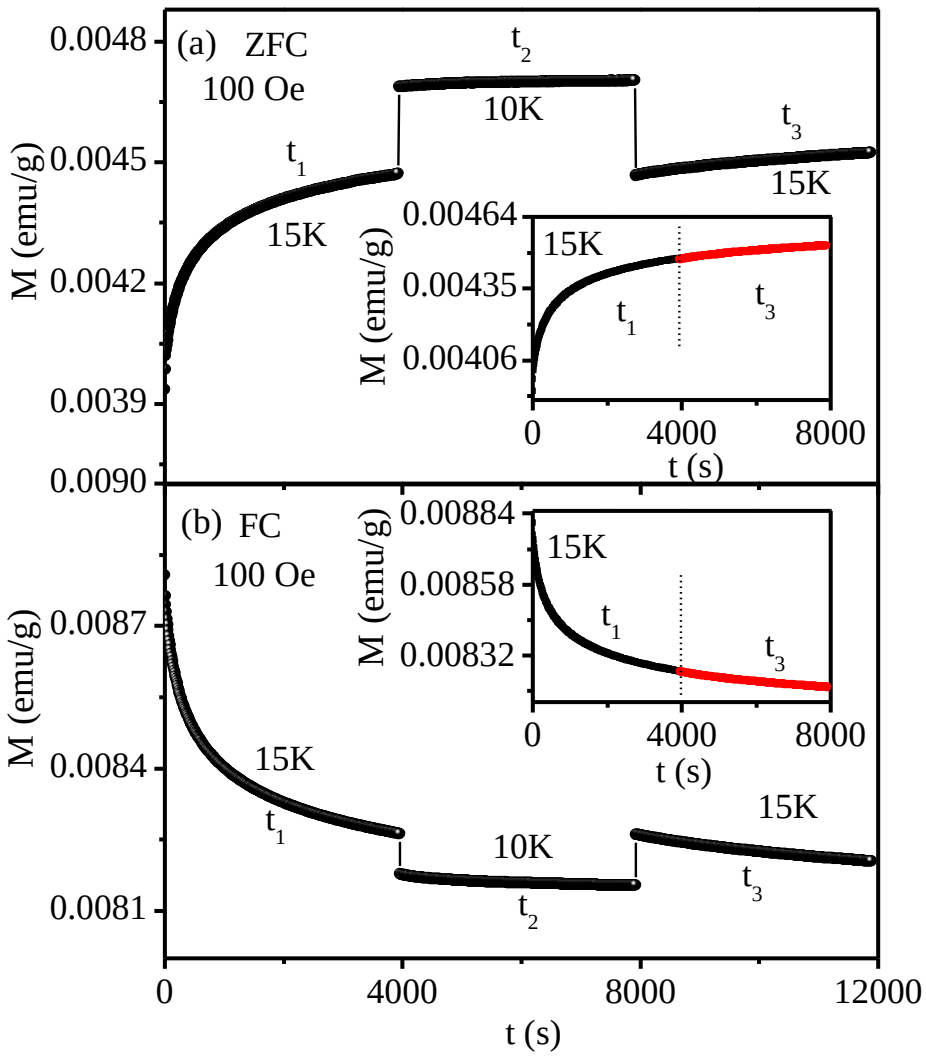

Figure 5.11: Magnetic relaxation of $CaFe_{1/2}Nb_{1/2}O_3$ sample at 15 K for 100 Oe field with temporary cooling (i.e. negative cycling) at 10K using (a) the ZFC and (b) FC protocols. The insets show the same data versus total time spent at 15K. The relaxation curve clearly reveals that, the curve during t_3 is in continuation of the curve during t_1 (memory effect).

clearly in the inset of the same panel. Our observed relaxation behaviour can be explained in the context of Hierarchical model of SG system. At a given temperature say T_0 =15K, several multi-valleyed states are organized in the free-energy landscape as per this model. When the sample is quenched down from T_0 =15K to T_0-ΔT =10K, then each valley is expected to split into new sub valleys as per the Hierarchical model. However, if ΔT is very large, the relaxation occurs only between the newly born sub-valley of each set. When the sample was heated back to T_0 =15K, the new born sub valleys merge back to

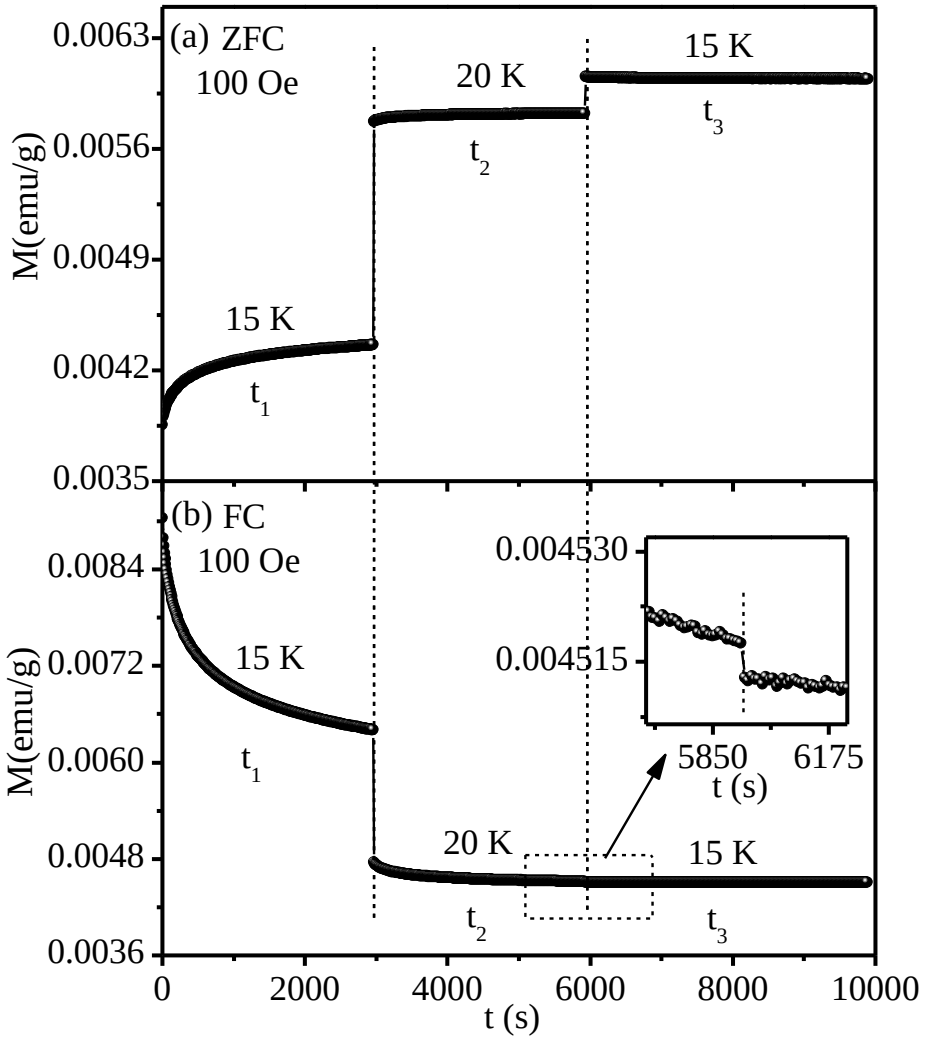

Figure 5.12: Magnetic relaxation of $CaFe_{1/2}Nb_{1/2}O_3$ sample at 15K for 100 Oe field with temporary heating (i.e. positive cycling) at 20K using (a) the ZFC and (b) FC protocols. The relaxation curve clearly reveals that during heating cycle the curve during t_3 is not in continuation of the curve during t_1 which is consistent Hierarchical model.

reproduce the initial free-energy landscape. In this way, one can explains the above observed memory and rejuvenation effect of temporary cooling cycle using the Hierarchical model. Further, we have also checked the positive temperature cycling effect on the time dependence of magnetic relaxation M(t) of CFN sample [279]. Figs. 5.12(a) and (b) display the time dependence of relaxation of CFN sample below T_{SG} under ZFC and FC conditions, respectively with positive temperature cycling. It is clearly seen from

the figures that no memory effect is observed for positive temperature cycling consistent with the Hierarchical model of SG. In the Droplet model, one expects a symmetric behaviour corresponding to negative or positive cycling of temperature while in Hierarchical model, an asymmetric behaviour is expected. Thus, our results about the memory and rejuvenation effect under both ZFC and FC protocols with temperature cycling support the Hierarchical model of spin glass state.

5.4.7 Direct evidence for the presence of spin clusters in CFN using neutron diffraction:

As mentioned in section 5.4.2 the small dip in FC M(T) plot just below the SG freezing temperature T_f in the ZFC M(T) plot points towards the possibility of a CSG phase [198]. Similarly, the large value of attempt time τ_0 (~10^{-6}s), obtained from power law and V-F law fits to the temperature dependence of the spin relaxation time, also suggests that the SG phase of CFN may be of CSG type [24,42]. Neutron scattering technique can provide evidence not only for the presence of LRO AFM structure but also for short-range ordered (SRO) AFM clusters of spins in the CSG systems. The presence of SRO AFM spin clusters gives rise to diffuse scattering in the neutron scattering patterns [173,296,310–314]. Accordingly, we carried out neutron powder diffraction (NPD) measurements on powder samples of CFN to obtain direct evidence for the presence of AFM spin clusters. Fig. 5.13(a) depicts the NPD patterns of CFN at three selected temperatures, 300K, 100K and 5K, over a limited 2θ range from 5 to 90 deg. For LRO AFM phase, one expects a sharp magnetic peak corresponding to the pseudocubic Q=½½½ position shown with an arrow in Fig. 5.13(a). It can be clearly seen from this figure that no sharp magnetic Bragg peak characteristic of LRO AFM phase is observed in the NPD patterns of CFN down to 5K in marked contrast to PFN where such a peak has been observed below T_N~150K [172]. Instead, a broad diffuse peak, whose peak

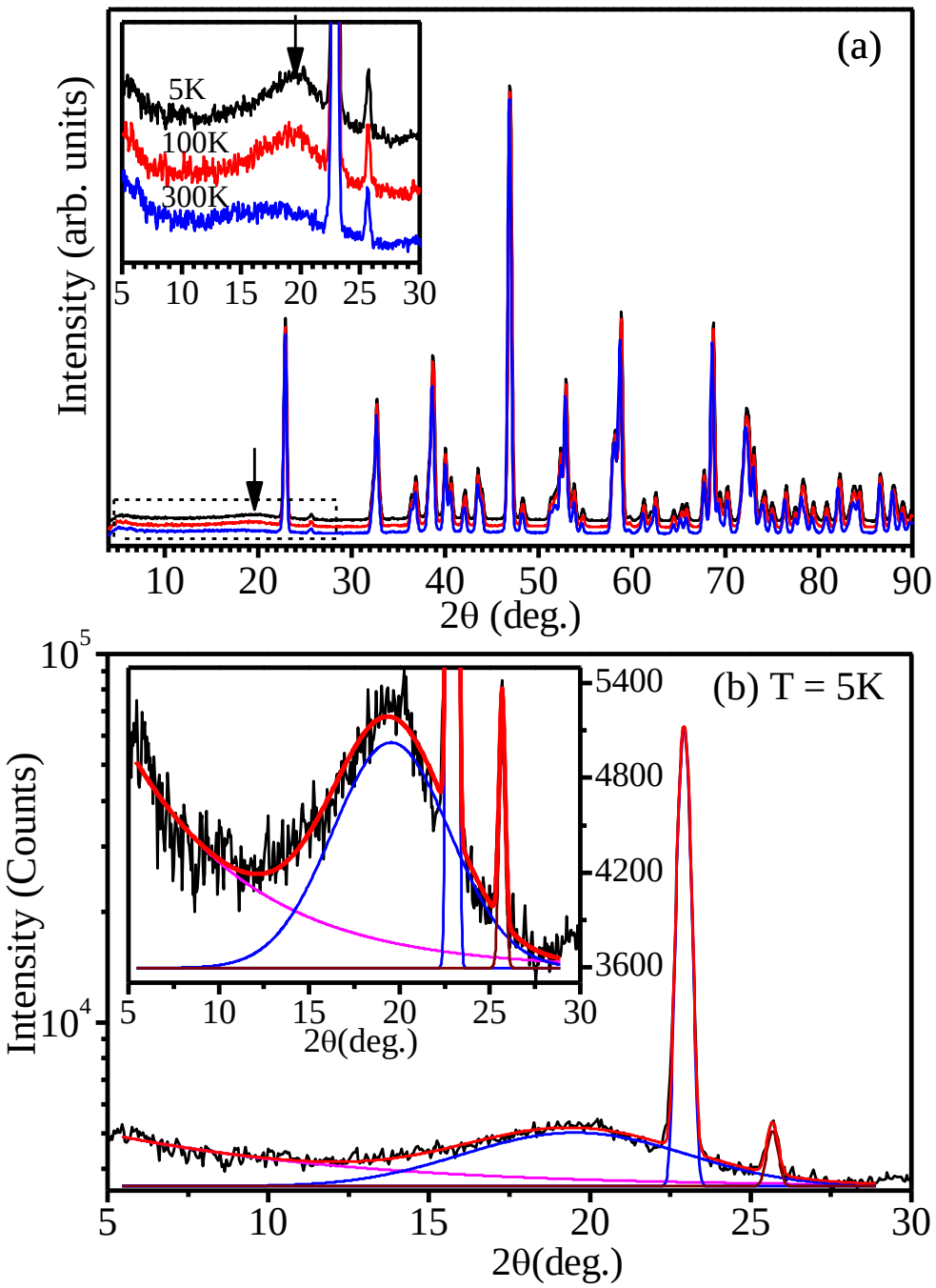

Figure 5.13: Panel **(a)** depicts neutron powder diffraction patterns of $Ca(Fe_{1/2}Nb_{1/2})O_3$ collected at 300K, 100K and 5K. The patterns are shifted vertically for the purpose of presentation. Inset of (**a**) depicts the enlarged scale of broad diffuse magnetic scattering peak corresponding to short-range antiferromagnetic correlations. Panel **(b)** depicts the deconvolution of the NPD profile peaks at 5K. Insets of panel (**b**) shows enlarged scale of deconvoluted peaks at 5K.

intensity is about 4% of the strongest nuclear peak, centred at the expected position of AFM LRO peak is clearly seen in Fig. 5.13(a) (see inset also). The observation of broad diffuse peak provides direct evidence for the presence of SRO AFM spin clusters. A similar broad diffuse peak has been reported in geometrically frustrated pyrochlores [310,311], spin-chain compounds [312,313], and spinels [314] showing CSG freezing.

It is interesting to note from Fig. 5.13(a) that the broad peak due to the short-range AFM correlated spin clusters are present even at room temperature which is much higher than T_f ~25K. It is also evident from the figure that with decreasing temperature, the intensity of the broad diffuse peak increases. In order to determine the correlation length for AFM spin clusters from the magnetic diffuse scattering, we deconvoluted the diffuse peak and the two neighbouring stronger peaks using three Gaussians and the result of the peak deconvolution is shown in Fig. 5.13(b) at 5K. The deconvoluted diffuse magnetic peak centered at $2\theta = 19.7^{o}$ at 5K is shown in the inset of Fig. 5.13(b). It is possible to determine the correlation length (ξ) from the FWHM of the deconvoluted diffuse magnetic peak using Scherrer formula $\xi = 0.9\lambda/\beta\cos\theta$ (Å), after removing the instrumental broadening from the observed FWHM of the diffuse peak (β_{obs}). We use the relationship $\beta = \sqrt{\beta_{obs}^2 - \beta_{inst}^2}$, where β is the intrinsic FWHM and β_{ins} is the FWHM of the instrumental resolution function to obtain the intrinsic broadening of the diffuse peak. The correlation length for the SRO spin clusters obtained from the intrinsic FWHM are (22±1), (19±1) and (14±2) Å at 5K, 100K and 300K, respectively. Thus our neutron scattering studies reveal that the size of the AFM correlated spin clusters increases slightly on lowering the temperature, but the AFM correlations could not develop to long length scales presumably due to the frustrated nature of the superexchange interactions in CFN. Our neutron scattering studies thus provide direct microscopic evidence for the

presence of SRO AFM correlated spin clusters of ~2nm average size for CSG freezing in CFN.

5.5. Conclusions:

In summary, we have synthesized phase pure $Ca(Fe_{1/2}Nb_{1/2})O_3$ (CFN) by conventional solid state route and characterised it its phase purity, crystal structure, microstructure and composition using the techniques discussed in chapter II and III.

We have investigated the low temperature magnetic transition in CFN using M(T), $\chi(\omega, T)$, M(T, H), M(T, t) and neutron scattering measurements. The analysis of dc magnetization measurements reveals a spin-glass (SG) phase with T_f ~25K with characteristic history dependent irreversibility. Analysis of the ac susceptibility measurements reveals power law/Vogel-Fulcher type critical spin dynamics with a time scale of $\tau_0 \sim 10^{-6}$s which suggests the existence of a cluster spin-glass (CSG) phase in CFN below T_{SG}~24K. The field dependence of the irreversibility temperature T_{irr} (H) and the peak temperature T_f(H) of the ZFC M(T) falls on de Almeida-Thouless (A-T) line in the $T_{irr}(H)/T_f$ (H) versus $H^{2/3}$ plot. The zero-field SG freezing temperature $T_f(0) = 25.2$K, obtained from the extrapolation of T_f(H) versus $H^{2/3}$ plot to H = 0, is in close agreement with the ergodicity breaking temperature T_{SG}~24K obtained from the analysis of the ac susceptibility $\chi(\omega, T)$ data. The observation of slow relaxation of thermoremanent magnetization, memory and rejuvenation effects below the SG transition temperature T_{SG}~24K supports glassy phase. Neutron diffraction study confirms the absence of any long-range AFM ordering but shows diffuse scattering due to the presence of short-range ordered (SRO) AFM spin clusters with a correlation length ξ ~2nm involved in the CSG freezing.

Chapter 6 $Ca(Fe_{1/2}Nb_{1/2})O_3$ as an incipient antiferromagnet: Role of critical percolation threshold concentration

6.1. Introduction

Magnetoelectric multiferroic materials, in which ferroelectric and magnetic orders not only coexist but also couple with each other, have received enormous attention in the current research [29,31,32,68,95]. Such materials have great promises for the development of new multifunctional devices for technological applications like sensors, actuators, storage devices, spintronics etc [29,32,34,68]. It has been shown that the ferroelectricity in ABO_3 perovskites arises due to the off-centring of the B-site cation which requires empty d-orbitals (d^0) [37] while the magnetism requires partially filled d orbitals (d^n). Since the two conditions are mutually exclusive the magnetoelectric multiferroics were believed to be rare [38]. The last two decades have witnessed the discovery of new multiferroic compounds like $RMnO_3$ (R = Tb, Dy, Y), $MnWO_4$, $LiCu_2O_2$, $Ni_3V_2O_8$, $LiCuVO_4$, $CoCrO_4$, CuO, $Ba_2Mg_2Fe_{12}O_{22}$, $Ba_{0.5}Sr_{1.5}Zn_2Fe_{12}O_{22}$ etc. in which polarization is induced as a result of magnetic order through inverse D-M interaction [39,40,315,316]. In such multiferroics, the mutually exclusiveness due to d^0 and d^n requirement is avoided, since ferroelectric polarization is an off-shoot of the magnetic transition itself coming from d^n element. The magnetic transition temperature in these materials is well below the room temperature. Unlike these multiferroics where ferroelectric polarization is a secondary order parameter where as the primary order parameter is magnetization, nature has also provided materials like $BiFeO_3$ where ferroelectricity originates from the hybridization of the $6s^2$ orbital of Bi^{3+}-ion containing stereochemically active lone pair of electrons with 2p orbitals of O^{2-}, while magnetism results from the $3d^5$ electrons of Fe^{3+} ion. This compound shows ferroelectric and antiferromagnetic transition temperatures as T_C ~1103K and T_N ~650K,

respectively [68,95]. In such materials, both ferroelectric polarization (P) and magnetization (M) are primary order parameters which emerge below T_C and T_N and also couple with each other [89,90,94]. Such multiferroics are termed as type-I whereas the former are termed as type-II multiferroics. In general, type-I multiferroics exhibit large ferroelectric polarization (~100μC/cm^2 for $BiFeO_3$) but weak magnetoelectric coupling whereas type-II multiferroics result in weak ferroelectric polarization ($\leq 10^{-2}$μC/cm^2) but strong magnetoelectric coupling [39,40,315,316].

Nearly six decades back, Russian researchers adopted another strategy to produce type-I multiferroicity by substituting both magnetic transition metal ion with d^n electrons like Fe, Co, Ni etc and ferro-active transition metal ions with d^0 electronic configuration, such as Nb^{5+}, Ta^{5+}, W^{6+} [147,152,171,172,174,191,192], at the B-site of the ABO_3 perovskite structure [183,184]. Using this idea, multiferroicity was reported in B-site disordered compounds like $Pb(Fe_{1/2}Nb_{1/2})O_3$ (PFN), $Pb(Fe_{1/2}Ta_{1/2})O_3$ (PFT) and $Pb(Fe_{2/3}W_{1/3})O_3$ (PFW) [147,152,171,172,174,183,184,191,192]. The d^0-ness of the Nb^{5+}, $Ta^{5+}$and W^{6+} and $6s^2$ lone pair of Pb^{2+} are believed to facilitate the development of ferroelectric order through hybridization of $4d^0$ Nb^{5+}, $5d^0$ Ta^{5+}, $5d^0$ W^{6+} and $6s^2$ Pb^{2+} orbitals with $2pO^{2-}$ orbitals [37,38]. One of the biggest puzzles about such complex perovskites is that only the Pb-based compounds PFN, PFT, and PFW show the expected long-range ordered (LRO) ferroelectric (FE)/ relaxor FE behaviour below T_C and also LRO AFM transition at T_N, whereas the corresponding Pb-free compounds like $Ca(Fe_{1/2}Nb_{1/2})O_3$ (CFN), $Sr(Fe_{1/2}Nb_{1/2})O_3$ (SFN), $Ba(Fe_{1/2}Nb_{1/2})O_3$ (BFN), $Ca(Fe_{1/2}Ta_{1/2})O_3$ (CFT), $Sr(Fe_{1/2}Ta_{1/2})O_3$ (SFT), $Ba(Fe_{1/2}Ta_{1/2})O_3$ (BFT) neither show LRO FE/relaxor FE nor LRO AFM transition [176–178]. The only common feature in both group of compounds is that they exhibit spin-glass (SG) transition in the range 10-25K. In the preceding chapter, we discussed at length the role of short range ordered AFM spin

clusters in the spin glass phase of these compounds taking CFN as an example. In this chapter, we address the issue of absence of LRO AFM in Pb-free disordered compounds of the type $A(Fe_{1/2}B_{1/2})O_3$ taking $Ca(Fe_{1/2}Nb_{1/2})O_3$ (CFN) and its solid solutions with $BiFeO_3$ (BF) and $LaFeO_3$ (LF) as examples.

Raeviskii et al. [203] proposed that the stability of the LRO AFM phase is significantly enhanced in Pb-based compounds as compared to Pb-free compounds due to the critical role of lone pair electrons of $6s^2Pb^{2+}$ orbital. They proposed that in these compounds, the superexchange interactions can also be mediated by Pb^{2+} (Fe^{3+}-Pb^{2+}-Fe^{3+}) in the $<111>_{pc}$ direction to form the LRO AFM phase in contrast to Pb-free perovskite compounds where the superexchange interaction is via oxygen only, i.e. Fe^{3+}-O^{2-}-Fe^{3+} [194]. Theoretically, the stabilisation of LRO magnetic phase in disordered Ising and Heisenberg systems is decided by the percolation threshold concentration (c_p) [24,195–197]. The percolation threshold value is highly sensitive to the strength of the exchange interactions and therefore varies from material to material [238,239,242,243]. Monte-Carlo calculations for 3D Heisenberg systems with simple cubic lattice have predicted a percolation threshold (c_p) value of ~0.307 [195–197] while for the 3D Ising system this value is ~0.88 [195]. Since some of the Pb-free complex perovskites like CFN and SFN have tilted octahedral configuration, which makes the Fe^{3+}-O^{2-}-Fe^{3+} bond angles deviate from 180°, in marked contrast to the paraelectric/paramagnetic phase of the Pb-based PFN, PFT and PFW. Such a bending of Fe^{3+}-O^{2-}-Fe^{3+} bonds would make Dzyaloshinskii-Moriya (D-M) interaction non zero and lead to spin canting [317]. This makes the systems like CFN effectively Heisenberg type. Since the concentration of magnetic ion (Fe^{3+}) on the B-site of the CFN is 50%, which is considerably higher than the percolation threshold limit for 3D Heisenberg systems, it is surprising that such Pb-free complex perovskites do not show any transition to a LRO AFM phase. Theoretical models have

predicted a LRO AFM transition around 200K in such systems [318] but the transition does not happen in real systems. Therefore, it is of interest to verify if the absence of the LRO AFM phase could be due to the percolation threshold problem in such Pb free complex perovskites.

With this objective in mind, we present in this chapter the results of dc magnetization neutron scattering and dielectric measurements on CFN and its solid solutions. Our neutron diffraction results reveal that CFN is an incipient AFM whose SRO AFM correlation length start growing below 200K eventhough the size of the AFM spin-clusters remains limited to ~2 nm at the lowest temperature (4K). We also show that the LRO AFM state of CFN can be stabilized with T_N~175K by increasing the Fe^{3+} content slightly by about 5% through a solid solution formation with compounds like $BiFeO_3$ and $LaFeO_3$. Observation of significant magnetoelastic and magnetodielectric coupling in the vicinity of T_N in these solid solutions, raises the possibility of CFN being a multiferroic.

6.2. Sample preparation:

Polycrystalline $Ca(Fe_{1/2}Nb_{1/2})O_3$ (CFN), and $0.90Ca(Fe_{1/2}Nb_{1/2})O_3$-$0.10BiFeO_3$ (CFN-0.10BF), $0.90Ca(Fe_{1/2}Nb_{1/2})O_3$-$0.10LaFeO_3$ (CFN-0.10LF) were prepared by standard solid-state thermochemical route using high purity carbonates ($CaCO_3$), and oxides (Bi_2O_3, Fe_2O_3, La_2O_3, and Nb_2O_5) supplied by Sigma Aldrich. The details of sample preparation of CFN is given in the preceding chapter. We followed the same procedure for the preparation of CFN-0.10BF and CFN-0.10LF solid solution samples also. Here, we would like to mention that the sintering of the CFN-0.10BF was carried out in a closed alumina crucible with calcined powder of the same composition as spacer powder for preventing the loss of Bi_2O_3 during sintering. CFN-0.10LF was, on the otherhand, sintered in an open crucible.

6.3. Characterizations:

The characterization of CFN is already given in the previous chapter. Microstructure of the CFN-0.10BF pellet was obtained using a Carl-Zeiss Scanning Electron Microscope (SEM), model no. EVO 18. The chemical compositions were checked by Energy Dispersive X-ray spectroscopy (EDX) attachment (Oxford, model no. 51-ADD0048) in the above-mentioned SEM. The sintered pellet was coated with conducting gold using sputter coater (Royal life Sciences, model no. DSR1) under vacuum before taking the SEM images.

X-ray powder diffraction (XRD) measurements were carried out on CFN-0.10BF and CFN-0.10LF using an 18-kW Cu rotating anode powder diffractometer (Rigaku, model no. RINT 2500/PC series) operating in the Bragg-Brentano geometry and fitted with a curved crystal monochromator in the diffraction beam. The data were collected in the 2θ range 20 to 120° at a step of 0.02 degrees.

High-resolution neutron powder diffraction (NPD) patterns were collected on CFN in the temperature range 4-300K at close temperature intervals using structure powder diffractometer SPODI at FRM-II research reactor in Garching, Germany. The incident neutron wavelength was 1.5482Å as obtained from germanium (551) reflection of vertically focussed monochromator at a take-off angle of 155°. Approximately 12g powder sample was kept in a cylindrical vanadium (V) can of diameter 4mm which was cooled to different temperatures using close cycle helium refrigerator. The temperature dependent NPD data on CFN-0.10BF and CFN-0.10LF samples were collected in the range 290 K to 3 K at Druva reactor, BARC, Mumbai at a wavelength of 1.48 Å using high-resolution powder diffractometer PD-3 over 2θ =5 to 120 degrees. A close cycle helium refrigerator (CCR) (Cryogenic, A S Scientific UK) with variable temperature insert (VTI) was used for sample temperature variation. For this also, the powder sample

was filled in a vanadium can of 6mm diameter and attached to the sample rod of the VTI. The nuclear and magnetic structures were analysed by Rietveld technique using FullProf suite [253].

DC magnetization measurements were carried out on vibrating sample magnetometer (VSM) option attached to physical property measurement system (Dynacool PPMS, Quantum Design).

For the dielectric measurements, the pellets were gently polished with 0.25μm size diamond paste. After then acetone was used to clean the surfaces and then put on the isopropyl alcohol to remove the moisture on the surfaces. The electroding of the pellets on both sides was done using fired-on silver paste which is cured at 773K for 5 minutes. Low temperature dielectric measurement was performed at a heating rate of 1K/minute using a fully computer-controlled measuring system involving Novocontrol (Alpha-A) high performance frequency analyzer and 7T cryogen free superconducting magnet-based measurement system (Cryogenic, model no. 7 Tesla mini CFM).

6.4. Results and discussion:

6.4.1 Microstructure and chemical composition:

The details of microstructure and chemical composition of $Ca(Fe_{1/2}Nb_{1/2})O_3$ are already given in the previous chapter V. A typical scanning electron micrograph image of ceramic sample of CFN-0.10BF is shown in Fig. 6.1(a). The average grain size was estimated using Image J software and is found to be approximately (2.8±0.3) μm. The EDX spectrum of CFN-0.10BF sample shown on the right panel (b) of Fig.6.1 reveals that the ceramic sample consists of calcium (Ca), iron (Fe), niobium (Nb), bismuth (Bi), and oxygen (O) atoms. The EDX analyses were carried out at several randomly selected regions and the results of the average composition is given in Table 6.1. It is evident from these table that the average composition obtained by EDX analysis is close to the nominal

(expected) composition within the limit of standard deviation for Ca, Fe, Nb, Bi, and O. This confirms the excellent quality of the sample. We expect CFN-0.10LF sample to be of the same quality.

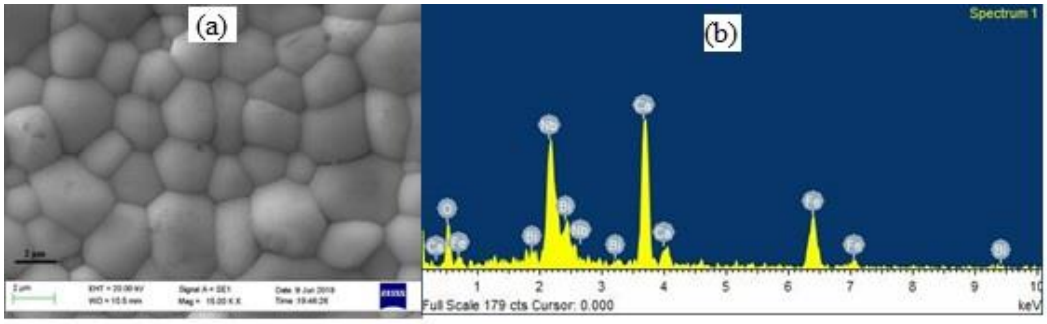

Figure 6.1: **(a)** Microstructure and **(b)** EDX spectra of CFN-0.10BF ceramic sample.

Table 6.1: Quantification of chemical composition of CFN-0.10BF sample.

Elements	Average chemical composition in wt %	
	Expected	Observed
Ca	20.3	19.9 ± 0.8
Bi	11.8	11.7 ± 0.9
Fe	17.3	16.7 ± 0.8
Nb	23.6	24.9 ± 0.8
O	27.0	26.8 ± 0.7

6.4.2 Room temperature crystal structure:

The room temperature crystal structure of CFN has already been discussed in chapter V. In CFN samples, we observed three types of superlattice reflections having indices odd-odd-odd (ooo), odd-odd-even (ooe) and even-even-odd (eeo). The presence of ooo and ooe type superlattice reflections confirms the anti-phase and in-phase tilts in these compounds. The superlattice reflections with indices of eeo-type arise due to the

antiparallel cation displacement of the A-site cation. Such superlattice reflections are also observed similar to that for the well-known perovskite compound $CaTiO_3$ which belongs to $a^-a^-c^+$ tilt system in Glazer's notation [204] with orthorhombic structure in the Pbnm space group. In the previous chapter, we confirmed this structure for CFN. Since diffraction peaks of CFN-0.10BF and CFN-0.10LF are identical to CFN with no extra peaks or additional peak splitting, we expect the orthorhombic structure in the Pbnm space group for these solid solutions of CFN also. The room temperature crystal structure of CFN-0.10BF and CFN-0.10LF was further confirmed by Rietveld refinement using XRD data. As for the asymmetric unit of orthorhombic phase of CFN-0.10BF and CFN-0.10LF is concerned, the Ca/Bi/La occupy 4c Wyckoff site at (x, y, 1/4) position, Fe/Nb occupy 4b Wyckoff site at (1/2, 0, 0) position. The two oxygen atoms O_1 occupy the Wyckoff 4c and 8d sites with positional coordinates (x, y, 1/4) and (x, y, *z*), respectively. We used linear interpolation and pseudo-Voigt function for modelling of the background and peak shape. During the refinement, the occupancy of all the atoms was fixed to the nominal composition and all other parameters like zero correction, scale factor, background, lattice parameters, half width parameters (u, v and w), positional coordinates and thermal parameters were varied. The refinements converged after a few cycles. Fig. 6.2 compares the results of the Rietveld refinement of CFN, CFN-0.10BF and CFN-0.10LF at room temperature. The observed (filled-circles) and calculated (continuous line) profiles show excellent fit as can be seen from the nearly flat difference (bottom line) profile. This confirm that all the three compounds belong to orthorhombic crystal structure in the Pbnm space group with $a^-a^-c^+$ tilt system. The refined unit cell parameters, positional coordinate and thermal parameters are given in Table 6.2.

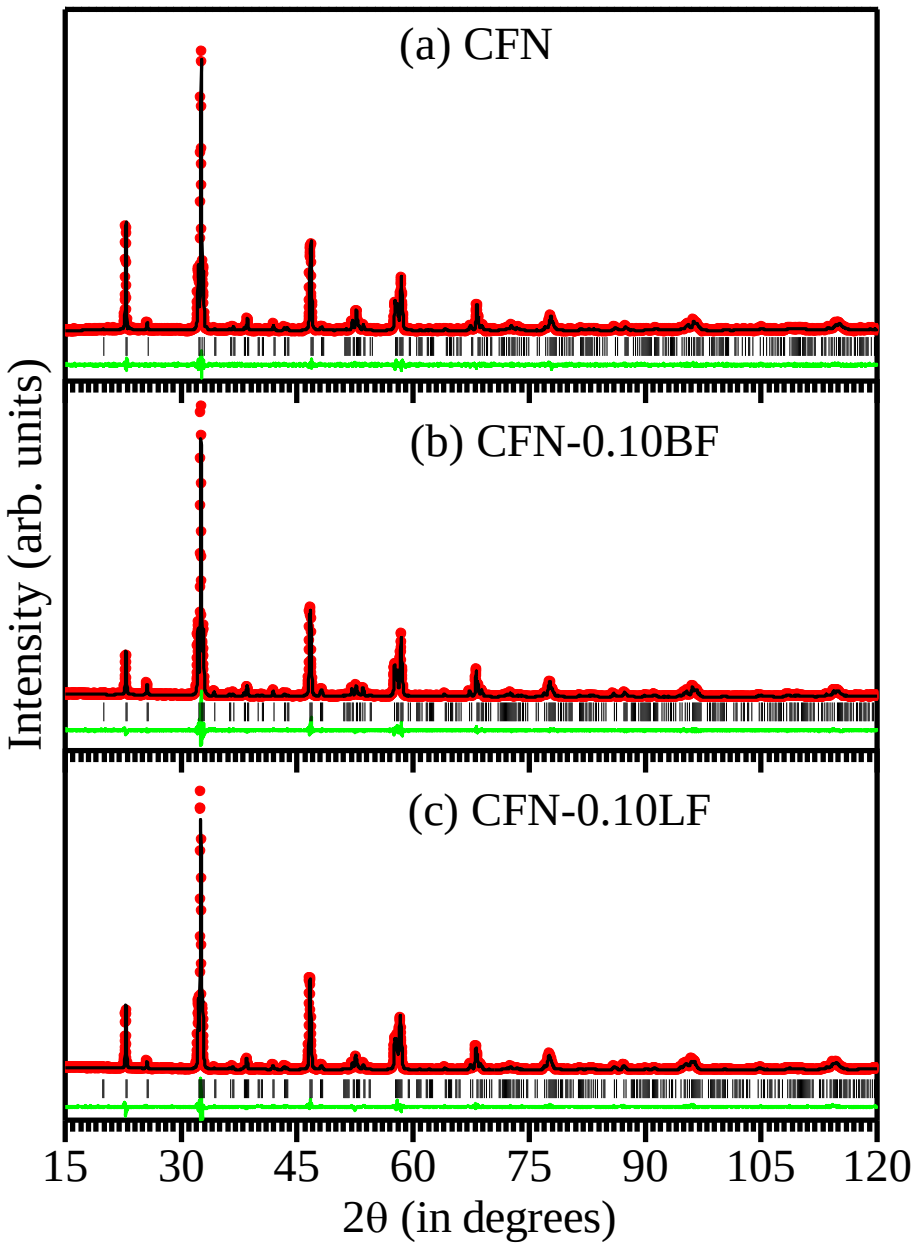

Figure 6.2: Observed (red dots), calculated (black continuous line) and difference (green continuous line) profiles obtained from Rietveld refinement using x-ray diffraction data of **(a)** $Ca(Fe_{1/2}Nb_{1/2})O_3$ **(b)** $Ca(Fe_{1/2}Nb_{1/2})O_3$-0.10$BiFeO_3$ **(c)** $Ca(Fe_{1/2}Nb_{1/2})O_3$-0.10$LaFeO_3$ at room temperature using Pbnm space group. Vertical tick marks above the difference profile represent the Bragg peak positions.

Table 6.2: Rietveld refined structural parameters and agreement factors for CFN, CFN-0.10BF and CFN-0.10LF using Lab XRD data at 300K with Pbnm space group.

Parameters	CFN	CFN-0.10BF	CFN-0.10LF
$A_{O\,(Å)}$	5.4455 (1)	5.4499 (1)	5.4609 (2)
$B_{O\,(Å}$	5.5501 (2)	5.5613 (9)	5.5531 (2)
$C_{O\,(Å}$	7.7556 (2)	7.7669 (1)	7.7727 (1)
$V_{O\,(Å^3)}$	234.398 (11)	235.413 (7)	235.710 (12)
α, β, γ	$\alpha=\beta=\gamma=90^0$	$\alpha=\beta=\gamma=90^0$	$\alpha=\beta=\gamma=90^0$
Ca/Bi (x)	0.010 (1)	0.006 (7)	0.006 (7)
Ca/Bi (y)	0.042 (5)	0.046 (3)	0.038 (3)
Ca/Bi (z)	0.25	0.25	0.25
Fe/Nb (x)	0.5	0.5	0.5
Fe/Nb (y)	0	0	0
Fe/Nb (z)	0	0	0
O1 (x)	0.9194 (2)	0.9155 (1)	0.9128 (2)
O1 (y)	0.4476 (2)	0.4802 (1)	0.473 (1)
O1 (z)	0.25	0.25	0.25
O2 (x)	0.2995 (1)	0.2894 (1)	0.2932 (9)
O2 (y)	0.2922 (1)	0.2937 (9)	0.2987 (8)
O2 (z)	0.0436 (9)	0.0461 (8)	0.045 (8)
$\beta_{Ca/Bi}$ (Å^2)	1.05 (6)	1.21 (4)	1.21 (4)
$\beta_{Fe/Nb}$ (Å^2)	0.51 (4)	0.51 (2)	0.51 (2)
β_{O1} (Å^2)	1.43 (2)	0.36 (1)	0.36 (1)
β_{O2} (Å^2)	0.75 (2)	0.34 (2)	0.34 (2)
R_{wp} (%)	17.3	18.3	18.8
χ^2	1.43	1.46	1.51

6.4.3 Magnetic transitions in CFN, CFN-0.10BF and CFN-0.10LF:

6.4.3.1 DC magnetization studies:

Fig. 6.3 depicts the temperature dependence of dc magnetization M(T) of CFN, CFN-0.10BF and CFN-0.10LF samples measured in the temperature range 2-395K at 500 Oe field during heating cycle after zero-field cooled (ZFC) and field cooled (FC) conditions of the sample. It is evident from Fig. 6.3(a) that the ZFC curve for CFN gradually increases with decreasing temperature from 395K and reveals a cusp at 25K due to spin-glass transition discussed in the previous chapter and a kink around 10K of unknown origin. While the ZFC M(T) curve of CFN-0.10BF and CFN-0.10LF also increases gradually upto around 175K (see Figs. 6.3(c) and (e)) but it begins to increase sharply below 175K revealing the occurrence of a LRO magnetic transition. On further

cooling, the ZFC M(T) shows two anomalies around 50K and 16K. We believe that as a result of substitution of 10%$BiFeO_3$ or 10%$LaFeO_3$ in CFN, the low temperature transitions at 25K and 10K of CFN have shifted towards higher temperature side. What is most significant is the appearance of a new magnetic transition around 175K which is not seen in the case of pure CFN. This indicates that the CFN is at the verge of acquiring LRO state and increasing the Fe^{3+} content slightly from 50% to 55% led to the stabilization of the LRO state, presumably as a result of crossing the percolation threshold value.

In order to check what type of LRO correlation is developing below 175K in these two solid solutions, we plot the temperature dependence of inverse of ZFC magnetic susceptibility (see Figs. 6.3(b) (d) and (f)). A least-squares fit using Curie-Weiss (C-W) law $\chi(T) = \left(\frac{C}{T-\theta_W}\right)$ above 350K yields Curie constant C = 1.241, 1.254, and 1.293 emuK $mol^{-1}Oe^{-1}$ and Curie-Weiss temperature θ_W = -(113.7±0.8), -(137.9±1) and –(131.8±5)K for CFN, CFN-0.10BF, CFN-0.10LF, respectively. The effective magnetic moment (μ_{eff}) determined from Curie constant using relationship $\mu_{eff} = 3Ck_B/N_A$ comes out to be 3.15, 3.18 and 3.22μ_B for the three compositions. The large negative value of Curie-Weiss temperature confirms the presence of strong antiferromagnetic correlations in CFN. It also confirms that the LRO state of the two solid solutions corresponds to AFM ordering. The effective magnetic moment is approximately half of the expected moment (5.92μ_B) for the high spin Fe^{3+} (S=5/2) state. This is consistent with the fact that there is 50% to 45% dilution of the magnetic sublattice due to the presence of nonmagnetic Nb^{5+} ions. The low value of the effective moment may also be due to the presence of AFM clusters above T_N. To capture the atomic moments of Fe^{3+} in the paramagnetic state, one has to go to still higher temperatures to destroy such AFM clusters.

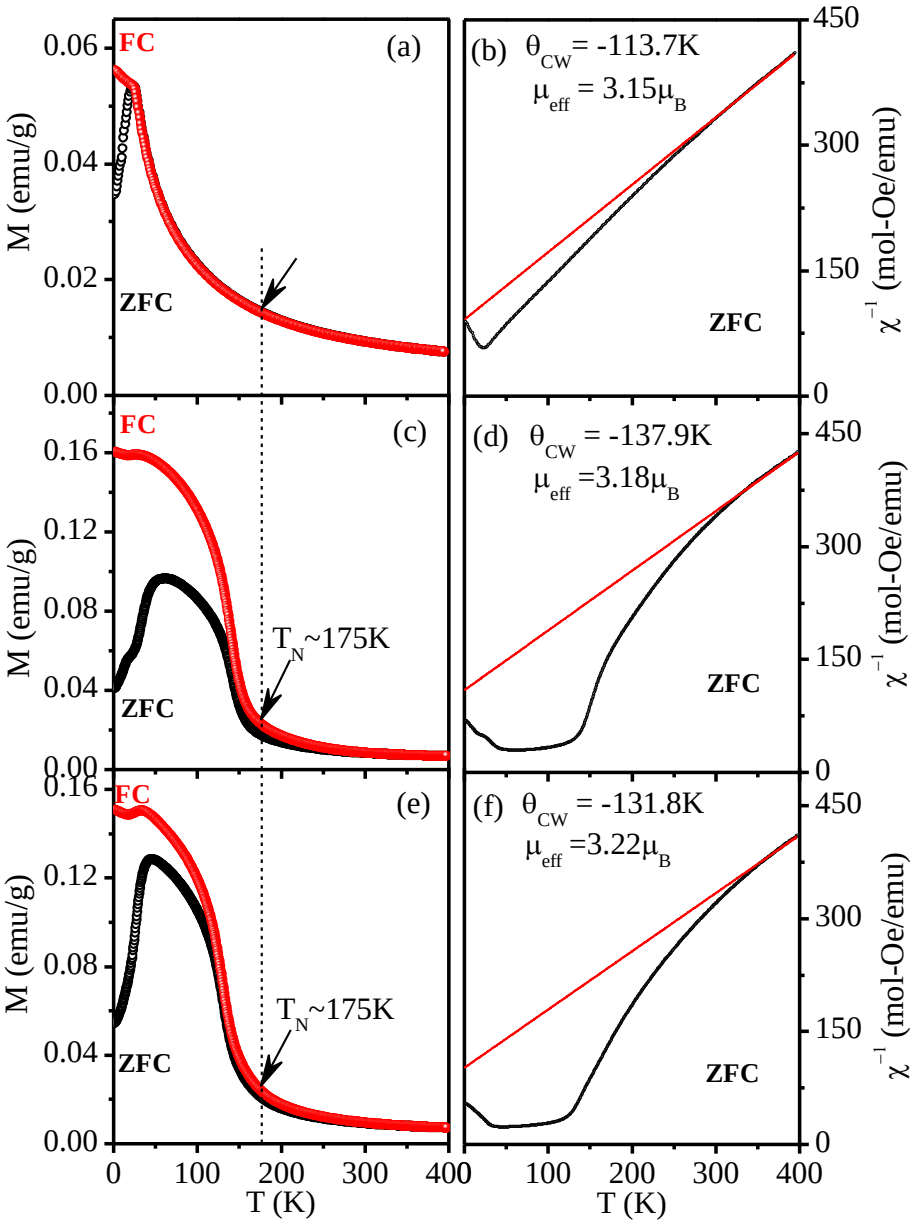

Figure 6.3: Left panel (a, c, e) depicts the ZFC and FC dc magnetization versus temperature plots for CFN, CFN-0.10BF and CFN-0.10LF, respectively and right panel (b, d, f) shows the corresponding Curie-Weiss plot using ZFC M(T) data.

6.4.3.2 Confirmation of LRO AFM state in CFN-0.10BF and CFN-0.10LF by neutron powder diffraction studies:

The LRO AFM nature of CFN-0.10BF and CFN-0.10LF below T_N~175K was confirmed by neutron scattering studies of the powder samples. Figs. 6.4 and 6.5 depict

the temperature evolution of the neutron powder diffraction (NPD) patterns of CFN-0.10BF and CFN-0.10LF in the temperature range 3-290K over a limited 2θ range of 5-70º. It is evident from the temperature evolution of the NPD patterns of both the solid solutions that a magnetic peak appears at 2θ = 19.04º corresponding to the **k** = ½½½ position of the AFM peak in the elementary perovskite unit cell. At room temperature, the peak is very broad indicating the presence of short-range ordered (SRO) AFM spin clusters even above T_N~175K. With decreasing temperature, the peak gets sharper. One may also notice a sudden increase in the peak intensity of this peak at T≲T_N ~175K revealing the growth of SRO AFM spin clusters into LRO AFM phase. This is in perfect agreement with the dc magnetization measurements of both the solid solution which show sudden increase in M(T) around 175K. It was verified that the nuclear structure does not change down to the lowest temperature of measurement (3K) as the two systems undergo an AFM phase transition. All the nuclear structure peaks in Figs. 6.4 and 6.5 are well indexed with respect to the unit cell of the Pbnm space group of CFN. Further, the observation of the 311, 310 and 021 peaks of ooo, ooe and oee type at 2θ = 36.88º, 35.16º and 24.52º, respectively, confirms the presence of anti-phase tilt, in-phase tilt and antiparallel displacement of Ca/Bi as well as Ca/La as expected for the $a^-a^-c^+$ tilt system in Glazer's notation [204]. The 311, 310 and 021 indices for the superlattice peaks are with respect to a doubled pseudocubic perovskite cell. Since the nuclear unit cell is already doubled, the AFM peaks corresponds to the propagation vector **k** = (0, 0, 0) of the doubled pseudocubic unit cell. It would correspond to **k** =½½½ position of AFM structure with respect to the elementary perovskite cell.

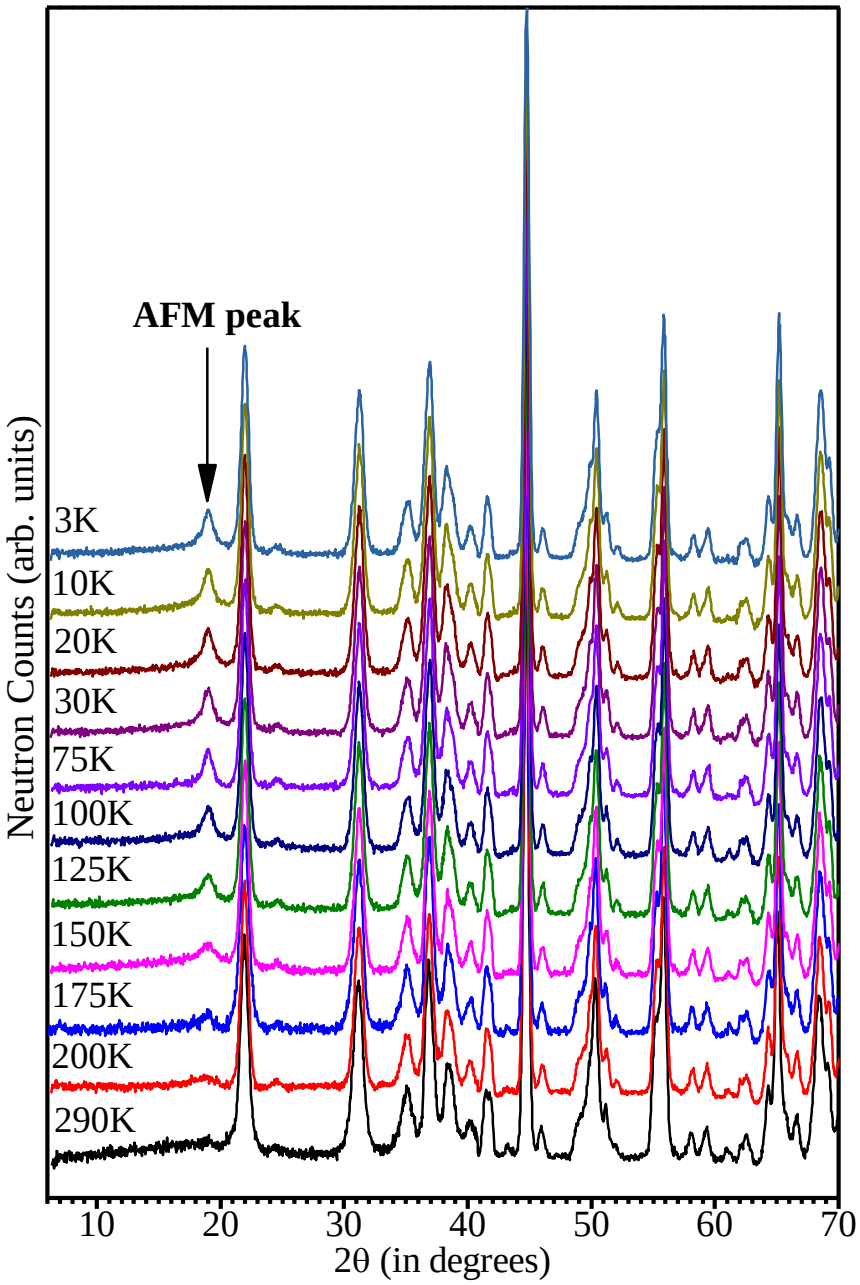

Figure 6.4: Temperature dependent evolution of NPD patterns of CFN-10BF over a limited 2θ range 5 to 70 degrees. Arrow marks the antiferromagnetic (AFM) ordering peak.

The magnetic peaks in the NPD patterns were indexed by considering additional phase in the refinement with propagation vector **k** = (0,0,0). We use representation theory approach to determine the magnetic structure of both the solid solutions below T_N ~175K. In the Pbnm space group, the list of irreducible representations corresponding to

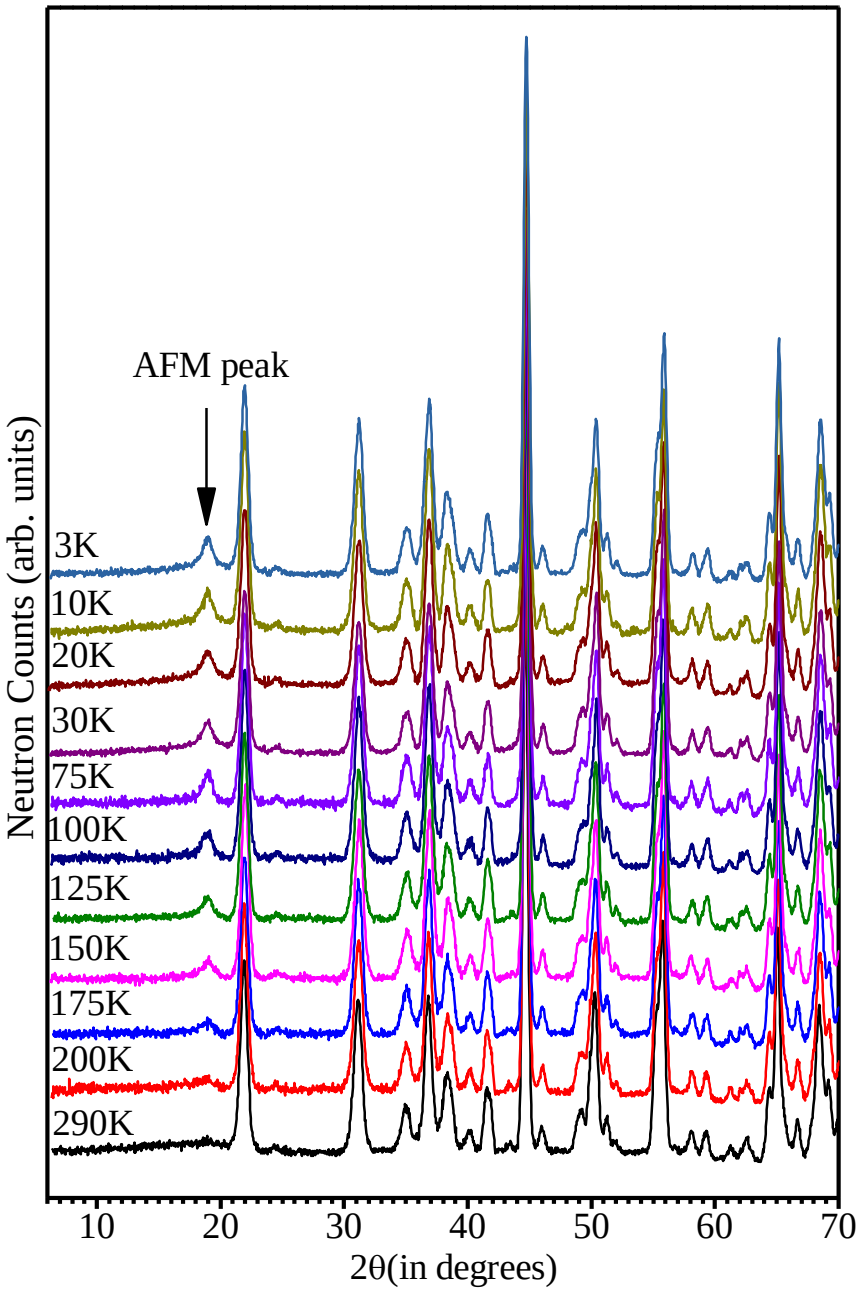

Figure 6.5: Temperature dependent evolution of NPD patterns of CFN-0.10LF over a limited 2θ range 5 to 70 degrees. Arrow marked the antiferromagnetic (AFM) ordering peak.

propagation vector **k** = (0,0,0) are Γ_1, Γ_2, Γ_3, Γ_4, Γ_5, Γ_6, Γ_7 and, Γ_8. All these irreps are one dimensional. In the orthorhombic unit cell with Pbnm space group, the magnetic ions Fe^{3+} occupy the 4b Wyckoff site with coordinates (1/2, 0, 0). As the Wyckoff position 4b contains a centre of symmetry, four of the above irreps, i.e. Γ_2, Γ_4, Γ_6, Γ_8, are not

allowed [319]. The magnetic reducible representation for the magnetic Fe^{3+} at the 4b site can therefore be decomposed as a direct sum of the irreducible representations as follows:

$$\Gamma(4b) = 3\Gamma_1 \oplus 3\Gamma_3 \oplus 3\Gamma_5 \oplus 3\Gamma_7 \quad \ldots\ldots\ldots (6.1)$$

The basis vectors associated with each irreducible representation are given in Table 6.3. All the four irreducible representations were considered in the Rietveld refinement of CFN-0.10BF to determine which irrep would give the best fit. The initial input parameters for Rietveld refinement of nuclear structure were taken from the Rietveld refinement using XRD data. The magnetic structure was considered as a second phase in the P-1 space group. Use of this space group in conjunction with representation theory

Table 6.3: The basis vectors of the irreducible representations of the space group Pbnm appearing in the magnetic representation at the Wyckoff position 4b for the wave vector k = (0, 0, 0).

IRs	Fe (4b)				
	Basis vectors	(x,y,z)	(-x,-y,z+1/2)	(x+1/2,-y+1/2,-z)	(-x+1/2,y+1/2,-z+1/2)
Γ_1	Ψ_1	(1 0 0)	(-1 0 0)	(1 0 0)	(-1 0 0)
	Ψ_2	(0 1 0)	(0 -1 0)	(0 -1 0)	(0 1 0)
	Ψ_3	(0 0 1)	(0 0 1)	(0 0 -1)	(0 0 -1)
Γ_3	Ψ_1	(1 0 0)	(-1 0 0)	(-1 0 0)	(1 0 0)
	Ψ_2	(0 1 0)	(0 -1 0)	(0 1 0)	(0 -1 0)
	Ψ_3	(0 0 1)	(0 0 1)	(0 0 1)	(0 0 1)
Γ_5	Ψ_1	(1 0 0)	(1 0 0)	(1 0 0)	(1 0 0)
	Ψ_2	(0 1 0)	(0 1 0)	(0 -1 0)	(0 -1 0)
	Ψ_3	(0 0 1)	(0 0 -1)	(0 0 -1)	(0 0 1)
Γ_7	Ψ_1	(1 0 0)	(1 0 0)	(-1 0 0)	(-1 0 0)
	Ψ_2	(0 1 0)	(0 1 0)	(0 1 0)	(0 1 0)
	Ψ_3	(0 0 1)	(0 0 -1)	(0 0 1)	(0 0 -1)

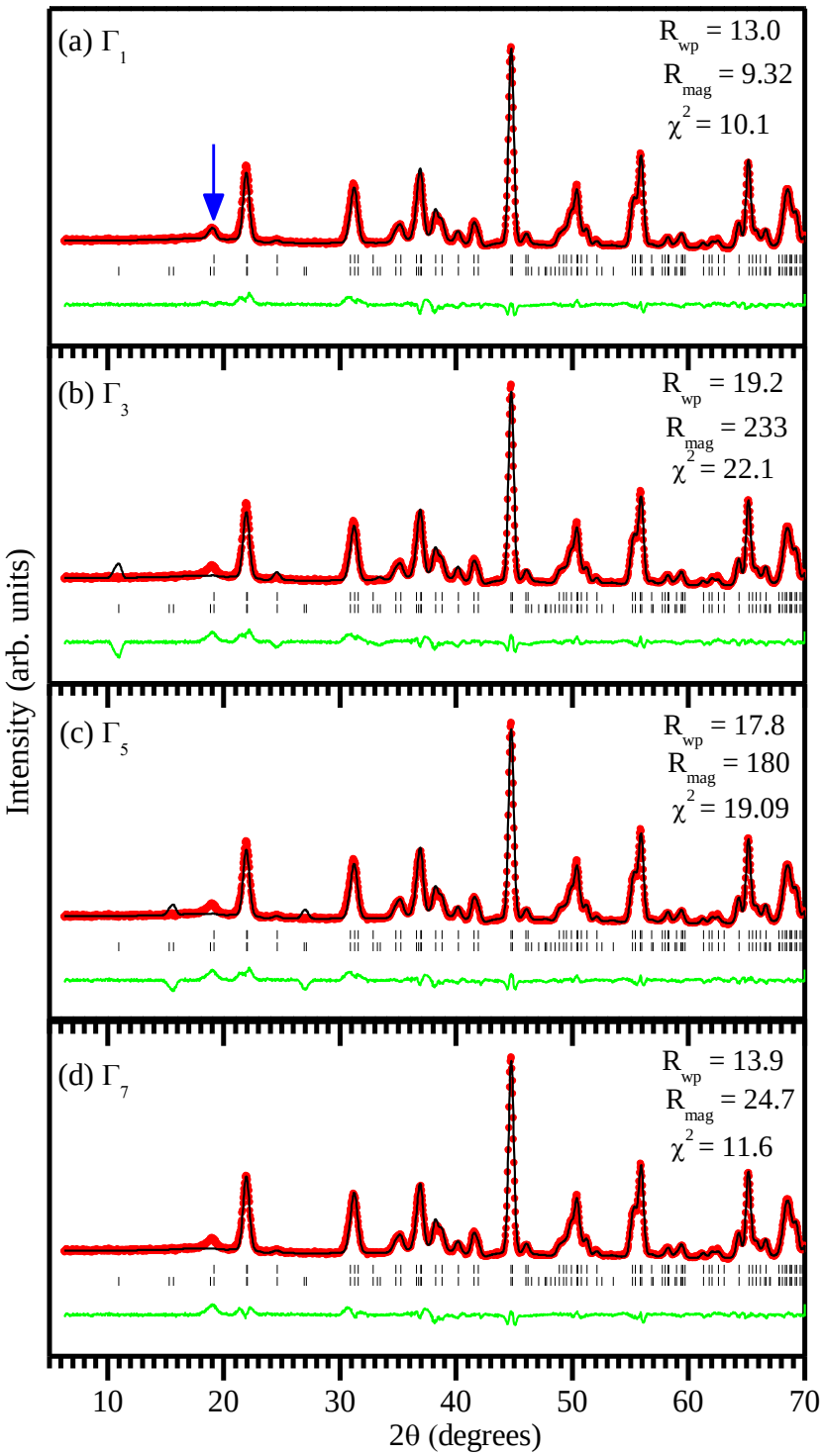

Figure 6.6: Observed (filled circles), calculated (continuous line), and difference (bottom line) profiles obtained from Rietveld refinement using NPD data of CFN-0.10BF at 100K for propagation vector k = (0,0,0) and the irreducible representations (a) Γ_1 (b) Γ_3 (c) Γ_5 and (d) Γ_7. Arrow marked the AFM peak. The vertical tick marks correspond to the position of all allowed Bragg reflections for the nuclear (top) and magnetic (bottom) reflections.

approach in FULLPROF package generates many fictitious magnetic peak positions also. Both the nuclear and magnetic structures were refined, and the refinement converged successfully after a few cycles. Figs. 6.6(a-d) compare the fits between the observed (filled-circles) and calculated (continuous line) profiles of CFN-0.10BF corresponding to the four irreps. It is evident from the figure that the irreps Γ_3, Γ_5 and Γ_7 fail to model the observed magnetic peak and therefore these irreps were rejected. The magnetic peak is well accounted by the irrep Γ_1. Hence, the irreducible representation Γ_1 represents the correct magnetic structure of CFN-0.10BF. A schematic depiction of the spin arrangement corresponding to the four irreps are shown in Fig. 6.7.

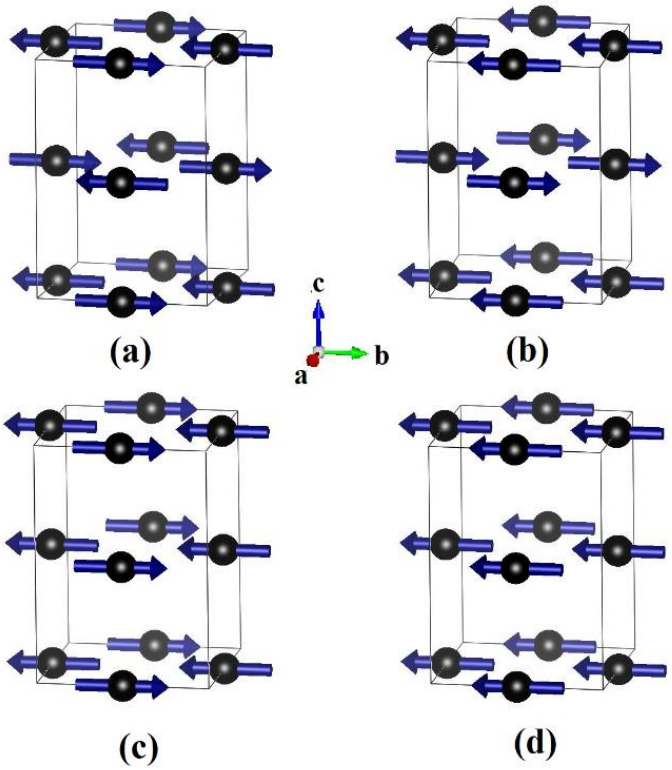

Figure 6.7: The magnetic structure of 0.90CFN-0.10BF corresponding to representation (a) Γ_1 (G-type AFM ordering) (b) Γ_3 (A-type AFM ordering) (c) Γ_5 (C-type AFM ordering) and (d) Γ_7 (FM-type Ordering).

In a similar way, we refined the magnetic structure of CFN-0.10BF and CFN-10LF solid solutions using the irreducible representation Γ_1 using the NPD pattern at 100K. Figs. 6.8 (a) and (b) show the results of the Rietveld refinements of CFN-0.10BF and CFN-0.10LF at 100K using Pbnm space group and magnetic structure corresponding to the irrep Γ_3. It can be clearly seen from the figures that the fit between the observed and calculated profiles is very good corresponding to the irrep Γ_1 which leads to G-type AFM

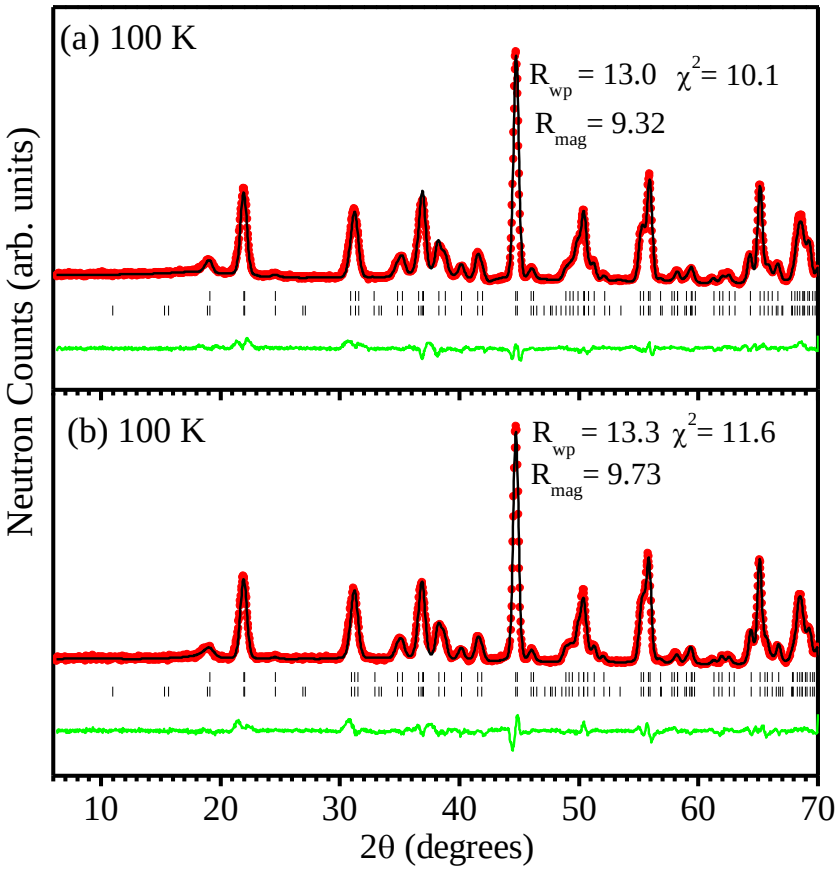

Figure 6.8: Observed (filled circles), calculated (continuous line), and difference (bottom line) profiles obtained from Rietveld refinement using NPD data at 100K for (a) CFN-0.10BF and (b) CFN-0.10LF for propagation vector k = (0,0,0) and the irreducible representation Γ_1. The vertical tick marks correspond to the position of all allowed Bragg reflections for the nuclear (top) and magnetic (bottom) reflections.

ordering as shown in Fig. 6.7(a). The refined lattice parameters, positional coordinates, thermal parameters and magnetic moment are listed in Table 6.4.

Table 6.4: Rietveld refined structural parameters and agreement factors for CFN-0.10BF and CFN-0.10LF using NPD data at 100K.

Parameters	**CFN-0.10BF**	**CFN-0.10LF**
$A_{O\,(Å)}$	5.4460 (2)	5.4566 (3)
$B_{O\,(Å}$	5.5589 (3)	5.5556 (2)
$C_{O\,(Å}$	7.7635 (4)	7.7705 (4)
α, β, γ	$\alpha=\beta=\gamma=90^0$	$\alpha=\beta=\gamma=90^0$
Ca/Bi (x)	0.006 (3)	0.005 (7)
Ca/Bi (y)	0.046 (3)	0.037 (3)
Ca/Bi (z)	0.25	0.25
Fe/Nb (x)	0.5	0.5
Fe/Nb (y)	0	0
Fe/Nb (z)	0	0
O1 (x)	0.9176 (1)	0.9128 (2)
O1 (y)	0.4758 (9)	0.473 (1)
O1 (z)	0.25	0.25
O2 (x)	0.2946 (1)	0.2932 (9)
O2 (y)	0.2958 (3)	0.2987 (3)
O2 (z)	0.0452 (5)	0.045 (1)
$\beta_{Ca/Bi}$ (Å^2)	1.24 (2)	1.31 (6)
$\beta_{Fe/Nb}$ (Å^2)	0.59 (4)	0.73 (2)
β_{O1} (Å^2)	0.52 (2)	0.68 (5)
β_{O2} (Å^2)	0.71(5)	0.89 (4)
$\mu Fe\,(\mu_B)$	3.09	2.97
R_{wp} (%)	13.0	13.3
R_{mag} (%)	9.32	9.73
χ^2	10.1	11.6

It is interesting to note that both $BiFeO_3$ and $LaFeO_3$ substitutions stabilize the LRO AFM phase with T_N~175K. This raises doubts about the earlier proposition [175] that the absence of LRO AFM phase in Pb-free $A(Fe_{1/2}B_{1/2})O_3$ systems is due to the absence of $6s^2$ lone pair electrons of Pb^{2+} in Ca^{2+}, Sr^{2+} and Ba^{2+}. We deliberately chose $LaFeO_3$ substitution to rule out the possible role of $6s^2$ lone pair electrons of Bi^{3+} in the CFN-0.10BF system. La^{3+} has no such lone pair, whereas both CFN-0.10BF and CFN-0.10LF exhibit LRO AFM transition with T_N~175K. Thus the stabilization of the LRO AFM state is due to the increase in the concentration of Fe^{3+} ion by 5% in the magnetic

sublattice, which, we believe, enabled crossing the percolation threshold value for both the solid solution systems to exhibit LRO AFM state.

6.4.4 Evidence for incipient-AFM nature of CFN:

In order to obtain insight into the possible reason for the stabilization of the LRO AFM as a result of 10% $BiFeO_3$/ $LaFeO_3$ substitution in CFN, we carried out a careful study of CFN itself. The basic idea was to verify if there is any anomaly occurring around T_N~175K in CFN also. We present the results of NPD and dielectric studies in this section to show that CFN is an incipient AFM and is at the verge of acquiring LRO AFM state.

6.4.4.1 Temperature dependent neutron powder diffraction studies:

We have carried out NPD measurements on CFN to explore the growth of local AFM SRO clusters, already mentioned in the previous chapter. Fig. 6.9(a) depicts the temperature evolution of the NPD patterns of CFN in the 300K-4K range over a limited 2θ region 13 to 50º at 25K interval. It can be clearly seen from the figure that magnetic Bragg peaks showing LRO AFM state are not present in the NPD patterns down to 4 K. However, a broad diffuse peak is seen at the AFM peak position (see Fig. 6.9(b)). This broad peak arises due to magnetic diffuse scattering as a result of the development of the short-range antiferromagnetic AFM correlations as discussed in the previous chapter. The evolution of the magnetic diffuse scattering as a function of temperature shown in Fig. 6.9(b) reveal that the broad diffuse peak due to short-range AFM ordering becomes sharper. This indicates that the short-range AFM correlation length increases with decreasing temperature. To determine the magnetic correlation length (ξ) of the AFM spin clusters using Scherrer formula ($\xi = 0.9\lambda/\beta\cos\theta$), we first deconvoluted the diffuse magnetic peak along with two neighbouring peaks to determine the FWHM of the diffuse

peak using three Gaussian functions, as explained in the preceding chapter. The deconvoluted patterns of the diffuse magnetic peak at two selected temperatures 250K and 100K are shown in Figs. 6.10(a) and (b). The FWHM (β) of the diffuse magnetic peak was further corrected for the instrumental broadening as in the preceding chapter. The temperature variation of correlation length ξ, obtained from the intrinsic FWHM of the diffuse peak, is shown in Fig. 6.11.

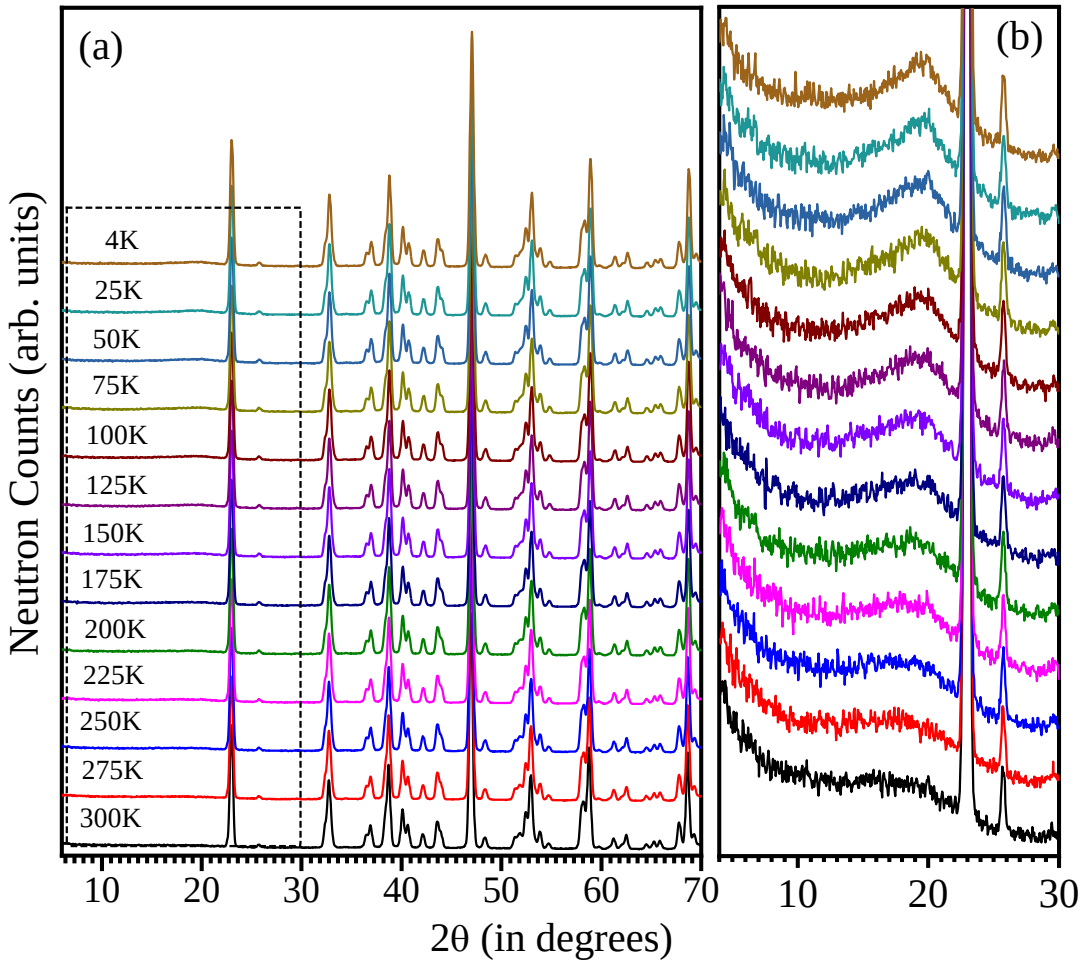

Figure 6.9: (a) Temperature evolution of NPD patterns of $Ca(Fe_{1/2}Nb_{1/2})O_3$ in the 4 to 300K range and (b) shows the temperature evolution of diffuse magnetic peak on a magnified scale.

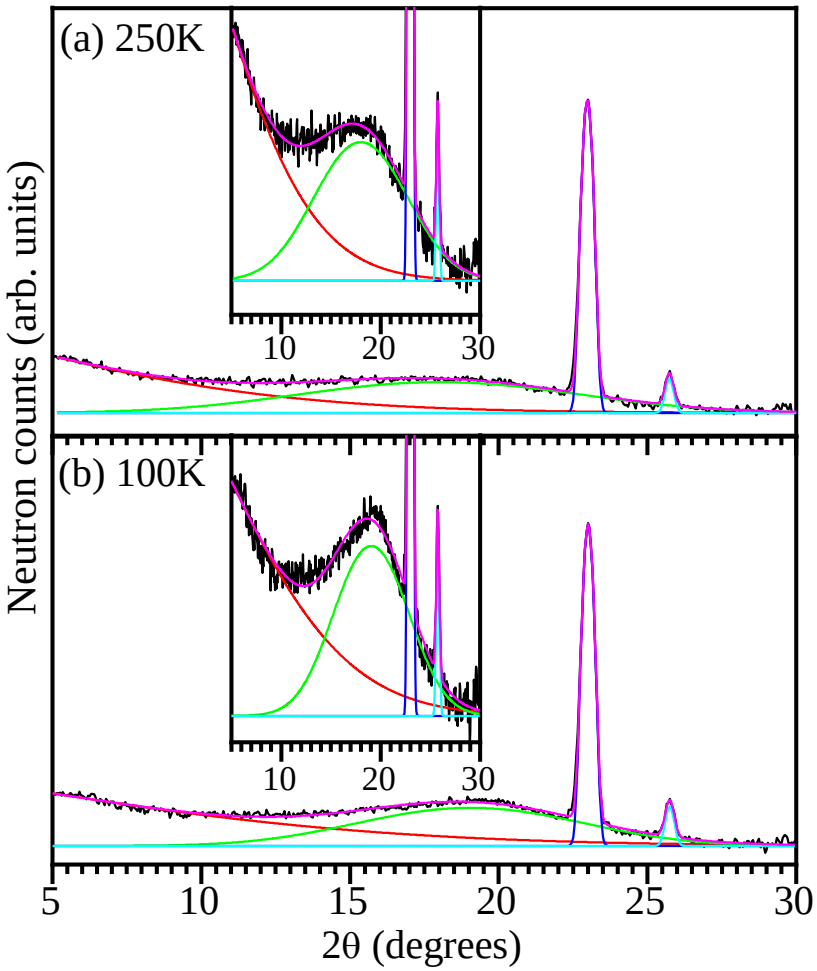

Figure 6.10: (a) Shows the deconvoluted peak profiles for diffuse magnetic peak using Gaussian function at (a) 250K and (b) 100K for CFN. Insets depict the magnetic diffuse peak on a magnified scale.

It is evident from the figure that the AFM correlation length ξ is nearly constant up to ~200K but starts growing gradually with decreasing temperature down to 4K ((~20Å). This suggests that the short-range ordered AFM correlations have a tendency to grow further below~200K. However, the correlation length grows very slowly and does not show any sharp divergence expected for a LRO transition down to 4K. On the contrary, the largest correlation length corresponding to 4K is still <2nm. This shows that

while CFN is at the verge of a criticality below 200K, the AFM interactions are highly restricted and are not able to stabilize the LRO AFM phase in CFN.

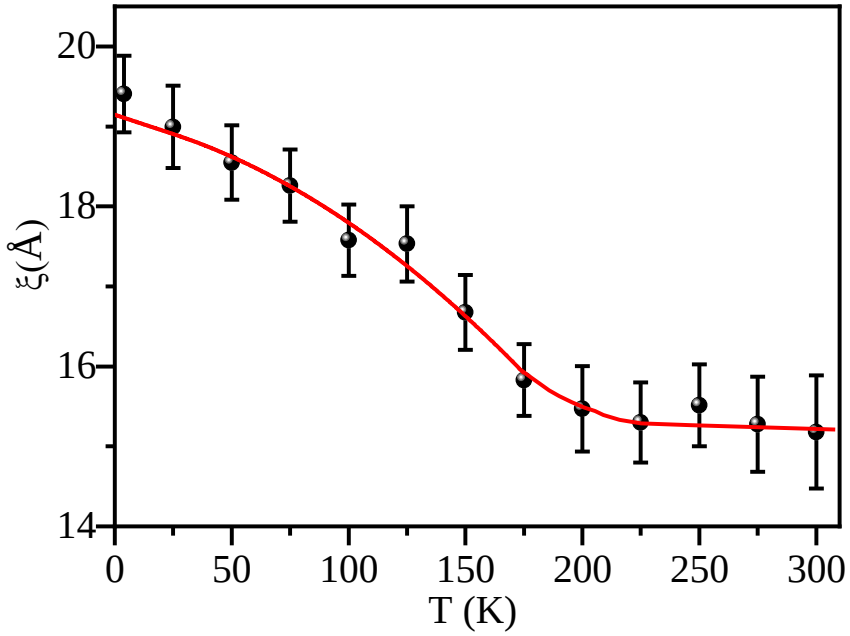

Figure 6.11: Variation of correlation length (ξ) with temperature for CFN.

6.4.4.2 Evidence for magnetoelastic and magnetodielectric couplings around 160 to 175K:

It is evident from the qualitative inspection of the NPD profiles of CFN shown in Fig. 6.9(a) that no new peaks appear/disappear in the 4 to 300K temperature range. As pointed out in the previous chapter, the room temperature crystal structure of CFN corresponds to orthorhombic Pbnm space group with $a^-a^-c^+$ tilt system. The absence of any structural transition below 300K was further confirmed by the Rietveld refinements using the NPD data after excluding the diffuse magnetic peak. Fig. 6.12 depicts the fits obtained between the observed and calculated profiles obtained by Rietveld refinement of CFN at a few selected temperatures. The observed and calculated profiles show excellent fit at all temperatures as can be seen from the difference profile shown at the bottom of the figure.

The temperature dependence of the unit cell parameters A_o, B_o, C_0 and unit cell volume (V_o) of the CFN, as obtained from Rietveld refinements, is shown in Figs. 6.13 (a) (b), (c) and (d), respectively. It is evident from this figure that the lattice parameter A_o and C_o show usual thermal expansion behaviour whereas the lattice parameter B_o shows a dip around 175K. This anomaly in the B_0 parameter correlates with the temperature at which the correlation length of the AFM spin clusters starts growing, as can be seen from a comparison of Fig. 6.13 (b) with Fig. 6.11. We believe that the growth of SRO AFM clusters is accompanied with magnetoelastic coupling which gives rise to this anomalous dip in B_0 lattice parameter around 175K.

To capture the signature of magnetoelastic coupling, we modelled the unit cell volume of CFN using Debye-Grüneisen equation given by [264]:

$$V \cong V(0) + \frac{9\gamma N k_B}{B} T \left(\frac{T}{\Theta_D}\right)^3 \int_0^{\Theta_D/T} \frac{x^3}{e^x - 1} dx, \qquad \text{……..(6.2)}$$

where V(0), γ, B and Θ_D are unit cell volume at 0K, Grüneisen parameter, bulk modulus, and Debye temperature, respectively. A least square fit to the observed unit cell volume in the temperature range 200K≤T≤300K gives the value of V(0), Θ_D, and C (=9γNk_B/B) as (233.313±0.005) $Å^3$, (612 ± 5) K and (0.0266±0.0002)$Å^3$/K, respectively. The best fit curve is shown as a continuous line in Fig 6.13 (d). It can be clearly seen from the figure that the observed unit cell volume starts deviating from the Debye-Grüneisen curve at T≲175K revealing an excess volume (ΔV) over the phonon contribution. We have plotted volume strain ΔV/V versus M^2 (obtained from DC M(T) data at 1T field) which shows linear dependence in the temperature range 125-175K (see inset of Fig. 6.13). The quadratic dependence of the excess volume on magnetization suggests the appearance of magnetoelastic coupling at T≃175K.

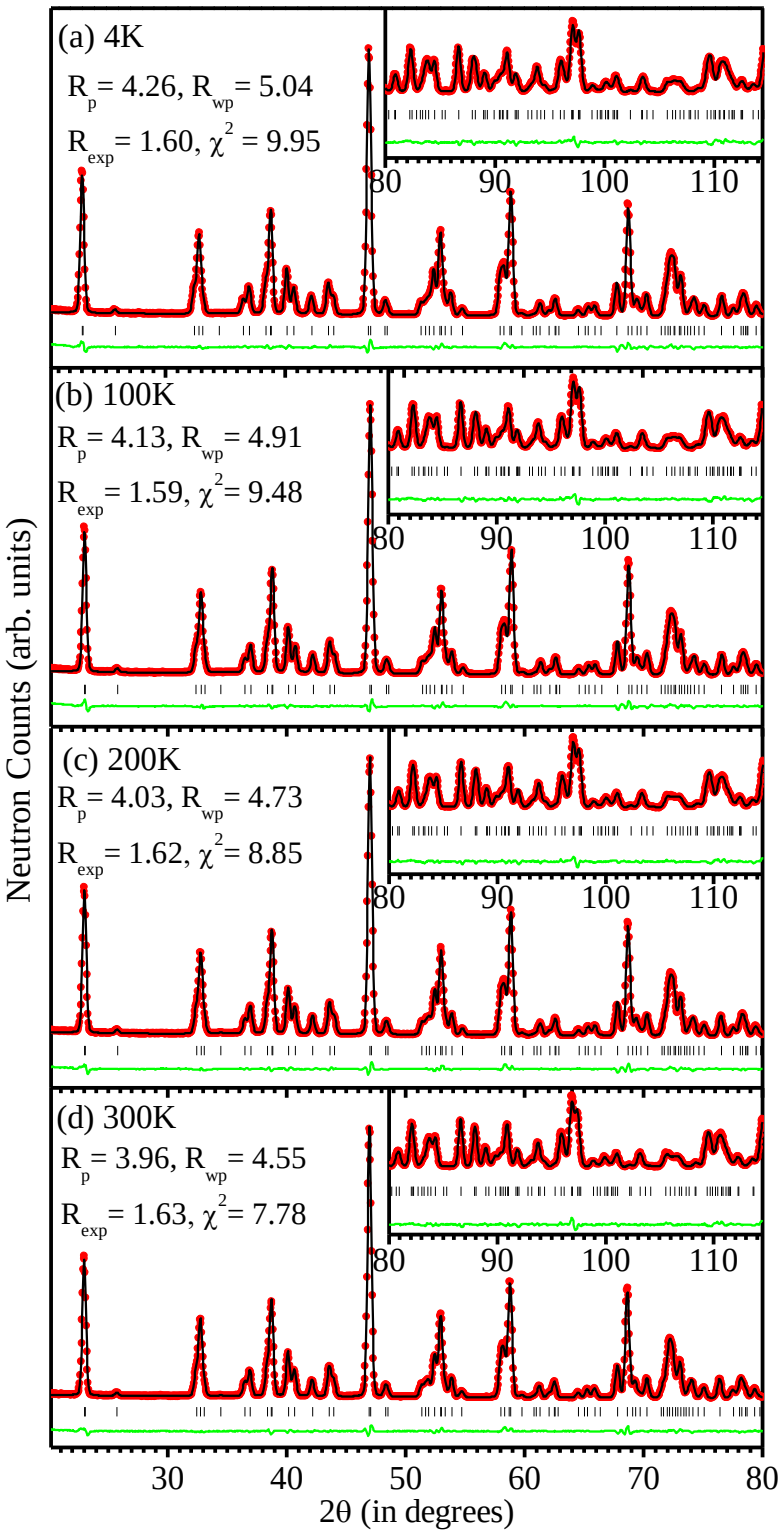

Figure 6.12: (a to d) Observed (red dots), calculated (black continuous line) and difference (green continuous line) profiles obtained from Rietveld refinement using NPD patterns of $Ca(Fe_{1/2}Nb_{1/2})O_3$ at 4K,100K 200K and 300K, respectively, for Pbnm space group. Vertical tick marks above the difference profile represent the Bragg peak positions. Here, we have excluded the magnetic diffuse scattering region on the refinement.

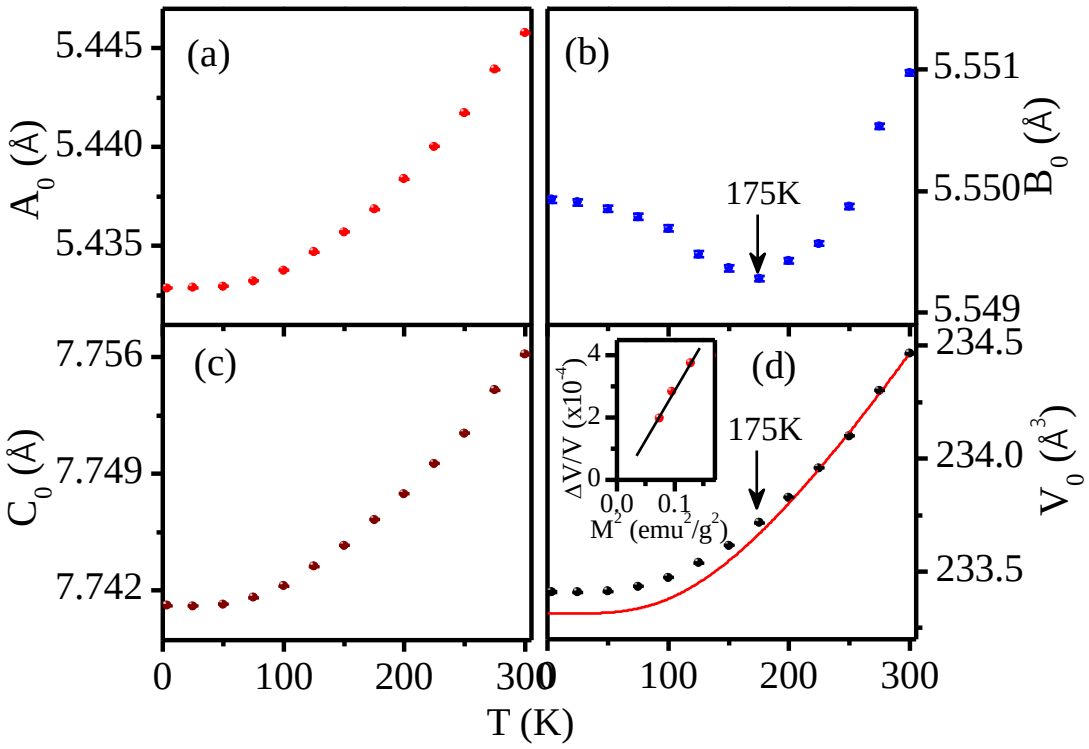

Figure 6.13: Temperature variation of lattice parameters (a to c) and unit cell volume (d) of $Ca(Fe_{1/2}Nb_{1/2})O_3$ obtained from Rietveld refinement using NPD patterns.

We have also calculated the in-phase and anti-phase tilt angles φ and γ using following relationships for the $a^-a^-c^+$ tilt system [320]:

$$tan\varphi = \frac{4zC_o}{\sqrt{[(A_o)^2+(B_o)^2\,]}}\text{, and} \qquad \text{…….(6.3)}$$

$$tan\gamma = 4\left[\frac{\{(xA_o)^2+(yB_o)^2\}}{(A_o)^2+(B_o)^2}\right]^{\left(\frac{1}{2}\right)} \qquad \text{……..(6.4)}$$

where A_o, B_o and C_o are the lattice parameters of the orthorhombic cell and x, y and z, are positional coordinates of oxygen atom O_{II} at the 8d Wyckoff position. To calculate the in-phase (φ) and anti-phase (γ) tilt angles, we have used unit cell parameters and positional coordinates obtained from NPD data by Rietveld refinement at various temperatures in the range 4 to 300K. The temperature variation of both the tilt angles are shown in Fig. 6.14. It is evident from the figure that distinct anomalies occur not only at T~175K but also at the spin glass freezing temperature $T_f \simeq 25K$. As mentioned earlier, tilting of the

oxygen octahedra bends the Fe^{3+}-O^{2-}-Fe^{3+} bonds and makes the bond angle to deviate from ideal 180° in the cubic perovskite structure. As a result of such a bending of the Fe^{3+}-O^{2-}-Fe^{3+} bonds, the Dzyloshinkii-Moriya (D-M) interaction becomes non-zero and leads to spin canting. The Hamiltonian for the spin-spin interaction is written as [40]:

$$H_{D\text{-}M} = \sum_{ij}[J_{i,j}\,\mathbf{S}_i.\mathbf{S}_j + \mathbf{D}_{ij}.(\mathbf{S}_i \times \mathbf{S}_j)] \qquad \ldots\ldots(6.5)$$

Here, $J_{i,j}$ is the superexchange interaction between the nearest neighbour spins, i and j are the site indices, and **S** are spin vectors, D_{ij} is the D-M vector. Since the D-M interaction is a consequence of the spin-orbit (lattice/phonon) coupling which is reflected through the dip in the B_0 lattice parameter at T≃175K (see Fig. 6.13(b)), the dip in the B_0 parameter and the tilt angles at T≃175K seem to correlate with each other and lead to possible spin canting through D-M interaction term.

The temperature dependence of the real part of the dielectric constant (ε') of CFN in the range 4-300K measured at 100kHz is shown in Fig. 6.15. It is evident from the inset to Fig. 6.15 that the real part of dielectric constant reveals a step jump around 160K, while no such anomaly/jump is observed across the spin-glass freezing temperature T_f≃25K. A similar step jump in the dielectric constant across the AFM transition has been reported in PFN at the Néel temperature T_N~150K [194] and explained in terms of magnetoelectric/magnetodielectric couplings. We believe that the step jump in the dielectric constant of CFN around 160K is also due to magnetodielectric coupling. The gradual increase in the AFM correlation length at T≲175K clearly suggests that the growth of AFM cluster size has magnetoelectric character giving rise to magnetodielectric effect shown in Fig. 6.15. The reason why the step jump in the dielectric constant occurs around 160K whereas the AFM correlation length ξ starts growing 175K is possibly because the neutron measurements were made at 25K interval

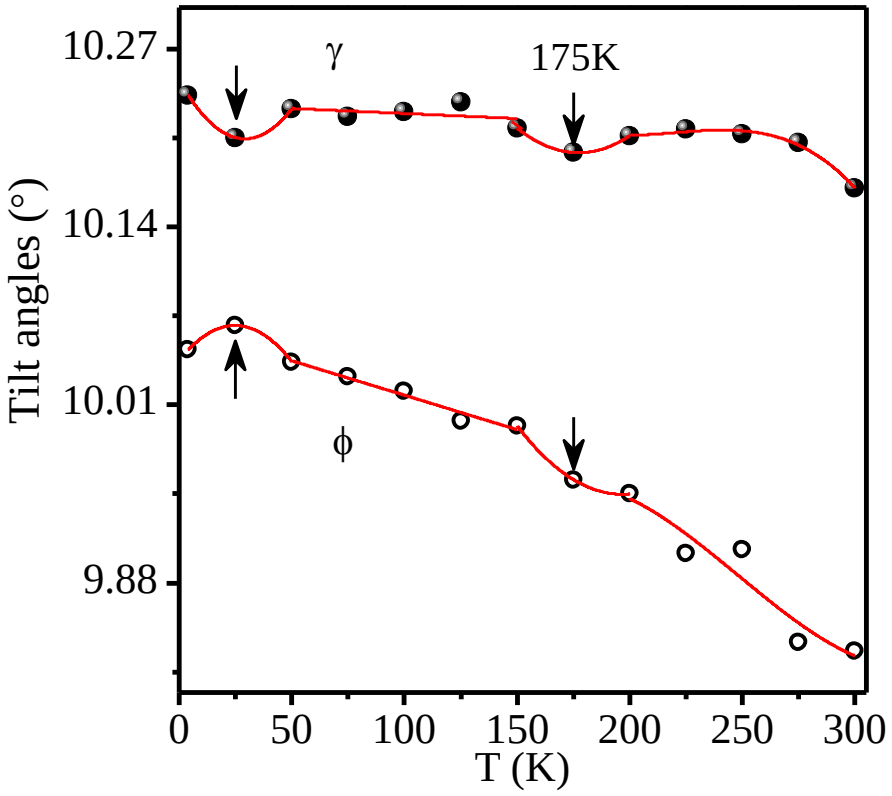

Figure 6.14: Temperature variation of in-phase (φ) and antiphase (γ) tilt angles of CFN.

whereas the dielectric data was collected at 3K interval. The dip around 175K may correspond to any temperature in the range 150K<T<200K. To locate the exact temperature, one needs NPD data at finer temperature intervals. Since the dielectric constant measurement was done at 3K interval, it gives more accurate value of the critical temperature below which CFN would show an anomalous growth of ξ accompanied with magnetoelastic and magnetodielectric couplings. All these results indicate that CFN ia at the verge of transforming into an LRO AFM, but since the concentration of magnetic spins in the magnetic sublattice is below the critical percolation threshold value, the LRO transition does not occur at T_N~175K. our results thus show that CFN is an incipient AFM and just 10% substitution by $BiFeO_3$ or $LaFeO_3$ in CFN is sufficient to stabilize LRO AFM state below this critical temperature T_N~175K.

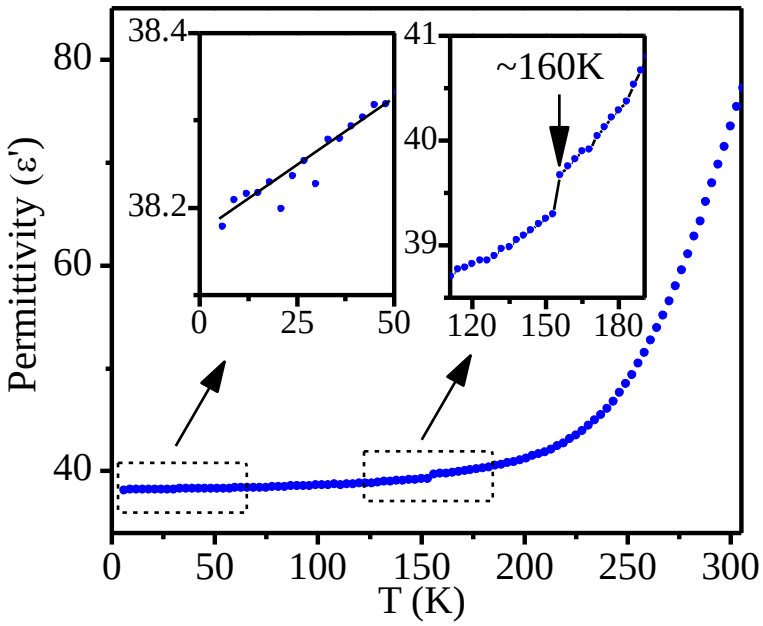

Figure 6.15: Shows the temperature dependence of dielectric permittivity (ε') of CFN. Insets depict the magnified scale across the AFM and SG transitions.

6.5. Conclusions:

We presented results of dc magnetization and neutron scattering measurements on CFN as well as CFN-0.10BF and CFN-0.10LF solid solutions. Our results reveal that CFN is an incipient AFM whose SRO AFM correlation length starts growing at T≲175K eventhough the size of the AFM spin-clusters remains limited to ~2 nm at the lowest temperature (4K). We showed that CFN is at the verge of acquiring LRO AFM state below T_N~175K if the Fe^{3+} content can be slightly increased by about 5% through a substitution of $BiFeO_3$ and $LaFeO_3$. We have also presented evidence for significant magnetoelastic and magnetodielectric coupling below T≲175K in CFN suggesting that CFN could become a multiferroic through suitable compositional engineering. More work, however, is needed to capture the signatures of ferroelectric distortion, even if it is at the local scale in CFN and its solid solutions with $BiFeO_3$ and $LaFeO_3$, through atomic pair distribution function analysis.

Chapter 7 Summary and Suggestions for Future Work

7.1. Summary of the present work:

In the present thesis, low temperature magnetic transitions in the well-known multiferroic $BiFeO_3$ (BF) and a potential multiferroic compound $Ca(Fe_{1/2}Nb_{1/2})O_3$ (CFN) were investigated. In addition, three solid solution compositions $(1-x)BiFeO_3$-$xBaTiO_3$ (BF-xBT), $(1-x)Ca(Fe_{1/2}Nb_{1/2})O_3$-$xBiFeO_3$ (CFN-xBF) and $(1-x)Ca(Fe_{1/2}Nb_{1/2})O_3$-$xLaFeO_3$ (CFN-xLF), based on the two compounds, were also investigated. The major emphasis of the thesis was on the spin-glass (SG) transition in these systems (chapters – II, III, IV and V). One chapter (VI) was dedicated to long range ordering (LRO) transition also in the CFN-xBF and CFN-xLF solid solutions in relation to pure CFN.

All the samples were synthesized by the conventional solid state route and were characterised for their phase purity, crystal structure, microstructure and composition using laboratory/synchrotron XRD, neutron powder diffraction, SEM, EDX and EPMA. Further, temperature dependent DC magnetization (M(T), M(H), M(T,H), M(t)), and AC susceptibility ($\chi(\omega,T)$) measurements were carried out to explore the low temperature magnetic transitions, especially the spin-glass transition in these systems. These studies were complemented with temperature dependent neutron and/or X-ray diffraction studies to capture the signatures of SG and LRO transitions as well as magnetoelectric and/or magnetoelastic couplings at the SG transitions. In addition, specific heat and dielectric measurements were also carried out on some of the samples to explore the role of magnons and magnetodielectric coupling in these systems.

The results of these investigations have been summarised at the end of each chapter (II to VI) and have been consolidated below:

In chapter II, we investigated the role of 0.3 wt% MnO_2 doping in $BiFeO_3$ used by various workers on the oxygen ion vacancy and Fe^{2+} ion concentration, on one hand, and the low temperature magnetic transitions, on the other. Iodometric titration and XPS studies reveal that the oxygen ion vacancy and Fe^{2+} ion concentrations decrease significantly as a result of Mn doping and acquire near stoichiometric proportions in the doped samples. The low temperature transitions occurring around 25 K, 150 K and 260 K are common to both the undoped and doped samples. However, the spin glass transition reported around 50 K by earlier workers, is absent in the Mn-doped $BiFeO_3$ and may be associated with the higher concentration of oxygen ion vacancies and Fe^{2+} ions in the undoped samples. The spin glass character of the transition around 25K is confirmed in both the samples and a significant change in the unit cell volume is observed around this transition confirming that this transition is a bulk behaviour and not due to the isolated superparamagnetic impurities. No signature of the other transitions is seen in ($\chi(\omega,T)$) plots suggesting that they may be of non-spin glass type.

In chapter III, evidence for two spin-glass transitions (SG1 and SG2) with T_f~ 250K and 25K in a solid solution of $BiFeO_3$ containing 20% $BaTiO_3$ (BF-0.20BT) was presented using a series of bulk measurements revealing history dependent effect, critical slowing down of the spin dynamics leading to ergodicity breaking at two characteristic spin glass transition temperature T_{SG1}~219K and T_{SG2}~18K, existence of A-T and G-T lines due to freezing of the longitudinal and transverse components of the spins and stretched exponential type decay of the thermoremanent magnetization. Using neutron powder diffraction (NPD) measurements, which provide evidence on microscopic scales, the two spin-glass transitions are shown to occur on the same magnetic sublattice in coexistence with the long range ordered antiferromagnetic phase with. The spontaneous polarization (P_s) and unit cell volume (V), obtained from the Rietveld analysis of low

temperature NPD and XRD data, respectively, show significant variation across the SG1 and SG2 transitions confirming the presence of magnetoelectric and magnetoelastic couplings, respectively. These couplings, and possibly the presence of electromagnons not investigated in the present work, constitute unique features of a multiferroic spin-glass system like BF-xBT that distinguish it from the conventional spin glass systems. Our results provide the first unambiguous evidence for the theoretical predictions on concentrated Heisenberg systems with low single ion anisotropy about the occurrence of a succession of two spin glass transitions due to the freezing of longitudinal and transverse components in coexistence with the LRO phase. This chapter also gives a complete magnetic phase diagram for the BF-xBT solid solution system upto the critical percolation threshold value x_c~0.55.

Chapter IV is devoted to the study of low temperature magnetic transitions in the BF-xBT solid solution compositions using temperature dependence of specific heat (C_p). Both the total specific heat and the magnetic contribution (C_m), obtained after subtracting phonon contributions, show the presence of a Boson peak in the C_p/T^3 or C_m/T^3 vs T plots whose peak temperature varies as $T_{Boson}\sim(x - x_c)^{1/2}$ suggesting the possibility of a quantum critical point at x_c~0.55. The magnetic specific heat (C_m) below the Boson peak temperature cannot be explained without considering coexistence of spin glass and LRO AFM phases. It is shown than C_m in the temperature range 1.8 to 12 K is best described using a functional dependence $C_m = AT^3 + BT\exp(-\Delta E/k_BT)$ where the AT^3 term is due to the long-range ordered (LRO) antiferromagnetic (AFM) phase and the exponential term is due to gapped magnons in the spin-glass (SG) phase. We believe that this is the first evidence for the coexistence of LRO and SG phases in concentrated systems using specific heat studies.

Chapter V presents results of low temperature magnetic transition in $Ca(Fe_{1/2}Nb_{1/2})O_3$ (CFN) using M(T), χ (ω,T), M(T, H), M(T, t) and neutron scattering measurements. Analysis of the dc magnetization measurements reveals a spin-glass (SG) transition with T_f ~25K with characteristic history dependent irreversibility. Analysis of the ac susceptibility data reveals power law/Vogel-Fulcher type critical spin dynamics with a time scale of $\tau_0 \sim 10^{-6}$s which suggests the existence of a cluster spin-glass (CSG) state in CFN with T_{SG}~24K. The field dependence of the irreversibility temperature T_{irr} (H) and the peak temperature T_f(H) of the ZFC M(T) falls on the A-T line in the $T_{irr}(H)/T_f$ (H) versus $H^{2/3}$ plot. The zero-field SG freezing temperature $T_f(0) = 25.2$K, obtained from the extrapolation of T_f(H) versus $H^{2/3}$ plot to H = 0, is in close agreement with the ergodicity breaking temperature T_{SG}~24K obtained from the analysis of the ac susceptibility $\chi(\omega, T)$ data. The observation of slow relaxation of thermoremanent magnetization, memory and rejuvenation effects below the SG transition temperature T_{SG}~24K supports the presence of glassy phase. Neutron diffraction study confirms the absence of any long-range AFM ordering but shows diffuse scattering due to the presence of short-range ordered (SRO) AFM spin clusters with a correlation length ξ ~2nm which are involved in the CSG freezing. The present results raise doubts about the origin of the spin glass transition in the related compound $Pb(Fe_{1/2}Nb_{1/2})O_3$ in terms of the freezing of the transverse component of the Fe^{3+} spins whose longitudinal component continues to remain long-range ordered.

Chapter VI addresses a long standing puzzle about the absence of LRO AFM phase in Pb^{2+} free complex perovskites $A(Fe_{1/2}B_{1/2})O_3$, where A = Ba, Sr, Ca and B = Nb, Ta, W, taking $Ca(Fe_{1/2}Nb_{1/2})O_3$ as an example. Theoretically all these compounds should exhibit LRO AFM transition since the Fe^{3+} ion concentration is above the percolation threshold value required for stabilizing the LRO percolative phase. Results of dc

magnetization and neutron scattering measurements on CFN as well as its solid solutions containing 10% $BiFeO_3$ or $LaFeO_3$ (i.e., CFN-0.10BF and CFN-0.10LF) reveal that only a slight increase in Fe^{3+} ion concentration in CFN helps stabilise the LRO AFM phase with T_N~ 175K. Neutron diffraction measurements reveal that CFN is an incipient AFM whose SRO AFM correlation length starts growing at T≲175K, but the size of the AFM spin-clusters remains limited to ~2 nm even at the lowest temperature (4K). This shows that CFN is at the verge of acquiring LRO AFM state below T_N~175K. ZFC M(T) measurements reveal that the LRO AFM phase gets stabilised by increasing the Fe^{3+} ion concentration slightly (~ 5%) in CFN through a substitution of $BiFeO_3$ and $LaFeO_3$, This was confirmed by neutron diffraction studies on CFN-0.10BF and CFN-0.10LF which reveal AFM phase with G-type LRO AFM state below T_N. Presence of significant magnetoelastic and magnetodielectric coupling below T≲175K in CFN suggests that CFN could become a multiferroic also through suitable compositional engineering. The results presented in this thesis demonstrate the role of critical percolation threshold composition for stabilising LRO AFM phase in CFN.

7.2. Suggestions for future study

Notwithstanding the strong experimental evidences presented in this thesis for the existence of spin glass phase in $BiFeO_3$ (BF), solid solutions of BF with $BaTiO_3$ (BT) (i.e., BF-xBT) and $Ca(Fe_{1/2}Nb_{1/2})O_3$ (CFN), the following aspects need further investigation in a future study:

1. The occurrence of spin glass transition in an ordered compound like $BiFeO_3$ is quite intriguing in the absence of any apparent disorder and randomness. While spin glass transition in recent years has been reported in some ordered compounds but the magnetic interactions in such systems are geometrically frustrated. In such

systems, even infinitesimal disorder due to magnetoelastic strains has been shown to stabilize spin glass phase at low temperature. While we have presented evidence for magnetoelastic strain accompanying spin glass transition, there in no evidence for geometrical frustration in $BiFeO_3$. Thus the origin of spin glass phase in $BiFeO_3$ remains an open issue and requires further exploration.

2. While the robust evidence presented for the succession of two spin glass transitions due to the freezing of the transverse and longitudinal components of the Fe^{3+} spins in coexistence with LRO AFM is in broad agreement with theoretical predictions for concentrated systems with Heisenberg spins, the origin of magnetoelectric coupling mediated by isostructural phase transitions needs more theoretical investigation. There is a need to revisit the existing theories of spin glass transitions to take into account the magnetoelastic and magnetoelectric coupling terms in the Hamiltonian for understanding the characteristic of spin glasses in multiferroic systems.
3. We presented experimental evidence for incipient AFM nature of $Ca(Fe_{1/2}Nb_{1/2})O_3$ and the stabilization of LRO AFM phase below T_N~175K due to 10% substitution by $BiFeO_3$ (BF) or $LaFeO_3$ (LF). More theoretical work is required to calculate the percolation threshold for $Ca(Fe_{1/2}Nb_{1/2})O_3$ taking into account the nearest and higher neighbour superexchange interactions.
4. Below the LRO AFM phase transition temperature T_N~175K, there is evidence for two more transitions in M(T) plots in solid solutions of $Ca(Fe_{1/2}Nb_{1/2})O_3$ with $BiFeO_3$ and $LaFeO_3$. Understanding the nature and the origin of these transitions needs further investigation. In particular, it needs to be understood if the drop in the ZFC magnetization at T~50K below the AFM T_N~175K is due to the appearance of a re-entrant spin glass phase.

References:

[1] V. M. Goldschmidt, “The Laws of Crystallochemy,” *Natural Sciences*, vol. 14, pp. 477–485, 1926.

[2] M. E. Lines and A. M. Glass, "Principles and Applications of Ferroelectric and Related Materials," *Claredon*, Oxford, 1977.

[3] “https://www.semanticscholar.org/paper/Ferroelectric-metal-organic-frameworks.-Zhang-Xiong/4d208f23b840cb6b13d865d72001e9ecfc7257ff/figure/7,”.

[4] R. Blinc and B. Zeks, "Soft Modes in Ferroelectrics and Antiferroelectrics," *North Holand Publishing Co.*, Amsterdam, Oxford, 1974.

[5] F. Jona and G. Shirane, "Ferroelectric Crystals" *Pergamon Press Inc.*, Oxford, 1962.

[6] H. D. Megaw, "Ferroelectricity in Crystals," *Methuen & Co. Ltd.*, London, 1957.

[7] W. Martienssen and H. Warlimont, "Hand Book of Condensed Matter and Materials Data XVII, 904," *Springer US*, 2005.

[8] W. Kanzig, "Solid State Physics," *Academic Press Inc.*, Publisher New York, 1957.

[9] S. K. Mishra and D. Pandey, “Low Temperature X-ray Diffraction Study of the Phase Transitions in $Sr_{1-x}Ca_xTiO_3$ (x = 0.02, 0.04): Evidence for Ferrielectric Ordering,” *Applied Physics Letters*, vol. 95, p. 232910, 2009.

[10] S. Tripathi, A. Kumar, U. V. Waghmare, and D. Pandey, “Effect of $NaNbO_3$ Substitution on the Quantum Paraelectric Behavior of $CaTiO_3$,” *Physical Review B*, vol. 81, p. 212101, 2010.

[11] M. I. Aroyo, A. Kirov, C. Capillas, J. M. Perez-Mato, and H. Wondratschek, “Bilbao Crystallographic Server. II. Representations of Crystallographic Point Groups and Space Groups,” *Acta Crystallographica Section A: Foundations of Crystallography*, vol. 62, pp. 115–128, 2006.

[12] M. I. Aroyo, A. Kirov, C. Capillas, J. M. Perez-Mato, and H. Wondratschek, “Bilbao Crystallographic Server: I. Databases and Crystallographic Computing Programs,” *Zeitschrift fur Kristallographier*, vol. 221, pp. 15–27, 2006.

[13] G. Shirane and Y. Yamada, “Lattice-Dynamical Study of the 110 K Phase Transition in $SrTiO_3$,” *Physical Review*, vol. 177, pp. 858–863, 1969.

[14] A. M. Glazer and H. D. Megaw, “The Structure of Sodium Niobate (T_2) at 600°C, and the Cubic-Tetragonal Transition in Relation to Soft-Phonon Modes,”

Philosophical Magazine, vol. 25, pp. 1119–1135, 1972.

[15] J. Harada, J. D. Axe, and G. Shirane, "Neutron-Scattering Study of Soft Modes in Cubic $BaTiO_3$," *Physical Review B*, vol. 4, pp. 155–162, 1971.

[16] G. Burns and B. A. Scott, "Raman Studies of Underdamped Soft Modes in $PbTiO_3$," *Physical Review Letters*, vol. 25, pp. 167–170, 1970.

[17] G. A. Smolensky, "Physical Phenomena in Ferroelectrics with Diffuse Phase Transition," *Journal of the Physical Society of Japan*, vol. 28, pp. 26–38, 1970.

[18] L. E. Cross, "Relaxor Ferroelectrics," *Ferroelectrics*, vol. 76, pp. 241–267, 1987.

[19] L. E. Cross, "Relaxorferroelectrics : An Overview," *Ferroelectrics*, vol. 151, p. 305, 1994.

[20] D. Viehland and L. E. Cross, "Dipolar-Glass Model for Lead Magnesium Niobate," *Physical Review B*, vol. 43, pp. 8316–8320, 1991.

[21] W. Kleemann, A. Albertini, R. V. Chamberlin, and J. G. Bednorz, "Relaxational Dynamics of Polar Nanodomains in $Sr_{1-x}Ca_xTiO_3$, x = 0.002," *Europhysics Letters*, vol. 37, pp. 145–150, 1997.

[22] R. Blinc, *et al.*, "Local Polarization Distribution and Edwards-Anderson Order Parameter of Relaxor Ferroelectrics," *Physical Review Letters*, vol. 83, pp. 424–427, 1999.

[23] F. Chu, I. M. Reaney, and N. Setter, "Investigation of Relaxors that Transform Spontaneously into Ferroelectrics," *Ferroelectrics*, vol. 151, pp. 343–348, 1994.

[24] K. Binder and A. P. Young, "Spin glasses: Experimental Facts, Theoretical Concepts, and Open Questions," *Reviews of Modern Physics*, vol. 58, pp. 801–976, 1986.

[25] George A. Samara, "The Relaxational Properties of Compositionally Disordered ABO_3 Perovskites," *Journal of Physics: Condensed Matter*, vol. 15, pp. R367–R411, 2003.

[26] B. D. Culity, "Introduction to Magnetic Materials". Addison-Wesely, Publishing Company Inc., Philippin, 1972.

[27] "https://www.ndeed.org / Education Resources / CommunityCollege / MagParticle /Physics/HysteresisLoop.htm".

[28] E. O. Wollan and W. C. Koehler, "Neutron Diffraction Study of the Magnetic Properties of the Series of Perovskite-Type Compounds [(1-x)La, xCa]MnO_3," *Physical Review*, vol. 100, pp. 545–563, 1955.

[29] W. Eerenstein, N. D. Mathur, and J. F. Scott, "Multiferroic and Magnetoelectric

Materials," *Nature*, vol. 442, pp. 759–765, 2006.

[30] K. F. Wang, J. M. Liu, and Z. F. Ren, "Multiferroicity: The Coupling Between Magnetic and Polarization Orders," *Advances in Physics*, vol. 58, pp. 321–448, 2009.

[31] M. Fiebig, T. Lottermoser, D. Meier, and M. Trassin, "The Evolution of Multiferroics," *Nature Reviews Materials*, vol. 1, p. 1, 2016.

[32] N. A. Spaldin and R. Ramesh, "Advances in Magnetoelectric Multiferroics," *Nature Materials*, vol. 18, pp. 203–212, 2019.

[33] M. Fiebig, "Revival of the Magnetoelectric Effect," *Journal of Physics D: Applied Physics*, vol. 38, pp. R123–R152, 2005.

[34] R. Ramesh, N. A. Spaldinn, N. A. Spaldin, and R. Ramesh, "Multiferroics: Progress and Prospects in Thin Films," *Nature Materials*, vol. 6, p. 21, 2007.

[35] J. F. Scott, "Data Storage: Multiferroic Memories," *Nature Materials*, vol. 6, pp. 256–257, 2007.

[36] D. Khomskii, "Classifying Multiferroics: Mechanisms and Effects," *Physics*, vol. 2, p. 20, 2009.

[37] R. E. Cohen, "Origin of Ferroelectricity in Perovskite Oxides," *Nature*, vol. 358, p. 136, 1992.

[38] N. A. Hill, "Why Are There so Few Magnetic Ferroelectrics?," *The Journal of Physical Chemistry B*, vol. 104, pp. 6694–6709, 2000.

[39] T. Kimura, T. Goto, H. Shintani, K. Ishizaka, T. Arima, and Y. Tokura, "Magnetic Control of Ferroelectric Polarization," *Nature*, vol. 426, pp. 55–58, 2003.

[40] Y. Tokura, S. Seki, and N. Nagaosa, "Multiferroics of Spin Origin," *Reports on Progress in Physics*, vol. 77, p. 076501, 2014.

[41] J. A. Mydosh, "Spin Glasses: Redux: An Updated Experimental/Materials Survey," *Reports on Progress in Physics*, vol. 78, p. 052501, 2015.

[42] J. A. Mydosh, "Spin Glasses: An Experimental Introduction". Taylor & Francis, Washington DC, US, 1993.

[43] I. Y. Korenblit and E. F. Shender, "Spin Glasses and Nonergodicity," *Sov. Phys. Usp.*, vol. 32, pp. 139–162, 1989.

[44] K. Binder and W. Kob, "Galssy Materials and Disordered Solids", *World Scientific, Singapore*. 2005.

[45] L. Balents, "Spin Liquids in Frustrated Magnets," *Nature*, vol. 464, pp. 199–208, 2010.

[46] S. Nagata, P. H. Keesom, and H. R. Harrison, “Low-dc-Field Susceptibility of CuMn Spin Glass,” *Physical Review B*, vol. 19, pp. 1633–1638, 1979.

[47] L. P. Levy, “Critical Dynamics of Metallic Spin Glasses,” *Physical Review B*, vol. 38, pp. 4963–4973, 1988.

[48] R. Mathieu, M. Hudl, and P. Nordblad, “Memory and Rejuvenation in a Spin Glass,” *Euro Physics Letter*, vol. 90, p. 37003, 2010.

[49] J. R. L. de Almeida and D. J. Thouless, “Stability of the Sherrington-Kirkpatrick Solution of a Spin Glass Model,” *Journal of Physics A: Mathematical and General*, vol. 11, p. 983, 1978.

[50] D. Sherrington and S. Kirkpatrick, “Solvable Model of a Spin-Glass,” *Physical Review Letters*, vol. 35, p. 1792, 1975.

[51] M. Gabay and G. Toulouse, “Coexistence of Spin-Glass and Ferromagnetic Orderings,” *Physical Review Letters*, vol. 47, p. 201, 1981.

[52] D. M. Cragg and D. Sherrington, “Spin-Glass with Local Uniaxial Anisotropy,” *Physical Review Letters*, vol. 49, p. 1190, 1982.

[53] S. A. Roberts and A. J. Bray, “Phase Diagram for Spin Glasses with Uniaxial Anisotropy,” *Journal of Physics C: Solid State Physics*, vol. 15, p. L527, 1982.

[54] P. W. Anderson, B. I. Halperin, and C. M. Varma, “Anomalous Low-Temperature Thermal Properties of Glasses and Spin Glasses,” *Philosophical Magazine*, vol. 25, p. 1, 1971.

[55] H. v. Lohnesysen, R. van den Berg, G. V. Lecomte, and W. Zinn, “Specific Heat of $Eu_xSr_{1-x}S$ in High Magnetic Fields,” *Physical Review B*, vol. 31, p. 2920, 1985.

[56] D. Meschade, F. Steglich, W. Felsch, H. Maletta, and W. Zinn, “Specific Heat of Insulating Spin-Glasses, (Eu,Sr)S, Near the Onset of Ferromagnetism,” *Physical Review Letters*, vol. 44, pp. 102–105, 1980.

[57] K. Westerholt, H. Endrikat, R. Dahlbeck, H. Bach, and J. M. Friedt, “Magnetic Phase Diagram of $Eu_xLa_{1-x}S$,” *Physical Review B*, vol. 33, p. 567, 1986.

[58] J. A. Morrison and D. M. T. Newsham, “Analyses of Low-Temperature Heat Capacities Containing Two or More Contributions: Application to the Rare Earth Metals,” *Journal of Physics C: Solid State Physics*, vol. 1, pp. 370–377, 1968.

[59] A. Schroder, H. v. Lohneysen, and W. Bauhofer, “Magnetic Susceptibility and Specific Heat of an Anisotropic Spin-Glass: $Eu_xSr_{1-x}As_3$,” *Physical Review Letters*, vol. 57, pp. 622–625, 1986.

[60] A. Del Maestro and M. J. P. Gingras, “Low-Temperature Specific Heat and

Possible Gap to Magnetic Excitations in the Heisenberg Pyrochlore Antiferromagnet Gd_2 Sn_2O_7," *Physical Review B*, vol. 76, p. 064418, 2007.

[61] J. C. Lashley *et al.*, "Specific Heat and Magnetic Susceptibility of the Spinels $GeNi_2O_4$ and $GeCo_2O_4$," *Physical Review B*, vol. 78, p. 104406, 2008.

[62] J. A. Quilliam, K. A. Ross, A. G. Del Maestro, M. J. P. Gingras, L. R. Corruccini, and J. B. Kycia, "Evidence for Gapped Spin-Wave Excitations in the Frustrated $Gd_2Sn_2O_7$ Pyrochlore Antiferromagnet from Low-Temperature Specific Heat Measurements," *Physical Review Letters*, vol. 99, p. 097201, 2007.

[63] J. O. Thomson and J. R. Thompson, "Low-Temperature Excitations in Spin Glasses: Evidence for a $T^{3/2}$ Behaviour," *Journal of Physics F: Metal Physics*, vol. 11, pp. 247–260, 1981.

[64] R. Caudron, P. Costa, and B. Levesque, "Power Law Behaviour for the Specific Heat of Spin Glasses at very Low Temperatures," *Journal of Physics F: Metal Physics*, vol. 11, pp. 451–456, 1981.

[65] W. Kaczmarek, Z. Pajak, and M. Polomska, "Differential Thermal Analysis of Phase Transitions in $(Bi_{1-x}La_x)FeO_3$ Solid Solution," *Solid State Communications*, vol. 17, pp. 807–810, 1975.

[66] Y. E. Roginskaya, T. Y. Tomashpolskii, Y. N. Venevtsev, V. M. Petrov, and G. S. Zhdanov, "The Nature of the Dielectric and Magnetic Properties of $BiFeO_3$," *Soviet Journal of Experimental and Theoretical Physics*, vol. 23, p. 47, 1966.

[67] R. Palai *et al.*, "β Phase and γ-β Metal-Insulator Transition in Multiferroic $BiFeO_3$," *Physical Review B*, vol. 77, p. 014110, 2008.

[68] G. Catalan and J. F. Scott, "Physics and Applications of Bismuth Ferrite," *Advanced Materials*, vol. 21, pp. 2463–2485, 2009.

[69] A. K. Pradhan *et al.*, "Magnetic and Electrical Properties of Single-Phase Multiferroic $BiFeO_3$," *Journal of Applied Physics*, vol. 97, p. 093903, 2005.

[70] M. M. Kumar, V. R. Palkar, K. Srinivas, and S. V. Suryanarayana, "Ferroelectricity in a Pure $BiFeO_3$ Ceramic," *Applied Physics Letters*, vol.76, pp. 2764–2766, 2000.

[71] D. Lebeugle *et al.*, "Room-Temperature Coexistence of Large Electric Polarization and Magnetic Order in $BiFeO_3$ Single Crystals," *Physical Review B*, vol. 76, p. 024116, 2007.

[72] C. Tabares-Munoz, J. -P. Rivera, A. Bezinges, A. Monnier, and H. Schmid, "Measurement of the Quadratic Magnetoelectric Effect on Single Crystalline

$BiFeO_3$," *Japanese Journal of Applied Physics*, vol. 24, pp. 1051–1053, 1985.

[73] I. Sosnowska, T. Peterlin-Neumaier, and E. Steichele, "Spiral Magnetic Ordering in Bismuth Ferrite," *Journal of Physics C: Solid State Physics*, vol. 15, pp. 4835–4846, 1982.

[74] A. J. Jacobson and B. E. F. Fender, "A Neutron Diffraction Study of the Nuclear and Magnetic Structure of $BiFeO_3$," *Journal of Physics C: Solid State Physics*, vol. 8, pp. 844–850, 1975.

[75] P. Fischer, M. Polomska, I. Sosnowska, and M. Szymanski, "Temperature Dependence of the Crystal and Magnetic Structures of $BiFeO_3$," *Journal of Physics C: Solid State Physics*, vol. 13, pp. 1931–1940, 1980.

[76] I. Sosnowska, W. Schafer, W. Kockelmann, K. H. Andersen, and I. O. Troyanchuk, "Crystal Structure and Spiral Magnetic Ordering of $BiFeO_3$ Doped with Manganese," *Applied Physics A*, vol. 74, pp. 1040–1042, 2002.

[77] A. Palewicz, R. Przeniosło, I. Sosnowska, and A. W. Hewat, "Atomic Displacements in $BiFeO_3$ as a Function of Temperature: Neutron Diffraction Study," *Acta Crystallographica Section B: Structural Science*, vol. 63, pp. 537–544, 2007.

[78] A. Lubk, S. Gemming, and N. A. Spaldin, "First-Principles Study of Ferroelectric Domain Walls in Multiferroic Bismuth Ferrite," *Physical Review B*, vol. 80, p. 104110, 2009.

[79] J. B. Neaton, C. Ederer, U. V. Waghmare, N. A. Spaldin, and K. M. Rabe, "First-Principles Study of Spontaneous Polarization in Multiferroic $BiFeO_3$," *Physical Review B*, vol. 71, p. 014113, 2005.

[80] P. Ravindran, R. Vidya, A. Kjekshus, H. Fjellvåg, and O. Eriksson, "Theoretical Investigation of Magnetoelectric Behavior in $BiFeO_3$," *Physical Review B*, vol. 74, p. 224412, 2006.

[81] D. Lebeugle, D. Colson, A. Forget, and M. Viret, "Very Large Spontaneous Electric Polarization in $BiFeO_3$ Single Crystals at Room Temperature and its Evolution Under Cycling Fields," *Applied Physics Letters*, vol. 91, p. 022907, 2007.

[82] J. Park *et al.*, "Magnetoelectric Feedback Among Magnetic Order, Polarization, and Lattice in Multiferroic $BiFeO_3$," *Journal of the Physical Society of Japan*, vol. 80, p. 114714, 2011.

[83] H. Schmid, "Multi-Ferroic Magnetoelectrics," *Ferroelectrics*, vol. 162, pp. 317–

338, 1994.

[84] Y. -F. Popov, A. K. Zvezdin, G. P. Vorob'ev, A. M. Kadomtseva, V. A. Murashev, and D. N. Rakov, "Linear Magnetoelectric Effect and Phase Transitions in Bismuth Ferrite, $BiFeO_3$," *JETP Letters,* vol. 57, pp. 69–73, 1993.

[85] D. Lebeugle, D. Colson, A. Forget, M. Viret, A. M. Bataille, and A. Gukasov, "Electric-Field-Induced Spin Flop in $BiFeO_3$ Single Crystals at Room Temperature," *Physical Review Letters*, vol. 100, p. 227602, 2008.

[86] S. Lee, W. Ratcliff, S. W. Cheong, and V. Kiryukhin, "Electric Field Control of the Magnetic State in $BiFeO_3$ Single Crystals," *Applied Physics Letters*, vol. 92, p. 192906, 2008.

[87] T. J. Park, G. C. Papaefthymiou, A. J. Viescas, A. R. Moodenbaugh, and S. S. Wong, "Size-Dependent Magnetic Properties of Single-Crystalline Multiferroic $BiFeO_3$ Nanoparticles," *Nano Letters*, vol. 7, pp. 766–772, 2007.

[88] W. Eerenstein, F. D. Morrison, J. Dho, M. G. Blamire, J. F. Scott, and N. D. Mathur, "Comment on Epitaxial $BiFeO_3$ Multiferroic Thin Film Heterostructures," *Science*, vol. 307, p. 1203a, 2005.

[89] A. Singh, V. Pandey, R. K. Kotnala, and D. Pandey, "Direct Evidence for Multiferroic Magnetoelectric Coupling in $0.9BiFeO_3$-$0.1BaTiO_3$," *Physical Review Letters*, vol. 101, p. 247602, 2008.

[90] A. Singh, A. Senyshyn, H. Fuess, T. Chatterji, and D. Pandey, "Neutron Powder Diffraction Study of Nuclear and Magnetic Structures of Multiferroic $(Bi_{0.8}Ba_{0.2})(Fe_{0.8}Ti_{0.2})O_3$: Evidence for Isostructural Phase Transition and Magnetoelastic and Magnetoelectric Couplings," *Physical Review B*, vol. 83, p. 054406, 2011.

[91] A. Singh, A. Senyshyn, H. Fuess, S. J. Kennedy, and D. Pandey, "Magnetic Transitions and Site-Disordered Induced Weak Ferromagnetism in $(1-x)BiFeO_3$-$xBaTiO_3$," *Physical Review B*, vol. 89, p. 024108, 2014.

[92] T. J. Park, G. C. Papaefthymiou, A. J. Viescas, Y. Lee, H. Zhou, and S. S. Wong, "Composition-Dependent Magnetic Properties of $BiFeO_3$-$BaTiO_3$ Solid Solution Nanostructures," *Physical Review B*, vol. 82, p. 024431, 2010.

[93] R. A. M. Gotardo *et al.*, "Ferroic States and Phase Coexistence in $BiFeO_3$-$BaTiO_3$ Solid Solutions," *Journal of Applied Physics*, vol. 112, p. 104112, 2012.

[94] J. P. Patel, A. Senyshyn, H. Fuess, and D. Pandey, "Evidence for Weak Ferromagnetism, Isostructural Phase Transition, and Linear Magnetoelectric

Coupling in the Multiferroic $(Bi_{0.8}Pb_{0.2})(Fe_{0.9}Nb_{0.1})O_3$ Solid Solution," *Physical Review B*, vol. 88, p. 104108, 2013.

[95] J. G. Park, M. D. Le, J. Jeong, and S. Lee, "Structure and Spin Dynamics of Multiferroic $BiFeO_3$," *Journal of Physics Condensed Matter*, vol. 26, p. 433202, 2014.

[96] A. V. Zalessky, A. A. Frolov, T. A. Khimich, A. A. Bush, V. S. Pokatilov, and A. K. Zvezdin, "^{57}Fe NMR Study of Spin-Modulated Magnetic Structure in $BiFeO_3$," *Euro Physics Letter*, vol. 50, pp. 547–551, 2000.

[97] A. V. Zalesskii *et al.*, "Effect of Spatial Spin Modulation on the Relaxation and NMR Frequencies of ^{57}Fe Nuclei in a Ferroelectric Antiferromagnet $BiFeO_3$," *Journal of Experimental and Theoretical Physics*, vol. 95, pp. 101–105, 2002.

[98] D. F. Khozeev, A. V. Zalessky, A. A. Gippius, E. N. Morozova, and A. A. Bush, "Spin Modulation of ^{57}Fe NMR Frequency and Relaxation in $BiFeO_3$," *Physica B*, vol. 329–333, pp. 848–849, 2003.

[99] A. V. Zalesskii, A. K. Zvezdin, A. A. Frolov, and A. A. Bush, "^{57}Fe NMR Study of a Spatially Modulated Magnetic Structure in $BiFeO_3$," *Journal of Experimental and Theoretical Physics Letters*, vol. 71, pp. 465–468, 2000.

[100] M. Ramazanoglu, W. Ratcliff, Y. J. Choi, S. Lee, S. W. Cheong, and V. Kiryukhin, "Temperature-Dependent Properties of the Magnetic Order in Single-Crystal $BiFeO_3$," *Physical Review B*, vol. 83, p. 174434, 2011.

[101] I. Sosnowska and R. Przeniosło, "Low-Temperature Evolution of the Modulated Magnetic Structure in the Ferroelectric Antiferromagnet $BiFeO_3$," *Physical Review B*, vol. 84, p. 144404, 2011.

[102] M. K. Singh, W. Prellier, M. P. Singh, R. S. Katiyar, and J. F. Scott, "Spin-Glass Transition in Single-Crystal $BiFeO_3$," *Physical Review B*, vol. 77, p. 144403, 2008.

[103] B. Ramachandran and M. S. R. Rao, "Low Temperature Magnetocaloric Effect in Polycrystalline $BiFeO_3$ Ceramics," *Applied Physics Letters*, vol. 95, p. 142505, 2009.

[104] S. Vijayanand, M. B. Mahajan, H. S. Potdar, and P. A. Joy, "Magnetic Characteristics of Nanocrystalline Multiferroic $BiFeO_3$ at Low Temperatures," *Physical Review B*, vol. 80, p. 064423, 2009.

[105] R. Mazumder *et al.*, "Particle Size Dependence of Magnetization and Phase Transition Near T_N in Multiferroic $BiFeO_3$," *Journal of Applied Physics*, vol. 100, p. 033908, 2006.

[106] H. Naganuma and S. Okamura, "Structural, Magnetic, and Ferroelectric Properties of Multiferroic $BiFeO_3$ film Fabricated by Chemical Solution Deposition," *Journal of Applied Physics*, vol. 101, p. 09M103, 2007.

[107] S. K. Srivastav, A. Johari, S. K. S. Patel, and N. S. Gajbhiye, "Presence of Glassy State and Large Exchange Bias in Nanocrystalline $BiFeO_3$," *Journal of Magnetism and Magnetic Materials*, vol. 441, pp. 503–510, 2017.

[108] S. Nakamura, S. Soeya, N. Ikeda, and M. Tanaka, "Spin-Glass Behavior in Amorphous $BiFeO_3$," *Journal of Applied Physics*, vol. 74, pp. 5652–5657, 1993.

[109] S. A. T. Redfern, C. Wang, J. W. Hong, G. Catalan, and J. F. Scott, "Elastic and Electrical Anomalies at Low-Temperature Phase Transitions in $BiFeO_3$," *Journal of Physics Condensed Matter*, vol. 20, p. 452205, 2008.

[110] B. Ramachandran, A. Dixit, R. Naik, G. Lawes, and M. S. Ramachandra Rao, "Dielectric Relaxation Near 25K in Multiferroic $BiFeO_3$ Ceramics," *Journal of Applied Physics*, vol. 110, p. 104105, 2011.

[111] M. K. Singh, R. S. Katiyar, and J. F. Scott, "New Magnetic Phase Transitions in $BiFeO_3$," *Journal of Physics Condensed Matter*, vol. 20, p. 252203, 2008.

[112] J. F. Scott, M. K. Singh, and R. S. Katiyar, "Critical Phenomena at the 140 and 200K Magnetic Phase Transitions in $BiFeO_3$," *Journal of Physics Condensed Matter*, vol. 20, p. 322203, 2008.

[113] J. F. Scott, M. K. Singh, and R. S. Katiyar, "Critical Slowing Down of Spin Fluctuations in $BiFeO_3$," *Journal of Physics Condensed Matter*, vol. 20, p. 425223, 2008.

[114] P. Rovillain *et al.*, "Polar Phonons and Spin Excitations Coupling in Multiferroic $BiFeO_3$ Crystals," *Physical Review B*, vol. 79, p. 180411(R), 2009.

[115] R. Jarrier *et al.*, "Surface Phase Transitions in $BiFeO_3$ Below Room Temperature," *Physical Review B*, vol. 85, p. 184104, 2012.

[116] M. Cazayous, Y. Gallais, A. Sacuto, R. de Sousa, D. Lebeugle, and D. Colson, "Possible Observation of Cycloidal Electromagnons in $BiFeO_3$," *Physical Review Letters*, vol. 101, p. 037601, 2008.

[117] S. Kamba *et al.*, "Infrared and Terahertz Studies of Polar Phonons and Magnetodielectric Effect in Multiferroic $BiFeO_3$ Ceramics," *Physical Review B*, vol. 75, p. 024403, 2007.

[118] P. A. Kumar *et al.*, "Evidence for Superferrimagnetic Clusters and Spin-Glass Transition Involving 4f Dy^{3+} Spins in h-$DyMnO_3$: A New Twist to 4f Re^{3+} Spin

Ordering in Hexagonal Manganites," *arXiv:1804.05401*, pp. 1–24.

[119] W. G. Bisson and A. S. Wills, "Anisotropy-Driven Spin Glass Transition in the Kagome Antiferromagnet Hydronium Jarosite, $(H_3O)Fe_3(SO_4)_2(OH)_6$," *Journal of Physics Condensed Matter*, vol. 20, p. 452204, 2008.

[120] M. Fujihala *et al.*, "Short-Range Correlations and Persistent Spin Fluctuations in the Undistorted Kagome Lattice Ising Antiferromagnet $Co_3Mg(OH)_6Cl_2$," *Physical Review B*, vol. 85, p. 012402, 2012.

[121] M. Fujihala *et al.*, "Unconventional Spin Freezing in the Highly Two-Dimensional Spin-1/2 Kagome Antiferromagnet $Cd_2Cu_3(OH)_6(SO_4)_24H_2O$: Evidence of Partial Order and Coexisting Spin Singlet State on a Distorted Kagome Lattice," *Physical Review B*, vol. 89, p. 100401(R), 2014.

[122] H. D. Zhou, C. R. Wiebe, A. Harter, N. S. Dalal, and J. S. Gardner, "Unconventional Spin Glass Behavior in the Cubic Pyrochlore $Mn_2Sb_2O_7$," *Journal of Physics Condensed Matter*, vol. 20, p. 32501, 2008.

[123] D. K. Singh and Y. S. Lee, "Nonconventional Spin Glass Transition in a Chemically Ordered Pyrochlore," *Physical Review Letters*, vol. 109, p. 247201, 2012.

[124] H. J. Silverstein *et al.*, "Liquid like Correlations in Single-Crystalline $Y_2Mo_2O_7$: An Unconventional Spin Glass," *Physical Review B*, vol. 89, p. 054433, 2014.

[125] M. M. Kumar, A. Srinivas, and S. V. Suryanarayana, "Structure Property Relations in $BiFeO_3/BaTiO_3$ Solid Solutions," *Journal of Applied Physics*, vol. 97, p. 855, 2005.

[126] S. A. Ivanov *et al.*, "Influence of $PbZrO_3$ Doping on the Structural and Magnetic Properties of $BiFeO_3$," *Solid State Sciences*, vol. 10, pp. 1875–1885, 2008.

[127] S. K. Korchagina, S. A. Ivanov, V. Y. Proidakova, S. N. Rush, L. F. Rybakova, and N. V. Sadovskaya, "Synthesis, Structure, and Properties of Solid Solutions Based on Bismuth Ferrite," *Inorganic Materials*, vol. 45, pp. 568–573, 2009.

[128] R. N. P. Choudhary, K. Perez, P. Bhattacharya, and R. S. Katiyar, "Structural and Electrical Properties of $BiFeO_3$-$Pb(ZrTi)O_3$ Composites," *Applied Physics A: Materials Science and Processing*, vol. 86, pp. 131–138, 2007.

[129] M. Makarovic, A. Bencan, J. Walker, B. Malic, and T. Rojac, "Processing, Piezoelectric and Ferroelectric Properties of $(x)BiFeO_3$-$(1-x)SrTiO_3$ Ceramics," *Journal of the European Ceramic Society*, vol. 39, pp. 3693–3702, 2019.

[130] Q. Q. Wang, H. J. Zhao, and X. M. Chen, "Low-Temperature Dielectric Behavior

of $BiFeO_3$-modified $CaTiO_3$ Incipient Ferroelectric Ceramics," *Journal of Applied Physics*, vol. 111, p. 126101, 2012.

[131] S. Bhattacharjee, A. Senyshyn, P. S. R. Krishna, H. Fuess, and D. Pandey, "Simultaneous Changes of Nuclear and Magnetic Structures across the Morphotropic Phase Boundary in (1-x)$BiFeO_3$-x$PbTiO_3$," *Applied Physics Letters*, vol. 97, p. 262506, 2010.

[132] O. Diéguez and J. Añiguez, "First-Principles Investigation of Morphotropic Transitions and Phase-Change Functional Responses in $BiFeO_3$-$BiCoO_3$ Multiferroic Solid Solutions," *Physical Review Letters*, vol. 107, p. 057601, 2011.

[133] I. P. Raevski *et al.*, "Studies of Magnetic and Ferroelectric Phase Transitions in $BiFeO_3$-$NaNbO_3$ Solid Solution Seramics," *Ferroelectrics*, vol. 371, pp. 113–118, 2008.

[134] L. Pálová, P. Chandra, and K. M. Rabe, "Multiferroic $BiFeO_3$-$BiMnO_3$ Nanoscale Checkerboard from First Principles," *Physical Review B*, vol. 82, p. 075432, 2010.

[135] A. Singh, C. Moriyoshi, Y. Kuroiwa, and D. Pandey, "Evidence for Local Monoclinic Structure, Polarization Rotation, and Morphotropic Phase Transitions in (1-x)$BiFeO_3$-x$BaTiO_3$ Solid Solutions: A High-Energy Synchrotron X-ray Powder Diffraction Study," *Physical Review B*, vol. 88, p. 024113, 2013.

[136] S. O. Leontsev and R. E. Eitel, "Dielectric and Piezoelectric Properties in Mn-Modified (1-x)$BiFeO_3$-x$BaTiO_3$ Ceramics," *Journal of the American Ceramic Society*, vol. 92, p. 2957, 2009.

[137] X. H. Liu, Z. Xu, S. B. Qu, X. Y. Wei, and J. L. Chen, "Ferroelectric and Ferromagnetic Properties of Mn-Doped 0.7$BiFeO_3$-0.3$BaTiO_3$ Solid Solution," *Ceramics International*, vol. 34, pp. 797–801, 2008.

[138] H. Yang *et al.*, "Piezoelectric Properties and Temperature Stabilities of Mn- and Cu-Modified $BiFeO_3$-$BaTiO_3$ High Temperature Ceramics," *Journal of the European Ceramic Society*, vol. 33, pp. 1177–1183, 2013.

[139] Y. Guo *et al.*, "Critical Roles of Mn-ions in Enhancing the Insulation, Piezoelectricity and Multiferroicity of $BiFeO_3$-Based Lead-Free High Temperature Ceramics," *Journal of Materials Chemistry C*, vol. 3, pp. 5811–5824, 2015.

[140] D. J. Kim, M. H. Lee, and T. K. Song, "Comparison of Multi-Valent Manganese Oxides (Mn^{4+}, Mn^{3+}, and Mn^{2+}) Doping in $BiFeO_3$-$BaTiO_3$ Piezoelectric Ceramics," *Journal of the European Ceramic Society*, vol. in Press, 2019.

[141] S. Cheng, B. P. Zhang, L. Zhao, and K. K. Wang, "Enhanced insulating and

piezoelectric properties of 0.7BiFeO3-0.3BaTiO3 lead-free ceramics by optimizing calcination temperature: Analysis of Bi^{3+} volatilization and phase structures," *Journal of Materials Chemistry C*, vol. 6, pp. 3982–3989, 2018.

[142] I. Calisir and D. A. Hall, "Chemical Heterogeneity and Approaches to its Control in $BiFeO_3$-$BaTiO_3$ Lead-Free Ferroelectrics," *Journal of Materials Chemistry C*, vol. 6, pp. 134–146, 2018.

[143] J. S. Kim, C. Cheon, C. H. Lee, and P. W. Jang, "Weak Ferromagnetism in the Ferroelectric $BiFeO_3$-$ReFeO_3$-BaTiO3 Solid Solutions (Re=Dy,La)," *Journal of Applied Physics*, vol. 96, p. 468, 2004.

[144] M. H. Lee *et al.*, "High-Performance Lead-Free Piezoceramics with High Curie Temperatures," *Advanced Materials*, vol. 27, p. 6976, 2015.

[145] A. Singh, C. Moriyoshi, Y. Kuroiwa, and D. Pandey, "Evidence for Diffuse Ferroelectric Phase Transition and Cooperative Tricritical Freezing of Random-Site Dipoles Due to off-Centered Bi^{3+} ions in the Average Cubic Lattice of $(Ba_{1-x}Bi_x)(Ti_{1-x}Fe_x)O_3$," *Physical Review B*, vol. 85, p. 064116, 2012.

[146] A. Singh, A. Kumar, and D. Pandey, "Effect of Synthesis Route on Structure and Dielectric Properties of (1-x)$BiFeO_3$-x$BaTiO_3$ Solid Solutions and its Phase Diagram," *Journal of Applied Physics*, vol. 124, no. 224101, 2018.

[147] S. Vasala and M. Karppinen, "$A_2B'B''O_6$ Perovskites: A Review," *Progress in Solid State Chemistry*, vol. 43, pp. 1–36, 2015.

[148] H. J. Zhao, W. Ren, Y. Yang, J. Íñiguez, X. M. Chen, and L. Bellaiche, "Near Room Temperature Multiferroic Materials with Tunable Ferromagnetic and Electrical Properties," *Nature Communications*, vol. 5, p. 5021, 2014.

[149] R. A. Cowley, S. N. Gvasaliya, S. G. Lushnikov, B. Roessli, and G. M. Rotaru, "Relaxing with Relaxors: A Review of Relaxor Ferroelectrics," *Advances in Physics*, vol. 60, p. 229, 2011.

[150] V. Sivasubramanian, V. Subramanian, and S. Kojima, "Classical Ferroelectric Like Behavior of Highly Ordered $Pb(Sc_{1/2}Nb_{1/2})O_3$ Studied by Dielectric and Brillouin Scattering Spectroscopy," *Physical Review B*, vol. 93, p. 054115, 2016.

[151] N. Setter and L. E. Cross, "The Contribution of Structural Disorder to Diffuse Phase Transitions in Ferroelectrics," *Journal of Materials Science*, vol. 15, pp. 2478–2482, 1980.

[152] K. I. Kobayashi, T. Kimura, H. Sawada, K. Terakura, and Y. Tokura, "Room-Temperature Magnetoresistance in an Oxide Material with an Ordered Double-

Perovskite Structure," *Nature*, vol. 395, p. 677, 1998.

[153] M. C. Viola *et al.*, "Induction of Colossal Magnetoresistance in the Double Perovskite Sr_2CoMoO_6," *Chemistry of Materials*, vol. 14, p. 812, 2002.

[154] R. N. Mahato, K. Sethupathi, and V. Sankaranarayanan, "Colossal Magnetoresistance in the Double Perovskite Oxide La_2CoMnO_6," *Journal of Applied Physics*, vol. 107, p. 09D714, 2010.

[155] O. Erten, O. N. Meetei, A. Mukherjee, M. Randeria, N. Trivedi, and P. Woodward, "Theory of Half-Metallic Ferrimagnetism in Double Perovskites," *Physical Review Letters*, vol. 107, p. 257201, 2011.

[156] M. Retuerto *et al.*, "Half-Metallicity in Pb_2CoReO_6 Double Perovskite and High Magnetic Ordering Temperature in Pb_2CrReO_6 Perovskite," *Chemistry of Materials*, vol. 27, p. 4450, 2015.

[157] F. Estrada, E. J. Guzmán, O. Navarro, and M. Avignon, "Curie Temperature Behavior in Half-Metallic Ferromagnetic Double Perovskites within the Electronic Correlation Picture," *Physical Review B*, vol. 97, p. 195155, 2018.

[158] H. Kato *et al.*, "Metal-Insulator Transition of Ferromagnetic Ordered Double Perovskites: $(Sr_{1-y}Ca_y)FeReO_6$," *Physical Review B*, vol. 65, p. 144404, 2002.

[159] Y. Krockenberger *et al.*, "Sr_2CrOsO_6: End Point of a Spin-Polarized Metal-Insulator Transition by 5d Band Filling," *Physical Review B*, vol. 75, p. 020404(R), 2007.

[160] V. N. Antonov, L. V. Bekenov, and A. Ernst, "Electronic Structure and X-ray Magnetic Circular Dichroism in A_2FeReO_6 (A=Ca, Sr, and Ba) Oxides," *Physical Review B*, vol. 94, p. 035122, 2016.

[161] D. R. Harshman *et al.*, "Spin-Glass Behavior, Spin Fluctuations, and Superconductivity in $Sr_2Y(Ru_{1-u}Cu_u)O_6$," *Physical Review B*, vol. 67, p. 054509, 2003.

[162] M. H. K. Rubel *et al.*, "Superconducting Double Perovskite Bismuth Oxide Prepared by a Low-Temperature Hydrothermal Reaction," *Angewandte Chemie - International Edition*, vol. 53, p. 3599, 2014.

[163] F. Chu, N. Setter, and A. K. Tagantsev, "The Spontaneous Relaxor-Ferroelectric Transition of $Pb(Sc_{0.5}Ta_{0.5})O_3$," *Journal of Applied Physics*, vol. 74, p. 5129, 1993.

[164] A. Levstik *et al.*, "Magnetoelectric Relaxor," *Applied Physics Letters*, vol. 91, p. 012905, 2007.

[165] P. D. Battle, S. I. Evers, E. C. Hunter, and M. Westwood, "$La_3Ni_2SbO_9$: A Relaxor

Ferromagnet," *Inorganic Chemistry*, vol. 52, p. 6648, 2013.

[166] B. Yan *et al.*, "Lattice-Site-Specific Spin Dynamics in Double Perovskite Sr_2CoOsO_6," *Physical Review Letters*, vol. 112, p. 147202, 2014.

[167] D. Yang *et al.*, "Magnetostructural Coupling Behavior at the Ferromagnetic Transition in Double-Perovskite Sr_2FeMoO_6," *Physical Review B*, vol. 93, p. 024101, 2016.

[168] M. R. Li *et al.*, "$Mn_2(Fe_{0.8}Mo_{0.2})MoO_6$: A Double Perovskite with Multiple Transition Metal Sublattice Magnetic Effects," *Chemistry of Materials*, vol. 30, p. 4508, 2018.

[169] K. Naveen *et al.*, "Reentrant Magnetism at the Borderline Between Long-Range Antiferromagnetic Order and Spin-Glass Behavior in the B-Site Disordered Perovskite System $Ca_{2-x}Sr_xFeRuO_6$," *Physical Review B*, vol. 98, p. 224423, 2018.

[170] Y. K. Wakabayashi *et al.*, "Ferromagnetism Above 1000 K in a Highly Cation-Ordered Double-Perovskite Insulator Sr_3OsO_6," *Nature Communications*, vol. 10, p. 535, 2019.

[171] W. Kleemann, V. V. Shvartsman, P. Borisov, and A. Kania, "Coexistence of Antiferromagnetic and Spin Cluster Glass Order in the Magnetoelectric Relaxor Multiferroic $PbFe_{0.5}Nb_{0.5}O_3$," *Physical Review Letters*, vol. 105, p. 257202, 2010.

[172] S. Chillal *et al.*, "Microscopic Coexistence of Antiferromagnetic and Spin-Glass States," *Physical Review B*, vol. 87, p. 220403(R), 2013.

[173] G. M. Rotaru *et al.*, "Spin-Glass State and Long-Range Magnetic Order in $Pb(Fe_{1/2}Nb_{1/2})O_3$ Seen via Neutron Scattering and muon Spin Rotation," *Physical Review B*, vol. 79, p. 184430, 2009.

[174] S. Chillal *et al.*, "Magnetic Short- and Long-Range Order in $PbFe_{0.5}Ta_{0.5}O_3$," *Physical Review B*, vol. 89, p. 174418, 2014.

[175] V. V. Laguta *et al.*, "Effect of Ba and Ti Doping on Magnetic Properties of Multiferroic $Pb(Fe_{1/2}Nb_{1/2})O_3$," *Physical Review B*, vol. 87, p. 064403, 2013.

[176] P. D. Battle, T. C. Gibb, A. J. Herod, S.-H. Kim, and P. H. Munns, "Investigation of Magnetic Frustration in A_2FeMO_6 (A = Ca, Sr, Ba; M = Nb, Ta, Sb) by Magnetometry and Mossbauer Spectroscopy," *J. Mater. Chem.*, vol. 5, p. 865, 1995.

[177] K. Tezuka, K. Henmi, Y. Hinatsu, and N. M. Masaki, "Magnetic Susceptibilities and Mossbauer Spectra of Perovskites A_2FeNbO_6 (A = Sr, Ba)," *Journal of Solid State Chemistry*, vol. 154, p. 591, 2000.

[178] M. Maryško *et al.*, "Magnetic Susceptibility of Multiferroics and Chemical Ordering," *AIP Advances*, vol. 7, p. 056409, 2017.

[179] M. R. Li *et al.*, "Designing Polar and Magnetic Oxides: Zn_2FeTaO_6 - In Search of Multiferroics," *Journal of the American Chemical Society*, vol. 136, p. 8508, 2014.

[180] P. S. Wang, W. Ren, L. Bellaiche, and H. J. Xiang, "Predicting a Ferrimagnetic Phase of Zn_2FeOsO_6 with Strong Magnetoelectric Coupling," *Physical Review Letters*, vol. 114, p. 147204, 2015.

[181] M. R. Li *et al.*, "Mn_2FeWO_6 : A New Ni_3TeO_6 -Type Polar and Magnetic Oxide," *Advanced Materials*, vol. 27, p. 2177, 2015.

[182] J. Lohr, F. Pomiro, V. Pomjakushin, J. A. Alonso, R. E. Carbonio, and R. D. Sánchez, "Multiferroic Properties of $RFe_{0.5}Co_{0.5}O_3$ with R=Tm,Er,Ho,Dy,and Tb," *Physical Review B*, vol. 98, p. 134405, 2018.

[183] G. A. Smolenskii, V. A. Isupov, and A. I. Agranovskaya, "A New Group of Ferroelectrics-(with Layered Structure)," *Soviet Physics-Solid State*, vol. 1, p. 149, 1959.

[184] V. A. Bokov, I. E. Mylnikova, and G. A. Smolenskii, "Ferroelectric Antiferromagnetics," *Soviet Physics Jetp-Ussr*, vol. 15, p. 447, 1962.

[185] S. P. Singh, A. K. Singh, D. Pandey, H. Sharma, and O. Parkash, "Crystallographic Phases, Phase Transitions, and Barrier Layer Formation in (1 - x) $[Pb(Fe_{1/2}Nb_{1/2})O_3]$-$xPbTiO_3$," *Journal of Materials Research*, vol. 18, p. 2677, 2003.

[186] R. Blinc, M. Kosec, J. Holc, Z. Trontelj, Z. Jaglicic, and N. Dalal, "Magnetoelectric Effect in $Pb(Fe_{1/2}Nb_{1/2})O_3$," *Ferroelectrics*, vol. 349, p. 16, 2007.

[187] S. P. Singh, S. M. Yusuf, S. Yoon, S. Baik, N. Shin, and D. Pandey, "Ferroic Transitions in the Multiferroic (1-x)$Pb(Fe_{1/2}Nb_{1/2})O_3$-$xPbTiO_3$ System and its Phase Diagram," *Acta Materialia*, vol. 58, p. 5381, 2010.

[188] N. Lampis, P. Sciau, and A. G. Lehmann, "Rietveld Refinements of the Paraelectric and Ferroelectric Structures of $PbFe_{0.5}Ta_{0.5}O_3$," *Journal of Physics Condensed Matter*, vol. 11, p. 3489, 1999.

[189] S. P. Singh, D. Pandey, S. Yoon, S. Baik, and N. Shin, "Evidence for Monoclinic Crystal Structure and Negative Thermal Expansion Below Magnetic Transition Temperature in $Pb(Fe_{1/2}Nb_{1/2})O_3$," *Applied Physics Letters*, vol. 90, p. 242915, 2007.

[190] S. A. Ivanov, R. Tellgren, H. Rundlof, N. W. Thomas, and S. Ananta,

"Investigation of the Structure of the Relaxor Ferroelectric $Pb(Fe_{1/2}Nb_{1/2})O_3$ by Neutron Powder Diffraction," *Journal of Physics Condensed Matter*, vol. 12, p. 2393, 2000.

[191] L. Chen *et al.*, "Magnetoelectric Relaxor and Reentrant Behaviours in Multiferroic $Pb(Fe_{2/3}W_{1/3})O_3$ Crystal," *Scientific Reports*, vol. 6, p. 22327, 2016.

[192] V. V Laguta *et al.*, "Cluster Superconductivity in the Magnetoelectric $Pb(Fe_{1/2}Sb_{1/2})O_3$ Ceramics," *arXiv: 1611.09895v1*, 2016.

[193] V. V. Laguta *et al.*, "Superspin Glass Phase and Hierarchy of Interactions in Multiferroic $PbFe_{1/2}Sb_{1/2}O_3$: An Analog of Ferroelectric Relaxors?," *New Journal of Physics*, vol. 16, p. 113041, 2014.

[194] Y. Yang, J. M. Liu, H. B. Huang, W. Q. Zou, P. Bao, and Z. G. Liu, "Magnetoelectric Coupling in Ferroelectromagnet $Pb(Fe_{1/2}Nb_{1/2})O_3$ Single Crystals," *Physical Review B*, vol. 70, p. 132101, 2004.

[195] A. B. Harris, "Effect of Random Defects on the Critical Behaviour of Ising Models," *Journal of Physics C: Solid State Physics*, vol. 7, p. 1671, 1974.

[196] V. K. S. Shante and S. Kirkpatrick, "An Introduction to Percolation Theory," *Advances in Physics*, vol. 20, pp. 325–357, 1971.

[197] M. F. Sykes and J. W. Essam, "Critical Percolation Probabilities by Series Methods," *Physical Review*, vol. 133, p. A310, 1964.

[198] S. Bedanta and W. Kleemann, "Supermagnetism," *journal of physics D: Applied Physics*, vol. 42, p. 013001, 2009.

[199] Y. Y. Liu, X. M. Chen, X. Q. Liu, and L. Li, "Dielectric Relaxations in $Ca(Fe_{1/2}Nb_{1/2})O_3$ complex perovskite ceramics," *Applied Physics Letters*, vol. 90, p. 262904, 2007.

[200] I. O. Troyanchuk, N. V. Tereshko, and M. V. Bushinskiĭ, "Structural and Magnetic Phase Transformations in the $BiFeO_3$-$CaFe_{0.5}Nb_{0.5}O_3$ System," *Physics of the Solid State*, vol. 51, p. 785, 2009.

[201] P. W. Barnes, M. W. Lufaso, and P. M. Woodward, "Structure Determination of $A_2M^{3+}TaO_6$ and $A_2M^{3+}NbO_6$ Ordered Perovskites: Octahedral Tilting and Pseudosymmetry," *Acta Crystallographica Section B: Structural Science*, vol. 62, p. 384, 2006.

[202] M. W. Lufaso, P. M. Woodward, and J. Goldberger, "Crystal Structures of Disordered $A_2Mn^{3+}M^{5+}O_6$ (A=Sr, Ca; M=Sb, Nb, Ru) Perovskites," *Journal of Solid State Chemistry*, vol. 177, p. 1651, 2004.

[203] I. P. Raevski *et al.*, "Experimental Evidence of the Crucial Role of Nonmagnetic Pb Cations in the Enhancement of the Néel Temperature in Perovskite $Pb_{1-x}Ba_xFe_{1/2}Nb_{1/2}O_3$," *Physical Review B*, vol. 80, p. 024108, 2009.

[204] A. M. Glazer, "The Classification of Tilted Octahedra in Perovskites," *Acta Crystallographica B*, vol. 28, p. 3384, 1972.

[205] F. Kubel and H. Schmid, "Structure of a Ferroelectric and Ferroelastic Monodomain Crystal of the Perovskite $BiFeO_3$," *Acta Crystallographica Section B*, vol. 46, pp. 698–702, 1990.

[206] M. Kumar and K. L. Yadav, "Rapid Liquid Phase Sintered Mn Doped $BiFeO_3$ Ceramics with Enhanced Polarization and Weak Magnetization," *Applied Physics Letters*, vol. 91, p. 242901, 2007.

[207] G. S. Arya and N. S. Negi, "Effect of In and Mn Co-doping on Structural, Magnetic and Dielectric Properties of $BiFeO_3$ Nanoparticles," *Journal of Physics D: Applied Physics*, vol. 46, p. 095004, 2013.

[208] S. K. Singh, H. Ishiwara, and K. Maruyama, "Room Temperature Ferroelectric Properties of Mn-Substituted $BiFeO_3$ Thin Films Deposited on Pt Electrodes Using Chemical Solution Deposition," *Applied Physics Letters*, vol. 88, p. 262908, 2006.

[209] T. Kawae, Y. Terauchi, H. Tsuda, M. Kumeda, and A. Morimoto, "Improved Leakage and Ferroelectric Properties of Mn and Ti Codoped $BiFeO_3$ Thin Films," *Applied Physics Letters*, vol. 94, p. 112904, 2009.

[210] V. R. Palkar, D. C. Kundaliya, and S. K. Malik, "Effect of Mn Substitution on Magnetoelectric Properties of Bismuth Ferrite System," *Journal of Applied Physics*, vol. 93, pp. 4337–4339, 2003.

[211] W. Liu *et al.*, "Structure Transition and Multiferroic Properties of Mn-Doped $BiFeO_3$ Thin Films," *Journal of Materials Science: Materials in Electronics*, vol. 25, pp. 723–729, 2014.

[212] Z. Hu *et al.*, "Effects of Nd and High-Valence Mn Co-Doping on the Electrical and Magnetic Properties of Multiferroic $BiFeO_3$ Ceramics," *Solid State Communications*, vol. 150, pp. 1088–1091, 2010.

[213] J. Z. Huang, Y. Wang, Y. Lin, M. Li, and C. W. Nan, "Effect of Mn Doping on Electric and Magnetic Properties of $BiFeO_3$ Thin Films by Chemical Solution Deposition," *Journal of Applied Physics*, vol. 106, p. 063911, 2009.

[214] A. Ianculescu, F. P. Gheorghiu, P. Postolache, O. Oprea, and L. Mitoseriu, "The Role of Doping on the Structural and Functional Properties of $BiFe_{1-x}Mn_xO_3$

Magnetoelectric Ceramics," *Journal of Alloys and Compounds*, vol. 504, pp. 420–426, 2010.

[215] H. Wang, H. Huang, and B. Wang, "Effect of Mn Substitution for Fe in Multiferroic $BiFeO_3$: A First-Principles Study," *Science of Advanced Materials*, vol. 2, pp. 184–189, 2010.

[216] Y. Yoneda, Y. Kitanaka, Y. Noguchi, and M. Miyayama, "Electronic and Local Structures of Mn-Doped $BiFeO_3$ Crystals," *Physical Review B*, vol. 86, p. 184112, 2012.

[217] D. Kothari *et al.*, "Study of the Effect of Mn Doping on the $BiFeO_3$ System," *Journal of Physics Condensed Matter*, vol. 19, p. 136202, 2007.

[218] A. Mukherjee, S. Basu, P. K. Manna, S. M. Yusuf, and M. Pal, "Giant Magnetodielectric and Enhanced Multiferroic Properties of Sm Doped Bismuth Ferrite Nanoparticles," *Journal of Materials Chemistry C*, vol. 2, pp. 5885–5891, 2014.

[219] D. P. Dutta, B. P. Mandal, M. D. Mukadam, S. M. Yusuf, and A. K. Tyagi, "Improved Magnetic and Ferroelectric Properties of Sc and Ti Codoped Multiferroic Nano $BiFeO_3$ Prepared via Sonochemical Synthesis," *Dalton Transactions*, vol. 43, pp. 7838–7846, 2014.

[220] S. M. Lee and Y. S. Cho, "Optical and Grain Boundary Potential Characteristics of Sulfurized $BiFeO_3$ Thin Films for Photovoltaic Applications," *Dalton Transactions*, vol. 45, pp. 5598–5603, 2016.

[221] N. Koshizuka and S. Ushioda, "Inelastic-Light-Scattering Study of Magnon Softening in $ErFeO_3$," *Physical Review B*, vol. 22, pp. 5394–5399, 1980.

[222] Y. G. Chukalkin and B. N. Goshchitskii, "Radiation Amorphization of Orthoferrite $YFeO_3$," *Physica Status Solidi (a)*, vol. 200, pp. 9R-11R, 2003.

[223] S. Bhattacharjee, A. Senyshyn, H. Fuess, and D. Pandey, "Morin-Type Spin-Reorientation Transition Below the Néel Transition in the Monoclinic Compositions of $(1-x)BiFeO_3$-$xPbTiO_3$ (x=0.25 and 0.27): A Combined Dc Magnetization and X-ray and Neutron Powder Diffraction Study," *Physical Review B*, vol. 87, p. 054417, 2013.

[224] J. L. Tholence, "On the Frequency Dependence of the Transition Temperature in Spin Glasses," *Solid State Communications*, vol. 35, p. 113, 1980.

[225] P. Berge, P. Calmetter, C. Laj, M. Tournarie, and B. Volochine, "Dynamica of Concebtration Fluctuations in a Binary Mixture in the Hydrdynamical and

Nonhydrodynamical Regimes," *Physical Review Letters*, vol. 24, pp. 1223–1225, 1970.

[226] N. Zhang *et al.*, "Role of Oxygen Vacancies in Deciding the High Temperature Magnetic Properties of Ba and Sm Substituted $BiFeO_3$ Ceramics," *Journal of Alloys and Compounds*, vol. 677, pp. 252–257, 2016.

[227] K. Min, F. Huang, Y. Jin, X. Lu, H. Wu, and J. Zhu, "Control of Oxygen Vacancies and their Kinetic Behaviours via Reversible Oxygen Loss in $BiFeO_3$ Ceramics," *Journal of Physics D: Applied Physics*, vol. 48, p. 445301, 2015.

[228] C. E. Rodríguez Torres *et al.*, "Oxygen-Vacancy-Induced Local Ferromagnetism as a Driving Mechanism in Enhancing the Magnetic Response of Ferrites," *Physical Review B*, vol. 89, p. 104411, 2014.

[229] H. Wu *et al.*, "Significant Enhancements of Dielectric and Magnetic Properties in $Bi(Fe_{1-x}Mg_x)O_{3-x/2}$ Induced by Oxygen Vacancies," *Journal of Physics D: Applied Physics*, vol. 46, p. 145001, 2013.

[230] C. E. Rodríguez Torres, F. Golmar, M. Ziese, P. Esquinazi, and S. P. Heluani, "Evidence of Defect-Induced Ferromagnetism in $ZnFe_2O_4$ Thin Films," *Physical Review B*, vol. 84, p. 064404, 2011.

[231] T. R. Paudel, S. S. Jaswal, and E. Y. Tsymbal, "Intrinsic Defects in Multiferroic $BiFeO_3$ and their Effect on Magnetism," *Physical Review B*, vol. 85, p. 104409, 2012.

[232] C. Ederer and N. A. Spaldin, "Influence of Strain and Oxygen Vacancies on the Magnetoelectric Properties of Multiferroic Bismuth Ferrite," *Physical Review B*, vol. 71, p. 224103, 2005.

[233] Q. Wang, Q. Sun, G. Chen, Y. Kawazoe, and P. Jena, "Vacancy-Induced Magnetism in ZnO Thin Films and Nanowires," *Physical Review B*, vol. 77, p. 205411, 2008.

[234] R. Yang, S. Lin, X. Fang, X. Gao, M. Zeng, and J. Liu, "First-Principles Study on the Magnetic Properties in Mg Doped $BiFeO_3$ with and without Oxygen Vacancies," *Journal of Applied Physics*, vol. 114, p. 233912, 2013.

[235] H. Yamada, X. G. Zheng, Y. Soejima, and M. Kawaminami, "Lattice Distortion and Magnetolattice Coupling in CuO," *Physical Review B*, vol. 69, p. 104104, 2004.

[236] C. R. Dela Cruz *et al.*, "Structural Anomalies at the Magnetic and Ferroelectric Transitions in RMn_2O_5 (R=Tb, Dy, Ho)," *Physical Review B*, vol. 73, p.

100406(R), 2006.

[237] M. Matsuda *et al.*, “Magnetic Dispersion and Anisotropy in Multiferroic $BiFeO_3$,” *Physical Review Letters*, vol. 109, p. 067205, 2012.

[238] H. Yoshizawa, S. Mitsuda, H. Aruga, and A. Ito, “Mixed Phase of Spin-Glass Ordering and Antiferromagnetism in an Ising System, $Fe_xMn_{1-x}TiO_3$,” *Physical Review Letters*, vol. 59, pp. 2364–2367, 1987.

[239] P. Z. Wong *et al.*, “Coexistence of Spin-Glass and Antiferromagnetic Orders in the Ising System $Fe_{0.55}Mg_{0.45}Cl_2$,” *Physical Review Letters*, vol. 55, pp. 2043–2046, 1985.

[240] P. Z. Wong, H. Yoshizawa, and S. M. Shapiro, “Coexistence of Antiferromagnetism and Spin-Glass Ordering in the Ising System $Fe_{0.55}Mg_{0.45}Cl_2$,” *Journal of Applied Physics*, vol. 57, pp. 3462–3464, 1985.

[241] A. Ito, H. Aruga, E. Torikai, M. Kikuchi, Y. Syono, and H. Takei, “Time-Dependent Phenomena in a Short-Range Ising Spin-Glass , $Fe_{0.5}Mn_{0.5}TiO_3$,” *Physical Review Letters*, vol. 57, pp. 483–486, 1986.

[242] J. Lauer and W. Keune, “Magnetic Double Transition in Au-Fe Near the Percolation Threshold,” *Physical Review Letters*, vol. 48, pp. 1850–1853, 1982.

[243] D. H. Ryan, "Recent Progress in Random Magnets," *World Scientific, Singapore*. 1992.

[244] Y. Imry and M. Wortis, “Influence of Quenched Impurities on First-Order Phase Transitions,” *Physical Review B*, vol. 19, pp. 3580–3585, 1979.

[245] A. Ito, H. Aruga, M. Kikuchi, Y. Syono, and H. Takei, “Phase Diagram and Reentrant Spin-Glass Behavior in a Random Mixture of Two Ising-Antiferromagnets $Fe_xMn_{1-x}TiO_3$,” *Solid State Communications*, vol. 66, pp. 475–479, 1988.

[246] I. A. Campbell, S. Senoussi, F. Varret, J. Teillet, and A. Hamzić, “Competing Ferromagnetic and Spin-Glass Order in a AuFe Alloy,” *Physical Review Letters*, vol. 50, pp. 1615–1618, 1983.

[247] S. Murayama, K. Yokosawa, Y. Miyako, and E. F. Wassermann, “Two Successive Transitions in Uniaxially Anisotropic Spin-Glasses,” *Physical Review Letters*, vol. 57, p. 1785, 1986.

[248] H. Kawano, H. Yoshizawa, A. Ito, and K. Motoya, “Two Successive Spin Glass Transitions in Nondiluted Heisenberg-Like Spin Galss $Ni_{0.42}Mn_{0.58}TiO_3$,” *Journal of the Physical Society of Japan*, vol. 62, p. 2575, 1993.

[249] M. Itoh *et al.*, "Magnetic Phase Transitions in the Two-Dimensional Random Mixture $K_2Cu_xCo_{1-x}F_4$ with Competing Exchange Interactions," *Journal of the Physical Society of Japan*, vol. 59, pp. 1792–1800, 1990.

[250] S. Sharma, T. Basu, A. Shahee, K. Singh, N. P. Lalla, and E. V. Sampathkumaran, "Multiglass Properties and Magnetoelectric Coupling in the Uniaxial Anisotropic Spin-Cluster-Glass Fe_2TiO_5," *Physical Review B*, vol. 90, p. 144426, 2014.

[251] W. M. Zhu, H. Y. Guo, and Z. G. Ye, "Structural and Magnetic Characterization of Multiferroic $(BiFeO_3)_{1-x}(PbTiO_3)_x$ Solid Solutions," *Physical Review B*, vol. 78, p. 014401, 2008.

[252] Y. Wan *et al.*, "Microstructure, Ferroelectric, Piezoelectric, and Ferromagnetic Properties of Sc-Modified $BiFeO_3$-$BaTiO_3$ Multiferroic Ceramics with MnO_2 Addition," *Journal of the American Ceramic Society*, vol. 97, pp. 1809–1818, 2014.

[253] J. R. Carvajal, Laboratary, and FULLPROF, "A Rietveld amd Pattern Matching and Analysis Program," *Laboratary Leon Brillouin, CEA-CNRS, France*. 2010.

[254] H. D. Megaw and C. N. W. Darlington, "Geometrical and Structural Relations in the Rhombohedral Perovskites," *Acta Cryst.*, vol. A31, p. 161, 1975.

[255] A. K. Pramanik and A. Banerjee, "Interparticle Interaction and Crossover in Critical Lines on Field-Temperature Plane in $Pr_{0.5}Sr_{0.5}MnO_3$ Nanoparticles," *Physical Review B*, vol. 82, p. 094402, 2010.

[256] D. Kumar and A. Banerjee, "Coexistence of Interacting Ferromagnetic Clusters and Small Antiferromagnetic Clusters in $La_{0.5}Ba_{0.5}CoO_3$," *Journal of Physics Condensed Matter*, vol. 25, p. 216005, 2013.

[257] P. Dey, T. K. Nath, P. K. Manna, and S. M. Yusuf, "Enhanced Grain Surface Effect on Magnetic Properties of Nanometric $La_{0.7}Ca_{0.3}MnO_3$ Manganite: Evidence of Surface Spin Freezing of Manganite Nanoparticles," *Journal of Applied Physics*, vol. 104, p. 103907, 2008.

[258] A. Pimenov, A. A. Mukhin, V. Y. Ivanov, V. D. Travkin, A. M. Balabashov, and A. Loidl, "Possible Evidence for Electromagnons in Multiferroic Manganites," *Nature Physics*, vol. 2, p. 97, 2006.

[259] R. De Sousa and J. E. Moore, "Optical Coupling to Spin Waves in the Cycloidal Multiferroic $BiFeO_3$," *Physical Review B*, vol. 77, p. 012406, 2008.

[260] R. S. Fishman, N. Furukawa, J. T. Haraldsen, M. Matsuda, and S. Miyahara, "Identifying the Spectroscopic Modes of Multiferroic $BiFeO_3$," *Physical Review B*,

vol. 86, p. 220402(R), 2012.

[261] K. Gunnarsson, P. Svedlindh, P. Nordblad, L. Lundgren, H. Aruga, and A. Ito, "Dynamics of an Ising Spin-Glass in the Vicinity of the Spin-Glass Temperature," *Physical Review Letters*, vol. 61, p. 754, 1988.

[262] R. G. Palmer, D. L. Stein, E. Abrahams, and P. W. Anderson, "Models of Hierarchically Constrained Dynamics for Glassy Relaxation," *Physical Review Letters*, vol. 53, pp. 958–961, 1984.

[263] M. D. Mukadam, A. Kumar, S. M. Yusuf, J. V. Yakhmi, R. Tewari, and G. K. Dey, "Spin-Glass Behavior in Ferromagnetic $Fe[Fe(CN)_6]\cdot xH_2O$ Nanoparticles," *Journal of Applied Physics*, vol. 103, p. 123902, 2008.

[264] T. Kiyama, K. Yoshimura, K. Kosuge, Y. Ikeda, and Y. Bando, "Invar Effect of SrR: Itinerant Electron Magnetism of Ru 4d Electrons," *Physical Review B*, vol. 54, p. R756, 1996.

[265] M. I. Darby, "Tables of the Brillouin Function and of the Related Function for the Spontaneous Magnetization," *British Journal of Applied Physics*, vol. 18, p. 1415, 1967.

[266] J. Wang *et al.*, "Epitaxial $BiFeO_3$ Multiferroic Thin Film Heterostructures," *Science*, vol. 299, pp. 1719–1722, 2003.

[267] H. Béa *et al.*, "Investigation on the Origin of the Magnetic Moment of $BiFeO_3$ Thin Films by Advanced X-ray Characterizations," *Physical Review B*, vol. 74, p. 020101(R), 2006.

[268] H. Wang, L. He, H. Jiang, C. Steele, and X. Wu, "Electronic Origin of the Spin-Phonon Coupling Effect in Transition-Metal Perovskites," *Physical Review B*, vol. 96, p. 075121, 2017.

[269] J. G. Bednorz and K. A. Muller, "$Sr_{1-x}Ca_xTiO_3$: An XY Quantum Ferroelectric with Transition to Randomness," *Physical Review Letters*, vol. 52, p. 2289, 1984.

[270] K. Kumar and D. Pandey, "Quantum phase transitions in $Ba_{(1-x)}Ca_xFe_{12}O_{19}$ ($0 \leq x \leq 0.10$)," *Physical Review B*, vol. 96, p. 024102, 2017.

[271] H. Kawamura, "Chirality Scenario of the Spin-Glass Ordering," *Journal of the Physical Society of Japan*, vol. 79, p. 011007, 2010.

[272] H. Kawamura, "The Ordering of XY Spin Glasses," *Journal of Physics Condensed Matter*, vol. 23, p. 164210, 2011.

[273] T. Çağlar and A. N. Berker, "Phase Transitions Between Different Spin-Glass Phases and Between Different Chaoses in Quenched Random Chiral Systems,"

Physical Review E, vol. 96, p. 032103, 2017.

[274] M. Schmidt, F. M. Zimmer, and S. G. Magalhaes, "Spin Liquid and Infinitesimal-Disorder-Driven Cluster Spin Glass in the Kagome Lattice," *Journal of Physics Condensed Matter*, vol. 29, p. 165801, 2017.

[275] L. Shlyk, S. Strobel, B. Farmer, L. E. De Long, and R. Niewa, "Coexistence of Ferromagnetism and Unconventional Spin-Glass Freezing in the Site-Disordered Kagome Ferrite $SrSn_2Fe_4O_{11}$," *Physical Review B*, vol. 97, p. 054426, 2018.

[276] Z. Ma *et al.*, "Spin-Glass Ground State in a Triangular-Lattice Compound $YbZnGaO_4$," *Physical Review Letters*, vol. 120, p. 087201, 2018.

[277] M. V. Romitti, F. M. Zimmer, C. V. Morais, and S. G. Magalhaes, "Specific Heat and Nonlinear Susceptibility in Spin Glasses with Random Fields," *Physical Review B*, vol. 99, p. 014203, 2019.

[278] J. F. Gebbia *et al.*, "Glassy Anomalies in the Low-Temperature Thermal Properties of a Minimally Disordered Crystalline Solid," *Physical Review Letters*, vol. 119, p. 215506, 2017.

[279] Y. Sun, M. B. Salamon, K. Garnier, and R. S. Averback, "Memory Effects in an Interacting Magnetic Nanoparticle System," *Physical Review Letters*, vol. 91, p. 167206, 2003.

[280] E. S. R. Gopal, *Specific Heat at Low Temperatures*. Plenun Press, New York, 1966.

[281] C. M. N. Kumar *et al.*, "Hyperfine and Crystal Field Interactions in Multiferroic $HoCrO_3$," *Journal of Physics Condensed Matter*, vol. 28, p. 476001, 2016.

[282] D. L. Martin, "Specific Heat of Spin-Glass CuMn below 3 K," *Physical Review B*, vol. 20, p. 368, 1979.

[283] W. E. Fogle, J. D. Boyer, R. A. Fisher, and N. E. Phillips, "Specific-Heat Anomaly and Phase Boundary for the Spin-Glass-Paramagnet in CuMn," *Physical Review Letters*, vol. 50, pp. 1815–1818, 1983.

[284] T. Pérez-Castañeda, R. J. Jiménez-Riobóo, and M. A. Ramos, "Two-level Systems and Boson Peak remain Stable in 110-million-year-old Amber Glass," *Physical Review Letters*, vol. 112, p. 165901, 2014.

[285] L. R. Walker and R. E. Walstedt, "Computer Model of Metallic Spin-Glasses," *Physical Review Letters*, vol. 38, pp. 514–518, 1977.

[286] J. Lu *et al.*, "On the Room Temperature Multiferroic $BiFeO_3$: Magnetic, Dielectric and Thermal Properties," *European Physical Journal B*, vol. 75, no. 4, pp. 451–

460, 2010.

[287] Y. Wang *et al.*, "First-Principles Lattice Dynamics and Heat Capacity of $BiFeO_3$," *Acta Materialia*, vol. 59. pp. 4229–4234, 2011.

[288] L. Wei *et al.*, "Lattice Dynamics of Bismuth-Deficient $BiFeO_3$ from First Principles," *Computational Materials Science*, vol. 111, pp. 374–379, 2016.

[289] C. Xu, B. Xu, B. Dupé, and L. Bellaiche, "Magnetic Interactions in $BiFeO_3$: A first-principles study," *Physical Review B*, vol. 99, p. 104420, 2019.

[290] A. I. Chumakov *et al.*, "Equivalence of the Boson Peak in Glasses to the Transverse Acoustic van Hove Singularity in Crystals," *Physical Review Letters*, vol. 106, p. 225501, 2011.

[291] B. C. Melot *et al.*, "Large Low-Temperature Specific Heat in Pyrochlore Bi_2TiO_7," *Physical Review B*, vol. 79, p. 224111, 2009.

[292] D. J. Safarik, R. B. Schwarz, and M. F. Hundley, "Similarities in the Cp/T^3 Peaks in Amorphous and Crystalline Metals," *Physical Review Letters*, vol. 96, p. 195902, 2006.

[293] A. N. Vasiliev, T. N. Voloshok, A. V Granato, D. M. Joncich, and V. A. Khonik, "Relationship Between Low-Temperature Boson Heat Capacity Peak and High-Temperature Shear Modulus Relaxation in a Metallic Gass," *Physical Review B*, vol. 80, p. 172102, 2009.

[294] A. Giuntoli and D. Leporini, "Boson Peak Decouples From Elasticity in Glasses with Low Connectivity," *Physical Review Letters*, vol. 121, p. 185502, 2018.

[295] J. Wosnitza, H. v. Lohneysen, W. Zinn, and U. Krey, "Magnetic Excitations in $Eu_xS_{1-x}S$ in High Magnetic Fields," *Physical Review B*, vol. 33, pp. 3436–3440, 1986.

[296] V. K. Anand *et al.*, "Evidence for a Dynamical Ground State in the Frustrated Pyrohafnate $Tb_2Hf_2O_7$," *Physical Review B*, vol. 97, p. 094402, 2018.

[297] N. Hanasaki *et al.*, "Nature of the Transition Between a Ferromagnetic Metal and a Spin-Glass Insulator in Pyrochlore Molybdates," *Physical Review Letters*, vol. 99, p. 086401, 2007.

[298] L. J. Vera Stimpson, J. M. Powell, G. B. G. Stenning, M. Jura, and D. C. Arnold, "Spin-Glass Behavior in $K_xRu_{4-y}Ni_yO_8$ Hollandite Materials," *Physical Review B*, vol. 98, p. 174429, 2018.

[299] G. Parisi, "Infinite Number of Order Parameters for Spin-Glasses," *Physical Review Letters*, vol. 43, p. 1754, 1979.

[300] P. Bag, P. R. Baral, and R. Nath, "Cluster Spin-Glass Behavior and Memory Effect in $Cr_{0.5}Fe_{0.5}Ga$," *Physical Review B*, vol. 98, p. 144436, 2018.

[301] P. M. Shand, T. Rash, M. Streicher, T. E. Kidd, K. R. Boyle, and L. H. Strauss, "Coercivity and Exchange Bias of $Mn_{0.25}Ti_{1.1}S_2$ in the Cluster-Glass State," *Physical Review B*, vol. 82, p. 214413, 2010.

[302] B. Martinez, X. Obradors, L. Balcells, A. Rouanet, and C. Monty, "Low Temperature Surface Spin-Glass Transition in γ-Fe_2O_3 Nanoparticles," *Physical review letters*, vol. 80, p. 181, 1998.

[303] M. D. Mukadam, S. M. Yusuf, P. Sharma, S. K. Kulshreshtha, and G. K. Dey, "Dynamics of Spin Clusters in Amorphous Fe_2O_3," *Physical Review B*, vol. 72, p. 174408, 2005.

[304] S. Ghara, B. G. Jeon, K. Yoo, K. H. Kim, and A. Sundaresan, "Reentrant Spin-Glass State and Magnetodielectric Effect in the Spiral Magnet $BiMnFe_2O_6$," *Physical Review B*, vol. 90, p. 024413, 2014.

[305] X. K. Zhang *et al.*, "Phase Coexistence and Exchange-Bias Effect in $LiMn_2O_4$ Nanorods," *Physical Review B*, vol. 97, p. 104405, 2018.

[306] K. Jonason, E. Vincent, J. Hammann, J. P. Bouchaud, and P. Nordblad, "Memory Interference Effects in Spin Glasses," *Physical Review Letters*, vol. 81, p. 3243, 1998.

[307] A. Bray and M. Moore, "Chaotic Nature of Spin-Glass phase," *Physical Review Letters*, vol. 58, pp. 57–60, 1987.

[308] D. S. Fisher and D. A. Huse, "Nonequilibrium Dynamics of Spin Glasses," *Physical Review B*, vol. 38, pp. 373–385, 1988.

[309] P. Sibani and K. H. Hoffmann, "Hierarchical Models for Aging and Relaxation of Spin Glasses," *Physical Review Letters*, vol. 63, pp. 2853–2856, 1989.

[310] E. Granado, J. W. Lynn, R. F. Jardim, and M. S. Torikachvili, "Two-dimensional Magnetic Correlations and Partial Long-range Order in Geometrically Frustrated Sr_2YRuO_6," *Physical Review Letters*, vol. 110, p. 017202, 2013.

[311] Z. Fu *et al.*, "Coexistence of Magnetic Order and Spin-glass-like Phase in the Pyrochlore Antiferromagnet $Na_3Co(CO_3)_2Cl$," *Physical Review B*, vol. 87, p. 214406, 2013.

[312] A. K. Bera, S. M. Yusuf, A. Kumar, M. Majumder, K. Ghoshray, and L. Keller, "Long-range and Short-range Magnetic Correlations, and Microscopic Origin of Net Magnetization in the spin-1 Trimer Chain Compound $CaNi_3P_4O_{14}$," *Physical*

Review B, vol. 93, p. 184409, 2016.

[313] A. K. Bera, S. M. Yusuf, A. Kumar, and C. Ritter, "Zigzag Antiferromagnetic Ground state with Anisotropic Correlation Lengths in the Quasi-two-Dimensional Honeycomb Lattice Compound $Na_2Co_2TeO_6$," *Physical Review B*, vol. 95, p. 094424, 2017.

[314] K. Tomiyasu, J. Fukunaga, and H. Suzuki, "Magnetic Short-range Order and Reentrant-spin-glass-like behavior in $CoCr_2O_4$ and $MnCr_2O_4$ by Means of Neutron Scattering and Magnetization Measurements," *Physical Review B*, vol. 70, p. 214434, 2004.

[315] C. N. R. Rao, A. Sundaresan, and R. Saha, "Multiferroic and Magnetoelectric Oxides: The Emerging Scenario," *Journal of Physical Chemistry Letters*, vol. 3, pp. 2237–2246, 2012.

[316] S. M. Yusuf and A. Kumar, "Neutron Scattering of Advanced Magnetic Materials," *Applied Physics Reviews*, vol. 4, p. 031303, 2017.

[317] C. Ederer and N. A. Spaldin, "Weak Ferromagnetism and Magnetoelectric Coupling in Bismuth Ferrite," *Physical Review B*, vol. 71, p. 060401, 2005.

[318] D. J. Breed, K. Gilijamse, J. W. E. Sterkenburg, and A. R. Miedema, "Ordering in Two- and Three-dimensional Diluted Heisenberg Antiferromagnets," *Journal of Applied Physics*, vol. 41, pp. 1267–1268, 1970.

[319] Jaun Rodríguez-Carvajal, "Tutorial on Magnetic Structure Determination and Refinement using Neutron Powder Diffraction and FULLPROF," France, 2014.

[320] R. Ranjan, "Structural Phase Transitions in (Sr,Ca)TiO_3 Ceramics," Ph.D. Thesis, *SMST, IIT (BHU)-India*, 2000.

List of Publications:

1. **Arun Kumar**, S. D. Kaushik, V. Siruguri and Dhananjai Pandey, "Evidence for two spin-glass transitions with magnetoelectric and magnetoelastic couplings in the multiferroic $(Bi_{1-x}Ba_x)(Fe_{1-x}Ti_x)O_3$ system" ***Phys. Rev. B 97, 104402 (2018).***
2. **Arun Kumar** and Dhananjai Pandey, "Magnetoelectric spin-glass transition(s) in pure and disordered $BiFeO_3$" ***AIP Advances 8, 101409 (2018).***
3. Anar Singh, **Arun Kumar** and Dhananjai Pandey, "Effect of synthesis route on structure and dielectric properties of $(1-x)BiFeO_3$-$xBaTiO_3$ solid solutions and its phase diagram" ***J. Appl. Phys. 124, 224101 (2018).***
4. **Arun Kumar**, A. Senyshyn and Dhananjai Pandey, "Evidence for cluster spin-glass phase with precursor short-range antiferromagnetic correlations in the B-site disordered $Ca(Fe_{1/2}Nb_{1/2})O_3$ perovskite" ***Phys. Rev. B 99, 214424 (2019).***
5. P. A. Kumar, **Arun Kumar**, Keshav Kumar, G. Anandha Babu, P. Vijayakumar, S. Ganesamoorthy, P. Ramasamy and Dhananjai Pandey, "Evidence for Spin-Glass Transition in Hexagonal-$DyMnO_3$ without Substitutional Disorder" ***J. Phys. Chem. C 123, 30499 (2019).***
6. **Arun Kumar**, Preetam Singh, Ram Janay Choudhary and Dhananjai Pandey, "Effect of Mn-doping on the low temperature magnetic phase transitions of $BiFeO_3$" ***J. Alloys and Compd. (Submitted).***